

Peeking and poking at a new quantum fluid: Studies of gaseous Bose-Einstein condensates in magnetic and optical traps

by

Dan M. Stamper-Kurn

Submitted to the Department of Physics
in partial fulfillment of the requirements for the degree of

Doctor of Philosophy

at the

MASSACHUSETTS INSTITUTE OF TECHNOLOGY

February 2000

© Massachusetts Institute of Technology 2000. All rights reserved.

Author Department of Physics
November 15, 1999

Certified by Wolfgang Ketterle
Professor
Thesis Supervisor

Accepted by Thomas J. Greytak
Professor, Associate Department Head for Education

**Peeking and poking at a new quantum fluid: Studies of gaseous
Bose-Einstein condensates in magnetic and optical traps**
by
Dan M. Stamper-Kurn

Submitted to the Department of Physics
on November 15, 1999, in partial fulfillment of the
requirements for the degree of
Doctor of Philosophy

Abstract

Bose-Einstein condensates of a dilute atomic gas were explored as a testbed for theories of the weakly interacting Bose gas, as a source of coherent matter waves, and as a new quantum fluid. A dc magnetic trap, various optical probing and manipulation techniques and an optical trap were developed for this work.

The density and momentum distributions and the interaction energies of ultra-cold Bose gases were measured and found to agree with mean-field theory. The reduction of the condensate fraction due to interactions was observed using a trapping potential created by magnetic and optical forces.

The formation of a Bose-Einstein condensate in a super-cooled Bose gas was time resolved, and showed evidence for bosonic stimulation. The reversible formation of a Bose-Einstein condensate through an adiabatic change in the trapping potential was predicted and demonstrated.

Excitations in a Bose gas were studied in various regimes. The speed of Bogoliubov sound was measured as a function of condensate density. The frequency and damping rates of collective excitations of both the condensate and the non-condensed cloud were measured over a wide temperature range, providing a critical test of mean-field theory and challenging finite-temperature descriptions. The onset of hydrodynamic oscillations was observed.

The dynamic structure factor of a Bose-Einstein condensate was measured by stimulated light scattering. Excitations in the free-particle and phonon regime were accessed, allowing for a measurement of the coherence length, a spectroscopic determination of the excitation spectrum, and the observation of suppressed small-angle light scattering.

The development of an all-optical trap for Bose-Einstein condensates led to the creation of spinor condensates, which are described by a vectorial order parameter. Ground-state spin structures were studied and a spin-domain diagram for their description was developed. Metastable Bose condensates were observed, caused by energy barriers much smaller than the temperature of the trapped gas. Metastable spin domains were found to decay to the ground state via quantum tunneling. The tunneling rates served as a probe for the structure of spin-domain boundaries.

Thesis Supervisor: Wolfgang Ketterle
Title: Professor

In the Jewish tradition, a Hebrew prayer is traditionally recited upon reaching an important and joyous milestone in which one thanks God for giving us life, sustaining us, and bringing us to this day.

Likewise, I would like to give thanks to all my teachers who helped create me as I am, encouraged my growth, and enabled me to finish this task.

To them I dedicate this work.

Acknowledgments

I would like to thank Wolfgang Ketterle for taking on the job of teaching me how to be a scientist. Wolfgang taught most powerfully by example through his focused leadership, his ability to distill the most basic and important constituents from a murky scientific puzzle, his manner of attentively listening to his colleagues, and his sparkling enthusiasm for science. At the pace of the last few years, we were both stretched to quickly learn about a wide range of topics as they came up in our research, and it has been a pleasure to develop together an insight and understanding of new physics.

I am grateful to have had the opportunity to collaborate at MIT with an impressive cadre of researchers. I relied heavily on the experience and leadership of fellow graduate students Marc–Oliver Mewes and Michael Andrews whose perseverance and ingenuity produced the reliable experimental infrastructure which enabled our later research. Dallin Durfee has been a dependable colleague and friend throughout my years at MIT, and I am grateful for his many lessons on experimental techniques and the countless times he lightened the mood with his wit. From Klaasjan van Druten and Christopher Townsend, postdocs in our group during my first years of research, I learned about the careful methodology of science and about the value of clearly communicating new ideas with one’s colleagues. I also thank Everest Huang and Charles Sestok for their many experimental contributions.

One member of the group whose support and friendship has been most valuable to me is Hans–Joachim Miesner. Soon after he joined our group as a postdoc, Hans and I joined in a close collaboration which was extremely fruitful, leading to many of the publications discussed in this dissertation. We were later joined by Ananth Chikkatur who has made important contributions since the summer before he started his inevitably brilliant graduate career. The companionship of Hans and Ananth was invaluable as we headed into so many late nights with the experiment, strung out by bad coffee, giddy with exhaustion, and buoyed by humor. I also thank Shin Inouye for his ceaseless contributions and his kindness, and Jörn Stenger for the example he set by his remarkable focus and leadership and for his liberal adaptations of the English language. I am grateful for being able to work with Deep Gupta, Axel Görlitz, and Tilman Pfau, who provided hard work and important insights to our most recent work. Finally, I’d like to thank Dave Pritchard who brought experience and an uncanny intuition when he began “officially” collaborating with the Ketterle group, but whose advice has been important to me throughout my graduate schooling.

It has been a pleasure to work with the creators of the “new lab” in the Ketterle group: Dallin Durfee, Chandra Raman, Roberto Onofrio, Chris Kuklewicz, Johnny Vogels, Michael Köhl, Zoran Hadzibabic and Jeff Gore. Having a second Bose–Einstein condensation experiment next door has greatly enriched my research, and I am grateful for the many insights we shared about experimental approaches and about new ideas. It was wonderful to see their efforts come to fruition with the completion of seminal experiments on surface excitations and superfluidity.

I also want to express my thanks to Carol Costa who helped me navigate the MIT bureaucracy, who enabled the important communication with our colleagues with a fortunate flood of reprints and preprints, but whose most important contribution was making the second floor of building 26 a friendlier place to spend one's days. I appreciate the help of the resourceful Gerry Power, the dependable Maxine Samuels, and the rest of the RLE staff.

Finally, I want thank my family and friends who made it possible for me to begin this work and to finish it. My parents Nurith and David and my sisters Carmit and Morli are my primary teachers. They have given me the most important tools for this task: curiosity, intelligence, patience and compassion. I thank my new sisters Juliet and Alison, my new brothers Mark and Jason, and Naomi and Bob for sharing their lives and endowing my life with more meaning and joy. I also thank little Benjamin for pointing out another way in which I have now become a teacher. My dear friends around Boston and around the globe have encouraged my growth, supported my spirits and rejoiced in my accomplishments. I am grateful for their love.

My lover and best friend Marjorie deserves my deepest gratitude. She tended my soul during times of great challenge and doubt and was understanding and patient with my work as we navigated this long road together. I am grateful to be traveling with her and happy to embark on our next journey.

This work was supported by the National Science Foundation (NSF), the Office of Naval Research (ONR), the Army Research Office and the Joint Services Electronics Program (JSEP) of the Army Research Office (ARO), the National Aeronautics and Space Administration (NASA), and the Packard Foudation. I appreciate the support of a NSF Graduate Fellowship and a JSEP Graduate Fellowship.

Contents

1	Introduction	14
1.1	Ingredients	15
1.1.1	Basic statistical mechanics — molecular chaos	15
1.1.2	Quantization of states	16
1.1.3	Indistinguishability of bosonic particles	16
1.2	Recipe	18
1.3	Ultra-cold and ultra-slow atoms	19
1.4	Macroscopic quantum mechanics	21
1.5	Outline of this thesis	22
2	From blackbodies to Boulder: the making of Bose–Einstein condensation	24
2.1	Discovery of Bose–Einstein condensation	25
2.2	Superfluidity and volume 141 of the journal <i>Nature</i>	29
2.3	Two two-fluid models	30
2.4	A tractable model for helium	31
2.5	The experimental pursuit of Bose–Einstein condensed gases	32
2.5.1	Spin-polarized hydrogen	33
2.5.2	Laser-cooled alkali atoms	33
3	The nuts and bolts of making a Bose–Einstein condensate	37
3.1	Typical operation	38
3.2	Computer control	40
3.3	Vacuum chamber	42
3.4	Optics	45
3.5	The cloverleaf magnetic trap	50
3.5.1	Spherical quadrupole traps and their modifications	52
3.5.2	Ioffe–Pritchard traps	53
3.5.3	Design considerations	54
3.5.4	Description of the cloverleaf trap	57
3.5.5	Operation of the cloverleaf trap	60

3.5.6	Properties of magnetically-trapped clouds in the linear and harmonic confinement regimes	61
3.6	Tools for manipulating Bose–Einstein condensates	63
3.7	Probing	65
3.8	The life of a Bose–Einstein condenser	70
4	Quantitative analysis of images	72
4.1	Thermal clouds above the BEC transition temperature	74
4.2	Bose–Einstein condensates at zero–temperature	75
4.2.1	Ideal–gas limit	75
4.2.2	Thomas–Fermi limit	76
4.3	Partly condensed clouds	77
4.4	Column densities	77
4.5	Extracting static quantities	78
4.6	Extracting dynamic properties	80
4.7	Comparison of time–of–flight and <i>in situ</i> images	81
5	Basic condensate physics	84
5.1	Introduction to a sodium Bose–Einstein condensate	84
5.2	The Bose–Einstein distribution	87
5.3	Bose–Einstein condensation of a trapped ideal gas	89
5.4	Density and momentum distributions of a non–condensed Bose gas	90
5.5	Critical temperature and condensate fraction	91
5.6	Effects of interactions	94
5.7	Non–zero temperature	96
6	Irreversible and reversible formation of a Bose–Einstein condensate	98
6.1	Formation of a Bose–Einstein condensate in a super–cooled vapor	99
6.2	Reversible formation of a Bose–Einstein condensate by adiabatic changes in the trapping potential	101
6.2.1	New opportunities for studying the formation of Bose–Einstein condensates	105
7	Dynamic properties of a Bose–Einstein condensate	108
7.1	The Bogoliubov theory	109
7.2	Experimental overview from Varenna proceedings (Ref. [22])	113
7.2.1	Collisionless excitations in a homogeneous Bose gas	114
7.2.2	Collisionless excitations in an inhomogeneous, trapped Bose gas	116
7.2.3	Experiments on collective excitations near $T = 0$	116
7.2.4	Measurements of the speed of Bogoliubov sound	118
7.2.5	Collective excitations at non-zero temperature	120

7.2.6	First and second sound in a Bose gas	123
7.2.7	Challenges ahead	125
7.2.8	Other dynamic properties	125
7.2.9	Free expansion and large amplitude oscillations of a Bose-Einstein condensate	126
7.2.10	The search for persistent currents	127
7.2.11	Collapse of a negative scattering length Bose condensate	128
7.2.12	Formation and decay of the condensate	129
7.3	One-dimensional sound propagation	130
7.4	Variational approach to reducing the Gross-Pitaevskii equation to an effective one-dimensional equation	131
8	Probing and manipulating a Bose-Einstein condensate with optical Bragg scattering	137
8.1	Scattering atoms and matter waves	139
8.2	Measuring the dynamical structure factor of a many-body system	141
8.3	The dynamic structure factor of a Bose-Einstein condensate	143
8.4	Bragg scattering as a probe of correlations in the condensate	144
8.5	Mean-field theory determination of $S(\vec{q}, \omega)$	145
8.6	Bragg scattering in the free-particle regime	148
8.7	A measurement of the coherence length of a Bose-Einstein condensate	151
8.8	Near-field and far-field measurements of the coherence length of a Bose-Einstein condensate	153
8.9	Bragg scattering in the phonon regime	155
8.10	Suppression of light scattering from a Bose-Einstein condensate	157
9	An optical dipole trap for Bose-Einstein condensates	160
9.1	Overview from the Varenna proceedings, Ref. [22]	161
9.2	Optical setup	166
9.3	Transfer efficiency	166
10	Spinor Bose-Einstein condensates	170
10.1	The implications of rotational symmetry	172
10.2	Tailoring the ground-state structure with magnetic fields	176
10.3	Spin-domain diagrams: a local density approximation to the spin structure of spinor condensates	179
10.4	Experimental methods	180
10.5	The formation of ground-state spin domains in spinor Bose-Einstein condensates	182
10.6	Miscibility and immiscibility of spinor condensate components	185

10.7 Metastable states of spinor Bose–Einstein condensates	187
10.7.1 Metastable spin–domain structures	187
10.7.2 Metastable spin composition	189
10.8 Quantum tunneling	191
10.9 Field dependence of the structure of spin–domain boundaries	195
11 Conclusion	202
A Image processing	206
A.1 Absorption image processing	207
A.2 Phase–contrast image processing	208
B Method for the numerical calculation of the spin structure of domain boundaries	211
C Bosonic stimulation in the formation of a Bose–Einstein condensate	214
D Optical confinement of a Bose–Einstein condensate	218
E Collisionless and hydrodynamic excitations of a Bose–Einstein condensate	223
F Analytical description of a trapped semi–ideal Bose gas at finite temperature	228
G Reversible formation of a Bose–Einstein condensate	233
H Observation of metastable states in spinor Bose–Einstein condensates	238
I Quantum tunneling across spin–domains in a Bose–Einstein condensate	243
J Excitation of phonons in a Bose–Einstein condensate by light scattering	248
Bibliography	253

List of Figures

1-1	Enumerating non-degenerate and degenerate states of three socks in three drawers	17
1-2	Ultra-cold temperatures reached with a dilute-gas Bose-Einstein condensate	20
3-1	Main portion of the UHV chamber	43
3-2	Level diagram for ^{23}Na	46
3-3	Optical setup for generating light near the sodium resonance	49
3-4	Energies of hyperfine states of sodium in a magnetic field	51
3-5	How to make a Ioffe-Pritchard trap with planar coils	55
3-6	Planar winding patterns for a Ioffe-Pritchard trap	56
3-7	The cloverleaf magnetic trap	57
3-8	Cloverleaf trap circuit diagram	59
3-9	Dispersive imaging methods: dark-ground and phase-contrast imaging . . .	68
3-10	Late night with BEC	71
5-1	Phase-contrast images of trapped Bose gases across the BEC phase transition	86
5-2	Axial column density profiles from phase-contrast images	87
5-3	Typical equilibrium properties of trapped Bose gases produced in the cloverleaf trap	88
5-4	Observation of Bose-enhanced density distributions above the Bose-Einstein condensation phase transition	92
5-5	Observation of Bose-enhanced momentum distributions of a non-condensed gas	93
6-1	Adiabatic increases in phase-space density by deformation of a power law potential	103
6-2	The interaction energy can be made larger than the thermal energy in the “dimple” trap	105
6-3	Adiabatic cycling through the phase transition	106
6-4	Formation of a Bose condensate in an excited state by shock condensation .	107
7-1	Shape of low-lying collective excitations	117

7-2	$m = 0$ quadrupolar condensate oscillations viewed in time-of-flight	117
7-3	$m = 0$ quadrupolar condensate oscillations viewed <i>in-situ</i>	118
7-4	Observation of sound propagation in a Bose condensate	119
7-5	Speed of sound versus condensate peak density	119
7-6	Temperature dependent frequencies and damping rates of $m = 0$ quadrupolar oscillations of the thermal cloud and condensate	121
7-7	Frequency and damping rate of excitations of the thermal cloud between the collisionless and hydrodynamic limits	124
7-8	The shape of things to come: a high-lying (eight-node) axial excitation of a cigar shaped condensate	126
7-9	Aspect ratio of expanding Bose condensates	128
7-10	Picture of rotating condensates	128
7-11	The speed of propagating blips and dips	131
7-12	Time-of-flight images of sound propagation	132
8-1	Optical setup for Bragg scattering	149
8-2	Pictorial depiction of a quasi-condensate	152
8-3	Doppler width of the Bragg resonance as a function of the coherence length	153
8-4	Suppression of Rayleigh scattering from a Bose-Einstein condensate	159
9-1	Transfer of atoms from the magnetic to the optical trap observed in time-of-flight images	167
9-2	Transfer of atoms from the magnetic to the optical trap observed <i>in situ</i> . .	168
9-3	Efficiency of transfer from the magnetic to the optical trap	169
10-1	Constructing the ground-state $\langle F_z \rangle = 0$ spinor in a trap	177
10-2	Spin-domain diagrams for $F = 1$ spinor condensates	179
10-3	Probing spinor condensates	181
10-4	Ground state spin domains in $F = 1$ spinor Bose-Einstein condensates . .	183
10-5	Representation of ground-state spin-domain structures on the spin-domain diagram	184
10-6	Quantum bubbles: a metastable arrangement of alternating spin domains in a two-component condensate	188
10-7	Evolution of metastable domain sizes after state preparation	188
10-8	Energy barriers responsible for the metastability of spin domains	190
10-9	Decay of a metastable state by thermal relaxation and quantum tunneling .	193
10-10A	Comparison of the decay of metastable states at different densities	194
10-11	Tunneling across spin domains of constant height and variable width	196
10-12	Variation of the metastable state lifetime with magnetic field	197

10-13Numerical calculation of the spin structure at the domain boundaries at different magnetic fields	200
10-14Variation of the spin-domain boundary width with magnetic field	201
10-15Maximum fractional population of the $ m_F = -1\rangle$ state in the spin-domain boundary at different magnetic fields	201
A-1 Obtaining a reliable transmission image	207
A-2 Comparison of two normalization methods for phase-contrast images	210

List of Tables

3.1	New tools and new science	39
3.2	Typical experimental operation	40
3.3	Fields produced by the cloverleaf trap	60
3.4	Initial conditions in the magnetic trap before and after compression	63
4.1	Length scales for thermal clouds and condensates in trap and in time-of-flight	82
7.1	The nature of collective excitations of the condensate and the thermal cloud	115
7.2	Studies of sound in gaseous Bose-Einstein condensates	127
8.1	Conditions for Bragg scattering in the phonon and the free-particle regimes	156
9.1	Optical dipole traps: a light sampler.	163
10.1	Interaction parameters for the $F = 1$ spinor system	174

Chapter 1

Introduction

Too far into the early morning hours, three young men sit in a cold room, darkened save for the phosphor glow of computer screens. Behind them lurks a disorderly ton of steel and glass, layered with hours of care like a wedding cake, but interlaced as a chaotic tower of Babel. From the ceiling a tangled drapery conducts invisible instructions on thin wires, vigorous flows through thick cables, and coolth via algae-clotted pipes. Yet amid this intractable chaos, the whirring counterpoint of a dozen instruments and staccato flares of light conduct an orchestra of precise movements. The three listen intently, not so much to a physical sound, but rather to an abstract music which accompanies an unobserved dance of light and atoms. In this unimaginably cold spot, a new form of matter is born and reborn every minute.

For the past four years, I have taken my place among these three (or two, or five) late-night observers. Repeatedly I was drawn to these sessions, not by a yearning for long dark nights in an ordinary room, but rather by the thrill of an exploration in an extraordinary space. The heavy contraption which my colleagues and I tended was, in actuality, a vehicle to an uncharted corner of Nature's realm.

The focus of our exploration was the behaviour of a dilute, weakly-interacting gas. An ordinary gas is perhaps the simplest and best-understood many-body system, and would be an unlikely candidate for cutting-edge research. In the 19th century, statistical methods for describing the behaviour of a many-particle system were remarkably successful in accounting for the macroscopic properties of monatomic gases based on a microscopic atomistic view. Yet, under extreme conditions, this classical description of a gas proves inadequate: both the micro-model and the statistical methodology are replaced with a quantum mechanical description. With this, the gas undergoes a dramatic transition and manifests its quantum mechanical nature on a macroscopic scale.

This phenomenon, which has captivated me and many other explorers around the world, is called Bose-Einstein condensation. In this dissertation, I recall the tale of my journey to the extreme world of nanokelvin temperatures and quantum degeneracy in which a gaseous Bose-Einstein condensate was found. To begin, I will explain the motivation for this journey

with a discussion of the basic foundations and salient features of this wondrous substance.

1.1 Ingredients

Bose–Einstein condensation is a phase transition which can occur in a gas at extremely low temperatures. Many other types of phase transitions exist in which, generally, a physical system composed of many pieces can dramatically change its character. Common examples include the condensation of water from a gas to a liquid, or the formation of ice as water turns from liquid to solid. For most phase transitions, the details of the transition and of the different phases depend critically on specific interactions which exist between components of the many–body system. Some universal characteristics of phase transitions in different systems can be identified, but there are several universality classes.

In contrast, Bose–Einstein condensation results not from a specific type of interaction between particles in a gas, but rather from three basic physical principles:

1.1.1 Basic statistical mechanics — molecular chaos

While each particle in a many–body system evolves according to deterministic laws of motion, this specific behaviour becomes increasingly intractable as the number of particles increases. Nevertheless, such a system does have characteristic properties which do not change over time or for slightly different methods of preparation. For example, a cup of water contains about 10^{25} molecules of H_2O . The full specification of the position, orientation, and external and internal motion of each of these molecules would require knowing more than 10^{26} numbers. However, even without this detailed knowledge, we know that this half–pound of water has a volume of eight fluid ounces at room temperature and pressure regardless of when we make a measurement. Even if we stir the water in one cup and not another, bulk properties of both fluids will, after a sufficient time for equilibration, be identical.

Statistical mechanics provides the tools for connecting the gross properties of a system at or near equilibrium to the microscopic behaviour of its constituents. Its validity rests on one basic assumption, that a closed system is equally likely to be found in each microscopic configuration available to it. Bulk properties are found by averaging over all such configurations. Such properties can vary greatly from one configuration to another, but one generally finds that the behaviour of a system is determined by an overwhelming majority of configurations which have very similar properties. The connection between this premise and various thermodynamic properties is detailed in textbooks on statistical mechanics.

In the experiments described below, a collection of about 10^8 sodium atoms with an average energy of about 4×10^{-22} ergs ($3k_B T$ where k_B is Boltzmann’s constant, and $T = 1 \mu\text{K}$ is a typical temperature) is isolated in a magnetic container of a certain stiffness. These atoms can be configured in myriad ways. Yet, for an overwhelming majority of these,

a large number of the atoms cohabit the lowest quantum state in the container, forming a Bose–Einstein condensate. Upon every repetition of the experiment, the system is probed, and a Bose–Einstein condensate is always observed.

1.1.2 Quantization of states

A second ingredient for Bose–Einstein condensation is that the microscopic description of the many–body system be given by quantum mechanics. One approximate way in which quantum mechanics can be incorporated in the description of a system is through the Heisenberg uncertainty relation, which states that the momentum p and position x of a particle can only be determined simultaneously to precisions Δp and Δx such that $\Delta p \Delta x \geq \hbar$, where \hbar is Planck’s constant h divided by 2π . For example, the behaviour of a gas particle in a three–dimensional box is described classically by its coordinates in a six–dimensional phase–space, in which each of three momentum components and spatial coordinates are specified. In classical mechanics, the particle can inhabit any point in phase–space and is fully distinguished by that point. But according to the Heisenberg uncertainty relation, phase–space points which lie in the same phase–space cell of volume \hbar^3 cannot be distinguished. Such “coarse–graining” of phase space for the purposes of statistical mechanics is necessary even for the classical statistical description of a gas as given by Boltzmann and Gibbs. However, a quantum mechanical description defines these regions of statistical indeterminacy as reflecting the truly quantized behaviour of particles, and gives the phase–space cells a specific size.

In a fully quantum statistical approach, a system is described not by a continuum of phase–space points, or even by a semi–classical division of phase–space into cells, but rather by a definite set of discrete quantum states. In the context of Bose–Einstein condensation, the use of a fully quantum rather than a semi–classical statistics introduces finite–size effects in one, two, or three dimensions which can modify the nature of Bose–Einstein condensates and which would be interesting to explore experimentally [23–26].

1.1.3 Indistinguishability of bosonic particles

The final ingredient for producing a Bose–Einstein condensate, and the one which was historically the last to be identified, is the indistinguishability of identical particles. The statistical implications of indistinguishability are profound. For illustration, let us consider, as one typically does in learning combinatorics, the possible arrangements of N (say 3) socks in M (say 3) drawers. Let us distinguish between two possible types of arrangements: non–degenerate arrangements, in which one never finds more than one sock in each drawer, and fully degenerate arrangements, in which all socks are found in one specific drawer (ignoring the many other somewhat degenerate states). Given that all possible arrangements of the socks are equally likely, what is the likelihood of occurrence for each of these types of arrangements?

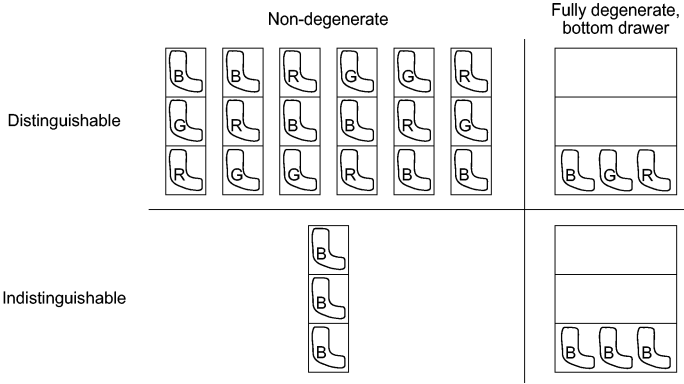


Figure 1-1: Enumerating non-degenerate and degenerate states of three socks in three drawers. In the top row, three distinguishable socks labeled as red (R), green (G), and blue (B) are arranged in three drawers. There are six ($N!$ for $N = 3$ socks) non-degenerate arrangements, and only one fully-degenerate bottom-drawer arrangement. Indistinguishability (bottom row) reduces the number of non-degenerate states by a factor of $N!$, making degenerate states more probable.

Consider first the familiar case of distinguishable socks. As shown in Fig. 1-1, the non-degenerate arrangements can be enumerated starting from some arbitrary placement of the socks. A new arrangement is then generated for each permutation of these socks. For example, exchanging the red sock for the green sock produces a new arrangement. In all, six possible non-degenerate arrangements are found. In contrast, there is only one arrangement of all the socks in the bottom drawer.

Now let us consider the case of indistinguishable socks. Again, one begins by an arbitrary placement of one sock in each of the drawers. As before, we may exchange socks in any of six permutations. However, these permutations do not produce new arrangements of the socks. This is not just a matter of incomplete knowledge reflecting our inability to see minute differences between the three socks. Rather, the quantum-mechanical principle of indistinguishability says that each of these arrangements are one and the same; there is only one non-degenerate arrangement. As for the fully-degenerate state, there is again only one possible arrangement, with one caveat: while it seems natural to allow many identical particles to inhabit the same quantum state, this is only possible for a specific class of particles called bosons which have integer spin. Particles with half-integer spin, called fermions, cannot cohabit a quantum state.

Comparing the two cases, we see that indistinguishability affects the statistics of a many-body system by reducing the number of non-degenerate states, and thereby increasing the relative weight of degenerate states. While for our case of three socks, the probability of the degenerate state was increased by a palatable sixfold, for arbitrary numbers of socks N , the increase is an enormous factor of $N!^*$.

*Do not try this at home! These metaphorical socks represent particles with identical constituents on

1.2 Recipe

To see how these three ingredients are combined to produce Bose–Einstein condensation, we might ask the question of when the factor of $N!$ decrease in the number of non-degenerate states is significant. Certainly if the total number of non-degenerate states is much larger than $N!$, these states will still be statistically favored, and degenerate states will remain very unlikely. The number of non-degenerate arrangements of N objects in $M > N$ quantum states is $M!/(M - N)!$, which becomes comparable to $N!$ only if $M \simeq N$. Thus, the recipe for Bose–Einstein condensation is to create a gas in which the number of available quantum states becomes equal to the number of particles.

Let us apply this criterion to the three-dimensional ideal Bose gas of volume V and temperature T by considering the number of quantum states which lie below an energy of $k_B T$. The condition $p_{max}^2/2m = k_B T$ gives $p_{max} = (2mk_B T)^{1/2}$ where m is the mass of each particle. The number of quantum states can be counted by dividing the available phase-space volume $\mathcal{V} = V \times 4\pi p_{max}^3/3$ by the volume of a phase-space cell \hbar^3 . Setting the number of particles N_c equal to the number of quantum states gives a critical particle density N_c/V at which the quantum statistics of indistinguishable particles favors a degenerate state:

$$\frac{N_c}{V} \simeq 1.3 \left(\frac{mk_B T}{2\pi\hbar^2} \right)^{3/2} \quad (1.1)$$

This simplified approach reproduces the true critical density for Bose–Einstein condensation within a factor of two (the leading numerical constant is replaced with 2.612).

Finding a physical system which is gaseous at proper densities and temperatures for Bose–Einstein condensation is not easy. For example, for a typical particle mass of 10 amu and taking the density of common materials as an upper bound ($\sim 10^{22} \text{ cm}^{-3}$), Bose–Einstein condensation would occur at temperatures below about 1 K. While within reach of large-scale cryogenic techniques, such temperatures would cause all known substances to liquefy or solidify in equilibrium, precluding a gaseous-phase Bose–Einstein condensate. This reflects the fact that interaction energies dominate over the thermal energy, creating long-range order (or short-range in the case of a liquid) which breaks the translational symmetry of a gas.

There are several strongly interacting systems which nevertheless behave as a gas, and thus manifest a form of Bose–Einstein condensation. For example, because of weak interactions between atoms and a low atomic mass, helium remains a liquid even at zero temperature. The helium atoms thus have enough translational freedom to undergo Bose–Einstein condensation, either directly as ${}^4\text{He}$ bosons, or by the pairing of ${}^3\text{He}$ atoms to form a composite boson. Similarly, electrons in metals or conduction electrons and holes in semi-conductors act as a nearly ideal gas inhabiting a periodic potential formed by the

an atomic level. The drawers represent single quantum states for both internal and external motion. Just getting two monatomic gas particles to cohabit the same quantum state was hard enough.

underlying lattice. As with ^3He , these constituents can form correlated pairs and Bose condense, leading to BSC-type superconductivity after the Cooper pairing of electrons, or to Bose–Einstein condensation of excitons (electron–hole pairs).

However, the study of gaseous Bose–Einstein condensates is still possible provided one relaxes somewhat the requirement of studying a substance in its true equilibrium state. A gas at the Bose–Einstein condensation transition temperature will eventually equilibrate to solid or liquid form, but the time for phase equilibration can be quite long provided the gas is sufficiently dilute. Bose–Einstein condensates can be formed and studied as long as motional equilibration occurs more quickly than phase equilibration.

This places daunting limits on the temperature which must be achieved to observe Bose–Einstein condensation. The rate of motional equilibration is limited either by the rate of elastic collisions (for local equilibrium), or by the frequencies of oscillation in the trap which holds the gas (for global equilibrium). The rate of phase equilibration is limited by the rate of inelastic three–body recombination collisions whereby a diatomic molecule is formed in the presence of a third atom which carries the excess energy and momentum. Requiring that the gas be stable for about a second requires densities lower than about 10^{15}cm^{-3} [†]. At this density, a million times less dense than air, Bose–Einstein condensation occurs at temperatures in the *microkelvin* range. Thus, to make a gaseous Bose–Einstein condensate, one takes a gas (say at room temperature) and lowers its temperature by a factor of a *billion* on timescales that are faster than the rate of phase equilibration.

1.3 Ultra–cold and ultra–slow atoms

The successful achievement of Bose–Einstein condensation in a dilute gas in 1995 was made possible by the development of novel cooling techniques, laser– and evaporative–cooling of neutral atoms, beginning in the 1980’s. With these methods, macroscopic samples (up to $\sim 10^{10}$ atoms in experiments on hydrogen [27]) could be cooled in minutes to a temperature regime which had never been attainable before. As shown in Fig. 1–2, various cryogenic techniques (Joule–Thompson expansion, evaporative cooling of ^4He , ^3He – ^4He dilution) are used in series to attain temperatures of about 10 mK, by which point many macroscopic quantum phenomena, such as superfluidity, superconductivity, and the quantum Hall effect, become accessible. Turning to evaporative cooling of neutral atoms has yielded temperatures which are lower by five orders of magnitude! Sub–recoil optical cooling and adiabatic demagnetization (of nuclear spins) have yielded even lower temperatures, but not yet in sufficiently dense gaseous systems for the study of Bose–Einstein condensation.

This remarkable advance in cooling technology can also be emphasized by considering the thermal velocity of gas atoms at various stages *en route* to Bose–Einstein condensation.

[†]The three–body recombination rate at low temperatures is given as Kn^2 where K is a rate constant and n the density. I use a typical value of $K = 10^{30}\text{cm}^6\text{s}$.

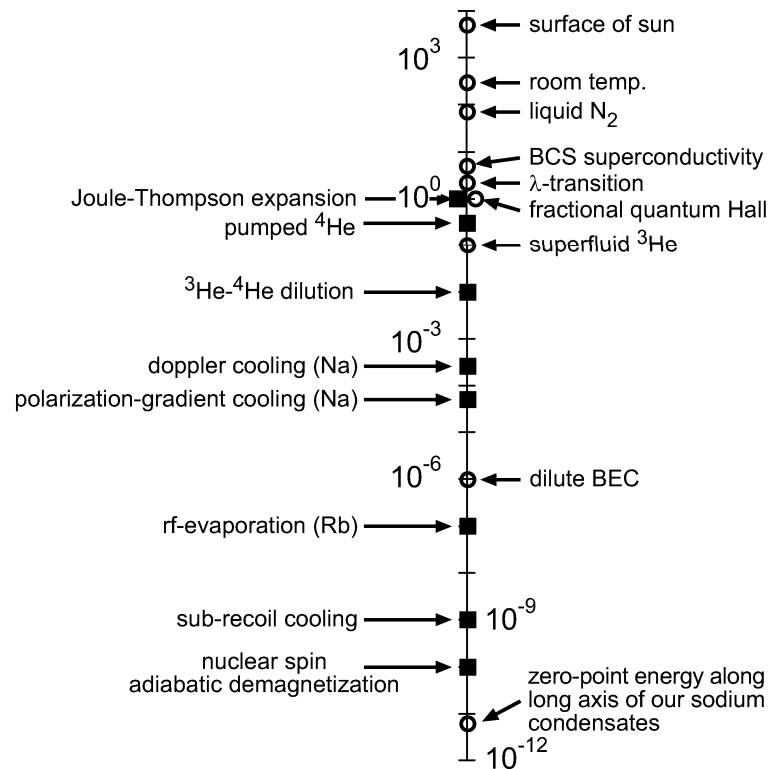


Figure 1-2: Ultra-cold temperatures reached with a dilute-gas Bose-Einstein condensate. Temperature benchmarks reached by different cooling techniques (squares), and at which various physical phenomena occur (circles) are shown on a logarithmic temperature scale labeled in Kelvin.

In the experiments described in this work, a sodium gas is generated in an oven at 260°C and thermal velocities $[(2k_B T/m)^{1/2}]$ of 620 m/s. After optical cooling to about 50 μK , the thermal velocity is reduced to just 19 cm/s. At the transition temperature of $\sim 1 \mu\text{K}$, the atoms are slowed to about 3 cm/s.

Further cooling causes the accumulation of atoms in the ground state of the trap in which they are held. This Bose–Einstein condensate contains no entropy and cannot sensibly be described as having a temperature. Nevertheless, trapped Bose–condensed atoms do have a momentum distribution of non–zero width [18]. Along the narrow dimension of the condensates in our experiments (10 μm radius), the typical velocity of the condensed atoms was a mere 0.5 mm/s. Along its long axis, a coherent condensate would have a velocity of 3 mm per minute, which is ten times slower yet. Thus, to summarize, in the experiments described in this work, about 10^7 sodium atoms were slowed down by seven orders of magnitude from velocities of 400 m/s to 3 mm per minute within a total cooling time of 30 seconds.

This slow velocity corresponds to a “temperature” of just 6 pK. This absurdly low value indicates that the behaviour of current Bose–Einstein condensates should be influenced by picokelvin–scale perturbations. For example, in the study of multi–component spinor Bose–Einstein condensates, metastable states were identified which persisted due to sub–nanokelvin energy barriers to equilibration.

1.4 Macroscopic quantum mechanics

This sudden transition from the microkelvin–scale transition temperature to a picokelvin–scale zero–point energy underscores a remarkable fact: Bose–Einstein condensation allows us to study matter at the level of a single quantum state at temperatures that are much higher than the spacing between quantum levels. Let us compare this situation with the requirements for preparing a single trapped atom (or ion) in the ground state of a trap. Given the spacing $\hbar\omega$ between energy levels in the trap, a single atom at a temperature T will be found in the ground state with a probability of $1 - \exp(-\hbar\omega/k_B T)$. Placing this atom in the ground state with high probability, as needed for the study of its motional quantum dynamics, requires cooling it to temperatures $k_B T \ll \hbar\omega$ at which the motional degrees of freedom are frozen out. In contrast, for a trapped gas of indistinguishable bosons, a macroscopic population of the ground state is statistically favored at much higher temperatures $k_B T \lesssim \hbar\omega \times N^{1/3}$ (in three dimensions).

In an ideal gas, the many–body wavefunction of N (a macroscopic number) Bose–condensed atoms is simply the product of N identical single–particle ground–state wavefunctions. This single–particle wavefunction is thus called the macroscopic (or condensate) wavefunction since macroscopic properties of the condensed gas are given by the quantum mechanical description of this one wavefunction and its dynamics. In an interacting sys-

tem, the ground-state many-body wavefunction becomes imbued with correlations between particles that lie beyond a simple product wavefunction description. Yet, as described by Bogoliubov [28] and refined by Penrose and Onsager [29], the concept of a macroscopic wavefunction retains its validity.

The macroscopic quantum behaviour of a Bose–Einstein condensate can be regarded as an ideal state preparation for studies and applications of quantum mechanics such as atom interferometry, coherent control, and quantum computation. For one, atoms are naturally prepared in the ground state of a trap which is a perfectly characterized initial condition for experiments. Second, a Bose condensate provides a large number of identically prepared atoms. Thus, rather than accumulating knowledge of the wavefunction through repeated measurements with single atoms, one can repeatedly sample the wavefunction by probing all the atoms (or even just a small fraction of them) at once, eliminating many sources of technical noise. In other words, rather than regarding the wavefunction as a probability distribution for repeated measurements on identically prepared systems, one can regard it as describing the density distribution of a gas. As such, repeated non-destructive measurements of the density of a condensate can be interpreted as a real-time visualization of the dynamics of a quantum system.

1.5 Outline of this thesis

In the following chapters, I summarize my contributions to the research on Bose–Einstein condensates which was conducted by my colleagues and I in the research group of Professor Wolfgang Ketterle at MIT. My aim is to complete the contextual background for this work, present some important aspects of the experiments which were not described in our publications, summarize some developments regarding our results since their publication, and provide some of my own perspective on the current and future directions of this field.

My graduate research at MIT was done in close collaboration with a capable and innovative group of scientists. In this dissertation, I focus on those projects to which I made significant contributions. Publications toward which I made leading contributions are reproduced in the appendices (ordered chronologically by publication date). Some topics, such as our earlier work (< 1997), our investigation of Feshbach resonances, and the recent observation of superradiance, I have decided not to discuss in depth, deferring to previous and future dissertations by others in my group who led those efforts.

This dissertation consists of three sections: the introductory section (Chapters 1 and 2), the technical section (Chapters 3 and 4), and the experimental section (Chapters 5 – 10).

Chapters 1 and 2 give a general, non-technical introduction to some of the basic features and the historical development of Bose–Einstein condensation. In reviewing some of the history of Bose–Einstein condensation, I have focused on the period leading to the theoretical discovery of Bose–Einstein condensation, attempting to trace the evolution of crucial

insights which led to Einstein’s prediction.

In Chapter 3, I describe the experimental apparatus which was used for our research, and the techniques which were developed for probing and manipulating (peeking and poking) Bose–Einstein condensates. Parts of this discussion, such as the description of the computer control system, the vacuum system, and the cloverleaf magnetic trap, are somewhat technical and are intended to serve current and future experimentalists in the field. After the description of the techniques used for imaging ultra–cold gases, including Appendix A on image processing, Chapter 4 reviews the methods by which we analyze those images and extract data.

The experimental section of this work begins with Chapter 5 which describes the static properties of Bose–Einstein condensates. Some unpublished measurements of the density and momentum distributions of non–condensed Bose gases which show quantum–statistical effects are presented. I also summarize the “semi–ideal” model of partly condensed gases which I developed in collaboration with Martin Naraschewski [13] (Appendix F).

Chapter 6 discusses two experiments which explored the process of condensate formation. In one, we time resolved the growth of a condensate in a super–cooled gas, and found evidence for the role of Bose–stimulated scattering in condensate formation [9] (Appendix C). In the second, a new method for increasing the phase–space density of a gas and crossing the Bose–Einstein condensation phase transition was demonstrated [14] (Appendix G). I also suggest some future experiments on the subject of condensate formation.

One major thrust of our research has been the study of the excitations of a Bose–Einstein condensate in various regimes. Chapter 7 summarizes this research. A large portion of the discussion is reproduced from a recent review paper [22], in which our study of collective excitations at non–zero temperature is discussed [12] (Appendix E). I also present some additional results from our observation of sound propagation [7, 8].

In Chapter 8, I present a comprehensive treatment of the use of Bragg spectroscopy for the study of Bose–Einstein condensates. After developing some concepts and deriving some theoretical predictions, I discuss the results of two publications: a study of Bragg scattering in the free–particle regime [18], and a study in the phonon regime [21] (Appendix J).

Chapter 9 briefly describes the use of an optical dipole trap to confine a Bose–Einstein condensate (Appendix D). A discussion of the salient features of this trap is reproduced from a review paper [22], and some further details about the optical setup and procedures are presented.

Finally, Chapter 10 is a thorough review of the experimental and theoretical study of spinor Bose–Einstein condensates. This chapter presents some of the basic features of this new quantum fluid. I discuss the results of three publications: a study of ground–state spin structures [15], the observation of metastable states [17] (Appendix H), and the study of quantum tunneling across spin domains [19] (Appendix I). At the end of the chapter, I present some unpublished work which explores the structure of spin domain boundaries.

Chapter 2

From blackbodies to Boulder: the making of Bose–Einstein condensation

The centennial meeting of the American Physical Society of the current year brought together thousands of physicists from around the world and scores of scientific luminaries who reflected on a hundred years of innovation and discovery. Coincidentally, the meeting also marked the (near) centennial of the first measurements of thermal blackbody radiation in the far-infrared. These measurements, of seemingly marginal importance at the time, effected a cascade of speculation and inference which led to the development of quantum mechanics, and thereby revolutionized our understanding of nature.

The topic of this dissertation, the behaviour of a quantum degenerate gas, finds its historical roots in these same measurements. In this chapter, I discuss several aspects of this hundred-year history, borrowing heavily from a variety of relevant historical accounts to which I refer the interested reader. History leading to the first prediction of Bose–Einstein condensation is discussed in works of Abraham Pais with a focus on Einstein’s role [30, 31]. Insightful articles by Oliver Darrigol [32, 33] and Alfred Kastler [34] trace the origins of the statistical-mechanical concepts which imply Bose–Einstein condensation. The first identification of Bose–Einstein condensation in the form of liquid helium is described by Kostas Gavroglou in a biography of Fritz London [35] and in an earlier article with Y. Goudaroulis [36]. The theoretical treatment of the interacting degenerate Bose–Einstein gas is chronicled in the monograph of Allan Griffin [37]. Further information on the experimental studies of ultra-cold atomic hydrogen can be found in various review articles [38–43]. The history of developments in laser cooling is nicely summarized in the addresses of Steven Chu [44], Claude Cohen-Tannoudji [45] and William Phillips [46] on the occasion of their award of the 1997 Nobel Prize in Physics.

2.1 Discovery of Bose–Einstein condensation

The phenomenon of Bose–Einstein condensation was first discussed by Albert Einstein in 1925, in the second of three papers which were catalyzed by a treatment by Satyendranath Bose [47] of thermal radiation as a photon gas. In direct analogy with Bose’s derivation, Einstein substituted the dispersion relation appropriate for a free massive particle while adding a constraint of particle conservation, which Bose had not considered. After his first paper [48], in which deviations between the thermodynamic properties of a classical gas and a non-degenerate Bose–Einstein gas (one without a condensate) were discussed, Einstein considered the case when the “degeneracy parameter” A (the fugacity $z = e^{\mu/k_B T}$) reached unity $A = 1$. He identified a limiting temperature T_0 , below which “a number of molecules steadily growing with increasing density goes over in the first quantum state (which has zero kinetic energy),” i.e. a Bose–Einstein condensate forms [49]. Together, Bose and Einstein are generally credited with the discovery of Bose–Einstein statistics, which they applied to both radiation (Bose) and matter (Einstein).

Yet, already at the turn of the century, Max Planck [50] correctly accounted for the blackbody spectrum (later treated by Bose) in response to the experimental observation [51, 52] of deviations from Wien’s spectrum in the far-infrared. Planck considered a collection of “resonators” which exchange energy with a thermal radiation field. To determine the thermodynamic properties (starting with the entropy) of such resonators, he suggested that one need only specify the energy of each resonator to the nearest integer in units of an energy quantum $h\nu$, where ν is the resonance frequency of the resonator, and h is a new physical (Planck’s) constant. The thermal radiation field was then determined statistically by enumerating the ways in which identical energy quanta can be distributed over the collection of resonators. With this, the essential elements of Bose–Einstein statistics — a statistical treatment of resonators, quantization, and indistinguishability of energy elements — were in place. Deviations from Wien’s spectrum, in which the photon occupation number per mode is given by a Boltzmann factor $e^{h\nu/k_B T}$, occur at frequencies ν and temperatures T such that $h\nu < k_B T$, where k_B is Boltzmann’s constant, implying an average of more than one photon per mode, i.e. quantum degeneracy. Thus, Planck’s calculation of the blackbody spectrum constitutes the first application of Bose–Einstein statistics in the quantum degenerate regime. Indeed, the deviations from Wien’s law observed in 1900 are exact analogues of the differences between the classical Maxwell–Boltzmann velocity distribution and the Bose–Einstein distribution at the transition temperature to Bose–Einstein condensation. Experimental observations of this phenomenon in a dilute gas are discussed in Sec. 5.4.

It is conceivable that Planck’s work could have been applied directly to an atomic gas. Already in the statistical treatment of a classical gas, Boltzmann and Gibbs had enumerated states of the gas only within energy or phase-space intervals within which all states were considered identical. Combined with Planck’s rule for the enumeration of states of a many-

body system, these concepts suffice for the “semi-classical” description of Bose–Einstein condensation (Sec. 1.1.2), specifically in the manner used by Einstein. In actuality, this development was delayed for a quarter century during which time a crucial and revolutionary development took place: the transformation of quantization and indistinguishability from the mathematical tools of statistical mechanics to true physical properties in a quantum mechanical world.

Let us return to the work of Planck to understand how Bose–Einstein statistics was used without the understanding of its general applicability. First, while Planck enumerated the states of a collection of resonators by counting energy in integer units, this step was not interpreted as reflecting a real physical quantization of energy. For example, Planck wrote “when this quotient ($E/h\nu$) is not an integer, P is taken to be a neighboring integer,” [53] i.e. while energy is continuous, it need only be specified to the nearest integer unit P for the sake of statistics. Second, while Planck’s subsequent enumeration of the distribution of energy quanta among a collection of resonators constituted an application of Bose–Einstein statistics, this step was not interpreted as based on indistinguishability. Insofar as Planck was dealing with the continuous distribution of energy rather than with a distribution of particles, his method of counting was obvious. Finally, since Planck chose to consider a particular set of resonators in contact with a radiation field rather than treat the radiation itself, the concepts of quantization and indistinguishability which were implicit in his work were not interpreted as properties of the electromagnetic field.

In the following years, physicists grappled with a disparate set of quantization rules which are known as the “old quantum theory,” and gradually connected Planck’s statistical method with physical properties. Progress can be divided into the development of three interpretations. First, the blackbody radiation spectrum was derived by considering explicitly the radiation field itself, rather than the resonators of Planck. Einstein noted that Wien’s law for the blackbody spectrum implied a non-classical result wherein the equipartition of energy was violated for high frequency radiation (1904), and later solved this by the introduction of the light–quantum (1906). Later, both Ehrenfest [54] and Debye [55] rederived Planck’s radiation law by considering electromagnetic waves in a cavity, and showed the necessity of quantizing the energy in each mode.

Second, starting with Einstein’s light–quantum hypothesis (the heuristic argument for which relied on classical statistics and number conservation [33]), a corpuscular theory of electromagnetism was reborn. From the photoelectric effect, the light–atom (*Lichtatome*) was endowed with a discrete energy. From considerations of radiation pressure, photon recoil, and the Compton effect, the photon was endowed with momentum as prescribed by relativity for a massless particle. Before such concepts were sufficiently developed, the unification of the statistics of radiation and of gases, which Einstein accomplished in 1924, was unlikely.

Finally, once radiative energy quanta became pictured as particles, the connection be-

tween Planck's radiation formula and the notion of indistinguishability was revealed. In particular, in 1911, Ladislas Natanson clearly laid out three possible statistical assumptions that can be made in enumerating states of a many-particle system (of course, not including the Pauli exclusion principle), and identified Planck's counting with the “collocation mode” (*Anordnungsart*) in which indistinguishable particles (energy quanta or photons) are distributed over distinguishable cells (resonators or cavity modes). Regarding the indistinguishability of photons he wrote: “we have in fact no other possibility for justifying Planck's method of calculating a probability, except for the appeal to the experimental proof, by which the conclusions of the calculation are found to be supported.” Thus, he identified indistinguishability as an independent axiom, which appeared to have been experimentally established [34, 56].

What remained to facilitate the jump from blackbody radiation to Bose–Einstein condensation in a gas was the concept of a photon gas. In 1913, Wolfke introduced this concept by considering radiation pressure and then the blackbody spectrum as being due to light-atoms, stating that “since all light-atoms are mutually identical, it does not matter which light-atoms are found in a given state, but only how many of them.” [57] Bose completed the separation between classical electromagnetism and corpuscular photons by replacing the discrete cavity modes with phase-space cells of volume \hbar^3 , and thereby reproduced the classical expression for the density of states of radiation [58].

In Bose's work, no explicit mention is made of the concept of indistinguishability. This has led some to speculate that the correct photon statistics used in his calculation were a serendipitous mistake [33, 59]. Yet, given the great body of work discussed above and the clear (but brief) description of his counting method, Bose may have just been adopting a consensus view and therefore not choosing to elaborate on this concept. The clear identification of an indistinguishability axiom was made by Einstein only in his second paper on the Bose–Einstein gas, in response to objections raised by Ehrenfest. Einstein commented that Bose's combinatorics “expresses indirectly a certain hypothesis of a mutual influence between molecules; presently this difference is quite mysterious.” [49] Contemporaneously, in a letter to Schrödinger, he wrote “I have applied a special statistics which, at the moment, cannot be justified by anything but success... the molecules appear not to be localized in a mutually independent way; instead they prefer to share a cell with another molecule.” [60]

Finally, with the development of matrix and wave mechanics, the indistinguishability of particles was connected to symmetry properties of a wavefunction. Defining indistinguishability (still taken as an axiom regarding elementary particles) as the invariance of all observables under exchanges of particles, two fundamental statistics arise: Bose–Einstein statistics in which many particles can occupy the same mode, and Fermi–Dirac statistics in which they cannot. Indistinguishability had thus acquired “legal status” as a fundamental physical property, and was thereafter built into theories of quantized fields and the method of second quantization.

Thus, the prediction of Bose–Einstein condensation was obtained by a rather circuitous route. Nature had left a readily accessible calling card for quantum degeneracy in the form of low–frequency blackbody radiation. In the 25 years after receiving this calling card, physicists discovered energy quantization, atoms of light, and the indistinguishability of elementary particles. Only then could the lessons from thermal radiation be construed as a message regarding the behaviour of matter.

It is somewhat puzzling, in hindsight, that the prediction of Bose–Einstein condensation was not obtained by the more direct route of applying indistinguishability to the material gas. The apparent indistinguishability of molecules in a gas was already posited by Gibbs as early as the 1870’s. Gibbs saw that distinguishable particles would contradict the apparent extensivity (proportionality to the size of a system) of entropy. He considered different axioms regarding the enumeration of states of a system, differentiating between “specific” phases in which the state of each particle is specified, and “generic” phases in which permutations of identical particles are disregarded. Regarding a fluid of identical particles divided into volumes, he wrote “the entropy of the whole is equal to the sum of the entropies of the parts. Suppose a valve is now opened [*between the two volumes*]... We do not regard this as making any change in the entropy... It is evident, therefore, that it is equilibrium with respect to generic phases, and not with respect to specific, with which we have to do in the evaluation of entropy.” [61] For particles existing in a continuous phase space, however, the axiom of indistinguishability simply adds a factor $1/N!$ in the enumeration of states of N particles, since in a continuous phase space, two particles have zero probability of exactly sharing a phase–space point. Thus, all states are non–degenerate, and the axiom of indistinguishability reduces the number of many–particle states by $1/N!$, but does not change the probability of occurrence of different states. The consequence is only one of properly defining the entropy.

Even in the quantum age, as the statistically convenient phase–space cell was recognized as a true quantization of action, indistinguishability continued to be applied in the old classical manner. For example, in attempting to prove that the entropy of an ideal gas satisfies Nernst’s theorem (zero entropy at zero temperature), Terode identified all phases of a many–particle system in a phase–space cell with volume $\propto h^{3N}$ with a discrete quantum state. Yet, in spite of such quantization, indistinguishability was still applied as if the system were continuous, resulting only in a global reduction of the number of many–particle states. In other words, the effect of indistinguishability on quantum statistics depends on the relative order in which indistinguishability and quantization are applied. Terode (and later Planck in his own quantum theory of gases) first accounted for permuted phases as if the gas were classical, and then accounted for quantization. When performed in the opposite order, Bose–Einstein statistics results.

2.2 Superfluidity and volume 141 of the journal *Nature*

Einstein's prediction of condensation in a Bose–Einstein gas soon acquired “the reputation of having only a purely imaginary existence” [62] for several reasons. For one, after the discovery of Fermi–Dirac statistics, it was unclear which statistics should apply to an ideal gas [31]. Other objections (by Uhlenbeck, for example) stemmed from the incomplete development of statistical concepts such as the thermodynamic limit and high-order phase transitions. But most importantly, no quantum degenerate material gas to which Einstein's theory might apply could be found — every known substance had solidified or, in the case of helium, liquefied at temperatures above the degeneracy temperature.

In truth, the “imaginary” Bose–Einstein condensation had a real manifestation, even at the time of Einstein's prediction, in superfluid helium. In 1908, helium was liquefied by the team of Kamerlingh Onnes in their first operation of a cryogenic system dedicated to the task. In an effort to create solid helium, the Leiden researchers continued to pump on the first helium liquid, lowering its temperature below the 2.2 K superfluid transition temperature (the λ -point) [63, 64]. While the achievement of such low temperatures led to years of successful experiments at Leiden, including the discovery of superconductivity, the peculiar properties of their refrigerant were not explored in earnest until the 1930's. Disparate signs of a phase–transition were reported, primarily by Keesom, such as an abrupt change in the specific heat, a sharp rise in the heat conductivity, and the sudden ability of the liquid to pass through small leaks.

Volume 141 of the journal *Nature* (1938) chronicles the identification of the first quantum fluid and the rebirth of Bose–Einstein condensation. On **January 8**, Kapitza in Moscow [65] and Allen and Misener in Cambridge, England [66] reported measurements of the viscosity of liquid helium by measuring the velocity of flow through narrow channels. Previous measurements using rotating disks had noted a gradual decrease in the viscosity below the helium I (normal fluid) to II (superfluid) phase transition. The Kapitza, Allen and Misener measurements were dramatically different: the viscosity of helium II was at least 1500 times smaller than that of helium I. The upper bound measured for the viscosity was “already very striking, since it is more than 10^4 times smaller than that of hydrogen gas (previously thought to be the fluid of least viscosity). The present limit is perhaps sufficient to suggest, by analogy with superconductors, that the helium below the λ -point enters a special state which might be called a ‘superfluid’.” [65]. The novel properties of helium II were underscored in the **February 5** issue with the report of Allen and Jones of the fountain effect. A tube packed on one end with a fine powder (providing narrow channels for flow) was immersed in helium with one end protruding above the liquid level. Heating the submerged end (by exposure to a flashlight) produced a steady jet of helium from the top of the tube [67].

On **April 9**, Fritz London resurrected Bose–Einstein condensation as an explanation for superfluid helium. Previous explanations for liquid helium had involved a possible lattice

configuration of the atoms, combined with a large zero-point motion which delocalizes the atoms. London suggested that, similar to delocalized electrons in metals, helium atoms move freely in a self-consistent periodic field and inhabit Bloch states with a quadratic particlelike dispersion relation and some effective mass. Unlike for fermionic electrons in a metal, though, one must use Bose-Einstein statistics in describing this effective gas of helium bosons, and therefore a momentum-space condensation is possible. Taking the effective mass to be the mass of a helium atom (for lack of a better estimate), a degeneracy temperature (3.1 K) close to the λ temperature (2.2 K) was obtained [62]*.

Based solely on London's work, the connection between the predicted Bose-Einstein condensation of an ideal gas and a phase transition in a strongly interacting liquid was tenuous. Even after a more detailed paper in which London rederived Bose-Einstein condensation and treated the specific heat at the phase transition [68], the only evidence for this connection was a coincidence of temperatures.

On **May 21**, Laslow Tisza made London's daring idea much more compelling. Bose-Einstein condensation allows for an effective distinction between two parts of a fluid: the condensed part (the superfluid) which occupies the lowest energy level, and the remaining part (the normal fluid) which occupies various excited states. As Tisza wrote, “atoms belonging to the lowest energy state do not take part in the dissipation of momentum. Thus, the viscosity of the system is entirely due to the atoms in excited states.” [69] Applying this two-fluid model, Tisza provided qualitative explanations for the different viscosity measurements and the fountain effect, and predicted the mechano-caloric effect (superfluid flow through a narrow channel causes a temperature gradient) and temperature waves (antisymmetric oscillations of the normal fluid and the superfluid, later called second sound). Thus, while its connection to liquid helium was unsubstantiated, Bose-Einstein condensation provided an intermediate conceptual framework (two-fluids) with which to regard superfluid helium as a macroscopic quantum system [36].

2.3 Two two-fluid models

On the other hand, rather than appealing to a questionable microscopic picture of liquid helium as a gas, one could justify a two-fluid model by its empirical success. This empirical approach characterized the quantum-hydrodynamical description proposed by L.D. Landau in 1941. Rather than beginning with a microscopic description of atomic motion, Landau directly treated the macroscopic hydrodynamic properties of the liquid such as density, current, and velocity, and then postulated their direct quantization. Helium is effectively divided into two fluids where the superfluid is the background structure which supports a collection of elementary excitations which behave as a normal fluid. In this context, detailed

*K. Gavroglou notes that discussions of degeneracy effects and Bose-Einstein statistics in liquid helium occurred earlier between M.C. Johnson and Lennard-Jones at a meeting of the Physical Society of London on February 14, 1930, but were not followed up (see Ref. [35], p. 177, note 50).

measurements by Kapitza and Andronikashvili were used as an empirical determination that the elementary excitations of the liquid were phonons at low momenta, and “rotons” at higher momenta.

One can regard these two different descriptions of liquid helium as the attempt to understand the properties of a liquid by extrapolation from one of two well understood extremes. The London–Tisza model approximated liquid helium as an imperfect gas, and assumed that the ideal–gas prediction of Bose–Einstein condensation retained its basic character in the presence of interatomic interactions. In contrast, in the Landau theory, liquid helium is treated in analogy with a solid where the superfluid takes the place of a crystal lattice, and the phonon–roton excitations take the place of lattice vibrations. In Landau’s words, “every consideration of the motion of individual atoms in the system of strongly interacting particles is in contradiction with the first principles of quantum mechanics.” [70] In effect, though, both theories resulted in a similar macroscopic picture of two fluids, and the modern view of superfluidity lies in a compromise between them.

The major quantitative difference between the two theories was the dispersion relation at low momentum, which was quadratic in the gas–like Tisza model, and linear in the solid–like Landau model. This gave different and experimentally testable predictions for the speed of second sound at low temperatures where the low energy portion of the excitation spectrum is most relevant. After preliminary experiments by Peshkov [71], Pellam and Scott confirmed Landau’s prediction in magnetically cooled helium [72]. With the advent of neutron scattering experiments in the 1950’s, the phonon–roton spectrum proposed by Landau was confirmed. Contemporaneously, though, the fermionic isotope ^3He became available as a result of the development of nuclear weaponry and showed no signs of superfluidity, confirming “by experiment the relevancy of the Bose–Einstein way of counting, without entering into the obscurities of complicated and approximate calculations.” [73]

2.4 A tractable model for helium

The gap between these two approaches was bridged by an imaginary substance (until 1995): the weakly interacting degenerate Bose gas. This theoretical substance was first treated by Bogoliubov in a paper which marked the birth of the many–body problem [74], and established the framework for understanding modern–day gaseous Bose–Einstein condensates. Bogoliubov showed that Bose–Einstein condensation in an interacting gas required that the excitations of the system be transformed from those describing the motion of single atoms to those describing the fluid as a whole. Furthermore, the excitation spectrum for these quasi–particles was linear at low momentum in accord with Landau’s description of liquid helium, and thus gave a microscopic explanation for superfluidity. The Bogoliubov theory is presented essentially in its original form in Sec. 7.1.

In the following years, the theory of the degenerate dilute Bose gas was developed exten-

sively as a model for understanding properties of liquid helium. Lee, Yang and Huang borrowed the concept of a pseudo-potential from nuclear physics to refine the Bogoliubov theory and extend its scope to the hydrodynamic regime. Beliaev developed a field-theoretical approach to describing the Bose gas which allowed for detailed calculations and introduced the key theoretical concepts of broken symmetries and connections between microscopic and macroscopic quantum phenomena. These and other key theoretical developments are treated by Griffin in Ref. [37].

With this work on the weakly interacting Bose gas, the history of Bose-Einstein condensation in strongly interacting systems diverges from that of direct relevance to modern-day gaseous condensates. Other crucial developments took place which were more specific to the study and understanding of liquid helium. Neutron scattering was used to finally reveal microscopic properties of liquid helium [37, 75, 76]. Work by Feynmann, Penrose and Onsager provided an interpretation for the macroscopic wavefunction of an interacting system (leading naturally to the prediction of quantized vorticity) and a physical picture for the elementary excitations of helium. In particular, based on the work of Bogoliubov, a critical differentiation was made between the superfluid fraction and the fractional population of a single quantum state. Penrose and Onsager [29] estimated that while the superfluid fraction in liquid helium approaches unity at zero temperature, the condensate fraction reaches only about 10%, a prediction that has stood the test of time.

Also important are the identification of the role of Bose-Einstein condensation in cold fermionic systems due to the pairing of fermions to form composite bosons. Thus, both superconductivity and the superfluid phases of ^3He at millikelvin temperatures can be regarded as Bose-Einstein condensation phenomena. These phenomena not only have direct relevance for current experiments on ultra-cold gases of fermionic atoms, but also have provided paradigms for understanding quantum phenomena such as Josephson oscillations and vectorial order parameters which have been or are expected to be observed in dilute Bose-Einstein condensates.

2.5 The experimental pursuit of Bose-Einstein condensed gases

While superfluidity and superconductivity represent macroscopic quantum phenomena arrived at by discovery, experimental efforts began to realize other macroscopic quantum systems by design. In particular, experimentalists set out to create the “imaginary” degenerate Bose gas in various physical systems. Experimental [77, 78] and theoretical work [79] showed that liquid helium which is adsorbed on Vycor, a sponge-like glass with nanometer-scale pores, shows features of dilute-gas Bose-Einstein condensation. Another candidate for a dilute-gas Bose-Einstein condensate is a gas of excitons, short-lived electron-hole pairs in semiconductors, which are created by a pulsed laser and which can thermally equilibrate

before decay. As reviewed in Refs. [80, 81], a variety of quantum degeneracy effects have been seen in fluorescence and photo-emission studies.

2.5.1 Spin-polarized hydrogen

The possibility of using extremely dilute atomic gases was triggered by the work of Hecht [82] and especially by Stwalley and Nosanow [83]. They showed that recombination in spin-polarized atomic hydrogen should be quite slow because there are no bound triplet molecular states. The experimental pursuit of a hydrogen Bose-Einstein condensate was then engaged, notably by Greytak and Kleppner at MIT and by Silvera and Walraven in Amsterdam, and a sample of spin-polarized hydrogen was first stabilized in 1980 [84, 85]. A crucial experimental advance was the introduction of magnetic trapping [86, 87], which then allowed the hydrogen gas to be evaporatively cooled [88, 89] below the temperature of the cryogenic apparatus in which it was produced. These techniques served as a building-block for later efforts with alkali gases. The pursuit of Bose-Einstein condensation in hydrogen also prompted a flurry of theoretical work on Bose-Einstein condensation in inhomogeneous potentials [90–92], multi-component Bose-Einstein condensates [93], and the theory of cold collisions (see e.g. [94]).

After the successful application of rf-induced evaporation, a hydrogen Bose-Einstein condensate was produced in 1998 by Greytak, Kleppner, and collaborators [27]. The hydrogen condensate is notable for its size (4 mm in length), the large number of condensed atoms ($\approx 10^8$), and for the extremely weak interactions which make the condensate density much greater than that of the surrounding thermal cloud. Furthermore, the simplicity of the hydrogen atom allows all properties of this many-body system to be calculated *ab initio*; the alkali condensates come close to this remarkable goal, but interatomic scattering properties are still currently determined from measurement. Also noteworthy are the efforts to reach quantum degeneracy in a two-dimensional gas of spin-polarized hydrogen adsorbed on a liquid helium surface. In two-dimensions, a superfluid phase-transition called the Kosterlitz-Thouless transition is predicted to occur, at which local phase-coherence is established while long range order is disturbed by phase fluctuations. Work on this system has been pursued at Harvard [95], Amsterdam [96], Kyoto [97], and the University of Turku, where evidence for the 2D phase transition was reported in 1998 [98].

2.5.2 Laser-cooled alkali atoms

A second route to Bose-Einstein condensation of an atomic gas was opened by a second route to ultra-cold atoms, the cooling of neutral atoms by laser light. One of the essential concepts in laser cooling was suggested as early as 1917 by Einstein, who noted that a hot gas would equilibrate with a cold thermal radiation field because an atom would preferentially scatter Doppler-shifted light from a direction opposing its motion [99]. Doppler cooling with laser light was proposed in 1975 by Hänsch and Schawlow [100] and Wineland and

Dehmelt [101] and later by Letokhov, Minogin and Pavlik [102] for cooling both neutral atoms and ions. Laser cooling was first applied to trapped ions [103, 104], and later to neutral atoms in an atomic beam [105]. It was realized that radiation pressure due to the repeated scattering of photons from a collimated laser beam could exert a powerful force: a sodium atom scattering resonant photons at a rate of $\Gamma/2$ (where Γ is the excited-state decay rate of 10 MHz) is decelerated 10^5 times faster than the gravitational acceleration on the Earth's surface. However, an atom which scatters photons from a fixed-frequency beam will soon change its velocity sufficiently to drop out of resonance. Methods were proposed to chirp the laser frequency (chirp slowing) [102] or to vary the atomic resonance frequency with a magnetic field (Zeeman slowing) [106] so that atoms could be continuously cooled from a high velocity to a final slow velocity, thereby compressing all atoms originally between those two velocities to a narrower velocity range. Such cold atomic beams were soon generated successfully (Zeeman slowing by Prodan, Phillips and Metcalf [107] and frequency-chirp slowing by Ertmer *et al.* [108]).

With these cold atomic sources, one could hope to trap neutral atoms. Magnetostatic trapping, which had been discussed by W. Paul and others in the 1950's and 60's and which was first used to trap neutrons [109], was applied to cold sodium atoms directly at the end of a Zeeman slower in 1985 [110]. Magnetic trapping works best with atoms which have unpaired valence electrons and hence a large magnetic moment; alkali atoms are thus ideal choices for both magnetic trapping and laser cooling.

Other efforts to trap neutral atoms relied on optical forces. Steven Chu and colleagues exposed atoms to six red-detuned laser beams which propagate in both directions on three orthogonal axes. Such an arrangement ensured that due to the Doppler shift, atoms preferentially scattered light from laser light which propagated counter to their direction of motion, and hence traveled diffusively in a viscous medium dubbed "optical molasses." This provided a long residence time for atoms loaded from a chirp-slowed atomic beam [111]. It was later discovered that optical molasses produced atoms at temperatures much colder than originally expected (on the order of the recoil temperature T_R defined by the kinetic energy due to a single photon recoil) due to a newly discovered "Sisyphus" cooling mechanism [112]. Another important advance by Chu and his group was the first optical trapping of atoms in a single-beam optical dipole trap, which confines atoms due to the off-resonant AC Stark effect [113]. Such an optical trap was used in our laboratory for the optical confinement of a Bose-Einstein condensate [10] (Chapter 9). Finally, following suggestions by Dalibard and Pritchard, a robust radiation-pressure trap was invented which combined the dissipative optical cooling of optical molasses with a confining radiation pressure mediated by an inhomogeneous magnetic field. This magneto-optical trap [114] provided the necessary starting conditions for the pursuit of Bose-Einstein condensation: a continuously loaded source which would ultimately trap a large number ($10^8 - 10^{10}$) of ultra-cold atoms.

However, while Bose–Einstein condensation was regarded early on as a “Holy Grail” of laser cooling, a direct all-optical route to Bose–Einstein condensation was fraught with difficulties. With the identification of polarization-gradient cooling [115, 116], atoms could be optically cooled to about the recoil temperature. At this temperature, the thermal de-Broglie wavelength is about equal to the optical wavelength. Thus, a gas at this temperature will Bose condense only at densities higher than one atom per cubic optical wavelength, coinciding with the regime where high optical densities wreak havoc with near-resonant laser cooling schemes. Sub-recoil cooling schemes have been developed, but only recently have phase-space densities near unity been approached by all-optical means (still short by a factor of about 50) [117–119].

Rather, following the example of experiments with atomic hydrogen, researchers at JILA (Cornell, Wieman and collaborators) and MIT (Pritchard, Ketterle and collaborators) began exploring a hybrid approach: optical cooling would be used to pre-cool an atomic gas and provide a starting point for evaporative cooling to reach Bose–Einstein condensation. A powerful method of evaporative cooling was proposed by Pritchard in which radio-frequency fields would be used to selectively flip the spin of magnetically trapped atoms with a large potential energy (rf-evaporation) [120]. As with any evaporative cooling technique, collisions between trapped atoms are required to bring the gas into thermal equilibrium after the high-energy atoms are ejected. Thus, the challenge to researchers was to create a gas with a high rate of elastic collisions by first laser cooling the gas and then transferring it to a magnetic trap. In 1990, a magnetic trap was loaded from a magneto-optical trap and optical molasses in Boulder [121, 122], employing a sequence of steps which is still used in most alkali BEC experiments today (including ours).

From there, the road to Bose–Einstein condensation was paved by three critical advances. First, concentrating on the need to produce a laser-cooled ultra-cold atomic gas at high densities, Ketterle, Pritchard *et al.* invented the dark-SPOT trap [123]. In this trap, atoms spend most of their time in a “dark” hyperfine state from which they do not scatter the light which is used for trapping and cooling. This means that the density of “bright” atoms, which ordinarily limits the number and density of atoms in a magneto-optical trap, is much smaller than the total density of atoms in the trap. The dark-SPOT thus yields cold, dense atomic gases with elastic collision rates which are high enough to begin efficient evaporative cooling. Second, building on this advance, rf-evaporation was demonstrated with atoms trapped magnetically in a spherical quadrupole trap [124–127]. Yet, Bose–Einstein condensation could not be reached until a major flaw in the spherical quadrupole trap, the high loss rate of atoms from the zero-field region in the trap center, was remedied. This third and final step to Bose–Einstein condensation was solved in different ways by the Boulder group (with the TOP trap) and the MIT group (with the optically-plugged trap).

Finally, in 1995, the first observation of a gaseous Bose–Einstein condensate was reported by the group of Cornell, Wieman, and collaborators at JILA [128]. The condensates

of about 2000 rubidium atoms were distinguishable in time-of-flight images by their slow, asymmetric expansion. This first experiment used a single low-pressure vapor cell in which atoms were first collected in a dark-SPOT trap, transferred to the magnetic trap, evaporatively cooled, and then imaged in an experimental cycle that took about 6 minutes. Soon thereafter, evidence for quantum degeneracy in a gas of atomic lithium was reported by the group of Randy Hulet at Rice University [129]. In their experiment, atoms were directly loaded into a magnetic trap from a Zeeman slower in the presence of Doppler cooling beams. After a long evaporation time (5 minutes), the trapped cloud was imaged. The sudden onset of imaging aberrations indicated the creation of a dense portion of the gas; this tentative indication later gave way to more conclusive and quantitative evidence in 1997 [130]. Finally, after a few months during which some problems with vacuum and mechanical vibrations were fixed, our group observed Bose-Einstein condensation in a gas of sodium atoms [1]. Condensates of about 5×10^5 atoms were produced in just 10 seconds. Rapid evaporative cooling resulted from the linear potential of the optically-plugged spherical quadrupole trap, which indeed produced two condensates in spatially separated potential minima.

Since 1995, progress in the study of gaseous Bose-Einstein condensates has been extremely rapid. Dozens of experimental studies have opened the door to many exciting avenues of research, and a number of new Bose-Einstein condensation experiments have come online. This experimental progress has triggered a concentration of theoretical explorations by researchers around the world. This most recent chapter in the history of Bose-Einstein condensation is perhaps best chronicled by the 1998 “Enrico Fermi” Summer School on Bose-Einstein condensation in Varenna, Italy (proceedings to be published in 1999). At this school, as a hundred physicists gathered to learn about and discuss the discoveries of the last few years, one could sense that a rich and intriguing research field had already been established in just three years, and that the long history of Bose-Einstein condensation would continue vibrantly into the future.

Chapter 3

The nuts and bolts of making a Bose–Einstein condensate

Following the example set by the initial experiments at Boulder, MIT and Rice, the route to Bose–Einstein condensation has been emulated and refined by numerous experimental groups around the world. Condensates are created by a two–stage approach: an initial cooling and compression stage followed by forced evaporative cooling in a magnetic trap. In experiments on alkali gases, the initial cooling uses various optical cooling and trapping techniques which require an optical setup to create laser beams at precise detunings from an atomic resonance and with sufficient power to collect and cool a large gaseous sample. Forced rf–evaporative cooling requires a stable, tightly–confining magnetic trap, and a well–controlled radio–frequency field. Producing and maintaining a μK –temperature gas requires ultra–high vacuum to minimize collisions with the room–temperature background gas. While each of these experimental components requires a moderate effort to construct and maintain, the real technical challenge of Bose–Einstein condensation experiments is getting all these components to operate simultaneously in a reliable, well–controlled, and flexible fashion.

In the following chapter, I discuss various aspects of the apparatus which was used not only for all the studies of Bose–Einstein condensates described in this work, but also for the development of many of the prerequisite cooling and trapping techniques. This apparatus has a long history of pioneering experimental innovations, such as the development of bright Zeeman–slowed atomic beams [131, 132], the achievement of high–density, cold atomic clouds in a dark–SPOT [123], and the first demonstration of rf–evaporative cooling [126]. The hard work of the innovators responsible for these developments serves as the backbone of all the experiments of the last few years, and much of their handiwork survives in the current apparatus. That my research at MIT has been so fruitful is a testament to their dedication and skill. For additional descriptions of this work, I refer to the previous dissertations of Michael Joffe, Kendall Davis, Marc–Oliver Mewes, and Michael Andrews.

Beyond these techniques for producing Bose–Einstein condensates, a variety of tools were developed for their study (Table 3.1). Each of these opened the door to new experimental progress. The cloverleaf magnetic trap, phase–contrast imaging, and the development of various tools for manipulating Bose–Einstein condensates are described in this chapter. Other developments are described in later sections. In addition, methods for image processing are discussed in Appendix A.

3.1 Typical operation

Before describing in detail the various components of our experiment, I begin with an overview of its typical operation. In our experiment, Bose–Einstein condensates of sodium are repeatedly produced with a cycle time of about one minute, divided as shown in Table 3.2. A dilute gas of sodium atoms is initially produced in an atomic oven, wherein up to 10 g of molten metallic sodium are held at a temperature of 260°C. Atoms are loaded into a dark–SPOT magneto–optical trap directly from a Zeeman slower yielding $\approx 10^{10}$ trapped atoms at a density of several times 10^{11} cm^{-3} . Thereafter, the atomic beam is blocked by a mechanical shutter in the oven region, leaving the trapped atoms in a UHV chamber with a background pressure of $\approx 10^{-11}$ torr. A short 5 ms pulse of dark polarization–gradient cooling provides the final stage of optical cooling, leaving the atoms unpolarized in the $|F = 1\rangle$ hyperfine ground–state manifold, at temperatures of $\approx 50 \mu\text{K}$.

The magnetic trap is then switched on by sending currents of $\approx 250 \text{ A}$ through a set of magnet coils within less than 1 ms. Those atoms in the $|F = 1, m_F = -1\rangle$ hyperfine state, about one third of the unpolarized atomic gas, are captured in the magnetic trap. Thereafter, the trapped cloud is compressed by lowering the bias field in the magnetic trap, raising the elastic collision rate to about 10 Hz. This provides suitable starting conditions for the final rf-induced evaporative cooling stage. An rf field is applied to the magnetically trapped atoms and is ramped down from an initial frequency of 30 MHz to a final frequency of about 1 MHz over 22 – 26 s. The final frequency is typically 10 – 500 kHz higher than the frequency which would spin–flip atoms at the bottom of the magnetic trap. This final cooling stage yields a Bose condensed gas. Typically, the BEC phase transition is reached at a temperature of $1 – 2 \mu\text{K}$ with $(50 – 100) \times 10^6$ atoms. Further rf–evaporation yields Bose condensates of $(5 – 20) \times 10^6$ atoms at a density of about $4 \times 10^{14} \text{ cm}^{-3}$. The total optical and evaporative cooling time is about 30 seconds.

Following the preparation of a gas near or below the BEC transition temperature, an experiment is conducted. As described in Sec. 3.6, a variety of tools are employed to manipulate the trapped gas. The time for the experiment can be as short as zero (for studies of static equilibrium properties) and as high as one minute (for measuring trap lifetimes). The outcome of this manipulation is optically probed by imaging the atomic cloud as described below. Taking a series of background images and processing the image data takes

New tools	Benefits	New science
Cloverleaf trap	<ul style="list-style-type: none"> • simple operation of dc currents • large aspect ratio — long dense cloud easy to probe and manipulate • variable shape and strength 	<ul style="list-style-type: none"> • 1-d sound propagation • collective excitations • studies of condensates at different densities • axial momentum resolution for small-angle Bragg scattering • superradiance in elongated condensate
Phase-contrast imaging	<ul style="list-style-type: none"> • <i>In situ</i> imaging of dense atomic clouds • non-destructive, multiple imaging 	<ul style="list-style-type: none"> • sound propagation • high-resolution measurements of collective excitations • formation of a BEC
Off-resonant light (condensate micro-surgery)	<ul style="list-style-type: none"> • μm-scale optical potentials 	<ul style="list-style-type: none"> • interference of two BEC's • excitation of sound pulses • anti-symmetric dipole oscillations • reversible formation of a BEC • condensate collisions
Optical dipole trap	<ul style="list-style-type: none"> • external degree of freedom (magnetic fields) • internal degree of freedom (atomic spin) 	<ul style="list-style-type: none"> • Feshbach resonances • spinor BEC
Near-resonant light scattering	<ul style="list-style-type: none"> • narrow Bragg resonance • excitation wavelength smaller than sample size 	<ul style="list-style-type: none"> • coherence length measurement • structure factor in phonon regime • superradiance

Table 3.1: New tools and new science. A variety of experimental tools were developed for the study of Bose-Einstein condensation. Each provided new capabilities and enabled a variety of experiments.

Stage	Duration	n	T	$n\lambda_{dB}^3$
Source: atomic oven		10^{14} cm^{-3}	533 K	10^{-13}
Zeeman slowing and dark-SPOT	3 s	10^{11} cm^{-3}	1 mK	10^{-7}
Polarization-gradient cooling	5 ms	10^{11} cm^{-3}	$100 \mu\text{K}$	10^{-6}
Magnetic trap: catching and compression	3.5 s	10^{11} cm^{-3}	$160 \mu\text{K}$	10^{-6}
rf-evaporation to BEC	22 – 26 s	$4 \times 10^{14} \text{ cm}^{-3}$	$0.5 - 2 \mu\text{K}$	2.6
Manipulation	0 – 60 s			
Probing, image processing	20 s			

Table 3.2: Stages in a typical experimental cycle for cooling a dilute gas of sodium atoms to Bose–Einstein condensation. For each cooling step, the final density, temperature, and phase–space density are indicated. Numbers are approximate. Note that the phase–space density refers just to atoms in a single internal state, while the overall density is that of all the atoms.

10 – 20 s, bringing the total experiment cycle time to about one minute, whereupon the experiment can be repeated.

3.2 Computer control

The operation of our experimental apparatus as an exploratory tool has been aided by the use of a flexible computer based control system which we call the Word Generator (WG). The basic task of the WG is to take as input a series of instructions which specify digital and analog signals (words) to be output at specific times during the experiment, i.e. to be a multichannel, easily programmable function generator. These digital and analog signals are then sent to the various instruments and devices which control the different parts of the apparatus, such as shutters, current switches, analog controls on power supplies, digital cameras, AOM drivers, etc. Our first computer based system, designed by Kendall Davis, was used until early in 1997. Once our experiments became more complex and required more accurate timing and more flexible output, I designed (with the help of Everest Huang, a gifted undergraduate working in our laboratory) and implemented a revised control system which is still currently in use.

The current WG control system uses a program written using National Instruments' LabVIEW software as its front end. The user enters data in two places. Digital output is specified in a series of digital words, arranged in an arbitrarily sized list. For each word, the user specifies the state of 32 digital outputs, the duration of the output, and indicates whether to begin or end a sweep of analog voltage outputs. Analog data is entered as a series of graph sets, in which an arbitrary waveform is specified for the output of four analog voltage channels as well as the amplitude and frequency to be output from an rf generator. The waveform is defined by a linear interpolation between an arbitrary number of cursors specified by the user. For example, an experimenter may input a series of digital output commands such as "output the loading word for 2.5 seconds," or "output the evaporation word for 22 seconds and call graph set 2" where graph set 2 specifies the rf-evaporation frequency sweep. We have found that specifying the sequence and timing of an experimental run in this manner allows for quick diagnosis of errors and for great flexibility in adding or modifying stages of the experiment.

The hardware for this software implementation consists of a Power Macintosh computer with four external NuBus data acquisition boards from National Instruments: two 32-bit digital input/output boards (the "timing" and "digital" boards), one six-channel analog input/output board, and one GPIB communication board. To ensure accurate timing and synchronization of the different outputs, we have relied on the ability of these digital boards to output data stored in a memory buffer without conflicting with other functions of the computer's central processing unit. The WG software routine takes the input specified by the user and places in memory a set of "words" consisting of digital and analog data which contain every change in the output which was requested by the user, i.e. every change in an analog output during a voltage sweep and every change in the digital output for different stages of the experiment. A "timing buffer" is assembled which outputs an 8-bit digital signal at regular intervals (as short as 10 μ s) in which a rising edge on one of the eight channels is output every time a new word output is requested. During the operation of the experiment, the output from the timing board triggers output on the digital and analog boards. This programming method allowed us to control long experiments with high resolution using a limited amount of on-board memory. Additionally, GPIB commands were sent out to a SRS DS345 Function Generator specifying the rf frequency and amplitude used for evaporation. This output was updated every 60 ms using a software routine (an unfortunate Achilles heel of the WG), and was synchronized with the digital and analog output to within about 10 ms.

While the specific implementation of the Word Generator was devised to accommodate the existing hardware, its basic function as a flexible and readily modified function generator is of general use. Research groups around the world have come up with various combinations of software and hardware to control the timing of experiments. I believe the Word Generator used by our group, which has also been implemented on a Windows-based system by my

colleague Chris Kuklewicz, is of general use. I hope in the future that such programs and tools become readily available, and allow easier scientific development.

3.3 Vacuum chamber

A Bose–Einstein condensation experiment is a race against time: one struggles to create an ultra–cold gas which will Bose condense before it thermally equilibrates with the warm vacuum chamber and before it phase–equilibrates to a solid. Phase–equilibration is fore stalled by keeping the gas at low densities. However, the low density also implies a low elastic collision rate which then limits the rate of evaporative cooling. Thermal equilibration with the room–temperature vacuum chamber walls occurs by collisions between the trapped ultra–cold gas and the background gas in the vacuum chamber. To ensure that evaporation cools faster than the background gas heats requires that the background gas be extremely dilute. Thus, Bose–Einstein condensates must be made in ultra–high vacuum (UHV) environments. Our experience and an estimation based on typical cross–sections for background gas collisions [22] both indicate that vacuum pressures on the order of 10^{-11} torr are required.

The vacuum chamber used in our experiments is described in detail in the Ph.D. thesis of Michael Joffe [133]. Briefly, the chamber is subdivided into two: an oven chamber which is maintained at typical pressures of 10^{-7} torr, and the main UHV chamber at pressures of about 10^{-11} torr. A narrow liquid–nitrogen–cooled differential–pumping tube between the two chambers allows for the 10^4 pressure difference. Furthermore, a gate–valve between the chambers is kept closed between experimental runs, and allows the oven region to be serviced without affecting the ultra–high vacuum. Since the initial construction of the vacuum chamber, which included the installation and successful operation of the Zeeman slower, a few changes have been made which are outlined below.

- The UHV chamber centers on a large stainless steel 18–way cross which has six flanges arranged on the face of a cube (five 8” flanges and one 4 1/2” flange), and twelve rotatable 4 1/2” flanges mounted on 2 1/2” tubing (on the twelve edges of a cube, see Fig. 3-1). While it allows for great flexibility in the use of different windows and ports, this large chamber was found to hinder access to the trapped atomic cloud. Thus, the chamber was retrofitted with specially designed vacuum inserts which fit onto the 8” flanges, and which bring the walls and windows of the vacuum chamber closer to the trapped gas. These inserts, designed by Dallin Durfee, include two “bucket” inserts (Fig. 3-1b) which have an inner diameter of 5” and a depth of 6 1/2”. The inside surfaces of these inserts, when mounted on opposite sides of the chamber, are spaced by 1”. Optical access down the axis of the buckets (the horizontal axis) is provided by 1 1/4” diameter “penny windows” of moderate optical quality which are mounted on a 2” high tube. Another vacuum insert places a vacuum window just above the

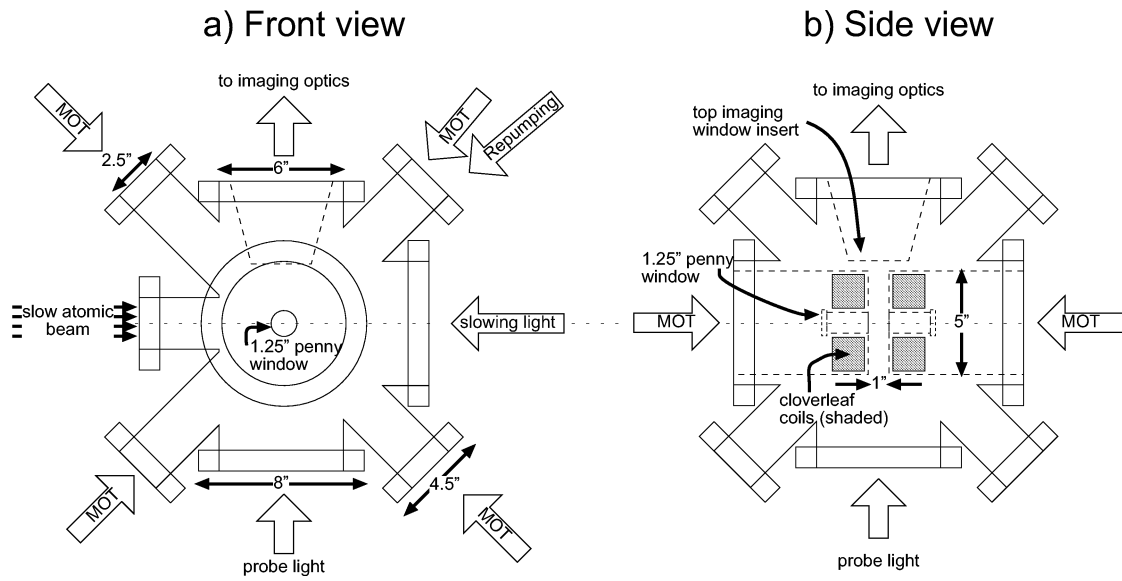


Figure 3-1: Main portion of the UHV chamber. The chamber has five 8" flanges and one 1 1/2" flange arranged on the faces of a cube, and twelve 4 1/2" flanges projecting from the center of the chamber through the sides of a cube (only those in the central plane of each projection are shown). Beams for the magneto-optical trap are sent in through two diagonal axes, and along the horizontal axis through the "penny window" vacuum inserts. These inserts also hold the magnetic trapping coils. The main imaging axis is vertical. Optical access is aided by another vacuum insert on the top flange. The Zeeman slowed atomic beam and counter-propagating slowing light are aligned as shown.

two buckets, about 3" from the center of the chamber where the atoms are trapped. This insert allows lenses to be placed close to the atoms for high-resolution imaging along the vertical axis. In many ways, this method of bringing external apparatus closer to the trapped atoms is not advisable since it increases the inner surface area of the vacuum chamber and thus increases the gas load from out-gassing. However, after baking the vacuum chamber at 300°C for several days, out-gassing was reduced to acceptable levels.

- To reduce mechanical vibrations of the experimental apparatus, we currently use exclusively non-mechanical pumps to maintain vacuum. These include 60-liter ion pumps in both the oven chamber and the UHV chamber, and a titanium sublimation pump and a nitrogen-cooled cold sleeve in the main chamber. Turbo-mechanical pumps are used during bake-outs after servicing the vacuum chamber.
- All electro-magnet coils were removed from inside the vacuum chamber. These water-cooled coils had been insulated with Kapton film, which is UHV compatible but which apparently limited the vacuum to pressures of about 10^{-10} torr. Furthermore, the feedthroughs for the cooling water failed several times, requiring a lengthy fixing and baking-out of the vacuum chamber. Instead, magnet coils are placed outside the vacuum chamber within the "bucket" vacuum inserts. This allows the electro-magnets to be replaced or fixed (as was necessary several times) without opening the main vacuum chamber. As a result of these changes, the UHV chamber has been under vacuum continuously since the beginning of 1996.
- While the dc-magnet coils can be safely placed outside the steel vacuum chamber, the rf antenna which is used for rf-evaporation is still located inside the chamber. This is necessary because the steel chamber walls were found to effectively shield the rf signal. The antenna consists of four rectangular loops (1" \times 5") of Kapton-insulated copper wire, which produce a magnetic field in the vertical direction. The coils are powered through a vacuum feedthrough, and current through the coils is monitored across a $5\ \Omega$ shunt resistor. In this regard, the use of a steel vacuum chamber has an advantage over recent all-glass cell designs in that the steel chamber shields the rf-signal from the remainder of the apparatus, preventing interference with power supplies, computers, laser locking circuitry, etc.
- The operating temperature of the oven is 260°C. At this temperature, an atomic beam with sufficient flux to eventually yield condensates of 2×10^7 atoms (our ultimate figure of merit) is generated. The atomic oven can be easily replenished with about 10 g of sodium at a time, which lasts for about 300 hours of operation. The oven is cooled to below 200°C between experimental runs. After about 50 g of sodium have been placed in the oven, we typically need to dismantle the oven chamber and thoroughly

clean out the sodium which has built up. After such a cleaning, the oven is typically baked out at temperatures of 150 – 300°C (depending on the temperature rating of various parts) and is ready for use after 2 – 3 days. This repeated servicing of the oven chamber is done without compromising the UHV chamber by closing the gate valve which separates the chambers.

3.4 Optics

The first step in cooling a hot sodium gas to quantum degeneracy is done by various methods of laser cooling and trapping. These techniques have become standard tools in atomic physics experiments around the world. In this section, I provide a brief description of the optical cooling methods used in our experiment: Zeeman slowing, a magneto-optical trap, and polarization-gradient cooling. A more complete explanation of these techniques is provided in a number of review articles [134–136]. I will then briefly describe the optical setup which we use to generate the various laser beams necessary to implement these optical cooling methods.

Alkali metals such as rubidium, lithium, and sodium are used in experiments on gaseous Bose-Einstein condensates primarily because they have simple optical properties due to the presence of a single valence electron. This makes these alkali atoms amenable to laser cooling by providing strong optical transitions at optical or near-infrared wavelengths where powerful lasers are available.

Fig. 3-2 shows the portion of the level diagram for ^{23}Na which is relevant to our work. A ground state sodium atom has a single valence electron in the $3S_{1/2}$ configuration. With a nuclear spin of $3/2$, sodium has two ground state hyperfine manifolds with a total spin of either $F = 1$ or $F = 2$, split by the hyperfine frequency of 1.77 GHz. This ground state has two strong absorption lines from transitions to the excited $3P$ state: the $D1$ line at 589.6 nm for excitation to the $3P_{1/2}$ state, and the $D2$ line at 589.0 nm for excitation to the $3P_{3/2}$ state. All of our optical cooling is done on the $D2$ line, with detunings much smaller than the fine structure splitting. The excited state has a natural lifetime of 16 ns (line width of 10 MHz on the $|F = 2\rangle \rightarrow |F' = 3\rangle$ transition), and has four hyperfine manifolds with total spin ranging from $F = 0$ to $F = 3$ with hyperfine splittings as shown [137].

Optical cooling relies on the fact that atoms absorb light only within a very narrow frequency range, allowing an experimenter to create a situation in which only atoms with select properties, such as having a specific velocity or being in a specific place, will scatter light. Upon scattering a photon with wavevector \vec{k} , an atom receives a small momentum kick $\hbar\vec{k}$ in the direction of light propagation, and then a second momentum kick upon remission of the photon in a random direction. Thus, light scattering can be used to change the momentum distribution of an atomic gas and thereby cool it and trap it.

Since the momentum of a sodium atom in the 260°C atomic oven, or even at the 100 μK

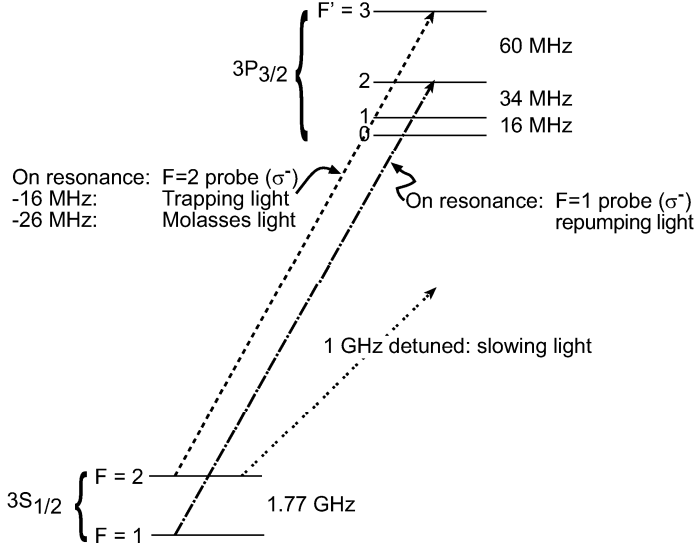


Figure 3-2: Level diagram for ^{23}Na showing hyperfine structure for the $3S_{1/2}$ ground state and the $3P_{3/2}$ excited state. Light used for $F = 2$ probing, trapping, and polarization-gradient cooling is on- or near-resonance with the $|F = 2\rangle \rightarrow |F' = 3\rangle$ cycling transition. $F = 1$ probing and repumping light is resonant with the $|F = 1\rangle \rightarrow |F' = 2\rangle$ transition, and thus 1.71 GHz blue-detuned from the cycling transition. Slowing light is 1 GHz red-detuned from the cycling transition.

temperatures of polarization-gradient cooling, is much larger than the photon momentum, many photons must be scattered to affect the atomic momentum. For this reason, optical cooling works best on a cycling transition, in which an atom returns to the same ground state after scattering a photon. For sodium, such a transition is the $3S_{1/2}|F = 2\rangle \rightarrow 3P_{3/2}|F' = 3\rangle$ transition. Thus, the light used for cooling and trapping is near-resonant with this transition. Occasionally, light scattering will transfer an atom from the “bright” $|F = 2\rangle$ state to the “dark” $|F = 1\rangle$ state. For sodium, since the cycling transition is separated only by a 60 MHz hyperfine splitting from a non-cycling transition to the $F' = 2$ manifold, atoms are regularly transferred during optical cooling from the bright to the dark state, and a repumping beam, which excites atoms from the $F = 1$ manifold, is used to transfer them back.

The specific cooling methods we use are the following:

- *Zeeman slowing:* The collimated atomic beam which emanates from the oven chamber into the UHV chamber is slowed using a Zeeman slower [107, 138, 139]. A Zeeman slower relies on the basic method of Doppler cooling. If one exposes atoms to light at a frequency lower than the resonant frequency (red-detuning), only atoms moving opposite to the direction of light propagation within a very narrow range of velocities will be in resonance, due to the Doppler shift, and will scatter light. Thus, atoms

within this velocity range can be made to slow down. In a Zeeman slower, the resonance frequency is made to vary spatially by varying the magnetic field along the axis, while a single, red-detuned, fixed-frequency beam of slowing light is sent down the axis. In this manner, the velocity at which atoms are resonant varies from a high velocity at the beginning of the slower (called the capture velocity) to a low velocity (the final velocity) at its end, so that all atoms which enter the slower at velocities below the capture velocity will be slowed to the final velocity.

We use an increasing-field Zeeman slower. Atoms entering the slower from the oven are exposed to a small magnetic field and to slowing light with a $\Delta \simeq 1$ GHz detuning, corresponding to a capture velocity of $\Delta \cdot \lambda \simeq 600$ m/s where $\lambda = 589$ nm is the optical wavelength. The field increases along the slower to about 700 G. At the end of the slower, the magnetic field is quickly brought to zero by an additional set of coils, and the slowed atomic beam passes into the capture region of a magneto-optical trap. Due to its large detuning, the slowing light can pass directly through the magneto-optical trap with little impact on its loading. Frequency sidebands at ≈ 1.7 GHz are added to the slowing light to repump atoms to the bright state. Details on the design and performance of the slower are found Refs. [132, 133, 140].

- *dark-SPOT magneto-optical trap*: A magneto-optical trap (MOT) combines the dissipation of Doppler and polarization-gradient cooling with the spatial tuning of the atomic resonance used in a Zeeman slower. Atoms are exposed to six circularly-polarized red-detuned laser beams, traveling in each direction along three orthogonal axes. This alone provides Doppler cooling in all directions (called optical molasses). In addition, the atoms are exposed to a spherical quadrupole magnetic field (see Sec. 3.5.1) which ensures that atoms which move away from the center of the magnetic field will scatter light preferentially from the laser beam which pushes them back toward the center. This provides an effective trapping potential which confines and compresses the atomic cloud [114].

Atoms are loaded continually from the atomic beam into the magneto-optical trap. The steady-state atomic number, density and temperature are determined by various processes of trap loss (excited state collisions) and repulsive forces (radiation trapping) which become more severe as the number of atoms in the bright state increases. These limiting factors are partly overcome by employing a dark-SPOT, developed earlier by my colleagues [123], which operates by limiting the amount of repumping light provided at the center of the MOT. As discussed above, off-resonant excitation continually transfers atoms from the bright $F = 2$ ground state manifold to the dark $F = 1$ manifold. To provide continuous cooling and trapping, the atoms must be exposed to repumping light which optically pumps the atoms from the $F = 1$ back to the $F = 2$ manifold. In our dark-SPOT, the atoms are exposed to a bright repumping

beam away from the center of the trap allowing atoms to be caught from the slowed atomic beam. A mask is placed in the path of the repumping light which occludes the light from the trap center, reducing trap loss [141] and repulsive forces and thereby increasing the number and density of trapped atoms. While the optical density for trapping light in a regular MOT is limited to the order of unity, the optical density in our dark-SPOT is on the order of 100 [123].

- *Polarization-gradient cooling:* Temperatures lower than the Doppler limit ($240 \mu\text{K}$ for sodium) can be reached by polarization-gradient cooling. Such cooling is provided at the center of a MOT, but is optimized by increasing the detuning of the cooling light and switching off the inhomogeneous magnetic field. Polarization-gradient cooling, first demonstrated in [112] and reviewed in [142], is a Sisyphus cooling scheme in which the light creates a periodic optical potential which differs for different hyperfine states. Atoms are preferentially pumped from one hyperfine state at an optical potential maximum to another hyperfine state at an optical potential minimum. Thus, the atom repeatedly “climbs uphill” and loses energy. In our experiment, we employ a dark polarization-gradient scheme where only a limited amount of repumping light is added to the cooling light as frequency sidebands. Thus, atoms remain in the dark $|F = 1\rangle$ states most of the time, and the cooling can proceed in a dense atomic sample.

The optical setup for implementing these optical cooling schemes is divided onto different optical tables in two different rooms. All laser light near the sodium transition is generated in the laser room. A simplified description of our scheme for generating this light is shown in Fig. 3-3.

Yellow light near the sodium $D2$ line is generated from a Coherent 899 dye laser using Rhodamine 6G dye pumped with light from a Coherent Sabre argon ion laser (Fig. 3-3a). Pumping with about 10 W at 514 nm generates about 1.6 W of yellow light. The dye laser is locked to a Fabry-Perot cavity which is provided with the laser. The cavity is referenced to the $3S_{1/2}|F = 2\rangle \rightarrow 3P_{3/2}|F' = 3\rangle$ cycling transition by a saturated absorption lock-in scheme (Fig. 3-3f). Light is generated from this beam for trapping and polarization-gradient cooling (Fig. 3-3b), slowing (Fig. 3-3c), repumping and $F = 1$ probing (Fig. 3-3d), and $F = 2$ probing (Fig. 3-3e). All beams are sent through free space to the experiment table in an adjacent room, with the exception of the probe beams which are carried by optical fibers. Occasionally some of the argon-ion light is split off and sent to the experiment table (recently by fiber) and used for an off-resonant manipulation tool as discussed in Sec. 3.6.

On the experiment table, the laser light is directed into the vacuum chamber through various windows. Trapping light is split into four beams: two horizontal trapping beams which pass through the “penny windows” at the center of the magnetic trap, and two trapping beams which are sent and then retro-reflected along two paths at 45° from vertical which are mutually orthogonal and orthogonal to the horizontal beams. The power in each of the four beams can be adjusted independently to optimize the beam balance. This beam

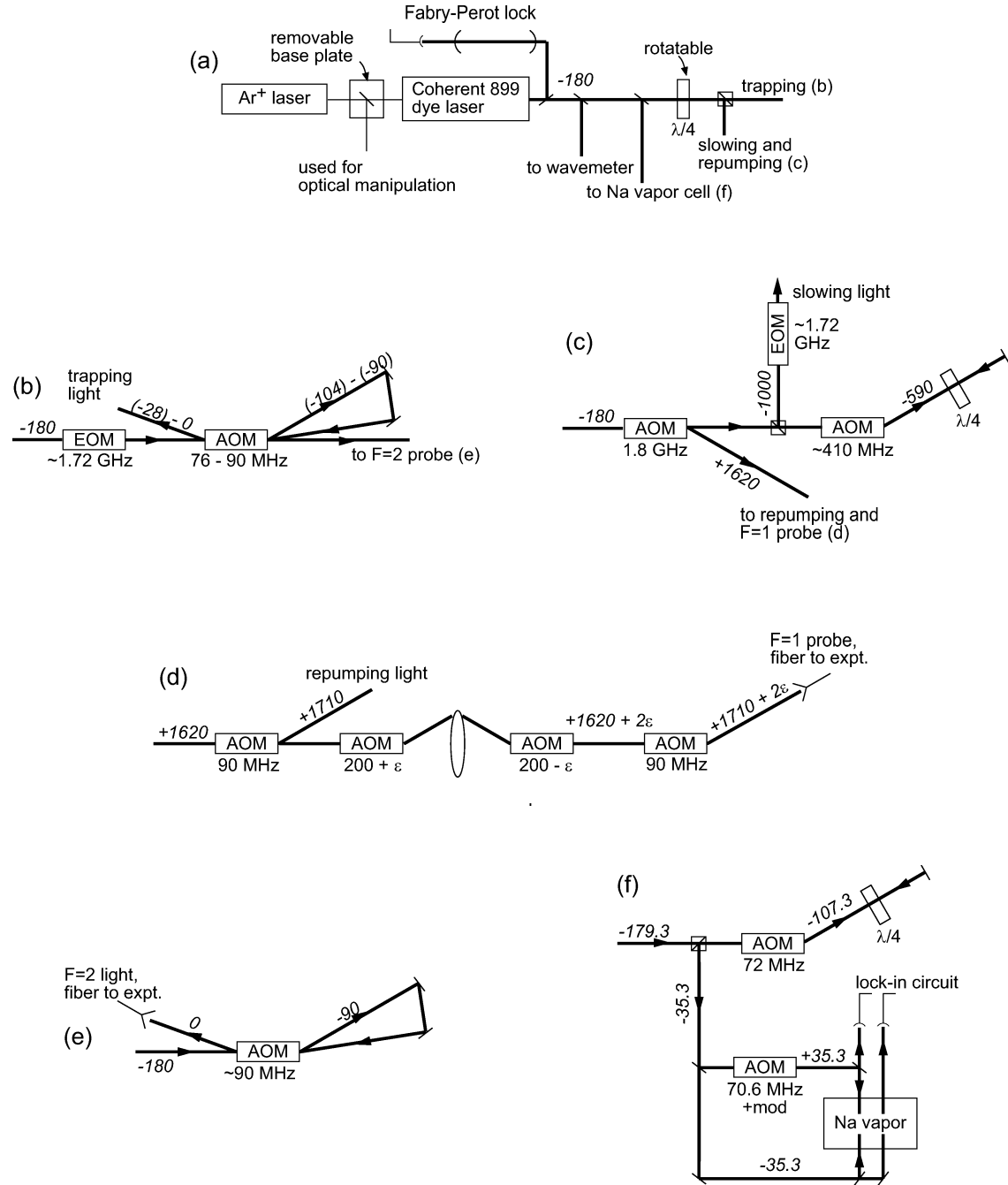


Figure 3-3: Optical setup for generating light near the sodium resonance. Figure shows (a) pumping of dye-laser with light from an argon-ion laser, generating about 1.6 W of light at 179.3 MHz below the $|F = 2\rangle \rightarrow |F' = 3\rangle$ cycling transition (shown as -180 for simplicity); (b) double-pass AOM for variable detuning on the trapping light and EOM for sidebands used in polarization-gradient cooling; (c) generation of slowing light with sidebands and light near the $|F = 1\rangle \rightarrow |F' = 2\rangle$ transition used for repumping and $F = 1$ probing; (d) splitting off of repumping light and generation of $F = 1$ probe light with variable detuning; (e) generation of $F = 2$ probe light at variable detuning; and (f) saturated absorption locking scheme. All numbers in italics represent the detuning in MHz from the cycling transition.

balance is particularly important and visible during the polarization–gradient cooling. The slowing light is sent along the slower axis, and is aligned by maximizing the fluorescence in the oven chamber. The repumping light is sent into the chamber by focusing the beam at the focus of a telescope which expands one of the trapping beam, and reflecting it into the trapping beam path with an edge mirror. The dark spot is created by passing the repumping light through a mask which is imaged onto the trapped atomic cloud. The repumping light passes through the cloud only once, and therefore defines a dark cylindrical tube through the cloud; adding a second repumping beam proved difficult to align and did not significantly improve the loading.

3.5 The cloverleaf magnetic trap

Bose–Einstein condensates are created at temperatures which are much colder than any available object with which they can be put in contact. Therefore, condensates must be contained, manipulated, and probed using non–contact techniques, i.e. using electro–magnetic fields.

One very important tool for handling condensates is an inhomogeneous magnetic field. In the presence of a magnetic field, the energy of an atom is shifted by an amount $U = -\vec{\mu} \cdot \vec{B}(\vec{r})$ where $\vec{B}(\vec{r})$ is the magnetic field at a point \vec{r} . At low fields, the magnetic moment of the atom $\vec{\mu}$ is directly proportional to its total spin \vec{F} as $\vec{\mu} = g\mu_B \vec{F}$ where g is the Landé g –factor, and μ_B is the Bohr magneton. The magnetic energy is then given by $U = -g\mu_B m_F |\vec{B}(\vec{r})|$. At higher fields, the separate magnetic energies of the nuclear and electron spins must be accounted for, as described by the Breit–Rabi formula. This gives rise to a low–field quadratic Zeeman shift and the eventual decoupling of the electron and nuclear spins at high field.

The magnetic field $\vec{B}(\vec{r})$ may generally vary in space and in time. Yet, so long as the field direction \hat{B} varies slowly compared to the transition frequencies between magnetic quantum states, the magnetic moment of the atom will follow the magnetic field adiabatically. For an atom moving with velocity \vec{v} in a static magnetic field (in the low–field regime), the adiabatic criterion can be written as

$$|\vec{v} \cdot \nabla \hat{B}| \ll \frac{g\mu_B |\vec{B}|}{\hbar} = \omega_L \quad (3.1)$$

where ω_L is the Larmour frequency.

A magnetic trap in free space (away from current carrying wires or magnets) is obtained by creating a magnetic field which has a minimum of the field strength. This creates a confining potential $U = |\mu||\vec{B}(\vec{r})|$ for atoms with a magnetic moment anti–aligned with the magnetic field, i.e. for low–field magnetic quantum states for which $gm_F < 1$ (weak–field seekers). Strong–field seekers ($gm_F > 1$) cannot be magnetically trapped in a static field because a magnetic field maximum cannot be created in free space [143].

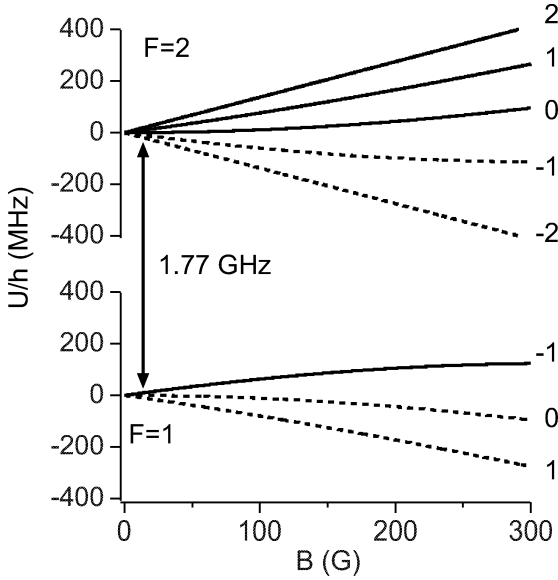


Figure 3-4: Energies of hyperfine states of sodium in a magnetic field B . States with a total spin $F = 2$ at zero field are shown in the top of the figure, and those with $F = 1$ at the bottom. The quantum number m_F of the spin-projection on the magnetic field axis is shown at right. Solid lines indicate weak-field seeking, magnetically-trappable states at low field. States indicated with dashed lines cannot be magnetically trapped. Resonant spin-flips from trappable to non-trappable states eject atoms from the trap.

Fig. 3-4 shows the energy levels of the electronic ground states of sodium in a magnetic field. ^{23}Na has a nuclear spin of $3/2$, and therefore the total atomic spin in the $3S_{1/2}$ ground state is either $F = 1$ or $F = 2$, giving eight different hyperfine states. In a magnetic field, these states are split as indicated in the figure. At low field, there are three magnetically trappable states: $|F = 1, m_F = -1\rangle$ (which we trap and cool), and $|F = 2, m_F = +1, +2\rangle$. Due to a quadratic Zeeman shift, the $|F = 2, m_F = 0\rangle$ hyperfine is also weak-field seeking, and has been trapped (inadvertently) by the group of Alain Aspect using ^{87}Rb , which has a similar level structure [144].

Magnetic traps serve three functions in a BEC experiment. First, they must hold the cold atomic sample in free space and isolate it from the much hotter walls of the vacuum chamber. Keeping the atomic sample cold further requires that the magnetic trapping fields be stable against vibrations of the trap center and strength. Second, the trap must catch the pre-cooled gaseous sample and increase its collision rate to ensure rapid thermalization. This requires that upon being switched on, the magnetic trap be sufficiently deep and be able to catch atoms in a “mode-matched” manner. Thereafter, one should be able to increase the trap strength sufficiently to compress the gas and increase its elastic collision rate. Finally, the magnetic trap must allow for evaporative cooling of the atomic gas to the BEC transition temperature. This function can be hampered by magnetic field fluctuations

or by an insufficient trap lifetime.

3.5.1 Spherical quadrupole traps and their modifications

Most of these requirements are met by a spherical quadrupole magnetic trap, which is easily produced by two coaxial electromagnet coils with current running in opposite direction (an “anti–Helmholtz” configuration). This field configuration provides linear confinement about a zero–field minimum, i.e.

$$\vec{B}(x, y, z) = B'/2 \times (x\hat{x} + y\hat{y} - 2z\hat{z}) \quad (3.2)$$

Such a magnetic trap is easy to implement since it uses the same coils as a magneto–optical trap. Evaporative cooling is not only easily jump–started by applying strong field gradients, but also is accelerated by the linear trapping fields which raise the collision rate as the gas cools (runaway evaporation, see Ref. [145]). Indeed, these traps were used for the first demonstrations of rf–induced evaporation [126, 127]. However, this trap does not provide sufficient trapping times for evaporative cooling. The adiabaticity criterion (Eq. 3.1) fails for atoms which pass near the zero–field point, where the Larmour frequency ω_L goes to zero. Thus, atoms at the trap center may undergo diabatic spin–flips (called Majorana flops [146]). This trap loss worsens as the trapped cloud becomes colder since atoms are more likely to be found near the trap center, and thus evaporative cooling comes to a halt before reaching Bose–Einstein condensation.

This detrimental trap loss was overcome by modifying the spherical quadrupole trap in two different ways. One approach, introduced by the Boulder group, is to add a rotating bias field $B_{\text{rot}} = B_0(\cos(\omega t)\hat{x} + \sin(\omega t)\hat{y})$ where the rotation frequency ω is much greater than the oscillation frequencies in the trap. Adding a bias field keeps the zero–field point away from the atomic cloud, and moving it quickly prevents atoms from catching up to it. The atoms then experience a time–averaged potential (the TOP trap) of the form

$$U_{\text{TOP}} = g\mu_B \left[\frac{B'^2}{2B_0}(x^2 + y^2) + \frac{4B'^2}{B_0}z^2 \right] \quad (3.3)$$

The linear confinement of the spherical quadrupole field is replaced by an oblate (pancake–shaped) trapping potential with harmonic confinement. This slows down evaporative cooling, but provides a stable and well–characterized trap. The TOP trap was used for the first observation of gaseous Bose–Einstein condensation by the group of Cornell, Wieman and colleagues at Boulder [128].

A second modification, introduced by our group, was the addition of an intense, blue–detuned laser beam focused to the magnetic trap center. This produced a several μK high optical potential which repelled atoms from the zero–field point. The confinement remains linear away from the $\approx 10 \mu\text{m}$ diameter of the optical potential, and thus evaporation can be

extremely effective. The optically plugged trap was used to create the first Bose–Einstein condensates of sodium [1]. These condensates were a much “brighter” source than those created at Boulder, with condensates containing about 5×10^5 atoms created after just 7 seconds of evaporation.

However, the combined magnetic and optical potential was difficult to characterize well, and was unstable to vibrations of the laser beam. Thus, already before its successful use to create the first sodium condensates (which took us somewhat by surprise), I began to design a new magnetic trap which would make the production and study of Bose–Einstein condensates easier and more robust. The product of this work, which was built by Dallin Durfee, Marc–Oliver Mewes and myself, is the cloverleaf magnetic trap, which has been used since 1996 for all the experiments described in this dissertation.

3.5.2 Ioffe–Pritchard traps

Our goal was to create a static magnetic trapping potential with a non-zero magnetic field at its minimum, and which would therefore not suffer from Majorana trap loss. The strongest trapping potential which meets this requirement is called a Ioffe–Pritchard trap after its proposed use for plasma confinement by Ioffe [147] and for trapping neutral atoms by Pritchard [148, 149]. The magnetic fields of a Ioffe–Pritchard trap are described at short distances from the center of the trap by three parameters. Letting the axis of the trap be the z -direction, with the origin lying at the center of the trap, these parameters are the following: the field curvature in the axial direction B'' ; the gradient of the quadrupole field in the $x - y$ (radial) plane B' ; and the uniform bias field in the z -direction B_0 . Separating the radial gradient field \vec{B}_G from the axial curvature field \vec{B}_C , we have

$$\vec{B}_G(x, y, z) = B'(x\hat{x} - y\hat{y}) \quad (3.4)$$

$$\vec{B}_C(x, y, z) = -\frac{B''z}{2}(x\hat{x} + y\hat{y}) + (B_0 + \frac{1}{2}B''z^2 - \frac{1}{4}(x^2 + y^2))\hat{z} \quad (3.5)$$

Thus, for the magnetic field strength in the trap, we find

$$B(x, y, z) = \sqrt{\left[B_0 + \frac{1}{2}B''z^2 - \frac{1}{4}B''(x^2 + y^2)\right]^2 + \left[B' - \frac{B''z}{2}\right]^2 x^2 + \left[B' + \frac{B''z}{2}\right]^2 y^2} \quad (3.6)$$

A Ioffe–Pritchard trap can be operated in two regimes, depending on the comparison between the trap potential at the trap minimum $|\mu|B_0$ and the thermal energy $k_B T$ of the trapped cloud. For a high temperature cloud $k_B T > |\mu|B_0$, the trap operates in the linear regime. The potential is harmonic in the \hat{z} -direction, and linear in the radial directions, taking the form

$$U_{IP} \simeq |\mu| (B'r + B''z^2/2) \quad (3.7)$$

where $r = (x^2 + y^2)^{1/2}$ is the radial coordinate. For a low temperature cloud ($k_B T < |\mu|B_0$),

the trap operates in the harmonic regime as the potential is harmonic in all three directions,

$$U_{\text{IP}} \simeq |\mu| (B_0 + B''_r r^2/2 + B'' z^2/2) \quad (3.8)$$

where the radial field curvature B''_r is given by

$$B''_r = \frac{B'^2}{B_0} - \frac{B''}{2} \quad (3.9)$$

3.5.3 Design considerations

The generic form of a Ioffe–Pritchard magnetic trap does not imply a unique winding pattern of electro–magnets or placement of permanent magnets to create the trapping field. For our experiment, an electro–magnet winding configuration was sought which would

- trap the ~ 5 mm diameter, ~ 100 μK cloud produced by optical cooling,
- increase the collision rate per particle to at least 10 Hz by subsequently compressing the cloud,
- provide a stable and reproducible trapping field to allow for evaporative cooling to sub– μK temperatures,
- allow sufficient optical access for lasers used for optical cooling and trapping, optical manipulation, and probing (12 laser beams at the time),
- use commercially available power supplies,
- safely dissipate the power consumed by resistive heating, and
- be compatible with an ultra–high vacuum environment by placing all coils outside the vacuum chamber.

Thus, for example, the straightforward implementation of a Ioffe–Pritchard trap using four current carrying bars with a pair of pinch coils [86, 149] could not be used since it limited optical access, and could not be placed wholly outside our vacuum chamber.

The basic innovation in our design was the realization (pointed out in [150]) that a Ioffe–Pritchard trapping field could be constructed with a planar coil geometry, i.e. without placing any coils in the $x - y$ (radial) plane. A simple way to see how this is done is shown in Fig. 3–5 (see also the Ph.D. thesis of Marc–Oliver Mewes [151]). Consider the magnetic field produced at the mid–point between two co–axial, circular electro–magnet coils carrying current in the same direction. Along the axis, each coil produces a field purely in the \hat{z} –direction which diminishes in strength away from the coil. Thus, midway between the coils, the field along the axis has a minimum, and rises in magnitude quadratically away from that point. This gives the axial \vec{B}_C field required for a Ioffe–Pritchard trap. The magnetic field

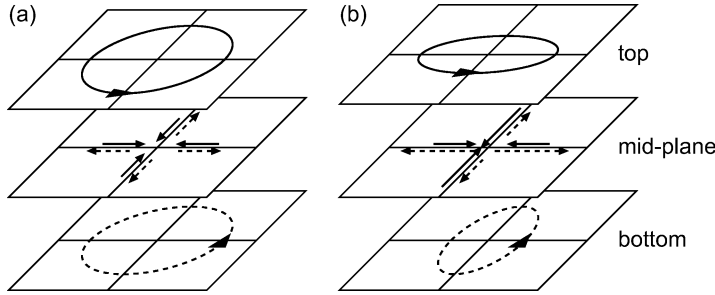


Figure 3-5: How to make a Ioffe–Pritchard trap with planar coils. Each circular coil in a Helmholtz pair produces a radial gradient field in the mid–plane between the coils, but the gradients from the top coil (solid) and bottom coil (dashed) cancel. If the coils are pinched in orthogonal directions, the radial gradient fields are no longer cylindrically symmetric, and thus do not cancel. This yields a Ioffe–Pritchard field configuration.

lines from each coil converge toward the axis below (from the $(-\hat{z})$ -direction) and diverge above the coil. Thus, in the radial plane between the coils, the bottom coil produces an outward–pointing radial field ($\vec{B} = \vec{B}_C/2 + |B'_z|(x\hat{x} + y\hat{y})/2$), while the top coil produces an inward–pointing radial field ($\vec{B} = \vec{B}_C/2 - |B'_z|(x\hat{x} + y\hat{y})/2$)*. The radial fields of the two coils cancel out, giving no net radial field in the mid–plane as required by symmetry.

This situation is altered if the two coils are pinched in orthogonal directions (Fig. 3-5b). The field lines of each coil diverge fastest in the direction in which the coil diameter is smallest (smaller coils produce a more inhomogeneous field). Thus, the radial field produced by the bottom coil ($\vec{B} = \vec{B}_C/2 + |B'_z|[(1 + \epsilon)x\hat{x} + (1 - \epsilon)y\hat{y}]/2$ with $0 < \epsilon < 1$) and that produced by the top coil ($\vec{B} = \vec{B}_C/2 - |B'_z|[(1 - \epsilon)x\hat{x} + (1 + \epsilon)y\hat{y}]/2$) no longer cancel, resulting in a radial quadrupole field \vec{B}_G , and thus a Ioffe–Pritchard trap.

This two–coil winding pattern (the “racetrack” trap) can be modified to yield various other trap designs (Fig. 3-6). These designs were compared according to the factor by which the collision rate is increased after the optically cooled cloud is fully compressed, a figure of merit which allows one to compare magnetic traps of different strengths and geometries. For a Ioffe–Pritchard trap in the harmonic regime, this factor is directly related to the geometric mean of the trap curvatures which is proportional to (approximately) $B'^{4/3}B''^{1/3}B_0^{-2/3}$. The linear regime is effectively treated by replacing B_0 with $k_B T/|\mu|$ for a cloud at a temperature T (see Sec. 3.5.5). Clearly, an optimal trap design will maximize the radial gradient B' rather than the axial curvature B'' .

This is the principle behind the design of the cloverleaf trap. Starting from the “race–track” design, the role of different parts of the coils can be identified by splitting each coil into three: a central coil which produces an axial curvature, and a pair of coils which primarily create the radial gradient. The radial gradient is maximized by placing as many

*Here B'_z is the axial field gradient of each coil at the mid–point between the coils. This field satisfies $\nabla \cdot \vec{B} = 0$

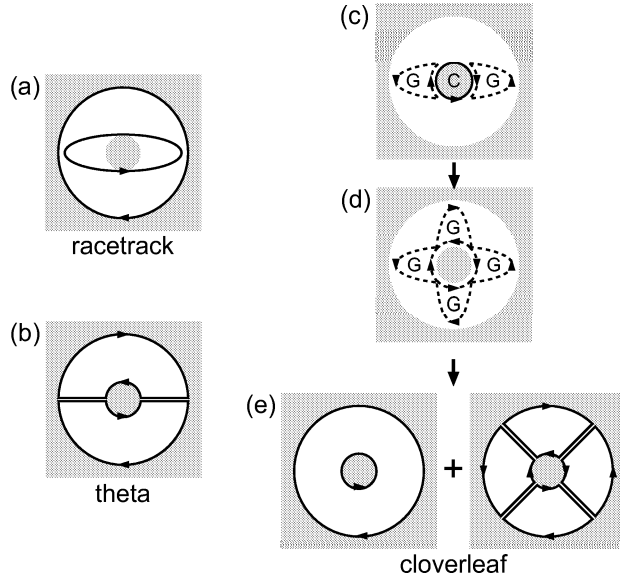


Figure 3-6: Planar winding patterns for a Ioffe–Pritchard trap. All designs are constrained to fit within an annular region of inner diameter $1\frac{1}{4}$ ", and outer diameter 5". (a) Adding a pair of anti–bias coils to the pinched–Helmholtz coils yields the “racetrack” design, (b) which can be modified to yield the “theta” design, which is quite similar to the four–Dee trap of Lene Hau [152]. (c) The racetrack coil can be divided into three smaller coils: a curvature coil (marked C), and two gradient coils (marked G). (d) Adding a second pair of gradient coils doubles the radial gradient, as desired for compressing the cloud. (e) Optimizing this design yields the cloverleaf trap. Four gradient coils arranged like a cloverleaf are placed in one plane, and two circular coils, the narrow curvature coils and the larger anti–bias coil, are placed in a second plane farther from the trap center.

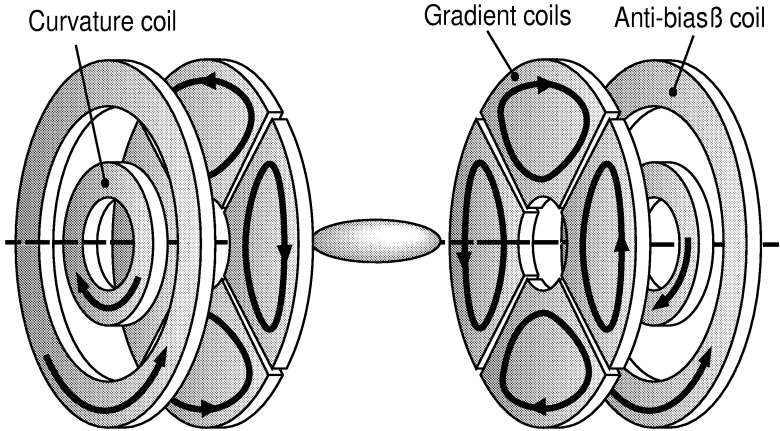


Figure 3-7: The cloverleaf magnetic trap. The trap consists of two identical units of electro-magnets mounted on opposite sides of the vacuum chamber. In each unit, four gradient coils arranged like a cloverleaf are placed in a plane close to the atoms, and two circular coils, the narrow curvature coils and the larger anti-bias coil, are placed in a second plane on top. The directions of current flow and the position and orientation of a trapped atomic cloud are indicated. Figure adapted from [151].

gradient coils as close as possible to the trap center. To utilize this space most effectively, the curvature coil is moved farther away, and a second set of gradient coils is added, related to the first by a rotation of 90° about the axis and a reversal of the current. After placing as many loops of wire as possible in these gradient coils (according to the available power), two more coils are added: a narrow pinch coil (the curvature coil) which produces axial field curvature and a large axial bias field, and a larger coaxial coil (the anti-bias coil) which cancels out the field without cancelling out the curvature. Aside from providing a strong trapping field and allowing a large degree of optical access, the cloverleaf trap design also allows for nearly independent control over the three trap parameters (B_0 , B' , B'') by producing each with a different set of coils. This has made the cloverleaf trap a flexible tool for manipulating Bose-Einstein condensates in a variety of studies.

The cloverleaf trap is now also used by other groups such as those of Randy Hulet at Rice University, and of Deborah Jin at JILA, Boulder, and has been adapted for use in the group of Lene Hau at the Rowland Institute (the “four-Dee” trap) [152]. A variety of innovative single-plane trap designs which could be constructed by laying wires down on a single substrate were described earlier by Weinstein and Libbrecht [153].

3.5.4 Description of the cloverleaf trap

The cloverleaf trap consists to two identical magnet units, each of which contains the four cloverleaf coils, one curvature coil, and one anti-bias coil. Each unit was designed to fit within a recessed vacuum viewport (see Sec. 3.3) which provided an annular space with

inner diameter of 1 1/4" and an outer diameter of 5". Each cloverleaf coil was composed of nine windings (stacked 3 high \times 3 deep), each curvature coil of twenty windings (5 \times 4), and each anti-bias coil of twelve windings (3 \times 4). The winding pattern was chosen to maximize the trap strength using a limited length of copper tubing — about 10 m for all gradient coils and 10 m for all curvature and antibias coils — which would yield an electrical resistance to match the specifications (20 A, 250 V) of available power supplies. The curvature and anti-bias coils were designed to cancel out the axial bias field within < 10 G when all coils are operated in series — each coil, alone, produces about 200 G of field when fully powered. Finer control of the bias field (down to 1 G) was first achieved by placing a variable shunt resistor in parallel with one of the anti-bias coils, but this setup was found to be sensitive to fluctuations in the temperature of the cooling water. Later, an additional bias coil (three turns, 5" diameter) was placed in one of the vacuum inserts and operated in series with the curvature and anti-bias coils. The nominal axial bias field was adjusted by sliding this coil (the "trombone" coil) toward or away from the trap. A future trap design should include such a coil placed in a strong mount which can be moved reproducibly.

The coils were wound using circular hollow copper tubing with an outer diameter of 1/8" and an inner diameter of 1/16", which is used commercially for refrigeration (ironically) and is thus easily purchased. The coils were first wrapped with at least two layers of a mylar tape made by 3M, providing a thin (\approx 20 mil = 0.5 mm), durable, and flexible insulating sheath. The coils were wound either by hand (for the odd-shaped cloverleaf coils), or using a lathe (for circular curvature and anti-bias coils) around specially designed steel mandrels. The coils in each unit were mounted against a thin perforated plastic board, secured by thin copper wires, and then set in epoxy. Four threaded, non-magnetic brass rods were also mounted on the plastic board, and then used to secure the magnet units tightly against the vacuum inserts.

The cloverleaf trapping coils were divided into two independent electrical circuits. One circuit connected all eight cloverleaf coils (four in each unit) in series, powered by a single power supply which provided a current of up to 250 A (Fig. 3-8). Connections between the thick current carrying cables and the copper tubing of the electro-magnets were made by hard-soldering the tubing against a large aluminum lug. This circuit demonstrates our basic technique for switching inductive loads on and off quickly. The power supply is operated in current-control mode. Thus, when the switch (an IGBT in this case) is open, capacitors in the power supply are charged up at maximal voltage. When the switch is suddenly closed, the high voltage allows the current to build up as quickly as possible (within less than a millisecond for the magnetic trap). To safely and quickly switch off the coils, a diode is added, sometimes in series with a resistor, which is backward-biased during the operation of the coil, but which provides a "burn-off" path for current once the switch is opened. The resistor in this path defines the maximum voltage across the switch during the turn-off.

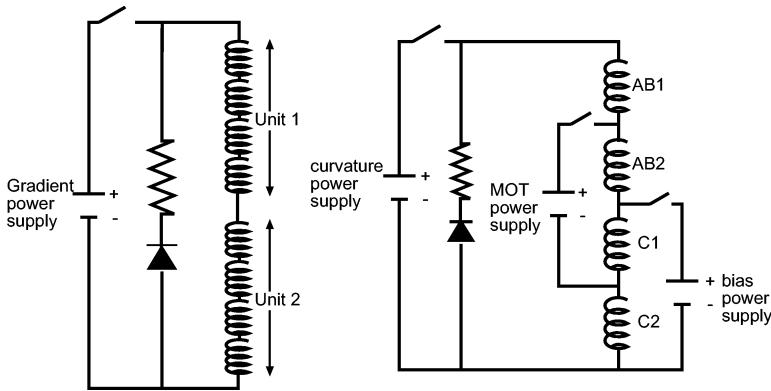


Figure 3-8: Cloverleaf trap circuit diagram. The cloverleaf magnetic trap is powered by two separate circuits: the gradient circuit (left), and the curvature/anti-bias circuit (right). The gradient circuit demonstrates the basic technique for switching high-current electromagnets. The curvature/anti-bias circuit also provides an adjustable bias field and the spherical-quadrupole field used for the magneto-optical trap.

This voltage should be kept as high as possible to lower the current across the inductive magnet coil as quickly as possible, without damaging the power supply and switch.

The curvature and anti-bias coils were connected in a second electrical circuit which allowed the coils to be used for three different purposes during the experiment. Operating all four coils in series produces the nominal axial trapping field with high axial curvature and a bias field of 1 – 2 G. To increase the bias field and produce a weaker trap, such as needed to catch the optically pre-cooled cloud, current is added from a second power supply to the two curvature coils. A third power supply is connected to a curvature coil in one of the magnet units and to an anti-bias coil from the other unit to yield the spherical-quadrupole field required for a magneto-optical trap. This setup requires that each of these three high-current power supplies provide a voltage difference without reference to ground (i.e. that they “float”). This requires that all digital and analog control voltages provided to these instruments and to the IGBT drivers be isolated from the computer control system by means of differential amplifiers.

After assembly, the fields produced by the trapping coils were measured on the bench with a Hall probe. These measurements were later verified by various probes of trapped atomic samples. The axial curvature, radial gradient, bias (from two curvature coils) and quadrupole (from a curvature/anti-bias pair) fields produced by the coils (Table 3.3) were somewhat smaller than those expected, presumably due to the imprecise shaping of the coils. During its typical operation, the trapping field is cigar shaped with a field curvature of 120 G/cm², a radial gradient of 100 G/cm, and a bias field of 1 – 2 G. For sodium atoms in the $|F = 1, m_F = -1\rangle$ state, this gives trap frequencies of $\omega_z \simeq 2\pi \times 17$ Hz axially and $\omega_r \simeq 2\pi \times 230$ Hz radially.

The ≈ 10 kW consumed in the cloverleaf coils by resistive heating are dissipated by water

radial gradient	0.56 G/cm
axial curvature	0.48 G/cm ²
axial bias	1.6 G
axial gradient	1.0 G/cm

Table 3.3: Fields produced by the cloverleaf trap at a current of one ampere. Indicated are the radial gradient produced by all eight cloverleaf coils, the axial curvature produced by all curvature and anti-bias coils, the axial bias field produced by the two curvature coils, and the axial field gradient produced by a curvature/anti-bias coil pair. Measurements were made with a Hall probe, and then confirmed by characterizing trapped clouds.

cooling. Water is pumped through each coil in parallel, with 40 PSI of pressure through the small gradient coils, and 100 PSI through the curvature and anti-bias coils. Flow rates of ≈ 500 ml/minute through each coil were sufficient to dissipate the heat with only a $\lesssim 50^\circ\text{C}$ temperature rise at the exit from the coils. These flows are monitored by in-line flow meters connected to an interlock system which would open all the current switches in case of little or no water flow.

3.5.5 Operation of the cloverleaf trap

During a typical experimental run, the cloverleaf trap is operated in three modes. First, a current of about 20 A from the MOT power supply is sent through a curvature coil in one unit and through an anti-bias coil in the other magnet unit. This produces a spherical-quadrupole field with an axial gradient of about 20 G/cm used for the magneto-optical trap. Using different sized coils implies that the field gradients vary away from the trap center (the curvature coil is indeed designed for this purpose), but this apparently has not impaired the operation of the MOT.

Second, after a pulse of polarization-gradient cooling, the atoms are caught in the magnetic trap. Ideally, the magnetic trap would have just the right trap center, strength, and aspect ratio to match the size and temperature of the pre-cooled cloud. Such an ideal transfer, called “mode-matching” prevents a lowering of the collision rate and phase-space density due to sloshing and re-equilibration. To this end, the cloverleaf is switched on as a roughly spherically-symmetric trap, with field curvatures of about 120 G/cm². At times, the position of the MOT was adjusted to overlap with the center of the cloverleaf trap using three additional magnet coils. However, since losses from an imperfect mode-matching are slight, these settings were rarely updated.

In principle, a radial field curvature $B''_r \simeq B'^2/B_0$ of 120 G/cm can be obtained using a small gradient field, which makes the trap easy to switch on and which can then be ramped up to full strength to compress the cloud. However, as we soon realized, this approach is not desirable because of distortions in the trapping field which arise due to high-order terms in

the magnetic field strength. Consider the field produced in the $x - z$ plane:

$$B(x, z) = \sqrt{\left[B_0 + \frac{1}{2}B''z^2 - \frac{1}{4}B''x^2\right]^2 + \left[B' + \frac{B''z}{2}\right]^2 x^2} \quad (3.10)$$

$$= \sqrt{\tilde{B}_0^2(z) + \left[B'(B' + B''z) - \frac{1}{2}B''B_0\right]x^2 + \frac{B''^2}{16}x^4} \quad (3.11)$$

The cloud is not confined to the z -axis at $z < z_d$ where the distortion point z_d is

$$z_d = \left(\frac{B'}{B''} - \frac{1}{2}\frac{B_0}{B'}\right) \quad (3.12)$$

This is the point where the magnetic field, as one proceeds along the \hat{x} direction from the z -axis, changes from providing a single quadratic minimum on the z -axis to having two minima away from the z -axis (at z_d the magnetic field provides only quartic confinement). The distortion arises because the radial field gradients produced by the curvature coils away from the trap center eventually cancel out the radial quadrupole field. Beyond the distortion point, the locus of the two minima provide “escape arms” through which the cloud expands away from the trap center. When viewed with the similar escape arms in the $y - z$ plane, this distortion shapes an improperly confined cloud into a characteristic “X” pattern which we have observed. To avoid this, the distortion points are moved far from the trapped cloud by switching on the cloverleaf trap at full strength, with about 200 A from both the curvature and gradient power supplies, with the addition of about 40 A of current from the bias power supply which weakens the trap for mode-matching.

3.5.6 Properties of magnetically-trapped clouds in the linear and harmonic confinement regimes

The trapped cloud is then compressed by gradually reducing the bias field to between 1 – 2 G, thereby increasing the radial confinement. This is the third, final setting for the cloverleaf trap. The goal of the compression is to increase the collision rate as much as possible, as is necessary for efficient evaporative cooling. To determine the increase in collision rate (the figure of merit of the cloverleaf trap), let us consider the equilibrium properties of a classical magnetically trapped cloud.

Consider a trapping potential such that at the trap minimum, $U(\vec{r}_{min}) = 0$. We define a volume

$$V = \int d\vec{r} e^{-U(\vec{r})/k_B T} \quad (3.13)$$

for a gas at a temperature T , so that the density at the trap minimum is given by $n_{peak} = N/V$, where N is the number of trapped atoms. From the relation between the partition function $Q = (V/\lambda_{dB}^3)^N/N!$ and the Helmholtz free energy ($A = -k_B T \ln Q$), we can

calculate the entropy per particle in the cloud:

$$\frac{S}{N} = -\frac{1}{N} \frac{\partial A}{\partial T} = \frac{k_B}{N} \left[\ln Q + T \frac{\partial \ln Q}{\partial T} \right] \quad (3.14)$$

Suppose $V \propto T^\alpha$. Then,

$$\frac{S}{N} = k_B \left[\frac{5}{2} + \alpha - \ln(n_{\text{peak}} \lambda_{dB}^3) \right] \quad (3.15)$$

where $\lambda_{dB} = \sqrt{2\pi\hbar^2/mk_B T}$ is the thermal de Broglie wavelength. Note that the above equation implies that the peak phase-space density $n_{\text{peak}} \lambda_{dB}^3$ can be increased adiabatically (constant entropy S) by changing the form of the trapping potential. This has been discussed and demonstrated by Pinkse *et al.* [154] and was later used by our group to create Bose–Einstein condensates reversibly [14] (see Sec. 6.2). Finally, using the average density in the cloud $\langle n \rangle = n_{\text{peak}}/2^\alpha$, the cloud averaged collision rate is

$$\Gamma = \sigma \times 4 \sqrt{\frac{k_B T}{\pi m}} \frac{1}{2^\alpha} n_{\text{peak}}. \quad (3.16)$$

Now let us apply these considerations to the two regimes of an Ioffe–Pritchard trap. In the harmonic regime, the trapping volume is

$$V_H = \left(\frac{2\pi k_B}{|\mu|} \right)^{\frac{3}{2}} T^{\frac{3}{2}} \frac{1}{B_r'' B''^{1/2}} \quad (3.17)$$

and thus $\alpha = 3/2$. In the linear regime, the trap volume is

$$V_L = \frac{3}{4\pi} \left(\frac{2\pi k_B}{|\mu|} \right)^{\frac{5}{2}} T^{\frac{5}{2}} \frac{1}{B''^2 B''^{1/2}} \quad (3.18)$$

giving $\alpha = 5/2$. Thus, changing the trapping potential from the harmonic to the linear regime during compression increases the phase-space density by a factor of e .

Consider the capture and compression of a spherical cloud of diameter 3 mm, and temperature 100 μK containing 2×10^9 atoms. Mode-matching requires curvatures of ≈ 120 G/cm² in the radial and axial directions. With a radial gradient of 100 G/cm, this requires a bias field of 55 G. The volume, peak density, phase-space density, and collision rate in this cloud are shown in Table 3.4, where the cross section is taken as $\sigma = 2 \times 10^{-12}$ cm².

The conditions after the cloud is compressed isentropically by ramping down the bias field to zero (Table 3.4) are determined by a scaling parameter $\zeta = |\mu|B_0/k_B T_H$ which is defined as the ratio of the potential at the trap minimum to the thermal energy $k_B T_H$ before compression. Aside from the numerical factors, these scaling laws are just those one would obtain in the harmonic regime were one to lower the bias field from its initial value to that where the energy at the bottom of the trap were equal to the initial temperature. Physically, this is to be expected since the cloud should be mostly insensitive to potential

	Before compression	After compression	Ratio (after/before)
temperature	$100 \mu\text{K}$	$161 \mu\text{K}$	$e^{-1/4}\zeta^{1/4}$
volume	$6.2 \times 10^{-2} \text{ cm}^3$	$1.1 \times 10^{-2} \text{ cm}^3$	$e^{-5/8}\zeta^{-3/8}$
peak density	$3.2 \times 10^{10} \text{ cm}^{-3}$	$1.8 \times 10^{11} \text{ cm}^{-3}$	$e^{5/8}\zeta^{3/8}$
phase-space density	1.5×10^{-6}	4.2×10^{-6}	e
collision rate	3.1 Hz	11 Hz	$e^{1/2}\zeta^{1/2}/2$

Table 3.4: Initial conditions in the magnetic trap before and after compression. Numbers assume a 3 mm diameter, $100 \mu\text{K}$ cloud of 2×10^9 atoms after transfer to the magnetic trap. The cloud is then compressed by ramping down the bias field from $B_0 = 55$ G to near zero. The relation between the conditions before and after compression is determined by the parameter $\zeta = |\mu|B_0/k_B T_H$.

energy changes smaller than its temperature.

3.6 Tools for manipulating Bose–Einstein condensates

Having achieved Bose–Einstein condensation, one would like to study condensates of different shapes and symmetries and explore their dynamic behavior. Therefore, we need tools to shape and excite the condensate. The extremely low temperature of the gas and the high sticking probability of atoms on cold surfaces forbid direct–contact manipulation of condensates, limiting us to various forms of electromagnetic fields.

- *Magnetic fields:* As discussed in Sec. 3.5, the interaction between the magnetic dipole moment of an atom and an inhomogeneous magnetic field results in a state-selective force. This force allows weak-field seeking atoms to be confined to magnetic traps. In a number of experiments, we have used inhomogeneous magnetic fields to influence the behaviour of condensates and study various static and dynamic properties. For example, condensates of variable density and aspect ratio were created for a number of studies [7, 9, 14, 18, for example] by varying the field parameters B_0, B' and B'' of the cloverleaf trap. As long as the variation in the magnetic trap was much slower than the relevant trap oscillation frequencies, this resulted in an adiabatic expansion or compression of the trapped gas. Pulsed or periodic applications of magnetic fields were used to study the dynamic response of trapped gases above and below the Bose–Einstein condensation temperature. For instance, collective excitations were produced by periodically modulating the axial or radial trap frequencies [4, 12]. Finally, in the study of spinor Bose–Einstein condensates (Chapter 10), bias and gradient fields were an important tool for modifying equilibrium and non-equilibrium properties and for separating components prior to imaging.
- *Rf fields:* Oscillating magnetic fields can be used to manipulate atomic gases by resonantly changing their hyperfine state. In our work, rf fields were applied to mag-

netically trapped atoms to switch them from a trapped to untrapped hyperfine states, thus realizing a variable output coupler for an atom laser [5]. This method also offered a convenient way to quickly change the number of trapped atoms. Rf fields were used in the study of optically trapped Bose–Einstein condensates to vary the population of different trapped hyperfine states. For example, atoms were prepared in specific hyperfine states for the observation of Feshbach resonances [11, 16]. Rf fields were also an important tool in the study of spinor Bose–Einstein condensates.

In our experiments, due to instabilities in magnetic fields which caused spin–flip resonance frequencies to vary by 10 – 50 kHz, we typically used rf–frequency sweeps to transfer atoms between hyperfine states [5]. Other groups have used either magnetic–field insensitive transitions (at JILA [155–157]) or magnetic shielding (in Munich [158–160]) to overcome magnetic field variations. This has permitted the use of long, frequency–selective rf–pulses for a variety of experiments.

Another important application of rf fields is their use to limit the trap depth of the magnetic trap. We introduced this method, referred to as “rf shielding,” to lengthen the lifetime of a magnetically trapped condensate [2]. A tentative explanation for this effect is that the limited trap depth ejects energetic atoms which are produced by background gas collisions before they can oscillate in the trap and collide with other atoms in the condensate. This converts a serious source of heating to a tolerable level of trap loss. This shielding mechanism is also operative in optical traps where the trap depth is also in the microkelvin range and in which long condensate lifetimes were observed (Sec. 9). However, a detailed study of the effects of “rf shielding” on heating and trap loss has not provided a consistent explanation [161, 162].

- *Optical dipole forces:* A particularly flexible tool for manipulating condensates is the optical dipole force of a focused off-resonant laser beam. The electric field of the laser light $\vec{E}_L(t)$ which oscillates at the optical frequency ω_L induces an oscillating electric dipole moment on an atom $\vec{d}(t) = \alpha(\omega_L)\vec{E}_L(t)$ proportional to the polarizability of the atom $\alpha(\omega_L)$. This oscillating electric dipole interacts with the electric field of the light giving a time–averaged optical potential or AC Stark shift [163].

For a two–level atom, the optical potential has a strength

$$U(\vec{r}) = -\frac{\hbar\omega_R^2(\vec{r})}{4} \left(\frac{1}{\omega_0 - \omega_L} + \frac{1}{\omega_0 + \omega_L} \right) \quad (3.19)$$

where ω_0 is the resonant frequency, ω_L the laser frequency and $\Delta = \omega_L - \omega_0$ its detuning. The Rabi frequency $\omega_R(\vec{r})$ is position dependent, and conveniently defined through $2\omega_R^2(\vec{r})/\Gamma^2 = I(\vec{r})/I_{\text{SAT}}$ where the intensity is scaled by the saturation intensity $I_{\text{SAT}} = \hbar\omega_0^3\Gamma/12\pi c^2$ which is 6 mW/cm² for sodium. The optical potential is repulsive in the case of blue detuning ($\omega_L > \omega_0$) and attractive for red detuning

$(\omega_L < \omega_0)$.

Using focused laser beams, one can optically “paint” a potential of nearly arbitrary form, using blue-detuned light to create potential “blips” and red-detuned light for potential “dips.” Since laser beams can be focused to spots with length scales on the order of an optical wavelength, they can be used for “microsurgery” on condensates which are typically tens or hundreds of microns in size. This is not possible with magnets or coils which are typically a few centimeters away from the trap center. Optical dipole forces have been used to create trapping potentials tailored for reversibly forming Bose-Einstein condensates [14] (Sec. 6.2), searching for persistent rotational currents [164, 165], and for observing the interference of two separated condensates [6]. Blue-detuned light was also used to “poke” Bose-Einstein condensates and excite sound waves [7] and to selectively push the non-condensed portion of a trapped cloud to study collective excitations [12]. Finally, infrared light has been used to achieve all-optical confinement of a condensate [10].

- *Bragg and Raman transitions:* Another useful optical manipulation tool is a two-photon transition induced by two intersecting laser beams. The absorption and stimulated emission of photons can transfer momentum to all or part of an atomic sample. This can either take the form of a Bragg transition, in which the internal state of the atom is left unchanged, or a Raman transition, in which the internal state is changed, say from one hyperfine state to another. Various uses of Bragg scattering are discussed in Chapter 8.

3.7 Probing

Following the creation and manipulation of an ultra-cold atomic gas, data is obtained by imaging the cloud. Let us distinguish clearly between image types and imaging techniques. In our work, we have used two different image types: *in situ* images, and time-of-flight images.

In situ images give the instantaneous column density of a trapped sample, integrated along the direction of propagation of the probe beam. Repeated *in situ* images can be used to trace the real-time dynamics of trapped atomic clouds. Using this tool, dynamical processes such as the formation [9] or collective excitations [12] of a condensate could be studied in a single experimental cycle, avoiding possible shot-to-shot technical fluctuations.

Time-of-flight images are taken after the trapped cloud has been suddenly released from its trap and allowed to freely expand and fall for a variable period of time. In the absence of interactions, atoms would propagate during the expansion at their instantaneous velocities at the time the trap was switched off. Collisional dynamics, such as collisional thermalization of a dense cloud or the release of mean-field interaction energy, alters this behaviour, as discussed in Chapter 4. Images record the position of atoms at a specific

time during the expansion. For short times of flight, the spatial distribution of the released atoms is indicative of their spatial distribution in the trap (near-field). For long times-of-flight, once a cloud has expanded far beyond its original size, the spatial distribution of the atoms indicates their velocity distribution modified by the effect of collisions (distorted far-field). Time-of-flight images have been used to study dynamical properties of trapped atomic samples [4, 155, 156, 166, 167] by allowing the gas to evolve in the trap for a variable amount of time before release from the trap. A time series of images is obtained over many repetitions of the experiment. While only one time-of-flight image per experimental cycle is typically taken, we have used repeated time-of-flight images to study the dynamics of the expansion of a Bose-Einstein condensate after its release from a magnetic trap and test predictions for this evolution [168].

These different image types have been taken using different imaging techniques: absorptive and dispersive imaging. As a thorough description of these two techniques can be found in Ref. [22], I shall summarize only the basic points.

The index of refraction of a dilute atomic vapor n_{ref} is directly related to the atomic density n as

$$n_{\text{ref}} = 1 + \frac{\sigma_0 n \lambda}{4\pi} \left[\frac{i}{1 + \delta^2} - \frac{\delta}{1 + \delta^2} \right] \quad (3.20)$$

Here σ_0 is the resonant cross-section, λ is the wavelength of the probe light, and $\delta \equiv (\omega - \omega_0)/(\Gamma/2)$ is the detuning of the probe light from the atomic resonance frequency in half line widths. If more than two levels are involved (as there are in our case), the index of refraction arises from several resonances and will generally be polarization-dependent. The index of refraction varies spatially across the cloud according to its density and polarization distribution.

Let us assume an atomic sample is illuminated uniformly by light propagating in the \hat{z} direction. Assuming the atomic cloud to be sufficiently thin so that light rays enter and exit the cloud at the same (x, y) coordinates (thin lens approximation), the complex electric field $\vec{E}(x, y)$ of the probe light after passage through the atomic sample is changed from \vec{E}_0 to

$$\vec{E}(x, y) = \vec{E}_0 \exp \left(-\frac{2\pi i}{\lambda} \int [n_{\text{ref}} - 1] dz \right) \quad (3.21)$$

$$= t \vec{E}_0 e^{i\phi} \quad (3.22)$$

where the integral extends across the entire cloud. We have neglected the possible tensor character of the index of refraction which can lead to optical rotation. Such optical rotation has been used to image Bose-Einstein condensates at Rice [130]. The transmission t and phase shift ϕ are simply related to the off-resonant optical density

$$\tilde{D}(x, y) = \frac{\sigma_0}{1 + \delta^2} \int n(x, y, z) dz \quad (3.23)$$

as $\ln t = -\tilde{D}(x, y)/2$ and $\phi = -\delta\tilde{D}(x, y)/2$. Thus by measuring either the transmission (which relates to the imaginary part of n_{ref}) or phase-shift (which relates to the real part of n_{ref}) of the probe light as a spatial image, one measures the column density $\tilde{n}(x, y)$ of the atomic cloud along the direction of probing.

An absorption image is taken by shining a probe light through the sample, and then imaging the atomic cloud onto a camera. This gives a spatial image of the transmission of the probe light (t^2) through the atomic sample. Because the transmission drops exponentially with the optical density, quantitative absorption imaging requires that the optical density be on the order of unity. Smaller optical densities yield a transmission which is too close to unity and thus hard to detect, while larger optical densities cause so much absorption that differences in optical density cannot be discerned (blacked-out images). For our trapped condensates, the resonant optical density is on the order of 300, and thus *in situ* absorption imaging yields no information on the trapped cloud. *In situ* off-resonant absorption imaging of condensates has been used to probe the surface of a condensate where the optical density is low [152]. However, the images must be interpreted with care because the condensate can deflect the near-resonant probe light at a wide angle due to the large phase-shifts across the cloud. In contrast, absorption imaging is particularly well suited for time-of-flight images, for which the trapped atomic sample can be allowed to expand to the point where the optical density drops to near unity.

Dispersive imaging measures the phase ϕ acquired by the probe light upon passage through the atomic sample. Such images are taken by converting phase variations in the probe light to intensity variations. In our work, we have used two types of dispersive imaging. Both techniques rely on the fact that scattered and unscattered probe light can be separated spatially at a Fourier plane in the imaging system. In dark-ground imaging, the unscattered probe light is blocked (Fig. 3-9a), and one images just the scattered light. This gives a light intensity proportional to ϕ^2 , and was used for the first *in situ* imaging of condensates [3]. In phase-contrast imaging (invented by Fritz Zernike in 1934 and used widely in biological microscopy), the phase of the unscattered light is advanced or retarded by a quarter wave (Fig. 3-9b). When the scattered and unscattered light are combined in the image plane, this converts phase modulations to intensity modulations which are linearly proportional to ϕ . Phase-contrast imaging is thus more sensitive, and has been used extensively in our experiments.

Dispersive imaging is superior to off-resonant absorption imaging for probing optically dense trapped condensates at high resolution. The explanation for this, given also in Refs. [3, 22], is as follows. Suppose one wants to image a small object of size d , which is at the resolution limit of the imaging system, with a resonant optical density $\tilde{D}_0 \gg 1$. A reliable absorption image requires that the optical density be on the order of unity, which can be attained by detuning the probe light by $\delta = \tilde{D}_0^{1/2}$. However, at this detuning, the phase shift across the cloud is $\phi = \tilde{D}_0^{1/2} \gg 1$. Thus the probe light is strongly bent by refraction

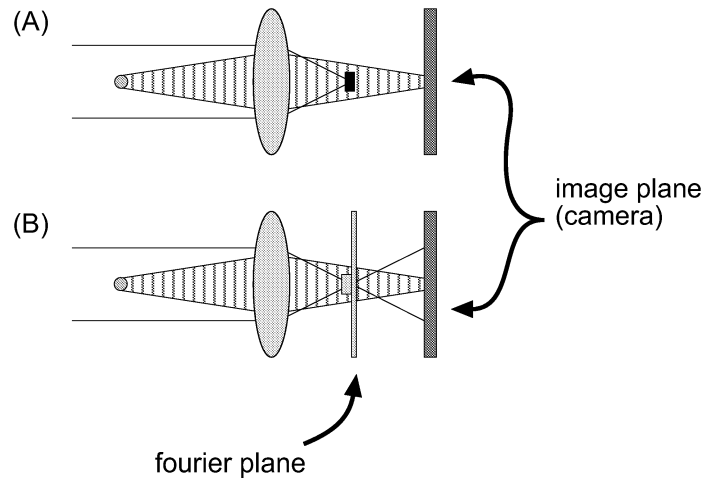


Figure 3-9: Dispersive imaging methods: dark-ground and phase-contrast imaging. Parallel probe light passes through an atomic gas and acquires a spatially dependent phase shift ϕ . At the Fourier plane of the imaging system, the diffracted and undiffracted light are separated. Spatial filtering can convert the phase modulation ϕ to an intensity modulation. (a) Blocking the undiffracted probe light yields a dark-ground image with an intensity $\propto \phi^2$. (b) A phase-contrast image is obtained by retarding or advancing the undiffracted light and combining it with the diffracted light at the image plane. In our experiment, this is accomplished by placing at the Fourier plane an optical flat with a raised bump at its center which retards the undiffracted light by a quarter cycle. Homodyne interference between the undiffracted light (local oscillator) and the diffracted light (signal) gives a signal $\propto \phi$ which is more sensitive to small phase shifts.

outside the diffraction angle λ/d and thus outside the collection angle of the imaging system. This degrades the resolution of the imaging system. To overcome this refractive bending of light, one must detune further to $\delta = \tilde{D}_0$. At this detuning, absorption is very small ($1 - t^2 \sim \tilde{D}_0^{-1}$) while the dispersive signal remains strong ($\phi \sim 1$) and provides good images.

In our experiment, light at two different frequencies is used for probing, at or near resonance on either the $3S_{1/2}|F = 1\rangle \rightarrow 3P_{3/2}|F' = 2\rangle$ transition ($F = 1$ probe) or the $3S_{1/2}|F = 2\rangle \rightarrow 3P_{3/2}|F' = 3\rangle$ transition ($F = 2$ probe) (Fig. 3-2). As shown in Fig. 3-3, the $F = 1$ and $F = 2$ probe beams are both sent through single-mode polarization-maintaining fibers from the laser room to the experiment table. The frequency of each of the beams can be adjusted about the resonance frequency, with a range of ± 50 MHz for the $F = 1$ light, and about ± 30 MHz for the $F = 2$ light.

The atomic cloud, which is trapped in the $|F = 1, m_F = -1\rangle$ state, could be directly absorption-imaged with the $F = 1$ light. Alternately, the $F = 1$ light was used to optically pump the atoms to the $F = 2$ hyperfine manifold, and then the $F = 2$ light was used for absorption imaging. Dispersive imaging was typically done using the $F = 2$ light (without optical pumping) giving a detuning of $\Delta = 1.71$ GHz. For some work, light at a detuning of $\Delta = 400$ MHz was used for dispersive imaging of more dilute clouds.

The two probe beams are used in a variety of imaging configurations. Our primary imaging axis is oriented vertically, with probe light sent from below the chamber, through the atomic cloud, and out the top of the chamber. From there, the light enters an optical setup which can be configured for different imaging methods (absorption, phase-contrast, and dark-ground) and three different magnifications ($M \simeq 1/2, 2, 8$) by placing and removing various optical elements on magnetic base plates[†]. A secondary imaging axis is oriented horizontally with probe light sent through the “penny windows” to an imaging station which allows for phase-contrast or absorption imaging with magnifications of $M = 2$ or $M = 8$. These small “penny windows” also provide access for a pair of dark-SPOT trapping beams, and, at times, an infrared laser used for an optical dipole trap and a pair of beams used for Bragg diffraction. These multiple uses are accommodated by using polarizing beam-splitters and edge, motorized, and dichroic mirrors. On one hand, this optical multiplexing makes the optical setup for each of these beams sub-optimal and inflexible. On the other hand, sending focused laser beams (such as the optical trapping beam) along an imaging axis makes their alignment fast and reproducible (see Sec. 9.2).

Images were taken with a CCD camera from Princeton Instruments with a large dynamic range (16-bit output), low dark current (signal collected due to current leakage even in the absence of light) and low-noise readout to an image processing computer. One very useful feature of the camera was a “kinetics mode” of operation in which all data stored on the

[†]Our use of magnetic base plates so close to the magnetic trap (as close as 25 cm) is certainly not advisable. These introduce stray magnetic fields which could disrupt evaporative cooling in an uncontrolled way. Whether the use of these base plates contributes to the slow ~ 50 mG fluctuations in our trapping fields is unclear.

CCD chip was rapidly advanced by a variable number of columns upon triggering. This mode was used to take rapid sequences of images by repeatedly exposing only a small portion of the camera, say the right side if the data was advanced from right to left, and shifting the data between images to store data on the unexposed portion of the chip. After a sequence of as many as 30 images at a repetition rate as high as 1 kHz, all the images were downloaded with low noise to the processing computer. Rapid-sequence phase-contrast images were used for several experiments studying dynamical processes in the trapped cloud, such as the formation of a condensate in a super-cooled vapor and collective excitations.

3.8 The life of a Bose–Einstein condenser

Since their first creation in 1995, Bose–Einstein condensates have been produced with regularity and used for a wide variety of studies. With a growing number of experimental groups entering the field, the complexity of the multi-stage cooling approach to create a condensate has been somewhat reduced and has been clearly managed. Nevertheless, at least from the experience of my colleagues and myself, Bose–Einstein condensation experiments still retain the challenge and thrill of their early years. Remaining on the rapidly advancing “cutting edge” requires quick implementations of new ideas, rapid reconfigurations of the experiments, and the management of an evolving complex apparatus. Indeed, over the last years, an experimental run was rarely routine; one was always trying a new approach, searching for a new effect, rapidly building, testing, or abandoning a new piece of equipment, or deciphering a newly encountered phenomenon.

This constant evolution dictated a certain character and design to our experiments. Runs of the experiment became a labor-intensive and consuming affair, with typically only one or two runs per week. Most of the beginning of a run was consumed by the alignment of the dye laser and optics to provide a large and stable magneto-optical trap and a cold optical molasses which were obtained by the repeated adjustment of laser beam profiles and balances. On a good day, typically within just a few days of a previous experiment, this alignment could take just a couple of hours and remain stable. On a bad day, the proper alignment could remain elusive for ten or twelve hours or require a frequent fiddling and tweaking throughout the day. Indeed, the initial optical loading and cooling were the most critical determinant of the success of an experimental run; if these optical methods were stable and optimally aligned, the subsequent evaporative cooling would always yield large Bose condensates of nearly constant number with little or no adjustment to the magnetic trap or the rf-evaporation route.

After creating stable experimental conditions, the experimental run often focused on the setting up, testing, and debugging of new experimental methods such as phase-contrast imaging, the optical trap, rf-sweeps, the operation of various magnet coils, etc. For this reason, the experiment was constructed in a way which would allow rapid reconfigurations of

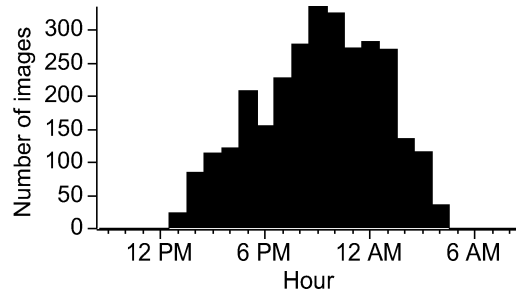


Figure 3-10: Due to the complexity of an ever-changing apparatus, experimental runs typically ran late into the night. A histogram shows the number of images saved for later analysis over a one year period (2/98 – 1/99) binned by the hour at which they were taken.

optics or electronics. This spirit influenced, for example, the design of the Word Generator computer control program and the use of patch panels of diodes and current switches for connecting power supplies to magnet coils.

Finally, overcoming all these hurdles to attain our experimental goals and collect data took persistence and time. Data were typically collected in the night, sometimes well after midnight (Fig. 3-10). But somehow, the reward of delving into the quantum world and encountering its mysteries made the lengthy pursuit worth while.

Chapter 4

Quantitative analysis of images

The following section is taken from Ketterle, Durfee, and Stamper-Kurn, “Making probing and understanding Bose-Einstein condensates,” in M. Inguscio, S. Stringari and C.E. Wieman eds., *Bose-Einstein Condensation in Atomic Gases*, Proceedings of the “Enrico Fermi” Summer School, July 1998, Varenna, Italy. To be published.

Some minor modifications have been made to conform to the symbols and section headings used in this dissertation. Equilibrium density distributions of trapped Bose-Einstein condensates are discussed further in Sec. 5 in relation to a number of experimental studies.

To this discussion, I would like to add the following point. In the Varenna paper [22] (here Sec. 4.5) we discussed methods for determining the condensate fraction. We noted that the determination of the condensate fraction from images of the density distribution is imprecise because of the ambiguous separation between the condensate and non-condensate distributions. In particular, thermal excitations with energies smaller than the chemical potential of the condensate (i.e. phonon excitations) will not separate from the condensate distribution during time-of-flight. We suggested that this ambiguity could be overcome by measuring coherence properties of the cloud, e.g. by interfering two portions of the cloud and determining the condensate fraction from the fringe contrast.

Such experiments have now been done. Recent experiments in Munich have used two narrow rf frequencies to couple atoms out of a magnetic trap at two well-defined locations. The two falling streams of atoms interfere with a contrast which determines directly the condensate fraction at the output coupling locations [160]. Another experiment along these lines is the coherence length measurement of Hagley *et al.* at NIST, Gaithersburg [169] who perform an autocorrelation measurement on the condensate wavefunction using diffraction from two pulses of an optical standing wave. Studying the fringe contrast as the time between the two pulses is varied similarly measures the condensate fraction. As in the Munich experiment, this contrast should be sensitive to low-energy excitations which reduce the condensate fraction but which would not be separated from the condensate during a time-of-flight measurement. Similarly, our spectroscopic measurement of the coherence length [18] should be sensitive to such excitations if the frequency resolution and signal-to-

noise ratio are improved.

The purpose of imaging and image processing is to provide reliable density distributions of the atomic cloud, either trapped or in ballistic expansion. All properties of condensates and thermal clouds are inferred from these density distributions. This is done by comparing the measured distributions with the results of models of the atomic gas.

We present below several such models, and the means by which physical properties are determined. We consider models appropriate for three regimes of temperature and density. At high temperatures ($T \geq T_c$) and low temperatures (pure condensates) these density distributions are well understood, experimentally verified, and reliable. In the intermediate regime, clouds contain both a condensed and uncondensed fraction, and there are only approximate predictions for their distributions.

4.1 Thermal clouds above the BEC transition temperature

Let us first consider a trapped gas above the BEC transition temperature in a harmonic trapping potential:

$$U(\vec{r}) = \frac{1}{2}m(\omega_x^2x^2 + \omega_y^2y^2 + \omega_z^2z^2). \quad (4.1)$$

An ideal Bose gas in this potential at thermal equilibrium can be described either in the canonical (constant N) or grand-canonical ensembles, taking into account the discrete energy levels. However, at temperatures higher than the level spacing, $k_B T \gg \hbar\omega_{x,y,z}$, we can use a semi-classical approach [90, 91, 170] to obtain the density

$$n_{th}(\vec{r}) = \frac{1}{\lambda_{dB}^3} g_{3/2}(z(\vec{r})) \quad (4.2)$$

where $\lambda_{dB} = (2\pi\hbar^2/mk_B T)^{1/2}$, $z(\vec{r}) = \exp((\mu - V(\vec{r}))/k_B T)$, μ is the chemical potential, and T is the temperature. The Bose function, generally given by $g_j(z) = \sum_i z^i / i^j$, introduces the effects of quantum statistics on the density distribution; compared to a distribution of distinguishable particles, the density of a Bose gas is increased by $g_{3/2}(z)/z$.

We can also use this semi-classical approach to determine the distribution in time-of-flight. When the trap is switched off, the trapped atoms fly ballistically from their position in the trap at their velocity at the time of the switch-off. For an atom starting at point \vec{r}_0 to arrive at a point \vec{r} after a time t of free expansion, its momentum must be $\vec{p} = m(\vec{r} - \vec{r}_0)/t$. Integrating over all initial positions \vec{r}_0 we determine the density distribution as a function of the expansion time t

$$n_{tof}(\vec{r}, t) = \frac{1}{h^3} \int d^3\vec{r}_0 d^3\vec{p} \frac{1}{e^{-(\mu - H(\vec{r}_0, \vec{p}))/k_B T} - 1} \delta^3(\vec{r} - \vec{r}_0 - \frac{\vec{p}t}{m}) \quad (4.3)$$

$$= \frac{1}{\lambda_{dB}^3} \prod_{i=1}^3 \left(\frac{1}{1 + \omega_i^2 t^2} \right)^{1/2} g_{3/2} \left(\exp \left[\mu - \frac{m}{2} \sum_{i=1}^3 x_i^2 \left(\frac{\omega_i^2}{1 + \omega_i^2 t^2} \right) \right] \right) \quad (4.4)$$

At large times ($t \gg \omega_x^{-1}, \omega_y^{-1}, \omega_z^{-1}$), neglecting collisions during the expansion (see Sec. 4.7), the density profile becomes

$$n_{t\rightarrow\infty}(\vec{r}, t) = \frac{1}{\lambda_{dB}^3} \frac{1}{\omega_x \omega_y \omega_z t^3} g_{3/2}(e^{(\mu - \frac{mr^2}{2t^2})/k_B T}) \quad (4.5)$$

Thus, the thermal cloud expands isotropically once it becomes much larger than its original size.

4.2 Bose–Einstein condensates at zero–temperature

The density distribution of a zero–temperature Bose–Einstein condensate has been extensively discussed theoretically [171–173]. Due to the diluteness of the gas, effects of quantum depletion can be neglected (at least in the density distribution). The many–body ground state is described by a single, complex order–parameter $\psi(\vec{r})$. This state and its dynamics are described by the Gross–Pitaevskii equation

$$i\hbar \frac{d\psi}{dt} = -\frac{\hbar^2}{2m} \nabla^2 \psi + U(\vec{r})\psi + g|\psi|^2\psi \quad (4.6)$$

The parameter $g = 4\pi\hbar^2 a/m$ describes the effect of two–body collisions, where a is the s –wave scattering length and $|\psi|^2$ the density. The ground–state wavefunction is $\psi(\vec{r}, t) = \psi(\vec{r})e^{-i\mu t}$, where μ is the energy of the ground state, and is identified as the chemical potential.

4.2.1 Ideal–gas limit

This wavefunction is easily described in two limits. In the limit of weak interactions ($ng \ll \hbar\omega_{x,y,z}$) one can neglect the interaction term. Then, the condensate wavefunction is simply the ground state of the harmonic oscillator, which gives a density for N particles of

$$n_c(\vec{r}) = \frac{N}{\pi^{3/2}} \prod_{i=1}^3 \frac{1}{x_i} e^{-x_i^2/x_i^2} \quad (4.7)$$

Here the length scales $x_i = x_{i,HO} = \sqrt{\hbar/m\omega_i}$ are the rms–widths of the condensate wavefunction in each of the three dimensions (labeled by i).

In free expansion, a Gaussian wavefunction remains Gaussian except for a phase factor. Thus, after a time t of expansion, the condensate size is simply rescaled according to $x_i^2 = x_{i,HO}^2 + v_{i,HO}^2 t^2$, where $v_{i,HO} = \sqrt{\hbar\omega_i/m}$ is the rms velocity of the trapped condensate. This length can also be written as $x_{i,HO}^2(1 + \omega_i^2 t^2)$. As with the expansion of the thermal cloud, the dependence on the initial size becomes negligible for expansion times much longer than ω_i^{-1} .

4.2.2 Thomas–Fermi limit

In the limit of strong interactions ($ng \gg \hbar\omega_{x,y,z}$), the determination of the trapped condensate wavefunction is simplified by neglecting the kinetic energy term in Eq. (4.6) which is now much smaller than the interaction term. In this limit, known as the Thomas–Fermi limit, the density is given by

$$n_c(\vec{r}) = \max \left(\frac{\mu - U(\vec{r})}{g}, 0 \right) \quad (4.8)$$

Thus, one can think of the condensate in the Thomas–Fermi limit as “filling in” the bottom of the trapping potential up to a “height” of the chemical potential μ . In a harmonic trap, the condensate has a parabolic density profile,

$$n_c(\vec{r}) = \frac{15}{8\pi} \frac{N}{\prod x_{i,c,0}} \max \left(1 - \sum_{i=1}^3 \frac{x_i^2}{x_{i,c,0}^2}, 0 \right) \quad (4.9)$$

characterized by the half-lengths of the trapped condensate $x_{i,c,0}$ where the density goes to zero (the subscript c indicates the condensate, and th the thermal cloud). These are determined by the chemical potential and the trap parameters as $x_{i,c,0} = \sqrt{2\mu/m\omega_i^2}$.

Conveniently, it has been shown that when such a condensate is released from the trap, it evolves simply as a rescaling of its parabolic shape [174–176] (sect. 7.2.9). For release from a cigar-shaped trap with radial frequency ω_r and aspect ratio $\omega_r/\omega_z = \epsilon^{-1}$, the half-lengths of the condensate evolve according to the following equations (to lowest order in ϵ):

$$r_0(t) = r_0(0)\sqrt{1 + \tau^2} \quad (4.10)$$

$$z_0(t) = \epsilon^{-1}r_0(0) \left(1 + \epsilon^2 [\tau \arctan \tau - \ln \sqrt{1 + \tau^2}] \right) \quad (4.11)$$

where $\tau = \omega_r t$.

This solution describes three stages in the time-of-flight expansion: (1) a radial acceleration as interaction energy is converted to kinetic energy ($\tau < 1$), (2) radial expansion with little axial expansion beyond the original axial size ($1 < \tau < \epsilon^{-2}$), and (3) radial and axial expansion at an asymptotic aspect ratio of $z_0(t)/r_0(t) = \pi\epsilon^2/2$ ($\epsilon^{-2} < \tau$). Note that the velocity of radial expansion for $t \gg \omega_r^{-1}$ satisfies $\frac{1}{2}mv_r^2 = \mu$. We typically use magnetic traps of frequencies $\omega_z = 2\pi \times 20$ Hz and $\omega_r = 2\pi \times 250$ Hz. In this case, the mean-field energy is released in about 1–2 ms as the cloud accelerates outward. The axial expansion is only noticeable after about 100 ms, by which time the atoms have fallen about 5 cm. We typically probe the cloud between 20 and 60 ms time-of-flight, and thus observe condensates that have not yet reached their asymptotic aspect ratios.

It is important to note that the validity of both the ideal-gas and Thomas–Fermi limits is generally different for each axis of the harmonic oscillator. For example, in the single-

beam optical traps used at MIT, the cigar-shaped traps are highly asymmetric, with aspect ratios as large as 70 and radial trapping frequencies as high as several kHz. A sodium condensate with a maximum density of $n_c(0) \simeq 1 \times 10^{14} \text{ cm}^{-3}$ has an interaction energy $gn_c(0) = h \times 1.4 \text{ kHz}$. In this case, the Thomas–Fermi approach would be valid along the long axis of the cloud, but not in the radial directions. The proper description of condensates in this intermediate regime requires numerical solutions to the Gross–Pitaevskii equation [177].

4.3 Partly condensed clouds

As we have noted above, the density distribution of a Bose gas in two limits (high and low temperatures) is well understood. Between these two limits, these distributions are the subject of current theoretical and experimental scrutiny [13, 91, 178–180]. Accurate measurements of the density distributions are needed to discriminate between the predictions of different finite-temperature theories.

These density distributions have one striking and useful feature: their bimodality. The assignment of the two components of the bimodal distribution to the condensate and non-condensate densities is an experimental advantage of dilute Bose–Einstein condensates over liquid helium, in which only indirect measurements of the condensate are made.

To glean properties of the mixed cloud from images, the observed density profiles are fit with a bimodal distribution. The choice of distribution is somewhat arbitrary. For our work, we chose a distribution that correctly described the cloud in the two limits described above: a Bose-enhanced Gaussian distribution at the transition temperature, and a parabolic density distribution at zero temperature. Thus, we fit the observed density $n_{tot}(\vec{r})$ to

$$n_{tot}(\vec{r}) = n_{th} g_{3/2} \left(\prod_{i=1}^3 e^{-x_i^2/x_{i,th,0}^2} \right) + n_c \max \left(1 - \sum_{i=1}^3 \frac{x_i^2}{x_{i,c,0}^2}, 0 \right) \quad (4.12)$$

We do not constrain these fitting parameters by the aspect ratios or maximum densities predicted by the ideal-gas or Thomas–Fermi models. Thus, Eq. 4.12 is a rather generic parameterization of a bimodal distribution.

4.4 Column densities

So far we have discussed the predicted density distributions for various regimes. However, with the exception of tomographic imaging using thin sheets of optical pumping light, all imaging techniques measure the column density of the cloud along the imaging axis. Taking this axis to be the y -axis, and labeling the remaining coordinates r and z , we obtain the

column densities for the thermal cloud \tilde{n}_{th} and the condensate \tilde{n}_c as

$$\begin{aligned}\tilde{n}_{th}(r, z) &= \frac{\tilde{n}_{th}(0)}{g_2(1)} g_2 \left[e^{(r^2/r_{th,0}^2 - z^2/z_{th,0}^2)} \right] \\ \tilde{n}_c(r, z) &= \tilde{n}_c(0) \max \left(1 - \frac{r^2}{r_{c,0}^2} - \frac{z^2}{z_{c,0}^2}, 0 \right)^{3/2}\end{aligned}\quad (4.13)$$

These column density distributions are used as fitting functions to the experimental images. This fitting function describes all our observations very well. In comparison, using a Gaussian distribution for the condensate gave inferior results.

4.5 Extracting static quantities

- *Temperature:* The temperature of the gas can be determined from the shape of the spatial wings of the distribution ascribed to the thermal cloud. The density in the wings of the spatial distribution decays generally as $e^{-x_i^2/x_{i,th,0}^2}$, even in the case of Bose enhancement. Using the results from above, we can determine the temperature T of the cloud as

$$k_B T = \frac{1}{2} m \left(\frac{\omega_i^2}{1 + \omega_i^2 t^2} x_{i,th,0}^2 \right) \quad (4.14)$$

where t is the time-of-flight.

To obtain temperature measurements for mixed clouds that are independent of the specific choice of bimodal density distributions, it is necessary to limit the fit to regions of the image in which the condensate is clearly absent. Further, to eliminate possible problems due to the Bose enhancement of the thermal cloud near the boundary of the condensate, it is advisable to further restrict the fit to the spatial wings. From our experience, the systematic errors introduced by fitting too close to the condensate distribution are on the order of 20% of the temperature.

- *Chemical potential and peak density:* The chemical potential μ is given by the size of the condensate. From a fit of the form given in Eq. (4.13) we determine μ from *in situ* measurements as

$$\mu = \frac{1}{2} m \omega_i^2 x_{i,c,0}^2 \quad (4.15)$$

where $x_{i,c,0}$ is the half the length of the condensate in the x_i direction. From condensates released from cigar-shaped clouds, we use the half-length of the cloud in the radial direction as

$$\mu = \frac{1}{2} m \left(\frac{\omega_r^2}{1 + \omega_r^2 t^2} r_{c,0}^2 \right) \quad (4.16)$$

Within the Thomas–Fermi approximation, this value of μ determines the maximum condensate density $n_c(0)$ of the trapped cloud as $n_c(0) = \mu/g$.

- *Total number:* The total number of atoms is determined by summing over the absorption or phase-contrast signal seen across the two-dimensional image of the cloud. Thus, in resonant absorption one obtains

$$N = \frac{A}{\sigma_0} \sum_{pixels} -\ln(t^2(x, y)) \quad (4.17)$$

and in phase-contrast

$$N = \frac{A}{\sigma_0} \frac{2(\Gamma^2 + 4\Delta^2)}{2\Delta\Gamma} \sum_{pixels} \phi(x, y) \quad (4.18)$$

Here, A is the imaged area per pixel, σ_0 is the resonant cross-section for light absorption, Γ is the natural line width, Δ is the detuning from resonance, $t^2(x, y)$ is the transmission observed in absorption images, and $\phi(x, y)$ is the phase measured in phase-contrast images. Note that σ_0 depends on the polarizations of the atomic cloud and the optical probe which must be known to properly quantify the total number of atoms. However the chemical potential and temperature are based on length measurements which are independent of the total signal strength.

- *Condensate number and condensate fraction:* While T , μ , and N can be determined with few assumptions, measuring the condensate fraction or number is less straightforward. Typically, one fits the total density distribution with a bimodal distribution, such as that given in Eq. (4.13), and ascribes the total number from the central distribution to the condensate. Thus, the condensate fraction depends critically on the assumed shape of the bimodal distribution, particularly in the central region where the non-condensed density distribution must be inferred. Determinations of the condensate number are most reliable near the transition temperature, where the thermal cloud is clearly defined and can be extrapolated reliably into the central region. For this reason, one can argue that instead of comparing the inferred condensate fractions with theory, one should rather directly compare the whole density distribution, which can be determined by these same theories. Finally, let us note that the condensate fraction could in principle be measured by exploiting the coherence of the condensate, and not the bimodal distribution. For example, if the original condensate is split in two and then recombined in time-of-flight, the observed fringe contrast determines the condensate fraction (see related discussion in Ref. [181]).
- *Derived quantities:* Other useful quantities can be derived from T , μ , N and the condensate number N_0 using relations among them. To begin with, the Thomas-Fermi expression for the chemical potential of a harmonically confined condensate is

$$\mu^{5/2} = \frac{15\hbar^2 m^{1/2}}{2^{5/2}} N_0 \bar{\omega}^3 a \quad (4.19)$$

where $\bar{\omega} = (\omega_x \omega_y \omega_z)^{1/3}$ is the geometric mean of the trap frequencies. This expression relates four quantities (μ , $N, \bar{\omega}, a$), and by knowing three of them, one can derive the fourth. For example, assuming a value for a , as derived from spectroscopic measurements, we have deduced the average trap frequency of an optical trap from single time-of-flight images of condensates.

Another useful relation is that for the number of atoms N_c at the critical temperature T_c , neglecting the small effect of interactions (consider Eq. (4.2) for $\mu = 0$, see [170]):

$$N_c = g_3(1) \left(\frac{k_B T_c}{\hbar \bar{\omega}} \right)^3 \quad (4.20)$$

From images of clouds at the critical temperature, one can again derive one of three quantities ($N, T, \bar{\omega}$) by knowing the other two. Note that this expression does not contain the scattering length. Thus, the combined use of these two equations is a powerful tool to check for and eliminate systematic errors in number or length measurements.

Other useful quantities are the reduced temperature, and the phase space density. The reduced temperature is the ratio of the observed temperature T to the BEC transition temperature $T_c^{(0)}$ for an ideal gas with the observed total number of atoms, i.e.

$$\frac{T}{T_c^{(0)}} = \frac{k_B T}{\hbar \bar{\omega}} \left(\frac{g_3(1)}{N} \right)^{1/3} \quad (4.21)$$

The maximum phase-space density of a non-condensed gas is given by $\mathcal{D} = n(0) \lambda_{dB}^3$, where $n(0)$ is the maximum density of the cloud, and λ_{dB} the thermal deBroglie wavelength. \mathcal{D} is determined from the relations

$$\mathcal{D} = g_{3/2}(z(0)) \quad (4.22)$$

$$N = g_3(z(0)) \left(\frac{k_B T}{\hbar \bar{\omega}} \right)^3 \quad (4.23)$$

Again, for the purpose of calibration, it is useful to compare clouds above the transition temperature with those at the transition, where $\mathcal{D} = g_{3/2}(1)$. Such calibration allowed for accurate measurements of the increase in phase-space density due to adiabatic deformation of a magnetic trapping potential by a focused infrared beam [14].

4.6 Extracting dynamic properties

Aside from revealing equilibrium thermodynamics, *in situ* and time-of-flight images also reveal the dynamic response of trapped Bose gases to external perturbations. Such responses are probed stroboscopically by taking a time-series of images, each of which measures the

state of the system at a fixed time after application of the perturbation. In this regard, there is an important difference between destructive and non-destructive imaging. Using destructive imaging to probe the gas implies that for each data point in the accumulated time-series the experiment is cycled through the entire loading and cooling cycle. Thus, such a time-series of data is susceptible to shot-to-shot fluctuations. On the other hand, by using non-destructive imaging techniques, a rapid sequence of images can be taken on a single atomic sample, leading to much faster data taking, and eliminating the problem of controlling experimental conditions precisely from shot-to-shot. For example, our observation of bosonic stimulation in the formation of a Bose condensate was only possible using rapid-sequence phase-contrast imaging since the formation process was acutely sensitive to the conditions of the trapped clouds on the verge of condensation [9].

The collective excitations of trapped atomic gases have been a major focus of BEC research. These excitations are analyzed by applying single- or bimodal fits to data from a time-series of probes after the perturbation. Three types of collective excitation have been studied:

- *Center-of-mass oscillations of the entire distribution:* Trap frequencies are measured unambiguously by tracing the center-of-mass motion of the cloud over time. We have used rapid sequences of phase-contrast images to measure frequencies of our magnetic trap to better than 10^{-3} single-shot precision, and to check for anharmonicities.
- *Shape oscillations of the condensate and the thermal cloud:* These excitations correspond to a periodic rescaling of the lengths and aspect ratios of the cloud. The frequency and damping of such modes have been studied both in time-of-flight [4, 156, 166, 167], and *in situ* [12]. High-precision (better than 10^{-2}) measurements were made using rapid-sequence imaging which provided a set of images before the perturbation, to determine the starting conditions, and three sets of images during the oscillation, covering periods as long as 0.5 s [12]. To obtain as many as 28 non-destructive images, a light fluence as low as $10 \text{ photons}/\mu\text{m}^2$ was used.
- *Sound propagation in a Bose-Einstein condensate:* One-dimensional sound propagation along the long axis of the cloud was analyzed using rapid-sequence phase-contrast imaging [7]. The location of the sound pulse was determined by subtracting out the shape of an unperturbed condensate, and determining the maximum or minimum of the resulting density difference. The axial length of the condensate was used to determine the condensate density using Eq. (4.16).

4.7 Comparison of time-of-flight and *in situ* images

As discussed above, detailed information about trapped Bose gases can be obtained from both *in situ* and time-of-flight images. Let us now compare the two methods, and find

	In-situ		Time-of-flight	
	r	z	r	z
Thermal cloud	$\sqrt{\frac{2k_B T}{m}} \frac{1}{\omega_r}$	$\sqrt{\frac{2k_B T}{m}} \frac{1}{\omega_z}$	$\sqrt{\frac{2k_B T}{m}} t$	$\sqrt{\frac{2k_B T}{m}} t$
Ideal-gas condensate	$\sqrt{\frac{\hbar}{m}} \frac{1}{\sqrt{\omega_r}}$	$\sqrt{\frac{\hbar}{m}} \frac{1}{\sqrt{\omega_z}}$	$\sqrt{\frac{\hbar}{m}} \sqrt{\omega_r} t$	$\sqrt{\frac{\hbar}{m}} \sqrt{\omega_z} t$
Thomas-Fermi condensate	$\sqrt{\frac{2\mu}{m}} \frac{1}{\omega_r}$	$\sqrt{\frac{2\mu}{m}} \frac{1}{\omega_z}$	$\sqrt{\frac{2\mu}{m}} t$	$\sqrt{\frac{2\mu}{m}} \frac{\pi \omega_z}{2\omega_r} t$

Table 4.1: Comparison of length scales for thermal clouds and condensates. For the thermal cloud and ideal-gas condensates we give the rms radius, and for the Thomas-Fermi condensates the half-lengths. Time-of-flight is long enough to ignore finite-size effects. Results for a Thomas-Fermi condensate in time-of-flight assume $\omega_z/\omega_r \rightarrow 0$.

when each is best applied.

The onset of BEC is most striking for anisotropic traps in time-of-flight images. The appearance of the condensate suddenly “breaks the symmetry” of the isotropic expansion above the transition temperature. The expansion of a cigar-shaped condensate into a disk-shaped object is easy to observe even with a misaligned imaging system. In contrast, in the Thomas-Fermi limit, the aspect ratios of the condensate and the thermal cloud are the same for *in situ* imaging, and observing the onset of BEC requires high-resolution imaging

The interpretation of time-of-flight images to determine temperature and chemical potential assumes a sudden, ballistic, and free expansion. A variety of effects may invalidate this assumption. These include residual magnetic fields, such as a slow shut-off of the trap (compared to the trap oscillation periods), or stray curvature fields during the free-expansion. Another impediment is that thermal clouds released from anisotropic traps can expand anisotropically due to collisions soon after the trap is switched off [182, 183].

The limitations to temperature measurements on non-spherical partly-condensed clouds are different for *in situ* and time-of-flight techniques. Table 4.1 compares the sizes of the thermal cloud and the condensate from cigar-shaped traps, both in the trap and in time-of-flight. Focusing our attention on the Thomas-Fermi case, one finds that in the trap, the two components have equal sizes at $k_B T = \mu$. Thus, *in situ* temperature measurements based on the density distribution are limited to $k_B T \geq \mu$ [12]. On the other hand, in time-of-flight, the condensate and the thermal cloud can be distinguished along the z -axis down to $k_B T = \mu \times 4\pi^{-2}\epsilon^2$ where $\epsilon = \omega_z/\omega_r$, stretching the limits of temperature measurements to much lower values.

Another aspect to consider in choosing between time-of-flight and *in situ* imaging for anisotropic clouds is the different column densities of the condensate and the thermal cloud. Recall that in time-of-flight from a cigar-shaped potential, the thermal cloud expands isotropically once $t > \omega_z^{-1}$ while the condensate expands axially beyond its initial length

only when $t > \omega_r/\omega_z^2$. For times $1 < \omega_z t < \omega_r/\omega_z$, if the imaging is done along a radial direction, the condensate optical density drops linearly with expansion time, while the non-condensate optical density drops quadratically. Thus, *in situ* imaging is preferable for imaging the entire cloud faithfully, while long time-of-flight expansions allow for more reliable measurements of the condensate number.

There are also differences in measuring dynamic properties. One goal of such measurements is the study of oscillations at the limit of zero amplitude. It has been shown that the relative amplitude of shape oscillations observed in time-of-flight was much greater than what would be observed *in situ* [174, 176]. Thus, time-of-flight imaging allows for the observation of smaller amplitude oscillations. On the other hand, this benefit of time-of-flight techniques may be offset by slower data taking and greater susceptibility to technical noise. Furthermore, for more complicated oscillations it is difficult to interpret time-of-flight images. For example, while sound pulses were easily observed and located *in situ*, time-of-flight images of such condensates revealed a complicated pattern of striations (Fig. 7-12).

Chapter 5

Basic condensate physics

This chapter discusses equilibrium properties of Bose gases above and below the Bose–Einstein condensation transition temperature, and includes experimental results which are not found in other publications. The last section discusses a model which is described in the following publication:

- *M. Naraschewski and D.M. Stamper-Kurn, “Analytical description of a trapped semi-ideal Bose gas at finite temperature,” Phys. Rev. A **58**, 2423 (1998). Included in Appendix F.*

Having reviewed in the previous sections some of the tools and methods used to produce and study Bose–Einstein condensates, let us now turn to the experimental studies themselves. I begin with a summary of some basic properties of Bose–Einstein condensation as manifested in these experiments, i.e. the condensation of a trapped weakly-interacting dilute Bose gas. A more thorough discussion can be found in Refs. [173, 184]. I also discuss a number of results obtained during my research at MIT regarding equilibrium properties of a Bose–Einstein condensate. Our first measurements of the Bose–Einstein condensation transition temperature, condensate fraction, and the relation between the condensate number and the mean-field interaction energy for condensates formed in a harmonic potential were reported in Ref. [2]. A similar analysis was made using *in situ* images of trapped condensates for the characterization of the initial conditions for a study of condensate oscillations at variable temperature in Ref. [12]. I also present several results which arose from this analysis, some of which are discussed in review articles [22, 168] and some of which are unpublished.

5.1 Introduction to a sodium Bose–Einstein condensate

Before entering a theoretical discussion of the equilibrium properties of trapped Bose–Einstein condensates, let me set the stage by presenting the typical Bose–Einstein condens-

sates produced in our laboratory. Fig. 5-1 shows a number of *in situ* phase-contrast images of trapped clouds of sodium at different temperatures above and below the Bose-Einstein condensation temperature. Axial profiles through a number of these images are shown in Fig. 5-2. The images were taken with probe light propagating along the radial direction of the Ioffe-Pritchard magnetic trap produced by the cloverleaf magnet coils. The trapping potential is cigar-shaped, with trapping frequencies of $\omega_r \simeq 2\pi \times 230$ Hz and $\omega_z \simeq 2\pi \times 17$ Hz in the radial and axial directions, respectively. The clouds are thus anisotropic with an aspect ratio inversely proportional to the ratio of frequencies. The anisotropy of these cigar-shaped clouds turned out to be quite useful for a number of experiments since the axial density distribution was easy to image and analyze.

The temperature of the trapped clouds was controlled by varying the final rf used in the rf-evaporation cycle. This also had the effect of varying the total number of trapped atoms since rf-evaporation cools by ejecting atoms from the trap; thus, lowering the final rf produced a colder cloud with fewer atoms. As discussed in the previous section, the extent of the non-condensed cloud is a measure of the temperature of the gas. Thus, for high values of the final rf, the temperature is high and the non-condensed cloud reaches far from the center of the harmonic trapping potential. As the rf is lowered, the thermal wings of the distribution become shorter as the temperature is lowered.

The onset of Bose-Einstein condensation in these images is immediately obvious. At the higher temperatures, above the Bose-Einstein condensation transition temperature, the density profile of the non-condensed cloud is smooth. As the temperature drops below the BEC phase transition, a high-density core of atoms appears in the center of the cloud and the density distribution becomes bimodal. This core of atoms is the Bose-Einstein condensate. Lowering the rf further, the fraction of atoms in the Bose-Einstein condensate grows until, finally, the temperature drops to the point where only the central peak remains. The Bose-Einstein condensation phase transition has also been characterized in time-of-flight images in the first observations of Bose-Einstein condensation by the JILA group [128] and by our group at MIT [1, 2].

Such phase-contrast images of trapped clouds at thermal equilibrium were analyzed as part of our study of collective excitations at non-zero temperature. The total number of trapped atoms N , their temperature T , the apparent condensate number N_0 and the condensate chemical potential μ were determined (Fig. 5-3). These data are typical of the Bose-Einstein condensates produced in the cloverleaf magnetic trap. The transition temperature of $1 - 2 \mu\text{K}$ is reached with 50 – 100 million atoms. Further evaporation produces “pure” condensates of 5 – 20 million atoms. These condensates are about $300 \mu\text{m}$ in length, have an aspect ratio of about 15, and a peak density of about $4 \times 10^{14} \text{ cm}^{-3}$. These “typical” conditions can be and have been greatly modified in our various projects; condensates densities have ranged from 2×10^{13} to $3 \times 10^{15} \text{ cm}^{-3}$, and transition temperatures from 100 nK to 5 μK . This wide range of conditions should enable the study of a variety of

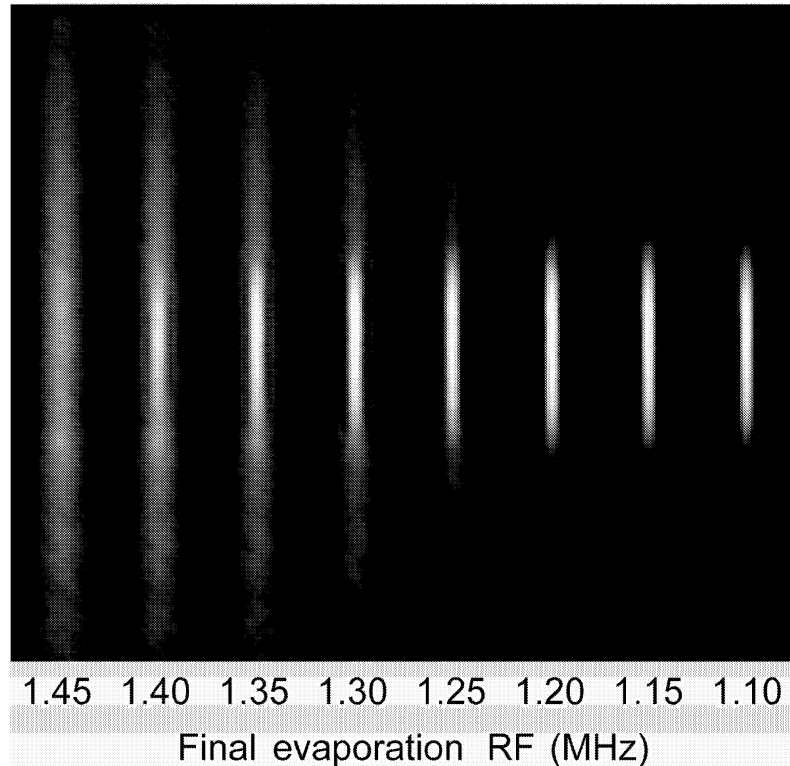


Figure 5-1: Phase-contrast images of trapped Bose gases across the BEC phase transition. As the final rf used in evaporation cooling is lowered, the temperature is reduced (left to right). Images show the onset of Bose condensation, the growth of the condensate fraction and contraction of the thermal wings, and finally a pure condensate with no discernible thermal fraction. The axial and radial frequencies are about 17 and 230 Hz, respectively. The pure condensate has a length of about $300 \mu\text{m}$.

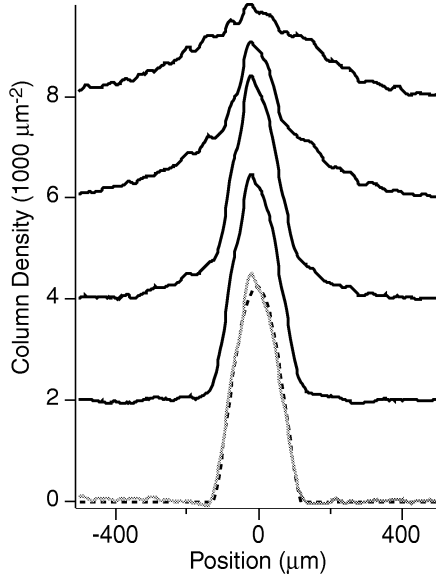


Figure 5-2: Axial column density profiles of trapped Bose gases across the Bose–Einstein condensation phase transition from phase-contrast images. The bottom curve shows a parabolic fit to the data (dashed), according to Eq. (4.13).

effects associated with the cross-over from an ideal to an interacting gas.

5.2 The Bose–Einstein distribution

As discussed in the introduction, the equilibrium properties of a system are determined by the assumption that the system is equally likely to be found in any of its accessible states. We consider a system \mathcal{A} which has free-particle energy levels $|i\rangle$ with energy E_i . The equilibrium properties of this system are determined once we specify the number of particles N and total energy E_{tot} of the system. These equilibrium properties are found by considering that system \mathcal{A} is equally likely to be found in any state consistent with the specified N and E_{tot} (the micro-canonical ensemble).

However, it is sometimes more convenient to proceed indirectly, and instead consider that system \mathcal{A} can exchange particles and energy with a larger reservoir \mathcal{R} . After applying the micro-canonical ensemble to the system $\mathcal{A} + \mathcal{R}$, one finds that the equilibrium in \mathcal{A} can now be determined by considering *all* possible states of \mathcal{A} , of any particle number \mathcal{N} and energy \mathcal{E}_{tot} , to occur with a likelihood proportional to the Boltzmann factor $e^{(\mu\mathcal{N}-\mathcal{E}_{\text{tot}})/k_B T}$. This is the grand-canonical ensemble.

In the case of indistinguishable bosons, a many-particle state in \mathcal{A} is fully specified by a set of occupation numbers $\{n_i\}$ which give the number of particles in each state $|i\rangle$. The statistical description of system \mathcal{A} begins with enumerating the possible states of the system

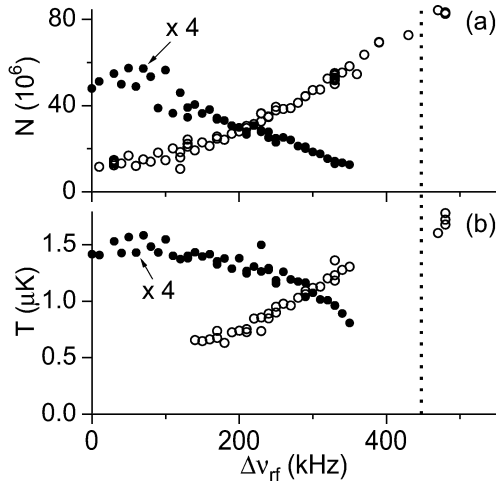


Figure 5-3: Typical equilibrium properties of trapped Bose gases produced in the cloverleaf trap above and below the Bose–Einstein condensation phase transition. The total number N (a, open circles) was determined by summing over the observed column densities. The approximate condensate number N_0 (a, closed circles, $\times 4$), temperature T (b, open circles) and chemical potential μ/k_B (b, closed circles, $\times 4$) were determined from fits. $\Delta\nu_{\text{rf}}$ is the trap depth determined by the final rf frequency in the evaporative cooling cycle. The dashed line indicates the observed transition temperature. Note that the number measurements (N , N_0) suffer from systematic errors of as much as 20% due to the calibration of our phase-contrast signal. Figure taken from Ref. [14].

(all different $\{n_i\}$) in the partition function \mathcal{Z} :

$$\mathcal{Z} = \sum_{\{n_i\}} \prod_i e^{-(E_i - \mu)n_i/k_B T} \quad (5.1)$$

$$= \prod_i \left(1 - e^{-(E_i - \mu)/k_B T}\right)^{-1} \quad (5.2)$$

The average occupation $\langle n_i \rangle$ of state $|i\rangle$ is then

$$\langle n_i \rangle = k_B T \frac{\partial}{\partial E_i} \ln \mathcal{Z} = \frac{1}{e^{(E_i - \mu)/k_B T} - 1} \quad (5.3)$$

This is the Bose–Einstein distribution function which specifies how bosons are most likely distributed among the energy levels of a system. The distribution has two “knobs” (formally derived from properties of the fictional reservoir \mathcal{R}) which change the distribution: the chemical potential μ and the temperature T . These “knobs” are turned to yield the correct total particle number $N = \sum_i \langle n_i \rangle$ and total energy $E_{\text{tot}} = \sum_i E_i \langle n_i \rangle$ which are now determined as statistical averages.

The chemical potential μ is bounded from above by the single-particle ground-state energy E_0 . As μ approaches its upper bound, the occupation in the ground state diverges $N_0 = (e^{(E_0 - \mu)/k_B T} - 1)^{-1} \rightarrow \infty$. Let us express the total number of particles in the system as the sum $N = N_0 + N_{\text{ex}}$ where $N_{\text{ex}} = \sum_{i \neq 0} \langle n_i \rangle$ is the sum of all particles in the excited states. For certain systems, in the limit $\mu \rightarrow E_0$, the number of particles in excited states tends to a finite value $N_{\text{ex}} \rightarrow N_{\text{ex}}^{\max}(T)$. If we prepare such a system at a temperature T and $N > N_{\text{ex}}^{\max}(T)$, the excess particles $N - N_{\text{ex}}^{\max}(T)$, potentially macroscopic in number, will accumulate in the ground state. This is the condition for Bose–Einstein condensation.

5.3 Bose–Einstein condensation of a trapped ideal gas

Let us apply these considerations to a Bose gas trapped in a harmonic potential

$$U(\vec{r}) = \frac{1}{2}m (\omega_x^2 x^2 + \omega_y^2 y^2 + \omega_z^2 z^2) \quad (5.4)$$

Here m is the mass of the gas particles and ω_i is the angular trap frequency in the \hat{i} direction. The harmonic potential is particularly amenable to a fully quantum statistical treatment since the free-particle energy eigenstates can be expressed analytically and the energy levels are simply quantized as

$$E = \hbar [(n_x + 1/2)\omega_x + (n_y + 1/2)\omega_y + (n_z + 1/2)\omega_z] \quad (5.5)$$

Bose–Einstein condensation in harmonic potentials can be treated using the discrete energy spectrum [25, for example], or by replacing the summation over energy levels with a contin-

uous integral [185]. These two approaches give slightly different results for small numbers of particles, accounting for certain “finite–size effects” which are predicted to influence the Bose–Einstein condensation phase transition in small samples (reviewed in Ref. [173]).

Alternatively, when the energy level spacings $\hbar\omega_i$ are much smaller than the thermal energy $k_B T$, one can treat the system semi-classically using integrals over phase space [90, 91, 170]. One replaces the discrete single-particle energy spectrum with a density of states $\mathcal{D}(E)$ and writes the partition function as

$$\ln \mathcal{Z} = -\ln(1 - e^{-(E_0 - \mu)/k_B T}) - \int dE \mathcal{D}(E) \ln(1 - e^{-(E - \mu)/k_B T}). \quad (5.6)$$

Here we have singled out the discrete ground state, with energy E_0 , from the rest of the states. The density of states is then obtained by equating $\mathcal{D}(E) dE$ with the number of phase-space cells of volume h^3 between the energies E and $E + dE$, where the energy is given by $E(\vec{r}, \vec{p}) = p^2/2m + U(\vec{r})$. Straightforward integration yields

$$\mathcal{D}(E) = \frac{4\sqrt{2}\pi m^{3/2}}{h^3} \int_{E > U(\vec{r})} d^3\vec{r} \sqrt{E - U(\vec{r})} \quad (5.7)$$

The number of atoms in excited states is given by

$$N = \frac{4\sqrt{2}\pi m^{3/2}}{h^3} \int d^3\vec{r} \int_{U(\vec{r})}^{\infty} dE \sqrt{E - U(\vec{r})} \frac{1}{e^{(E - \mu)/k_B T} - 1} \quad (5.8)$$

$$= \frac{4\sqrt{2}\pi m^{3/2}}{h^3} \int d^3\vec{r} \times (k_B T)^{3/2} \sum_{j=1}^{\infty} e^{j(\mu - U(\vec{r}))/k_B T} \int_0^{\infty} d\epsilon \epsilon^{1/2} e^{-\epsilon j} \quad (5.9)$$

$$= \left(\frac{2\pi m k_B T}{h^2} \right)^{3/2} \int d^3\vec{r} \sum_{j=1}^{\infty} \frac{e^{j(\mu - U(\vec{r}))/k_B T}}{j^{3/2}} \quad (5.10)$$

$$= \int d^3\vec{r} n(\vec{r}) \quad (5.11)$$

where in the final line we identify the particle density $n(\vec{r}) = g_{3/2}[z(\vec{r})]/\lambda_{dB}^3$ where $z(\vec{r}) = e^{(\mu - U(\vec{r}))/k_B T}$ is the local fugacity, λ_{dB} is the thermal deBroglie wavelength, and we define generally $g_i(x) \equiv \sum_{j=1}^{\infty} x^j/j^i$. The maximum phase-space density of the gas is given by $g_{3/2}[z(0)]$.

5.4 Density and momentum distributions of a non-condensed Bose gas

Already before the onset of Bose–Einstein condensation, the density distribution of a Bose gas ($n_{\text{Bose}} = g_{3/2}[z(\vec{r})]/\lambda_{dB}^3$) differs from that of a classical gas of distinguishable particles ($n_{\text{Clas}} = z(\vec{r})/\lambda_{dB}^3$). This effect was observed by our group in the analysis of *in situ* phase–

contrast images of harmonically trapped clouds just above the Bose–Einstein condensation phase transition. The phase–contrast images measured the integrated column density $\tilde{n}(r, z)$ along one of the radial directions which should be proportional to

$$\tilde{n}_{\text{Bose}}(x, z) \propto g_2 \left(z(0) e^{-\frac{1}{2}m[\omega_r^2 x^2 + \omega_z^2 z^2]/k_B T} \right) \quad (5.12)$$

for a Bose gas, and proportional to

$$\tilde{n}_{\text{Clas}}(x, z) \propto z(0) e^{-\frac{1}{2}m[\omega_r^2 x^2 + \omega_z^2 z^2]/k_B T} \quad (5.13)$$

for a classical gas (Sec. 4.4). Away from the center of the distribution where $U(\vec{r}) \gg k_B T$ the distributions are identical.

Axial profiles of the observed column density distributions ($\tilde{n}(0, z)$) were fit to either $\tilde{n}_{\text{Bose}}(0, z)$ or $\tilde{n}_{\text{Clas}}(0, z)$ (Fig. 5-4). Data in the center of the cloud were excluded from the fit, allowing us to determine the temperature T and the proportionality factor independent of the choice of fitting functions. As shown in Fig. 5-4, the interpolation of the Bose–enhanced column density distribution to the central portion of the cloud describes the observed profile better than the classical Gaussian density distribution.

The effects of quantum statistics on a non–condensed cloud were also observed in the momentum distribution of the gas. For this, column density distributions obtained in time–of–flight absorption images were examined (Fig. 5-5). As discussed in Sec. 4.1, these images show the momentum distribution of a trapped atomic sample provided that the time–of–flight is sufficiently long and that collisions during the free expansion can be neglected. The momentum distribution predicted by a quantum– or classical–statistical treatment have the same form as the density distributions described above, with the substitution $U(\vec{r}) \rightarrow p^2/2m$. As above, data away from the center of the cloud were fitted with either the quantum–statistical or classical distributions. At or below the Bose–Einstein condensation transition temperature, the momentum distribution was shown to be Bose enhanced at low momenta (Fig. 5-5a). Above the Bose–Einstein condensation transition temperature ($z(0) \ll 1$), the quantum– and classical–statistical descriptions are equivalent. Thus, a cloud which was significantly hotter than the Bose–Einstein condensation transition temperature was well described by a classical Maxwell–Boltzmann distribution (Fig. 5-5b).

5.5 Critical temperature and condensate fraction

The semi–classical expression for the density distribution in a harmonic oscillator potential can be integrated to give the total number of atoms in excited states:

$$N_{\text{ex}} = g_3[z(0)] \left(\frac{k_B T}{\hbar \bar{\omega}} \right)^3 \quad (5.14)$$

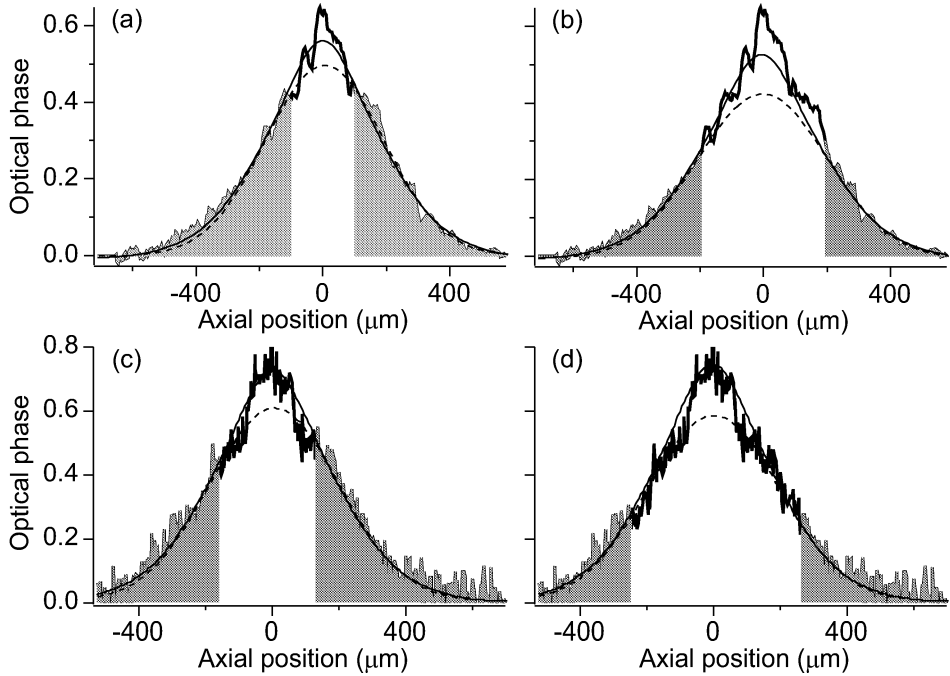


Figure 5-4: Observation of Bose–enhanced density distributions above the Bose–Einstein condensation phase transition. Axial profiles (thick solid line) were taken of phase–contrast images of a trapped sodium gas near, but above, the Bose–Einstein condensation transition temperature. Data away from the center of the cloud (shaded region) were fit to both a classical distribution (dashed line) and a quantum–statistical distribution for a saturated ($z(0) = 1$) non–condensed gas (thin solid line). The data are better described by the Bose–enhanced distribution. Figures (a,b) show the same data with fits to different ranges of data, demonstrating that the density distribution is fully determined by the wings of the distribution. Figures (c,d) show a similar comparison for a different data set. The trap frequencies were $\omega_r = 2\pi \times 230(20)$ Hz radially and $\omega_z = 2\pi \times 17(1)$ Hz axially. Temperatures T and number of trapped atoms N are $T = 1.4 \mu\text{K}$ and $N \simeq 50 \times 10^6$ for (a,b), and $T = 1.7 \mu\text{K}$ and $N \simeq 70 \times 10^6$ for (c,d).

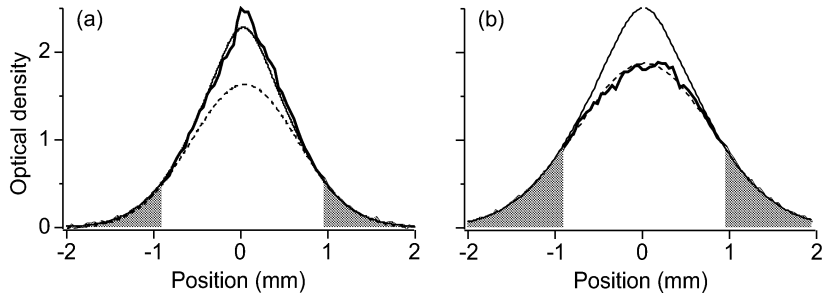


Figure 5-5: Observation of Bose–enhanced momentum distributions of a non–condensed gas. Axial profiles (thick solid line) were taken of time–of–flight absorption images of a gas slightly below, as indicated by the small condensate peak (a), and well above (b) the Bose–Einstein condensation transition temperature T_c^0 . Data away from the center of the cloud (shaded region) were fit to both a classical distribution (or $z(0) \ll 1$) (dashed line) and a quantum–statistical distribution for a saturated ($z(0) = 1$), non–condensed gas (thin solid line). At or below T_c^0 , the momentum distribution of the non–condensed cloud is Bose–enhanced at low momenta. Well above T_c^0 , the momentum distribution is well described by a classical Maxwell–Boltzmann distribution, as predicted for a Bose gas with $z(0) \ll 1$. The momentum distribution is shown as a profile across absorption images taken after 40 ms of ballistic expansion.

where $\bar{\omega} = (\omega_x \omega_y \omega_z)^{1/3}$ is the geometric mean trapping frequency. This number reaches a finite value at $\mu = E_0 = 0$, where we ignore the zero–point energy of the ground state. This gives the critical number of atoms N_c at which the trapped gas begins to Bose condense (Eq. 4.20), or equivalently the ideal–gas transition temperature T_c^0

$$k_B T_c^0 = \hbar \bar{\omega} \left(\frac{N}{g_3(1)} \right)^{1/3} \quad (5.15)$$

where $g_3(1) \simeq 1.202$. At temperatures below the critical temperature, the fraction of atoms in the ground state (the condensate fraction) is found to be [170]

$$\frac{N_0}{N} = 1 - \left(\frac{T}{T_c^0} \right)^3. \quad (5.16)$$

These predictions for the Bose–Einstein condensation transition temperature and the condensate fraction have been explored in a number of studies. In the first observations of Bose–Einstein condensation at JILA [128] and MIT [1, 2], the transition temperature and condensate fraction were in rough agreement with predictions. In a later experiment at JILA [186], the transition temperature and the condensate fraction were examined more closely and showed agreement with predictions for the ideal–gas within the experimental errors (a few percent). This experiment also sought evidence for finite–size and interaction effects (discussed further below) which were unfortunately predicted to be smaller than the experimental errors for the small atomic samples which were probed.

5.6 Effects of interactions

The nature of Bose–Einstein condensation is modified due to interactions between the gaseous particles. This is readily apparent from the images of Fig. 5-1. The Bose–Einstein condensate in our magnetic trap typically grows to 300 μm in length (Thomas–Fermi diameter). In contrast, the ideal–gas single particle ground state has an extent of just $2\sqrt{2\hbar/m\omega_z} \simeq 14 \mu\text{m}$ ($1/e^2$ diameter). The condensate swells to a much greater size due to self–repulsion.

The many–body Hamiltonian describing a system of trapped, interacting bosons has the general form

$$\begin{aligned}\hat{\mathcal{H}} = & \int d^3\vec{r} \hat{\Psi}^\dagger(\vec{r}) \left(-\frac{\hbar^2 \nabla^2}{2m} + U(\vec{r}) \right) \hat{\Psi}(\vec{r}) \\ & + \frac{1}{2} \int d^3\vec{r}_1 d^3\vec{r}_2 \hat{\Psi}^\dagger(\vec{r}_1) \hat{\Psi}^\dagger(\vec{r}_2) V(\vec{r}_1 - \vec{r}_2) \hat{\Psi}(\vec{r}_2) \hat{\Psi}(\vec{r}_1)\end{aligned}\quad (5.17)$$

Here $\hat{\Psi}(\vec{r})$ ($\hat{\Psi}^\dagger(\vec{r})$) are boson destruction (creation) field operators which obey the Bose commutation rule $[\hat{\Psi}(\vec{r}_1), \hat{\Psi}^\dagger(\vec{r}_2)] = \delta(\vec{r}_1 - \vec{r}_2)$ which ensures the symmetry of the many–body wavefunction, and $V(\vec{r})$ is the two–body interatomic potential. Accounting for the exact form of the interaction potential and keeping track of the complicated many–body correlations induced by high–order collision processes is quite difficult. Thus, one generally applies two simplifying assumptions.

First, at sufficiently low energies, the character of two–body collisions is described completely by a single parameter, the s –wave scattering length a . Furthermore, in a dilute gas, we can consider only binary collisions. This allows us to approximate the interaction potential with a pseudo–potential which has the same low–energy scattering properties. To lowest order we therefore identify $V(\vec{r}) = g\delta(\vec{r})$ where the coupling constant $g = 4\pi\hbar^2 a/m$.

Second, following Bogoliubov [28], one assumes that the nature of ideal–gas Bose–Einstein condensation carries over to the interacting system in that there is still a macroscopic population in one single–particle state*. Thus, the Bose field operator is expressed as the sum $\hat{\Psi}(\vec{r}) = \psi(\vec{r}) + \hat{\Psi}'(\vec{r})$ where $\psi(\vec{r}) = \langle \hat{\Psi}(\vec{r}) \rangle$ is the non–zero thermal average of the field operator resulting from broken symmetry [37] and $\hat{\Psi}'(\vec{r})$ describes the remaining fluctuations from this average and many–particle correlations. Equivalently, one can treat the many–body Hamiltonian (Eq. 5.17) variationally using an N –body Hartree trial wavefunction $\psi(\vec{r}_1, \vec{r}_2, \dots, \vec{r}_N) = \prod_i \psi(\vec{r}_i)$.

Using these two approximations, one obtains to zeroth–order in $\hat{\Psi}'$ the equation

$$i\hbar \frac{\partial}{\partial t} \psi(\vec{r}) = \left(-\frac{\hbar^2 \nabla^2}{2m} + U(\vec{r}) + g|\psi(\vec{r})|^2 \right) \psi(\vec{r}) \quad (5.18)$$

This is the time–dependent Gross–Pitaevskii equation [187, 188] originally used to describe

*The general validity of this age–old assumption is still not established. See discussion in Ref. [74]

excitations of vortices in superfluid helium. It represents a simplified mean–field description of the interparticle interactions which “covers up” all of the kinetic energy and many–body correlations induced by the binary interactions with an effective interaction energy $g|\psi(\vec{r})|^2$ which is simply proportional to the density of the gas. The mean–field approximation is accurate to the extent that the s –wave scattering length is much smaller than the separation between atoms, i.e. that the gas parameter $na^3 \ll 1$. This condition is satisfied in current experimental conditions. For example, our sodium Bose condensates have densities on the order of 10^{14} cm^{-3} . Taking the scattering length $a = 2.75 \text{ nm}$ determined by photoassociation spectroscopy [189] gives $na^3 \simeq 2 \times 10^{-6} \ll 1$. Thus, one expects a mean–field approach to describe these gaseous Bose–Einstein condensates quite accurately [173].

Let us assess how important these interactions are for determining properties of the thermal cloud and of the condensate. The importance of interactions for describing a thermal cloud at a temperature T and density n_{th} above the Bose–Einstein condensation transition is determined by comparing the interaction energy gn_{th} to the thermal energy $k_B T$. The conditions $n\lambda_{dB} \leq 2.6$ and $na^3 \ll 1$ imply that (neglecting some constants)

$$gn_{th} \lesssim \left(\frac{\hbar^2}{m\lambda_{dB}^2} \right) (na^3)^{1/3} \ll k_B T \quad (5.19)$$

Thus, the thermal cloud above the critical temperature is well–described as an ideal gas.

On the other hand, to determine the importance of interactions to the behaviour of Bose–Einstein condensates, one must compare the interaction energy gn_c to the zero–point kinetic energy of the condensate rather than the thermal energy. In our experiments, condensates were typically produced with mean–field energies $gn_c \sim k_B \times 300 \text{ nK}$ (where $n_c \sim 4 \times 10^{14} \text{ cm}^{-3}$ is a typical condensate density) which were much larger than the harmonic–oscillator energy spacings $\hbar\omega_i$ (and larger yet than the zero–point kinetic energy). Thus, the behaviour of condensates is dominated by interaction effects.

The ground–state, zero–temperature condensate wavefunction is determined by setting $\psi(\vec{r}, t) = \psi(\vec{r})e^{-i\mu t/\hbar}$ and solving the time–independent Gross–Pitaevskii equation

$$\left(-\frac{\hbar^2 \nabla^2}{2m} + U(\vec{r}) + g|\psi(\vec{r})|^2 - \mu \right) \psi(\vec{r}) = 0 \quad (5.20)$$

In considering condensates for which the mean–field energy dominates over the kinetic energy, one can neglect the kinetic energy term in Eq. 5.20, and obtain the Thomas–Fermi approximation for the condensate density

$$n_c(\vec{r}) = \max \left(\frac{\mu - U(\vec{r})}{g}, 0 \right) \quad (5.21)$$

The chemical potential μ is then given by $gn_c(0)$ were $n_c(0)$ is the maximum density of the condensate.

The mean-field description of interacting Bose–Einstein condensates has been confirmed by a number of studies. Interaction energies of condensates in the Thomas–Fermi limit were measured by our group in Ref. [2]. By integrating Eq. 5.21 it can be shown that the interaction energy μ of large condensates scales with the condensate number N_0 as $\mu \propto N_0^{2/5}$ (Eq. 4.19). This was experimentally confirmed by time-of-flight measurements. The expansion of a condensate in a regime intermediate to the ideal-gas and Thomas–Fermi limits was studied at JILA and also found to be well described by a mean-field approach [190].

The condensate density profile was also probed by *in situ* imaging. In a harmonic potential, the Thomas–Fermi description gives a condensate density which is parabolic with a maximum density at the center and which goes to zero at radii $x_{i,c,0} = \sqrt{2\mu/m\omega_i^2}$ along the \hat{i} -direction ($i = x, y, z$). This is confirmed by in-situ images taken of condensates near zero-temperature where no thermal cloud was visible. For example, the bottom curve of Fig. 5-2, which gives the density profile of a pure condensate, is well fit by a function of the form given in Eq. (4.13). Lene Hau and collaborators probed the boundary of a condensate in-situ with near-resonant absorption imaging [152] and found excellent agreement with the solution of the Gross–Pitaevskii equation for the known condensate number, trap frequencies, and scattering length.

5.7 Non-zero temperature

Interactions also modify the thermodynamic properties of Bose condensed gases in a number of ways. One effect is to shift the transition temperature due to two effects. In an inhomogeneous potential, the transition temperature is lowered because the density at the center of the trap is lowered by interparticle repulsion [191]. More subtle is an upward shift in the transition temperature due to many-body effects which actually lower the critical phase-space density for Bose–Einstein condensation [192–194]. These effects have not yet been tested experimentally.

Interactions also affect the condensate/non-condensate mixtures obtained below the critical temperatures. The behavior of a partly condensed gas is treated by mean-field theories for a non-zero temperature gas, in which the many-body Hamiltonian (Eq. 5.17) is treated to higher order in $\hat{\Psi}'(\vec{r})$. This results in a set of coupled equations which describe the Bose–Einstein condensate, the non-condensed gas which is comprised of thermally populated excitations, and correlations between particles (see discussions in [173, 184, 195, 196]). A commonly used approximation to these equations is the Popov approximation [197] which neglects correlations between particles (the so called “anomalous density”) and their effect on binary interactions [196]. The Popov approximation has failed to correctly describe low-energy collective excitations (see Chapter 7). However, its predictions for equilibrium properties which involve higher-energy thermal excitations have compared well with more

rigorous (but difficult) calculations [179, 191, 198, 199].

In order to gain further insight into the behavior of Bose–Einstein condensates at non-zero temperature, further simplifications to the Popov approximation have been proposed. A semi-classical approximation to the Popov prescription has been explored in which the condensate density $n_c(\vec{r})$ and the non-condensate density $n_{th}(\vec{r})$ are given by the self-consistent solution to the two coupled equations [90, 179]

$$n_c(\vec{r}) = \max \left(\frac{\mu - U(\vec{r}) - 2gn_{th}(\vec{r})}{g}, 0 \right) \quad (5.22)$$

$$n_{th}(\vec{r}) = \frac{g_{3/2}(e^{-(U(\vec{r})+2g[n_c(\vec{r})+n_{th}(\vec{r})]-\mu)/k_B T})}{\lambda_{dB}^3} \quad (5.23)$$

Finally, since typically $n_{th} \ll n_c$ and $gn_{th} \ll k_B T$, these equations can be further simplified by neglecting the self-repulsion of the non-condensate and the repulsion of the condensate by the non-condensed cloud. One thereby obtains a “semi-ideal” model of a non-zero temperature Bose gas, in which the condensate density is that of a zero temperature condensate with the appropriate number of atoms, while the non-condensate is described as an ideal gas of bosons confined in the combination of the external potential $U(\vec{r})$ and the repulsive mean-field potential due to the condensate $2gn_c(\vec{r})$. This model was developed by Martin Naraschewski and myself [13] (Appendix F) and by Minguzzi *et al.* [200] to obtain analytic expressions for the condensate fraction and the density distribution. These expressions were shown to agree rather well with the results of more complicated approaches, except near the critical temperature where the condensate density becomes small. Furthermore, the “semi-ideal” model offers a simple picture for the influence of interactions on the condensate fraction. As atoms accumulate in the Bose–Einstein condensate, the ground state energy rises due to interactions. This implies a rise in the chemical potential, and therefore an increase in the number of particles in the non-condensed cloud which lowers the condensate fraction from its ideal-gas value.

The magnitude of this reduction is characterized by the parameter $\eta = \mu_0/k_B T_c^0$ where μ_0 is the interaction energy if all trapped particles form a Bose condensate [178]. Since η is small for all current experiments with harmonic traps, the effects of interactions in such traps are small and difficult to detect if T_c^0 is not well calibrated by measurements of the particle number and temperature. Furthermore, since η scales only weakly with the particle number $\eta \propto N^{1/15}$ and trap frequency $\eta \propto \omega^{1/5}$, it appears difficult to accentuate the effects of interactions in harmonically trapped clouds.

Chapter 6

Irreversible and reversible formation of a Bose–Einstein condensate

This chapter focuses on the experiments reported in two publications:

- *H.-J. Miesner, D.M. Stamper-Kurn, M.R. Andrews, D.S. Durfee, S. Inouye, and W. Ketterle, “Bosonic stimulation in the formation of a Bose-Einstein condensate,” Science **279**, 1005 (1998). Included in Appendix C.*
- *D.M. Stamper-Kurn, H.-J. Miesner, A.P. Chikkatur, S. Inouye, J. Stenger, and W. Ketterle, “Reversible formation of a Bose-Einstein condensate,” Phys. Rev. Lett. **81**, 2194 (1998). Included in Appendix G.*

As discussed above with regard to equilibrium properties, gaseous Bose–Einstein condensates are a macroscopic many–body system whose equilibrium properties are rather easily described from a microscopic basis. This situation contrasts with the manifestations of Bose–Einstein condensation in more complicated systems, such as liquid helium, the microscopic characterization of which has been a major challenge due to the strong correlations induced by interactions. Furthermore, the parameters which govern the behaviour of condensed gases (trap stiffness and shape, atomic density and number, temperature) can be flexibly altered, allowing one to quantitatively test theoretical models over a wide range of physical conditions. Similarly, one can now perform detailed studies of a variety of non–equilibrium and dynamical properties of Bose condensates.

In particular, the kinetics of the formation of a phase–coherent Bose–Einstein condensate from an incoherent non–condensed gas has been a difficult and interesting theoretical problem (see for example Refs. [201–203]). Efforts have been underway to develop kinetic theories which will contain enough detail to describe accurately condensate formation and

other non-equilibrium processes while still reflecting the simplicity of the dilute gas. Experimental investigations of the intrinsic time scale for the formation process are a critical test for such theories.

In this chapter I summarize our experimental investigations of the formation of Bose-Einstein condensates. Two different experiments were performed. In one, a Bose gas on the verge of condensation was suddenly cooled to below the Bose-Einstein condensation transition temperature. The consequent evolution of the gas was observed, and the intrinsic time scales for the formation of a Bose condensate were measured [9]. In a second experiment, we used a combination of optical and magnetic forces to adiabatically change the form of the trapping potential, and thereby change the phase-space density of a trapped gas reversibly. This method allowed us to pass a trapped Bose gas through the Bose condensation phase transition reversibly, and opens the door to new probes of the formation process.

6.1 Formation of a Bose-Einstein condensate in a super-cooled vapor

To study the time scales for Bose condensation, we sought to create a non-equilibrium, non-condensed gas which would equilibrate to a gas containing a Bose-Einstein condensate. Such a non-equilibrium state is created during the evaporative cooling by which condensates are made: after atoms with a high potential energy are removed at the edge of a magnetic trap, creating a non-equilibrium energy distribution, the gas can equilibrate to below the Bose-Einstein condensation transition temperature. However, in order for evaporative cooling to be effective, the cooling rate must be much slower than the thermalization rate of the gas. Thus, the formation of a Bose condensate during evaporative cooling is quasi-static, with the gas remaining always near thermal equilibrium, and a determination of the intrinsic time scales for the formation of a condensate is difficult — unless small temporal lags between the state of the gas and the instantaneous equilibrium state can be measured (Sec. 6.2).

Thus, rather than applying a gradual evaporative cooling, we created a super-cooled trapped atomic gas far from equilibrium by applying a rapid rf-induced truncation of its energy distribution. For this, clouds at temperatures just slightly above the Bose-Einstein condensation transition temperature were created in our magnetic trap by rf evaporative cooling. Then, the rf frequency was rapidly swept from the frequency used at the end of the evaporative cooling to a final frequency which was about 50 kHz above the resonant frequency for atoms at the bottom of the magnetic trap. The total sweep ranged over 200 kHz and was performed over 10 ms. This rf sweep performed a sudden spatial truncation of the cloud, ejecting atoms with a high potential energy.

The cloud was then allowed to equilibrate freely while being imaged repeatedly by rapid phase-contrast imaging. The use of rapid-sequence imaging was critical to this study because it allowed us to observe and time-resolve the entire formation with measurements

from a single shot of the experiment. Shot-to-shot variations in the equilibrium conditions after the rf truncation, characterized by the equilibrium number of condensed atoms, were quite large. These arose because of variations in the initial number of atoms at the time of the rf truncation, and ~ 10 mG magnetic field variations which altered the trap depth at the end of the rapid rf sweep. In the end, such variations were actually helpful because they allowed us to study condensate formation under a variety of initial conditions.

The images clearly showed the growth in the condensate number as the truncated non-condensed cloud was allowed to equilibrate [9] (Appendix C). The temporal evolution of the condensate number showed evidence for bosonic stimulation in the growth of the condensate. Bosonic stimulation is the $(N + 1)$ -factor enhancement of a transition rate due to the presence of N bosons in the final state. This enhancement arises simply from the symmetry under particle exchange of the many-body wavefunction, and is indeed equivalent to the Bose-Einstein counting statistics presented in Sec. 5.2 (see discussion in Ref. [22]). If condensate formation is a Bose-enhanced process, one expects the number of condensate atoms N_0 to grow initially as

$$\frac{\partial N_0}{\partial t} = \gamma(N_0 + 1) \quad (6.1)$$

where γ is the initial exponential growth rate. Eventually, as the cloud equilibrates, the growth rate should become zero. Thus, one can simply parameterize the Bose-stimulated equilibration of N_0 by (neglecting the small $+1$ term above)

$$\frac{\partial N_0}{\partial t} = \gamma N_0 \left[1 - \left(\frac{N_0}{N_{0,eq}} \right)^\delta \right] \quad (6.2)$$

where $N_{0,eq}$ is the equilibrium condensate number.

The solution to this growth equation is an “S” shaped curve with an initial slow growth, a rapid growth as the condensate number increases, and then a final slow growth towards an equilibrium value. Our measurements of the temporal evolution of the condensate number were described quite well by such a curve. A more direct demonstration of bosonic stimulation was obtained by comparing the initial growth in the condensate number for different initial values of the condensate number at the time of the rf truncation (Fig. 3 of [9]). When no condensate was present right after the rf sweep, the growth started slowly and sped up only after a larger condensate had formed. In contrast, when a condensate was already present after the rf sweep, the condensate number grew rapidly without delay.

The initial exponential growth rates γ determined by our measurements were compared to a simple quantum kinetic theory proposed by Gardiner *et al.* [204], which is an approximation to a more thorough treatment [205–208]. In this theory, one divides the trapped gas into two populations according to some threshold energy above which lies a thermal bath at a constant temperature, and below which lie states associated with the Bose condensate. The observed growth rates were substantially larger than the predictions of that theory.

Moreover, the observed trend of γ to lower values when the equilibrium condensate number $N_{0,eq}$ was opposite to that predicted in Ref. [204].

Further progress in the development of quantum kinetic theories has reconciled some of these differences. Gardiner and collaborators extended their kinetic theory to account more explicitly for the population in low-lying excited states [209]. Their findings agree with the picture suggested earlier by Kagan [201] that there is an initial “kinetic stage” of equilibration during which population migrates towards the low-lying excited states, after which the condensate grows more rapidly while the low-lying states are depleted. The condensate growth curves predicted by this refined approach were in agreement with our measurements, although the trend of γ with variations in $N_{0,eq}$ was still not explained. Numerical simulations performed by Arimondo, Cerboneschi and Wu [210], which include the effects of Bose-enhanced scattering, also reproduce the correct temporal evolution for some parameters of our experiment.

The study of the formation of a Bose-Einstein condensate is also important for the development and eventual use of an atom laser. An atom laser is a device which generates and outputs a coherent matter wave [211]. It is for atoms what the optical laser is for light. The formation of a Bose-Einstein condensate from a non-equilibrium gas through Bose-stimulated scattering of atoms constitutes the gain mechanism of an atom laser. Other critical elements of an atom laser have also been demonstrated. A resonant atom cavity is simply provided by the magnetic or optical trap which confines the gas. Output coupling can be implemented in a variety of ways, such as the application of resonant rf [5] or optical fields [212].

Future studies of the condensate formation would benefit from detection schemes which are more sensitive to the presence of small condensates. For example, a variety of methods have recently been employed to accurately measure the spatial coherence of a trapped gas [18, 160, 169]. These would allow a more detailed look at the initial phase of condensate formation and reveal how the coherence of the condensate is established and how it affects the kinetic evolution of the gas. Measurements of the coherence length during the formation of a condensate would allow one to distinguish between the growth of population in low-lying excited states (a so called “quasi-condensate” [201], see also Sec. 8.7), and the growth of a phase-coherent condensate.

6.2 Reversible formation of a Bose-Einstein condensate by adiabatic changes in the trapping potential

Both typical evaporative cooling and the sudden rf truncation discussed above increase the phase-space density of a trapped gas through non-adiabatic, irreversible methods. Thus, these methods can only be used for single-shot probes of the Bose-Einstein condensation phase transition; one could certainly reheat the gas and cool it again to Bose condensation,

but only with a much smaller sample of atoms.

However, let us consider that one could contain a small portion of a trapped atomic sample in a vessel, and then slowly compress that vessel while keeping it in thermal contact with the remainder of the gas. The density of the compressed gas would increase, but its temperature rise, after thermalization with the larger uncompressed gas, would be slight. Thus, one would increase the phase-space density of the compressed gas. If the compression were performed slowly (quasi-statically), the total entropy of the gas would remain unchanged, and one could reversibly change the maximum phase-space density of the gas. Thereby, one could cross the Bose–Einstein condensation phase–transition reversibly.

Using a combination of magnetic and optical trapping forces, we implemented a similar scheme for adiabatically (i.e. isentropically) increasing the phase-space density of a trapped ultra–cold gas, and crossing the Bose–Einstein condensation transition reversibly [14] (Appendix G). This experiment was appealing (and fun!) as a case study in basic physical concepts such as adiabaticity, the relation between reversible and irreversible processes, and the chemical potential. Furthermore, it demonstrates a new technique that could be used for future studies of the dynamics of condensate formation.

The possibility of increasing the phase-space density of a trapped gas by an adiabatic change in the trapping potential had been overlooked for quite some time. While adiabatic changes in the *strength* of a trapping potential, for example by increasing the trap frequencies of a harmonic magnetic trap, cannot increase the population in the ground state, changes in the *shape* of the potential can.

This was suggested by Pinkse and collaborators [213] and demonstrated experimentally with an ultra–cold hydrogen gas. They considered a gas held in a power law potential

$$U(x, y, z) = c_x x^{n_x} + c_y y^{n_y} + c_z z^{n_z} \quad (6.3)$$

A classical gas held in such a potential with temperature T_i occupies a volume which scales as $V \propto T^{\alpha_i}$ where $\alpha_i = 1/n_x + 1/n_y + 1/n_z$. As discussed in Sec. 3.5.6, the entropy of such a gas is then (Eq. 3.15)

$$\frac{S}{N} = k_B \left[\frac{5}{2} + \frac{\partial \ln V}{\partial \ln T} - \ln(\Gamma_i) \right] \quad (6.4)$$

$$= k_B \left[\frac{5}{2} + \alpha - \ln(\Gamma_i) \right] \quad (6.5)$$

where $\Gamma_i = n_{\text{peak}} \lambda_{dB}^3$ is the maximum phase-space density of the gas, n_{peak} is the peak density, and $\lambda_{dB} = \sqrt{2\pi\hbar^2/mk_B T}$ is the thermal de Broglie wavelength. If the form of the potential is then adiabatically changed so that the scaling between volume and temperature is $V \propto T^{\alpha_f}$, then the phase-space density becomes

$$\Gamma_f = \Gamma_i e^{\alpha_f - \alpha_i} \quad (6.6)$$

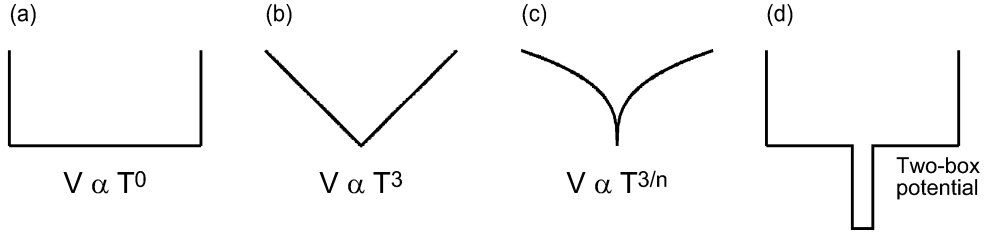


Figure 6-1: Adiabatic increases in phase-space density by deformation of a power law potential. The deformation from (a) a box potential to (b) a three-dimensional linear potential yields a phase-space density increase of e^3 , as discussed in Ref. [213]. (c) Further deformation produces a potential with a sharp central “dimple” and a larger increase in phase-space density. (d) The two-box potential has a similar form, and can be used for arbitrarily-large adiabatic increases in phase-space density.

Considering the deformation from a box potential ($\alpha_i = 0$) to a three-dimensional linear potential ($\alpha_f = 3$), the maximum increase in phase-space density is a factor of $e^3 \simeq 20$.

But, why not go further? Consider the deformation of a box potential to a potential of the form $U(\vec{r}) \propto r^n$ where $n \ll 1$ (Fig. 6-1). In that case, the increase in phase-space density, a factor of $e^{3/n}$, is unlimited. While such a potential may be difficult to create, its basic features — a narrow potential “dimple” within a broader potential — are precisely those used in our scheme for increasing the phase-space density adiabatically.

As discussed in our paper [14] (Appendix G), the type of trap deformations which we studied can be understood with a simple “two box” model, similar to that discussed at the beginning of this section. Consider a classical gas of N atoms with a phase-space density of Γ_0 confined in a box potential of volume $V_0 = V_1 + V_2$. Suppose that the potential is then adiabatically deformed by lowering the potential within a small sub-volume V_2 to a depth U , bringing the gas to a final temperature T_f . By considering the conditions of constant entropy and particle number, one finds the final maximum phase-space density (in volume V_2) is given by

$$\Gamma_f = \Gamma_0 \exp \left(\frac{U/k_B T_f}{1 + (V_2/V_1)e^{U/k_B T_f}} \right) \quad (6.7)$$

Considering the limit of shallow potential wells [$(V_2/V_1)e^{U/k_B T_f} \ll 1$], the increase in phase-space density is simply given by Boltzmann factor $e^{U/k_B T_f}$ by which the density in V_2 is greater than that in V_1 . This is essentially the same situation as considered at the beginning of this section: the gas in V_2 is compressed, but does not increase much in temperature because of the thermal contact with the remainder of the gas. This increase in phase-space density can be arbitrarily large insofar as the ratio of volumes V_2/V_1 is made extremely small.

The “two box” potential was experimentally realized using a combination of magnetic and optical trapping forces. A trapped gas was initially prepared in a magnetic trap,

analogous to the large potential of volume $V_0 = V_1 + V_2$. Then, a narrow potential well, corresponding to V_2 , was added by shining a focused infrared laser beam onto the magnetically trapped atoms. This same optical setup was used in other experiments for the all-optical confinement of Bose–Einstein condensates (Chapter 9). The parameters of both the magnetic and optical trapping forces were determined accurately to allow a quantitative comparison between data and theory. The magnetic trap was characterized by *in situ* frequency measurements (Sec. 4.6), while the optical forces were characterized by imaging the focused beam to determine its focal size and by measuring its power.

To measure the increase in phase-space density due to the deformation of the trapping potential, trapped gases were brought to a temperature above the Bose–Einstein condensation temperature. The infrared beam was then slowly ramped up to a power where the onset of Bose condensation was visible in time-of-flight images. The transition served as a benchmark indicating that the phase-space density had reached its critical value of $g_3(1) \simeq 2.612$. The measured increases in phase-space density were in good agreement with a simple theoretical prediction. By repeating these measurements for different magnetic and optical trapping parameters, we confirmed a universal characterization of the phase-space density increase.

Lowering the narrow potential well further takes the sample across the Bose–Einstein condensation phase transition. The adiabatic condensation of a trapped gas was studied by first preparing a trapped gas at the transition temperature in the magnetic trap, and then imposing an optical potential well of variable depth and determining the condensate fraction from time-of-flight images. Large condensates were produced, containing as many as 15×10^6 atoms, similar to the size of condensates that could be produced by evaporative cooling alone.

However, the observed condensate fractions were significantly smaller than those predicted by a model which treats the adiabatic condensation of an ideal gas. This observation constitutes the first experimental evidence that interatomic interactions reduce the condensate fraction, as discussed in Sec. 5.7. The importance of interactions on thermal properties can be characterized by the parameter $\eta = gn_0/k_B T_c$ which is the ratio of the interaction energy at zero temperature to the thermal energy at the transition temperature. In a harmonic potential with mean trapping frequency $\bar{\omega}$, the interaction energy scales as $\omega^{6/5}$ while T_c scales as ω . Thus, due to the weak scaling with the trapping frequency ($\eta \propto \omega^{1/5}$), it is difficult to significantly increase the parameter η beyond its typical value in the range of 0.3 to 0.4 [178]. On the other hand, the “dimple” trap which we have created is characterized by two different trapping frequencies, one (small) for the broad magnetic trap which determines T_c , and another (large) which determines the condensate interaction energy. Thus, the parameter η can be greatly increased. This fact is demonstrated by the time-of-flight image shown in Fig. 6-2. Even for a small condensate fraction, the free expansion of the condensate is faster than that of the thermal cloud, indicating $\mu = gn_0 > k_B T$.

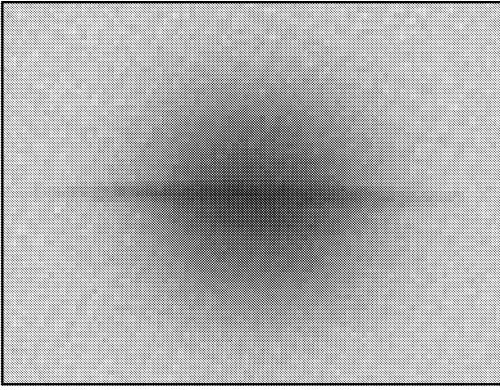


Figure 6-2: The interaction energy can be made larger than the thermal energy in the “dimple” trap. Shown is the ballistic expansion of a cloud released from the “dimple” trap formed by the combination of magnetic and optical forces. The disc-like expansion of the condensate (horizontal in image) is faster than the isotropic thermal expansion. This comparison indicates that interatomic interactions should greatly modify thermal properties of clouds trapped in such a potential.

Finally, the ability to cross the Bose–Einstein condensation phase–transition repeatedly was demonstrated. Again, clouds were prepared at the transition temperature in a magnetic trap. Then, the infrared power was cycled sinusoidally at a rate of 1 Hz. For this experiment, we used a weak magnetic trap (trap frequencies of $\omega_r = 2\pi \times 48$ Hz radially and $\omega_z = 2\pi \times 33$ Hz axially) and a large optical focus ($1/e^2$ beam–waist radius of $w_0 = 16 \mu\text{m}$) to avoid density–dependent trap losses. During the first seven condensation cycles, shown in Fig. 6-3, the condensate fraction oscillated between zero and 6%. The peak of these oscillations decreased in time apparently due to a slow 10 nK/s heating rate probably caused by instabilities in our optical setup.

6.2.1 New opportunities for studying the formation of Bose–Einstein condensates

This method of creating Bose condensates using a focused infrared laser beam offers a number of new opportunities for studying condensate formation. For example, in the experiment in which a gas was cycled repeatedly through the phase transition, the condensate fraction was observed to lag by about 70 ms behind the modulation of the infrared laser power. This lag time is a measure of the condensate formation time scale, and is in agreement with the order of time scales observed in our study of irreversible condensate formation. Measuring the formation time scale in this manner rather than by the rf truncation method may allow for a clearer separation between the time scales for condensate formation and other time scales associated with spatial equilibration of a truncated thermal cloud.

Another advantage of using the “dimple” trap for studies of condensate formation is the fine temporal control over the optical potential which varies the phase–space density of the

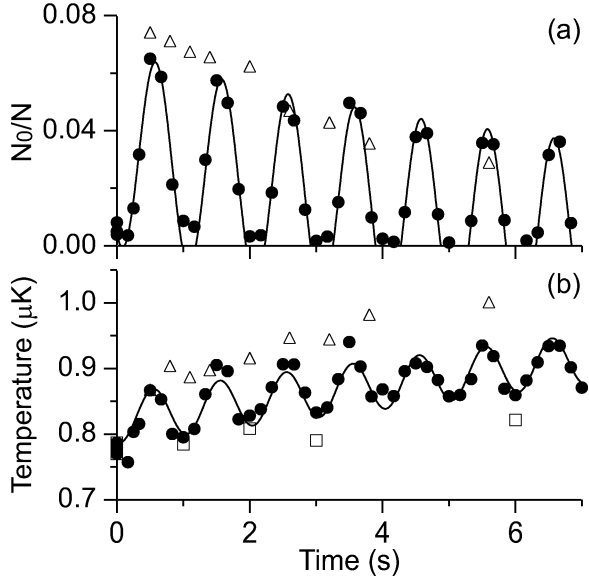


Figure 6-3: Adiabatic cycling through the phase transition. Shown is (a) the condensate fraction and (b) the temperature vs. time for the case of a modulated laser beam (circles), an infrared beam ramped up to a constant power (triangles), and no infrared light (squares). The solid lines are guides to the eye. Figure taken from [14].

gas. For instance, when we switched on the infrared light instantly, rather than ramping it up slowly to ensure quasi-static evolution, we observed the formation of condensates on time scales (5 – 10 ms) which were much faster than the oscillation periods along the weakly confining direction. The resulting condensates showed striations in time-of-flight images (Fig. 6-4), indicating that the condensates had formed with substantial motional excitations. These disjointed condensates may be related to the condensate droplets discussed by Côté and Kharchenko [214] as a non-equilibrium phenomenon which may be seen in experiments with condensates of atomic hydrogen. In future studies, it would be interesting to investigate these excited condensates, akin to the quasi-condensates discussed by Kagan [201], and probe for spatial phase fluctuations which may die out as the system equilibrates. Such measurements could be done, for example, using Bragg spectroscopy to measure the evolution of the coherence length. Alternatively, one could examine the interference of these quasi-condensates with a second, equilibrated condensate which can be stored nearby, perhaps in a second optical beam.

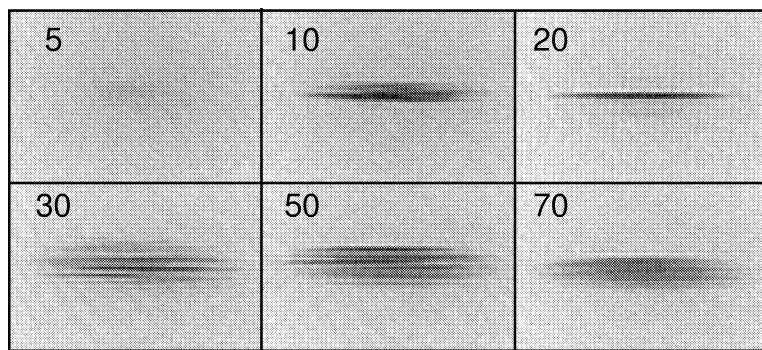


Figure 6-4: Formation of a Bose condensate in an excited motional state by shock condensation. A magnetically-trapped cloud above the Bose-Einstein condensation transition temperature was suddenly exposed to a deep optical potential. Time-of-flight images are shown, taken after variable durations (time indicated in ms) of dwell time in the combined magnetic and optical trap. Gross striations were observed in the expanding condensates which indicate their formation in an excited state or, equivalently, a spatially varying phase of the order parameter.

Chapter 7

Dynamic properties of a Bose–Einstein condensate

This chapter summarizes experimental work concerning the dynamic properties of Bose–Einstein condensates. Experiments performed by our group are reported in the following publications:

- *M.-O. Mewes, M.R. Andrews, N.J. van Druten, D.M. Kurn, D.S. Durfee, C.G. Townsend, and W. Ketterle, “Collective excitations of a Bose-Einstein condensate in a magnetic trap,” Phys. Rev. Lett. **77**, 988 (1996).*
- *M.R. Andrews, D.M. Kurn, H.-J. Miesner, D.S. Durfee, C.G. Townsend, S. Inouye, and W. Ketterle, “Propagation of sound in a Bose-Einstein condensate,” Phys. Rev. Lett. **79**, 553 (1997); Erratum Phys. Rev. Lett. **80**, 2967 (1998).*
- *D.M. Stamper-Kurn, H.-J. Miesner, S. Inouye, M.R. Andrews, and W. Ketterle, “Collisionless and hydrodynamic excitations of a Bose-Einstein condensate,” Phys. Rev. Lett. **80**, 500 (1998). Included in Appendix E.*

A large portion of the chapter (Sec. 7.2) is taken from the following review article:

- *W. Ketterle, D.S. Durfee, and D.M. Stamper-Kurn, “Making probing and understanding Bose-Einstein condensates,” in M. Inguscio, S. Stringari and C.E. Wieman eds., *Bose–Einstein Condensation in Atomic Gases, Proceedings of the “Enrico Fermi” Summer School, July 1998, Varenna, Italy* (to be published).*

A recurrent subject of experimental scrutiny in our group since the first observations of gaseous Bose–Einstein condensates has been the study of their dynamic properties. As with the study of any substance, observing the response of Bose condensates to various well-controlled perturbations provides a wealth of information about their structure and develops our intuition regarding their nature. To put it more simply, we experimental

physicists with an apparatus laden with advanced technologies followed the same protocol that a child would upon encountering a new substance: we poked it [7], shook it [4, 12], stirred it [164, 165], or wiggled it [18, 21] and saw what it did.

As a result of these playful pursuits by our group and others and through many theoretical explorations, a detailed picture of the basic nature of Bose–Einstein condensates has been assembled and tested. This advancing knowledge not only allows us perform increasingly stringent tests by which we refine our understanding of gaseous Bose condensates, but also provides us with a model system of macroscopic quantum mechanical phenomena which can be understood (almost) *ab initio*. Further, once the description of their dynamics is developed and tested, Bose–Einstein condensates become a general tool for studying things other than the properties of condensates. Such studies have already begun. For example, *s*–wave scattering lengths for collisions between ^{87}Rb atoms have been measured by observing the dynamic response of condensates to changes of internal states [156]. Observations of periodic output–coupling and Bloch oscillations from an array of trapped Bose–Einstein condensates have shown promise for measuring accelerations (such as that due to gravity) as an early use of Bose–Einstein condensates for atom interferometry [215]. In these studies, dynamic and coherence properties of Bose–Einstein condensates are used as assumptions in interpreting the observations as a measurement of some physical quantity. These experiments herald the future use of Bose–Einstein condensates for a variety of studies.

In this section, I present a theoretical and experimental overview of the dynamic behaviour of Bose–Einstein condensates, beginning with a summary of some basic theoretical considerations, and continuing with a portion of our recent review paper which was written for the proceedings of the 1998 “Enrico Fermi” Summer School in Varenna, Italy [22]. After this overview, I present some aspects of our measurement of the speed of one–dimensional sound propagation [7, 8] which have not been published elsewhere.

7.1 The Bogoliubov theory

The effect of weak interactions on gaseous Bose–Einstein condensates was treated by Bogoliubov in 1947 [28]. Some of this theory was presented in Sec. 5.6, where we showed that a positive *s*–wave scattering length $a > 0$ for collisions between gas particles results in an effective repulsive interaction which raises the chemical potential μ by an amount proportional to the density of the gas n . In terms of bulk properties of the gas, this mean–field result indicates that the compressibility of the gas $\chi = -V(\partial P/\partial V) = 4\pi\hbar^2an^2/m$ is finite. In an inhomogeneous potential, this finite compressibility causes the condensate to swell beyond the size of the ideal–gas ground state, just as a compressed gas in a cylinder will push against a piston and expand in volume. Thus, one can regard the trapping potential as a barometer which allows one to measure the pressure of the gas by spatially imaging its

equilibrium distribution.

This characteristic of a weakly-interacting gas also has implications for its dynamic behaviour. A finite compressibility implies that small-amplitude, long-wavelength density perturbations in the gas propagate as sound waves with a speed of sound given by $c = \sqrt{\partial\chi/\partial(mn)} = \sqrt{\mu/m}$ (see e.g. [192]), whereas in an ideal gas Bose condensate, such perturbations propagate ballistically (as free particles).

This dynamic behaviour is explained from a microscopic basis in the theoretical description of weakly-interacting Bose-Einstein condensates. As discussed in Sec. 5.6, one begins by considering the many-body Hamiltonian for a system of interacting particles as in Eq. 5.17. In second quantized notation where \hat{a}_k (\hat{a}_k^\dagger) are destruction (creation) operators of a particle of wavevector k , the Hamiltonian for a gas trapped in a box potential with volume V (as considered by Bogoliubov) is

$$\mathcal{H} = \mathcal{H}_0 + \mathcal{H}_{\text{int}} \quad (7.1)$$

$$= \sum_k \hbar\omega_k^0 \hat{a}_k^\dagger \hat{a}_k + \frac{g}{2V} \sum_{k,l,m} \hat{a}_k^\dagger \hat{a}_l^\dagger \hat{a}_m \hat{a}_{k+l-m} \quad (7.2)$$

In the free-particle Hamiltonian \mathcal{H}_0 , $\hbar\omega_k^0 = \hbar^2 k^2 / 2m$ is the energy of a free-particle with momentum $\hbar k$. \mathcal{H}_{int} describes binary interactions where $g = 4\pi\hbar^2 a/m$ gives the interaction strength, and a is the s -wave scattering length. Assuming the presence of a Bose-Einstein condensate, one replaces the zero-momentum operators with c -numbers $\hat{a}_0 = \hat{a}_0^\dagger = \sqrt{N_0}$ where N_0 is the number of zero-momentum particles. As shown by Bogoliubov, neglecting terms of order $N^{1/2}$, the Hamiltonian is diagonalized as

$$\mathcal{H} = \sum_k \hbar\omega_k^B \hat{b}_k^\dagger \hat{b}_k \quad (7.3)$$

by a canonical transformation to operators defined by $\hat{a}_k = u_k \hat{b}_k - v_k \hat{b}_{-k}^\dagger$. The coefficients u_k and v_k are defined by $u_k = \cosh \phi$, $v_k = \sinh \phi$ and $\tanh 2\phi = \mu/(\hbar\omega_k^0 + \mu)$ where $\mu = gN_0/V$.

The Bogoliubov creation and destruction operators \hat{b}_k and \hat{b}_k^\dagger thus define quasi-particle excitations of the system with energies $\hbar\omega_k^B = \sqrt{\hbar\omega_k^0(\hbar\omega_k^0 + 2\mu)}$. At high momentum, such that $\hbar\omega_k^0 \gg \mu$, the operators describe free-particle excitations ($\hat{b}_k \rightarrow \hat{a}_k$), and the dispersion relation becomes that of free-particles with an energy offset due to interactions: $\hbar\omega_k^B \rightarrow \hbar\omega_k^0 + \mu$. At low momentum ($\hbar\omega_k^0 \ll \mu$), the excitations are unlike free-particle excitations, and the dispersion relation becomes linear with $\hbar\omega_k^B \rightarrow \hbar ck$ where $c = \sqrt{\mu/m}$.

A similar spectrum is obtained by the Hartree approach as discussed in Sec. 5.6. There, one solves the time-dependent Gross-Pitaevskii equation (Eq. 5.18) with a condensate wavefunction of the form $\psi(\vec{r}, t) = e^{-i\mu t/\hbar} (\psi_0 + u(\vec{r})e^{-i\omega t} + v^*(\vec{r})e^{+i\omega t})$. To first order, the

functions $u(\vec{r})$ and $v(\vec{r})$ then obey the linear Bogoliubov–de Gennes equations

$$\hbar\omega u(\vec{r}) = \left(-\frac{\hbar^2 \nabla^2}{2m} + V(\vec{r}) + g|\psi_0|^2 \right) u(\vec{r}) - g|\psi(\vec{r})|^2 v(\vec{r}) \quad (7.4)$$

$$-\hbar\omega v(\vec{r}) = \left(-\frac{\hbar^2 \nabla^2}{2m} + V(\vec{r}) + g|\psi_0|^2 \right) v(\vec{r}) - g|\psi(\vec{r})|^2 u(\vec{r}) \quad (7.5)$$

Note that the solutions to these equations are not eigenmodes of the Gross–Pitaevskii equation, but rather describe small amplitude perturbations to the condensate wavefunction under a self-consistent Hartree–Fock approximation. Nevertheless, once properly normalized to describe a single-particle excitation, the functions $u(\vec{r})$ and $v(\vec{r})$ indeed describe quantized quasi-particle excitations in both homogeneous and inhomogeneous systems.

This microscopic excitation spectrum has a number of profound implications for the nature of weakly-interacting Bose–Einstein condensates. First, unlike in a normal fluid, these microscopic (i.e. single-particle) excitations are directly manifest as macroscopic density modulations due to the presence of a macroscopic wavefunction. Thus, the Bogoliubov excitation spectrum describes the collective response of the gas to perturbations. This can be seen easily in the Hartree treatment of a homogeneous system, where the density of the gas $n(\vec{r}, t) = |\psi(\vec{r}, t)|^2$ after the creation of a single quasi-particle at wavevector q is given by

$$n(\vec{r}, t) = \frac{N_0}{V} \left(1 + 2\sqrt{\frac{1}{N_0}}(u_q - v_q) \cos(\vec{q} \cdot \vec{r} - \omega t) + \mathcal{O}(N_0^{-1}) \right) \quad (7.6)$$

By heterodyne interference with the macroscopic wavefunction, a single quasi-particle has a macroscopic effect on the density of the gas, i.e. a single-particle excitation yields a density modulation of relative amplitude $\propto 1/\sqrt{N}$ rather than $\propto 1/N$. This effect is similarly described by the single quasi-particle contribution to the dynamical structure factor, as discussed in Chapter 8. Thus, for example, the linear dispersion relation of low-momentum Bogoliubov excitations describes sound propagation at the speed of Bogoliubov sound c .

Second, the diagonalization of the many-body Hamiltonian implicitly defines the ground-state many-body wavefunction $|g\rangle$ as one which is devoid of all quasi-particle excitations, i.e. $\hat{b}_k|g\rangle = 0, \forall k$. This condition profoundly changes the nature of a Bose–Einstein condensate. In a non-interacting gas, a Bose–Einstein condensate is composed of a macroscopic number of particles in the single-particle ground state, and is thus devoid of all free-particle excitations. In a homogeneous system, this is represented in the momentum basis as $|g\rangle_{\text{ideal}} = |N, 0_k, 0_{-k}, \dots\rangle$ where N particles have zero momentum, 0 particles have momentum $\hbar k$, etc. However, such a state *does* contain Bogoliubov quasi-particles

$$\hat{b}_k|g\rangle^{\text{ideal}} = -v_k|N, 0_k, 1_{-k}, \dots\rangle \neq 0 \quad (7.7)$$

and thus cannot represent the ground-state of an interacting gas.

Rather, collisions between zero-momentum particles mix into the condensate wavefunc-

tion pairs of atoms at momenta $\pm\hbar k$. As seen from a perturbative approach, the operator $(g/2V) \times \hat{a}_k^\dagger \hat{a}_{-k}^\dagger \hat{a}_0 \hat{a}_0$ which is part of the interaction Hamiltonian \mathcal{H}_{int} couples the ideal-gas ground state $|g\rangle_{\text{ideal}}$ with the state $|N - 2, 1_k, 1_{-k}, \dots\rangle$, and thus the ground state of the interacting system is a particular linear combination of these states. Indeed, it can be shown that the condition $\hat{b}_k|g\rangle = 0, \forall k$ implies [192]

$$|g\rangle = \prod_k \sum_{m=0}^{\infty} (-\alpha_k \hat{a}_k^\dagger \hat{a}_{-k}^\dagger)^m |N, 0, 0, \dots\rangle \quad (7.8)$$

where $\alpha_k = (\mu - \hbar[\omega_k^B - \omega_k^0])/\mu$. Thus, the condensate is no longer just a product of identical single-particle wavefunctions (as assumed in the Hartree–Fock approximation), but rather is replete with correlated pairs of excitations. The total population in these excited states $\langle g | \sum_k \hat{a}_k^\dagger \hat{a}_k | g \rangle$, called the quantum depletion, is proportional to $\sqrt{na^3}$, and is on the order of 1% for the dilute gas Bose–Einstein condensates [173]. The presence of these excitations is discussed further in Chapter 8.

Finally, the specific form of the Bogoliubov excitation spectrum provides an explanation for superfluidity. As discussed by Landau and Feynmann in the context of superfluid helium, a superfluid with a dispersion relation given by ω_k flowing at a uniform velocity v cannot lower its energy by the scattering of a single particle to lower momentum when $v < v_c = \min(\omega_k/k)$. For a Bose condensed weakly-interacting gas, the critical velocity is non-zero $v_c = c > 0$, and thus the gas is expected to be superfluid. Present experiments have begun to test the possible superfluid nature of gaseous Bose–Einstein condensates [216].

7.2 Experimental overview from Varenna proceedings (Ref. [22])

In this section, I include the section entitled “Sound and other dynamic properties” from Ketterle, Durfee, and Stamper-Kurn, “Making probing and understanding Bose-Einstein condensates,” in M. Inguscio, S. Stringari and C.E. Wieman eds., *Bose-Einstein Condensation in Atomic Gases*, Proceedings of the “Enrico Fermi” Summer School, July 1998, Varenna, Italy (to be published). This text discussed the distinction between excitations in different regimes based on a comparison of appropriate length scales, and reviews experimental work by our group and others as of the summer of 1998. Some minor modifications have been made to conform to the symbols and section headings used in this dissertation.

Important updates to this overview are:

- Excitations with wavelengths smaller than all dimensions of the condensate, discussed in Sec. 7.2.2, have now been studied using optical Bragg scattering. This is discussed thoroughly in Chapter 8.
- A wider range of discrete shape oscillations is now accessible by the flexible application of optical potentials. Surface excitations of high multipolarity have been observed and compared favorably with theory [217]

While Bose-Einstein condensates are produced and probed using the tools of atomic physics, their connection to decades-old condensed-matter physics is most evident in the study of sound. Much of our understanding of the nature of sound in quantum fluids comes from the context of liquid helium (see discussions in refs. [76] and [37]). However, due to the strong interactions in liquid helium (after all, it is a liquid) the fundamental connections of superfluidity and sound propagation to Bose-Einstein condensation were not immediately apparent. Indeed, as studies of liquid helium progressed deeper into its dynamic properties, two competing theoretical approaches emerged: the empirical quantum hydrodynamic approach of the Landau school, and the two-fluid picture of Tisza and London which emphasized the connection to Bose condensation.

The convergence of these two approaches was suggested by the Bogoliubov theory of weakly interacting Bose gases [28], which showed that Bose-Einstein condensation could produce features of the excitation spectrum which Landau's hydrodynamic theory postulated at its start. The theory of degenerate Bose gases was developed further in later years, providing further insight into the nature of sound propagation at finite temperature [218], the interpretation of experimental probes of liquid helium, and the nature of the BEC phase transition. Yet, these gases existed only in theoretical papers, and none of these theories could be verified experimentally.

Now, with gaseous Bose-Einstein condensates produced in more than a dozen laboratories around the world, researchers have turned to these decades-old theories and begun testing their validity. We leave the description of these theories to other chapters of this book [*in the Varenna proceedings*], and present this theoretical context only as it pertains to recent experiments on magnetically trapped Bose condensed gases. By considering a hierarchy of length scales (shown in Table 7.1), we divide the description of sound propagation into separate regimes, differentiating between pulse propagation at short wavelengths and collective modes at longer ones, and between collisionless and hydrodynamic behavior. Experiments in the collisionless regime and zero-temperature have confirmed the Bogoliubov mean-field description of Bose condensed gases, while findings at non-zero temperature have challenged the theoretical formalism for their description. Most recently, experiments have pushed toward the hydrodynamic limit, allowing a closer connection to the phenomena of first and second sound in superfluid helium.

7.2.1 Collisionless excitations in a homogeneous Bose gas

The nature of collective excitations in a homogeneous Bose gas depends on the hierarchy of three length scales:

- The reduced wavelength of the excitation λ_{ex}
- The healing length ξ which is given by the condensate density as $\xi = (8\pi a n_0)^{-1/2}$. Modifications of the condensate wavefunction on this length scale imply a kinetic

Table 7.1: The nature of collective excitations of the condensate and the thermal cloud. Various regimes are distinguished according to a hierarchy of length scales: the reduced wavelength of the excitation λ_{ex} , the healing length ξ , and the mean-free path for collisions between quasi-particles l_{mfp} .

Regime	Length scales	Condensate	Thermal cloud
collisionless	$\lambda_{ex} < \xi, l_{mfp}$	ballistic	ballistic
collisionless	$\xi < \lambda_{ex} < l_{mfp}$	zero sound	ballistic
hydrodynamic	$\xi < l_{mfp} < \lambda_{ex}$	second sound	first sound

energy which is equal to the chemical potential.

- The mean-free path l_{mfp} for collisions between quasi-particles, or more specifically, between the collective excitation and the other excitations which comprise the thermal cloud. This length scale can be estimated by considering collisions among free particles in a thermal cloud in the absence of the condensate. A more exact determination requires careful consideration of the modification of collisions due to the condensate (see chapter by K. Burnett in this volume).

The condition $\lambda_{ex} \ll l_{mfp}$ defines the collisionless regime (in the sense of collisions among quasi-particles), which applies at low densities of the thermal cloud. The excitations in this regime were derived for zero temperature by Bogoliubov [28]. The excitation energy ϵ_k at wavevector k is given by

$$\epsilon_k = \sqrt{\frac{\hbar^2 k^2}{2m} \left(\frac{\hbar^2 k^2}{2m} + 2\mu \right)} \quad (7.9)$$

$$= \frac{\hbar^2}{2m} \sqrt{\frac{1}{\lambda_{ex}^2} \left(\frac{1}{\lambda_{ex}^2} + \frac{2}{\xi^2} \right)} \quad (7.10)$$

where $\mu = 4\pi\hbar^2 a n_0 / m$ is the chemical potential as defined by the condensate density n_0 . At long wavelengths ($\lambda_{ex} \gg \xi$) the excitation energy depends linearly on the wavevector, implying phonon-like excitations; a packet of such excitations travels without spreading at the speed of *Bogoliubov (zero) sound* $c = \sqrt{\mu/m}$. At short wavelengths ($\lambda_{ex} \ll \xi$) the excitation energy is approximately $\epsilon_k = \hbar^2 k^2 / 2m + \mu$, i.e. the excitations are free-particle-like with a mean-field energy offset of μ . In an inhomogeneous trapping potential, this mean-field offset implies that the condensate repels the thermal cloud. Collisionless excitations have been described at finite temperature as well [37]. The distinction between Bogoliubov-sound phonons and free-particle excitation remains, while the condensate density $n_0(T)$ varies with temperature.

7.2.2 Collisionless excitations in an inhomogeneous, trapped Bose gas

The nature of collective excitations in an inhomogeneous, trapped Bose gas is influenced by the introduction of a new length scale: the length of the condensate $x_{i,c,0}$. This divides the description of condensate excitation into three regimes:

- For excitations of wavelengths smaller than *all* dimensions of the condensate, $\lambda_{ex} \ll x_{i,c,0}$, the condensate can be treated as locally homogeneous, and the distinction between phonons and free-particles is as before. Indeed, it has been shown that finite-temperature thermodynamic properties such as condensate fractions and density profiles are well-described by a semi-classical approach using the Bogoliubov spectrum to describe localized excitations [13, 179]. Excitations at these wavelengths have not been studied [*since the writing of these proceedings, such excitations have indeed been studied by Bragg scattering. See Chapter 8*].
- For longer wavelengths which approach the size of the condensate ($\lambda_{ex} \simeq x_{i,c,0}$), the excitation spectrum becomes discretized, i.e. the collective modes of the system become standing sound waves at specific frequencies. It is interesting to note that in the Thomas-Fermi limit, both the speed of Bogoliubov sound and the length of the condensate scale as $(an_0)^{1/2}$. Thus, the frequency of the collective excitation $\omega \propto c/x_{i,c,0}$ is independent of the speed of sound. Collective excitations in this regime have been studied over a wide range of temperatures, as we describe below.
- For Bose condensates in anisotropic potentials there is an intermediate regime in which the wavelength of the excitation is larger than the size of the condensate in one (the axial) or two dimensions, but smaller than the size of the condensate in the other directions. In this case, the axial discretization of the collective modes is not apparent, and thus the pulses propagate as sound waves. The connection between this phonon picture and the aforementioned discrete spectrum was laid out by Stringari [219].

7.2.3 Experiments on collective excitations near $T = 0$

Coming from the spectroscopy tradition of atomic physics, it was natural that researchers focused early on the discrete excitation spectrum of a condensate. First, low-lying excitations were studied at the limit of zero temperature. Researchers at JILA studied two shape oscillations of condensates confined in a TOP trap [166]. The first was a cylindrically symmetric $m = 0$ quadrupole mode wherein the axial (z -axis) and radial lengths of the condensate oscillate out of phase (fig. 7-1a). Here m denotes the angular momentum of the excitation about the z -axis. The second was the $m = 2$ quadrupole mode. For this mode, the cylindrical symmetry was broken, and the lengths of the condensate in the two radial directions oscillated out of phase (fig. 7-1c). The condensates in these experiments were

in a regime intermediate to the ideal-gas and Thomas-Fermi limits. Therefore, these low-lying oscillations were studied between the free-particle and the Bogoliubov-sound limits discussed above. The measurements agreed with the predictions of mean-field theory [220].

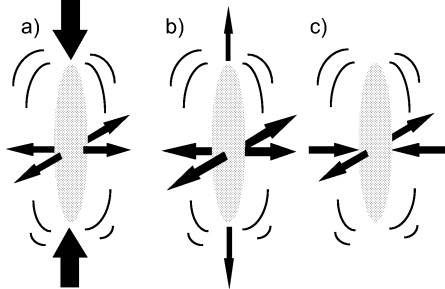


Figure 7-1: Shape of low-lying collective excitations: a) slow $m = 0$ quadrupolar oscillation (JILA, MIT), b) fast $m = 0$ radial oscillation (MIT), c) $|m| = 2$ oscillation (JILA).

We simultaneously studied oscillations near zero temperature of cigar-shaped condensates in a dc cloverleaf trap [4]. Collective modes were excited by sinusoidally varying the currents in the trapping coils. Since this excitation scheme preserved the axial symmetry of the trap, we only expected to excite $m = 0$ modes. Fortunately, imperfections in the trapping coils also allowed us to excite center-of-mass oscillations of the condensate in the trap, providing for accurate measurements of the trap frequencies. Again, two shape oscillations were excited. The lower frequency mode was similar to the $m = 0$ quadrupolar modes observed at JILA, with out-of-phase oscillations along the axial and radial directions. The higher frequency mode was primarily a radial breathing mode (fig. 7-1b). After locating the modes by a non-selective “step” excitation, we used a five-cycle sinusoidal modulation of the trapping coils to resonantly excite the shape oscillations. The subsequent free oscillations were clearly visible as periodic modulations of the aspect ratio in time-of-flight (fig. 7-2) and in phase-contrast (fig. 7-3) images as observed later [12].

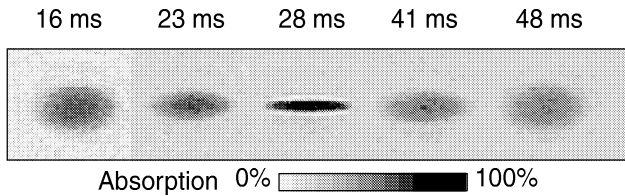


Figure 7-2: $m = 0$ quadrupolar condensate oscillations viewed in time-of-flight absorption imaging. Oscillations in the aspect ratio of the expanding condensate are clearly visible. The horizontal width of each cloud is 1.2 mm. Figure taken from ref. [4].

Our experiments were performed with condensates which were well in the Thomas-Fermi limit. The oscillations we observed were considered by Stringari, who provided the first analytical expression for their frequency and shape [221]. The agreement between the

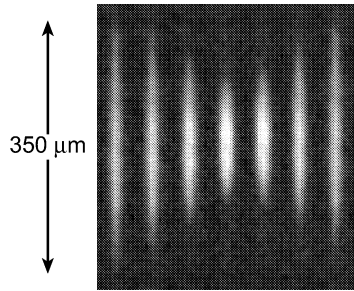


Figure 7-3: $m = 0$ quadrupolar condensate oscillations viewed *in-situ*. Repeated phase-contrast images, taken at 5 ms intervals, show large-amplitude oscillations of a low-temperature Bose-Einstein condensate. Figure taken from ref. [12].

predicted frequencies and the experimental results was quite good. The fast oscillation at $\nu = 2.04(6) \cdot \nu_r$ agreed with the prediction of $2 \cdot \nu_r$. For the slow oscillation, we measured a frequency $\nu = 1.556(14) \cdot \nu_z$ compared with the prediction of $1.580 \cdot \nu_z$. More recently, we improved our measurement to obtain a frequency of $1.569(4) \cdot \nu_z$ at the limit of low temperature (ν_r and ν_z are the radial and axial frequencies, resp.) [12]. This close agreement constitutes a critical quantitative test of the mean-field description of excited states of a Bose condensate.

7.2.4 Measurements of the speed of Bogoliubov sound

The experiments described above studied the low-lying discrete oscillation modes of a trapped condensate. In order to connect more closely with the continuous excitation spectrum of homogeneous system, we also studied density modulations at wavelengths of 20 – 30 μm that were smaller than the length of the condensate [7, 8]. For this, localized density perturbations were created using an off-resonant blue-detuned laser beam focused to the middle of the trap. Positive perturbations were created by suddenly switching on the laser beam after the condensate had formed. The repulsive optical dipole force expelled atoms from the center of the condensate, creating two density peaks which propagated symmetrically outward. Alternatively, we formed a condensate in the presence of the laser light and then switched the laser off. This created localized depletions of density which also propagated outward.

Fig. 7-4 shows the propagation of density perturbations observed by sequential phase-contrast imaging of a single trapped cloud. We observed one-dimensional axial propagation of sound at a constant velocity near the center of the cloud, where the axial density varies slowly. The density dependence of the speed of sound was studied using adiabatically expanded or compressed condensates, yielding maximum condensate densities n_0 ranging from 1 to $8 \times 10^{14} \text{ cm}^{-3}$ (fig. 7-5). The data were compared with the prediction of Bogoliubov theory, $c = (4\pi\hbar^2 a n / m^2)^{1/2}$, where the variation of the condensate density across the radius

of the cloud is accounted for by using $n = n_0/2$ [219, 222, 223]. The agreement between the data and this theory was good except at low density where the assumption that the sound pulse is longer than the radial extent of the condensate began to break down.

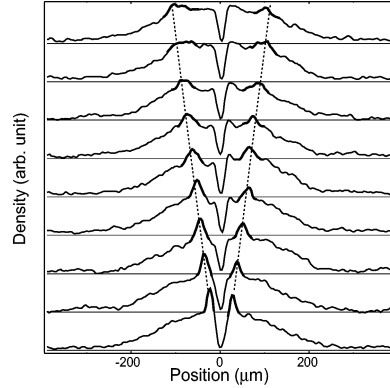


Figure 7-4: Observation of sound propagation in a Bose condensate. A non-destructive phase-contrast image was taken every 1.3 ms. Vertical profiles of the condensate density (early images on bottom) show two “blips” traveling out symmetrically from the center of the cloud. Figure taken from ref. [7].

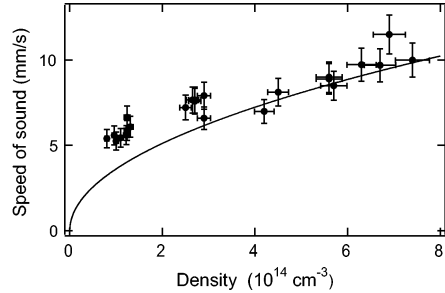


Figure 7-5: Speed of sound versus condensate peak density. The solid line is the theoretical prediction with no adjustable parameter. The error bars indicate only the statistical error. Figure taken from ref. [8], the erratum to the original experiment.

It has been discussed that our scheme for producing propagating density depletions (cutting a condensate and then removing the “knife”) should produce propagating dark solitons [224–226]. Such solitons, familiar from other applications of non-linear propagation equations, are predicted to be stable in one-dimensional Bose-Einstein condensates (in relation to the Thomas-Fermi condition). The condensates in our experiment were not one-dimensional, and the size of a soliton would be about a healing length ($\sim 0.2 \mu\text{m}$). Thus, individual solitons are unlikely to be observed in our experiment. Still, it is possible that the observed propagating “dips” formed the envelope of many unresolved solitons.

7.2.5 Collective excitations at non-zero temperature

While the above experiments were done with samples close to zero temperature, the observed damping gave an indication of behavior at non-zero temperature. The next set of experiments at JILA [167] and MIT [12] explored the excitations of a Bose gas as the temperature of the gas was varied.

The effects of non-zero temperature were three-fold: (1) shape oscillations of the thermal cloud were introduced, (2) the frequencies of the collective modes were influenced by interactions between the condensate and thermal cloud, and (3) the oscillations were increasingly damped at higher temperatures.

Oscillations of the thermal cloud

At non-zero temperature, a significant fraction of the gas is not condensed. This thermal fraction can be clearly discerned in the bimodal density profiles observed in-situ and in time-of-flight. Thus, one can examine separately the response of both the thermal cloud and of the condensate to modulations of the trapping potential. Thus, in accordance with the two-fluid picture of partly condensed Bose gases, there are two “collective excitations” of the system for each type of shape oscillation: a condensate oscillation, and an oscillation of the thermal cloud. The frequencies of the two oscillations are generally different.

In the JILA experiment [167], the shape oscillation frequency of the thermal cloud was about twice the trapping frequency for both the $m = 0$ and $m = 2$ quadrupolar modes. The thermal clouds in this experiment were in the collisionless regime. The dynamics of a thermal cloud in this regime is not sound-like, but ballistic. An oscillatory response comes only from the reflection of the free particles at the trap boundaries. Such oscillations are persistent only for a harmonic trapping potential, in which free-particles of any velocity have the same oscillation period. In contrast, for a collisionless thermal cloud in a box, in which the oscillation period scales inversely with the velocity, any collective response would quickly dephase.

In the MIT experiment [12], the thermal cloud oscillated at a frequency which was not a multiple of the trapping frequency. This response is due to the onset of hydrodynamic behavior in the thermal cloud which is discussed further in sect. 7.2.6.

Frequency shifts of condensate oscillations

Another effect of finite temperature is a shift in the frequency of the condensate excitations. Such a frequency shift is expected due to the decrease of the condensate density as the temperature rises, shifting the excitations from phonons to free-particles. However, other effects were clearly evident. For example, at JILA, the frequency of the $m = 2$ quadrupolar mode was found to *decrease* at higher temperatures, rather than tending toward the higher frequency expected in the free-particle regime [167]. In the MIT experiment, the condensates

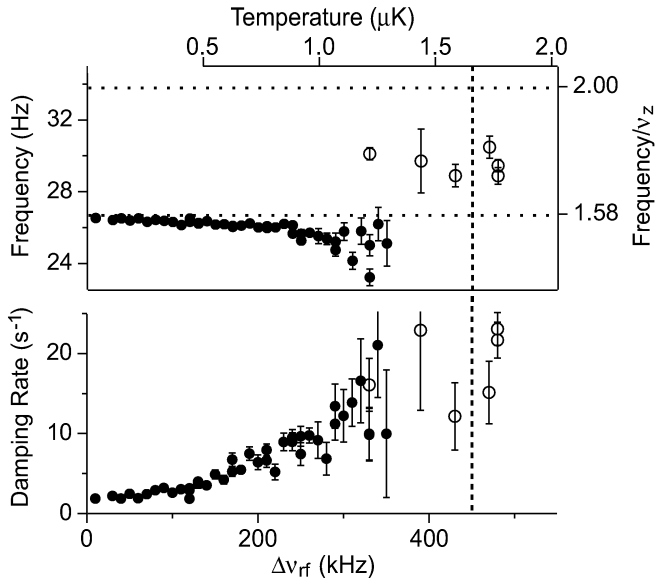


Figure 7-6: Temperature dependent frequency and damping rates of $m = 0$ quadrupolar collective oscillations of the thermal cloud (open circles) and condensate (closed circles). The free-particle limit of $2 \nu_z$ and the zero-temperature condensate oscillation limit of $1.580 \nu_z$ are indicated. The vertical dashed line marks the observed transition temperature. The temperature axis is based on observations of clouds at equilibrium for $T > 0.5 \mu\text{K}$.

that were studied were always in the Thomas-Fermi limit. Nevertheless, a distinct downward frequency shift of as much as 5% was observed (fig. 7-6) [12].

We also studied the effects of non-zero temperature on the propagation of Bogoliubov sound [7]. When we varied the condensate density, the speed of Bogoliubov sound scaled as $\sqrt{n_0(T)}$ where n_0 is the temperature dependent condensate density. This agrees with the expected behavior from finite temperature theories for homogeneous gases [37, 227]. Perhaps due to a lack of precision, we could not detect the $\sim 5\%$ shift seen in later experiments [12].

The behavior seen in these experiments is not yet fully understood, and constitutes a major challenge to the theories developed to describe non-zero temperature behavior of Bose gases (see discussion in several chapters of this book [*the Varenna proceedings*]). A variety of explanations have been proposed:

- The simplest extension of the Bogoliubov theory to finite temperatures uses an approximation introduced by Popov which neglects the correlations and motion of the thermal cloud [197]. In this approach, the condensate oscillates in an effective potential which is the sum of the trapping potential and the mean-field potential due to the thermal cloud (recall, the condensate repels and is repelled by the thermal cloud). Applications of this formalism to the experiments at JILA [198, 199] have failed to explain the results adequately.

- In response to the failure of the Popov approach, a finite-temperature Bogoliubov theory has been considered which goes beyond the Popov approximation by accounts for the influence of the condensate on collisions between particles in the thermal cloud, giving rise to an “anomalous density” term [228] (see also chapter by K. Burnett). This approach has had limited success in explaining the results of the JILA experiment: it explains the observed downward frequency trend of the $m = 2$ oscillation, but not the upward trend exhibited by the $m = 0$ oscillation.
- Finally, in recent work, attempts have been made to include the motion of the thermal cloud and understand its influence on the observed condensate excitations [229, 230]. Preliminary application of these ideas to the JILA experiment have been promising, while their application to the MIT data has not been done.

Damping of condensate oscillations

Early experiments on collective excitations had already noted the presence of damping, in spite of attempts to study oscillations at the limit of zero temperature. In the variable-temperature experiments at JILA and MIT, the damping rate was found to increase dramatically with temperature, by as much as ten-fold near the BEC phase transition temperature. The damping rates were found to vary even at temperatures where no thermal cloud was discernible by imaging. In this sense, damping rates may become sensitive “thermometers” of condensates at extremely low temperatures.

The dependence of the damping rate on temperature is another way in which the presence of the thermal cloud influences the motion of the condensate. The apparent mechanism for this damping is Landau damping, in which a quasi-particle disappears in a collision with a thermal excitation, promoting it to higher energy [231–234]. Recent treatments based on Landau damping have been quite successful in explaining the damping which was observed experimentally [234]. These treatments were discussed at Varenna by P. Fedichev.

Landau damping depends on the presence of thermal excitations, and thus is absent at zero-temperature. Nevertheless, collective excitations at zero-temperature can decay away. One mechanism, Beliaev damping, corresponds to the decay of a high-energy collective excitation into two lower energy ones [*i.e. an elastic collision with an atom in the condensate*]. For trapped Bose condensates and low-lying modes, this decay mechanism is not available since there are no modes into which to decay [232]. Collective excitations are also subject to zero temperature dephasing due to the atom-number uncertainty in the condensate and to amplitude dependence of the mode. Both can lead to an apparent damping [235–237]. Further, it has been shown that for higher amplitude oscillations, the non-linear mixing between modes can lead to ergodic behavior which results in an irreversible damping and an effective heating of the cloud [238]. This provides incentive for future experiments to continue studying collective excitations closer to the zero-temperature limit, perhaps using more controlled evaporative cooling (such as provided in optical traps) to get there.

7.2.6 First and second sound in a Bose gas

So far, we have discussed excitations of a Bose condensed gas in the collisionless regime, where the wavelength of the excitation is much smaller than the mean-free path $\lambda_{ex} \ll l_{\text{mfp}}$. This regime applies at zero temperature and at low densities of the thermal cloud. At higher densities of the normal component, when $\lambda_{ex} \gg l_{\text{mfp}}$, collective excitations become hydrodynamic in nature, and one expects two phonon-like excitations which are the in-phase and out-of-phase oscillations of two hydrodynamic fluids (the normal fraction and the superfluid). The presence of two hydrodynamic modes is similar to the case of bulk superfluid ^4He , where they are known as *first* and *second sound*. Superfluid ^4He has a small coefficient of thermal expansion. Thus the two eigenmodes decouple into density modulations (first sound) and temperature modulations (second sound), with both fluids participating equally in both modes. In contrast, a gas has a large coefficient of thermal expansion. This results in the oscillations of each fluid being nearly uncoupled. The in-phase oscillation, which is analogous to first sound, involves mainly the thermal cloud. The out-of-phase oscillation, which is analogous to second sound, is confined mainly to the condensate [37, 218, 239, 240]. Let us note another difference: the observation of second sound was dramatic evidence for the presence of two fluids in superfluid ^4He , whereas in trapped Bose gases, the visible separation between the normal and the superfluid components directly confirms the two-fluid approach.

In the finite-temperature experiment at MIT, the hydrodynamic regime was approached for the first time [12]. The onset of hydrodynamic behavior was indicated by the oscillations of the thermal cloud. In this experiment, the thermal cloud oscillated at a frequency of about $1.75 \nu_z$ with a damping rate of about 20 s^{-1} both above and below the BEC transition temperature (fig. 7-6). The observed frequency ν is between the predicted collisionless limit of $\nu = 2 \cdot \nu_z$ and the hydrodynamic limit of $\nu = 1.55 \cdot \nu_z$ [241]. These measurements indicate that the thermal cloud was in a density regime intermediate to the two limits. In this intermediate regime, the complex angular frequency of the oscillation ω (the imaginary part of which gives the damping rate) is described by the interpolation [242, 243]

$$\omega^2 = \omega_C^2 + \frac{\omega_H^2 - \omega_C^2}{1 - i|\omega\tau|} \quad (7.11)$$

where ω_C and ω_H are the angular frequencies of the excitation in the collisionless and hydrodynamic limits, respectively, and τ is the rate of collisions with thermally excited quasi-particles. The locus of points in the $\Gamma - \nu$ plane described by the interpolation (7.11) is shown in fig. 7-7 along with our measurement above the BEC phase transition.

One can also characterize the regime of our experiment by considering the length scales λ_{ex} and l_{mfp} . One can estimate the collisional mean-free path as $l_{\text{mfp}} \simeq (n_T \sigma)^{-1} = 96 \mu\text{m} \times (T/\mu\text{K})^{-3/2}$ using the peak density of the thermal cloud $n_T = 2.612 (mk_B T / 2\pi\hbar^2)^{3/2}$, and a collisional cross section $\sigma = 8\pi a^2$ with the scattering length $a = 2.75 \text{ nm}$ [189]. Around the

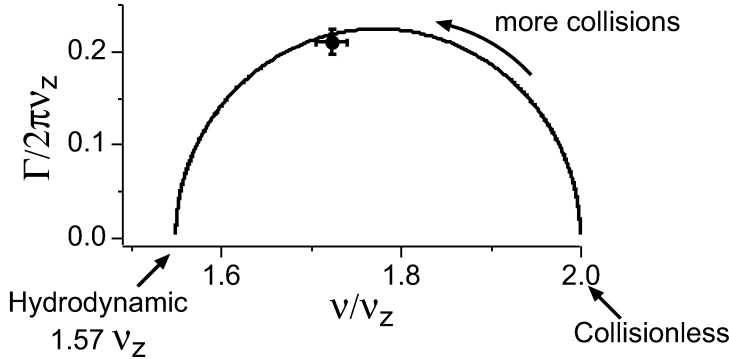


Figure 7-7: Frequency ν and damping rate Γ of excitations of the thermal cloud between the collisionless and hydrodynamic limits. Line shows interpolation according to eq. (7.11). The experimental data point shows that thermal clouds above the BEC transition temperature were probed in an intermediate regime.

transition temperature, we find the rms axial length of the thermal cloud to be $z_{th,0} \simeq 8 l_{\text{mfp}}$. This comparison of length scales, the observed frequency shift away from $2 \cdot \nu_z$, and the high damping rate all demonstrate that the collective behavior of the thermal cloud is strongly affected by collisions. Thus, the oscillations which we observe indicate the onset of hydrodynamic excitations, i.e. first sound. The hydrodynamic limit, characterized by low damping, would only be reached for even larger clouds.

Similarly, a comparison between l_{mfp} and the axial length of the condensate z_c at high temperatures ($z_c \simeq 4 l_{\text{mfp}}$) indicates that hydrodynamic effects may be influencing the condensate oscillations as well. Thus, these oscillations may constitute second sound in a Bose gas. There are few theoretical predictions regarding the transition from zero to second sound with which to compare our data. In future experiments with larger condensates, the signature of this cross-over may appear in the damping rate of the oscillations, which should decrease again at high-temperatures as one reaches the hydrodynamic limit. Indeed, a recent analysis by Fedichev *et al.* (see chapter in [*the Varenna proceedings*]) found the damping rates we observed at high temperature to be slightly lower than those expected based on a collisionless model of Landau damping, a tentative sign of the onset of hydrodynamic effects.

Another collective excitation related to second sound is the anti-symmetric dipole oscillation, in which the centers-of-mass of the thermal cloud and the condensate oscillate out-of-phase. This mode is analogous to second sound in liquid helium, where the superfluid and the normal fluid undergo out-of-phase oscillations of equal magnitude [222]. We excited this mode using an off-resonant laser beam which was directed at the edge of the cloud, where it overlapped only with the thermal cloud. By tilting a motorized mirror, the laser beam was steered toward and then away from the center of the cloud, thereby pushing the thermal cloud in the axial direction while not directly affecting the condensate. The

light was then turned off, and the cloud allowed to freely oscillate.

Over time, we observed the initially small oscillations of the condensate center-of-mass grow to an asymptotic oscillation with the center-of-mass of the entire cloud. In the frame of this overall center-of-mass motion, the cloud underwent the anti-symmetric dipole oscillation, as we sought. The downward frequency shift of this mode away from the trapping frequency (about 5%) and its eventual dissipation are further signs of the interactions between the condensate and the thermal cloud [12]. The description of these interactions requires a time-dependent treatment of the thermal cloud in contrast to the stationary treatment of most theoretical approaches.

7.2.7 Challenges ahead

The work over the last three years has elucidated the basic aspects of sound in a Bose condensed cloud (Table 7.2). Experiments have studied discrete standing-wave modes at zero and non-zero temperature, damping rates and frequency shifts, the propagation of sound pulses, and the onset of hydrodynamic behavior. These experimental advances were accompanied by enormous progress in our theoretical understanding. A comprehensive picture of collective excitations and sound propagation at zero temperature has been assembled. At non-zero temperatures, progress has been made in understanding the coupled motion of the condensate and the thermal cloud. Approaches to damping have been honed to the context of trapped Bose condensates with great success, and the hydrodynamic behavior of trapped gases above and below the BEC transition has been explored.

These advances point to many possibilities for further study. For example, the demonstrated ability to measure collective excitation frequencies at the 10^{-3} level enables the search for small, but conceptually important effects, such as the small (about a percent) frequency shift due to quantum depletion [244]. Only a few discretized collective modes have been studied closely, but the diverse ways which have been demonstrated to create excitations can be readily applied to study others. Indeed, we created one such mode inadvertently: in the process of exciting radial center-of-mass oscillations to measure trap frequencies, we came upon a wild high-lying condensate excitation with as many as eight nodes along the trap axis (fig. 7-8). Studying these other modes may reveal the connection between discrete modes and continuous sound propagation [219] or the possible chaotic propagation of localized excitations [245]. Advancements in the preparation of ever colder samples may make accessible the study of dephasing and damping near zero temperature, while the creation of ever larger and denser condensates opens the door to studying the true hydrodynamic limit.

7.2.8 Other dynamic properties

The previous discussion on the nature of sound in a Bose condensate focused on the linear response to external perturbations. The study of higher amplitude motion is another strong

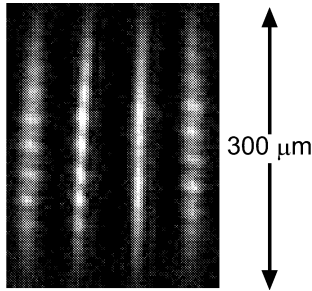


Figure 7-8: The shape of things to come. Four in-situ images at 1.3 ms intervals show a high-lying (eight-node) axial excitation of a cigar shaped condensate. The oscillation frequency is about 250 Hz in a trap with axial frequency of about 17 Hz.

test of the Gross-Pitaevskii equation. In this section, we present these studies as well as summarizing other dynamical processes which include the formation and decay of the condensate.

7.2.9 Free expansion and large amplitude oscillations of a Bose-Einstein condensate

The evolution of a Bose condensate during free expansion from a harmonic trap is described by the Gross-Pitaevskii equation (sect. 4.2.2). Careful study of this expansion is necessary, not only as a test of mean-field theory, but also to confirm the use of time-of-flight imaging to probe properties of trapped condensates. Early studies of this expansion at MIT [1, 2] and JILA [128, 177] agreed well with theoretical predictions [174, 175, 190, 246].

We recently probed this evolution in more detail, using both phase-contrast (short time-of-flight) and absorption (long time-of-flight) imaging [168]. The measured aspect ratios are presented in fig. 7-9. Two steps of the expansion are clearly shown: the initial radial acceleration in the first milliseconds, and the subsequent pure radial expansion. The axial expansion and the evolution toward an asymptotic aspect ratio would only become apparent at later times of expansion. The axial and radial trapping frequencies were also determined, using in-situ imaging. The theoretical prediction of ref. [174], which depends only on the measured trap frequencies, describes the data excellently, confirming mean-field description of large-amplitude dynamics.

Other studies focused on large amplitude motion of trapped condensates. To ensure that studies of collective excitations were done close enough to the limit of zero amplitude, where the excitation frequency reflects the quasi-particle spectrum, these frequencies were studied as a function of amplitude [4, 12, 166, 167]. For the low-lying $m = 0$ quadrupolar condensate oscillation at low temperature, we observed a 1 Hz upward shift of the excitation frequency from its low amplitude limit as the relative amplitude of the oscillation rose to 50%, in agreement with the theoretical analysis of Dalfonso *et al.* [176].

Table 7.2: Studies of sound in gaseous Bose-Einstein condensates. A comprehensive picture of the nature of sound has been assembled, but many phenomena remain to be explored.

≤ 1998		
Experiment	Bogoliubov (zero) sound	$T = 0$ discrete modes non-zero temperature damping speed of sound
	First and second sound	discrete modes damping
Theory	Landau damping zero, first, second sound discrete modes \leftrightarrow sound hydrodynamic theory	
Experiments to come?		
	$T = 0$ damping Higher lying modes Effects of quantum depletion Nonlinear effects Hydrodynamics	Beliaev damping dephasing, collapse, revival dynamic structure factor $S(\mathbf{q}, \omega)$ solitons, chaos, shock waves mode coupling, frequency doubling

Recently, the large amplitude dynamics of a two-component condensate were studied at JILA [155]. The observed sloshing and damping of the two-component system were treated theoretically as a manifestation of zero-temperature damping [238].

7.2.10 The search for persistent currents

Collective excitations, even those that possess angular momentum, describe single-particle excitations which can connect to the ground state by single-particle decays. Vortices, on the other hand, describe collective motion involving the entire condensate. The possible persistence of these rotating currents relies on their metastability against single-particle decay — although the energy of the condensate is lowered by placing it entirely in the non-rotating ground state, this many-particle relaxation is highly unlikely. As the discussions at the Varenna summer school showed (see chapter by A. Fetter), the search for quantized persistent currents is a major aim of future BEC research.

Efforts in our laboratory have laid some of the ground work for this search. While the stability of vortices in gaseous Bose condensates trapped in a singly-connected harmonic trap is in doubt [247], rotating currents should persist in a multiply-connected trap geometry [248, 249]. Thus, we created a “doughnut”-shaped container for Bose condensates

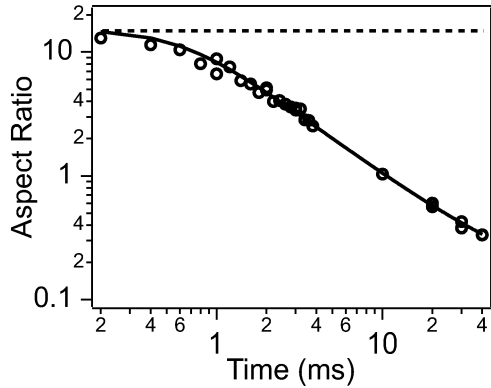


Figure 7-9: Aspect ratio (axial to radial widths) of expanding Bose condensates. Data collected for times less than 10 ms were taken in phase-contrast imaging, and for later times with absorption imaging. The dashed line indicates the ratio of trapping frequencies of 248(1) Hz radially and 16.23(3) Hz axially. The solid line gives the prediction of ref. [174].

by first forming a spherical harmonic magnetic trap by adiabatic decompression, and then shining a focused blue-detuned laser through the trap which repelled atoms from the trap center. Then, we displaced the center of the magnetic trap using magnetic bias and gradient fields, and rotated it about the optical plug. As shown in fig. 7-10, this set the condensate in rotational motion about the optical plug imparting angular momentum to a condensate while maintaining the “hole” inside it. We observed rotation after stopping the drive, and hoped that the system would relax into a state with a persistent current. Nevertheless, when we probed by looking for a depletion in the center of the ballistically expanding condensate, no evidence for persistent currents was found. However, we cannot rule out their presence in the condensate due to a low signal-to-noise ratio in our detection scheme [165].

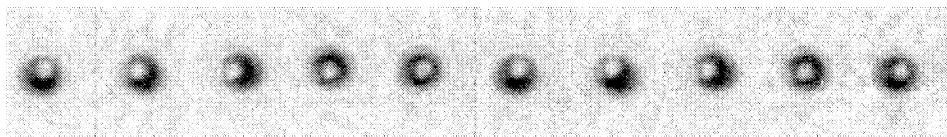


Figure 7-10: Phase-contrast images of a condensate being rotated at 1 Hz in a “doughnut” trap. The condensate (about 100 μm in diameter) remains pierced by an off-resonant laser beam during its motion. Although angular momentum was clearly imparted to the cloud, we could not detect persistent currents. Figure taken from ref. [165].

7.2.11 Collapse of a negative scattering length Bose condensate

Condensates with negative scattering length have attractive interactions, and therefore show the new dynamic property of collapse when they exceed a certain size. Formally, the

collapse can be regarded as an unstable collective excitation having imaginary frequency. Manifestations of the collapse are the finite maximum number of atoms observed in lithium condensates [130] and fluctuations in the number of condensed atoms [250].

7.2.12 Formation and decay of the condensate

Experiments have probed both the irreversible [9] and the reversible [14] formation of the condensate. An irreversible formation was observed after suddenly quenching a cold atom cloud below the BEC transition temperature in a magnetic trap. The intrinsic dynamics of condensate growth were in agreement with a model assuming bosonic stimulation (sect. 6.1). Studies of the reversible formation of a condensate in a hybrid optical and magnetic trapping potential are discussed in sect. 6.2.

Refs. [10, 251, 252] studied the decay of the condensate and explained it by three body recombination, which leads to molecule formation and loss of the atoms from the trap. The difference in the rate constant for losses from a Bose condensate and from a thermal cloud observed by Burt *et al.* [251] reveals higher-order coherence of the condensate. For typical experiments on sodium and rubidium, decay from dipolar relaxation (two-body collisions) is negligible, while it is the dominant decay mechanism for hydrogen [27]. Another important finding was the *non-observation* of fast decays from a mixture of two hyperfine states of ^{87}Rb in a magnetic trap [253], which reveals a near-degeneracy of ground-state scattering lengths for that system [254–256]. A dramatic increase of condensate decay was found in sodium near Feshbach resonances [16].

7.3 One-dimensional sound propagation

Finally, let me describe some unpublished results regarding our measurement of the speed of one-dimensional sound propagation in a Bose-Einstein condensate. The experiment is described in Refs. [7, 8]. Briefly, cigar-shaped Bose condensates were created in a harmonic magnetic trap with peak densities which were varied between 1 and $8 \times 10^{14} \text{ cm}^{-3}$ by changing the radial trap frequency. A localized density perturbation was created using a blue-detuned laser beam impinging upon the condensate from a radial direction of the trap and focused at the center of the condensate. The beam was focused tightly in the axial direction and loosely in the radial direction, thereby creating a radially uniform potential wall about $20 \mu\text{m}$ in width along the long axis of the trapped condensate. Density perturbations were created either by switching on the laser suddenly and creating density maxima at the edges of the light sheet, or else by keeping the laser on during the formation of the condensate and then suddenly switching it off, creating a density deficit at the condensate center. A rapid sequence of phase-contrast images was then used to image the subsequent dynamics.

Near the center of the condensate, the density perturbations propagated at a uniform speed along the condensates axis toward the ends of the condensate. The speed of sound propagation was easily determined by following the location of the density “blips” or “dips” as a function of time, as recorded in a single sequence of phase-contrast images. We determined the chemical potential by measuring the condensate length and determining the magnetic trap frequencies (Sec. 4). From this, the condensate density was determined using the scattering length of 2.75 nm [189].

These measurements are shown in Fig. 7-5 which is reproduced from an erratum to our original paper in which data were extracted from phase-contrast images with a better image processing routine (Sec. A). As expected, the speed of sound increases with increasing density. The data are compared with the mean-field prediction for one-dimensional axial sound propagation in a harmonically confined Bose-Einstein condensate in the Thomas-Fermi limit, as discussed below. The agreement is quite good except at low densities where the speed of sound is higher than predicted. This may be due to the fact that the low-density condensates were obtained by weakening the radial trapping frequency and therefore increasing the radial width of the condensates. As a result, the width of the propagating density perturbation (about $20 \mu\text{m}$) was no longer greater than the condensate radius, as assumed by the one-dimensional treatment upon which the prediction is based, and thus the sound speed should increase to its three-dimensional bulk value.

We also varied the amplitude (and sign) of the density perturbation by varying the intensity of the perturbing laser beam, and found no evidence for an amplitude dependence of the speed of sound (Fig. 7-11). Such a dependence has been predicted and discussed by Kavoulakis and Pethick [223], but was perhaps not detected in our data due to a lack of sensitivity.

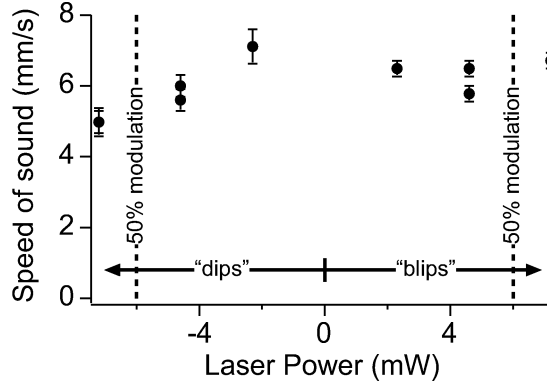


Figure 7-11: The speed of propagating blips and dips. The measured speed of sound shows no dependence on the amplitude and sign of the propagating density perturbation. The amplitude was controlled by adjusting the power of the perturbing laser beam between 0 and 8 mW. At a laser power of 6 mW, the optical potential fully separated the condensate into two pieces, thus generating a 50% density modulation propagating in either direction from the condensate center. Positive (negative) laser powers indicate the power used to generate positive (negative) density perturbations, i.e. blips (dips).

The development of rapidly sequenced *in situ* phase-contrast imaging was crucial for observing and analyzing the propagation of sound pulses. In contrast, time-of-flight absorption pictures, which were successfully used for studying collective shape oscillations, gave a complex picture of the propagation which was difficult to interpret. Fig. 7-12 shows a series of time-of-flight images which were taken after creating a condensate in an optically split potential, switching off the laser beam, allowing the negative density perturbations to propagate a variable period of time, and then releasing the cloud from the trap and allowing for a 40 ms free expansion. One can see fine striations about 15 μm in width at the center of the images as well as a coarser structure of straight and curved striations about 100 μm in width. The fine structure is probably due to interference between the two condensates [6], while the coarse structure reflects a coordinate and momentum space representation of the sound propagation.

7.4 Variational approach to reducing the Gross–Pitaevskii equation to an effective one-dimensional equation

The speed of Bogoliubov sound in a uniform condensate of density n_0 is

$$c = \sqrt{\frac{gn_0}{m}} \quad (7.12)$$

where $g = 4\pi\hbar^2a/m$, a is the scattering length and m the atomic mass. Yet, the density of the trapped condensates which we studied was inhomogeneous. In particular, the density

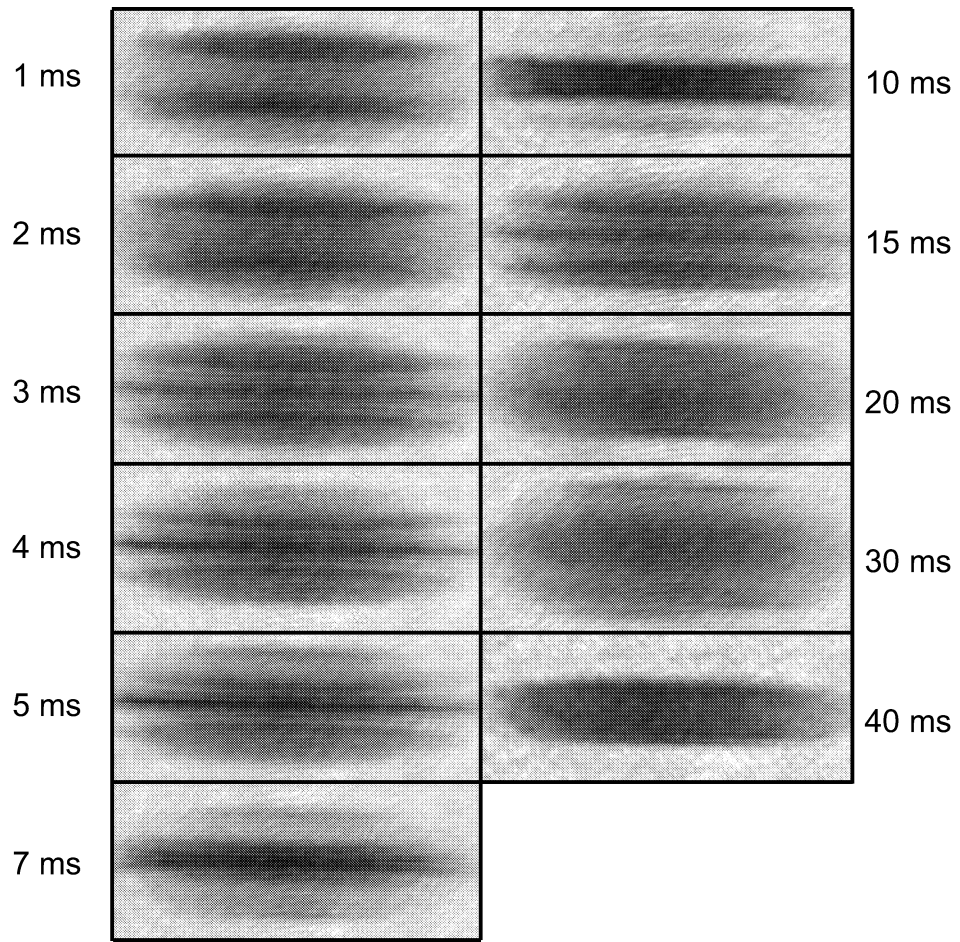


Figure 7-12: Time-of-flight images taken after variable durations of propagation of negative density perturbations in a condensate (indicated for each image). Fine striations ($\approx 15 \mu\text{m}$ wide) are probably due to interference between the two halves of the condensate, while coarse striations ($\approx 100 \mu\text{m}$ wide) represent the sound propagation.

perturbations produced by our methods had dimensions which were generally greater than the radial extent of the condensate. Thus, one expects that radial boundary conditions should modify the behaviour of sound propagation. On the other hand, the axial length of the condensate was much larger than the size of the density perturbation. Thus the sound pulse should propagate along the condensate axis freely until it approaches the end of the condensate.

To compare our data with the predictions of mean-field theory, we therefore had to reduce the three-dimensional Gross–Pitaevskii equation to an effective one-dimensional equation describing axial sound propagation. We initially employed a variational approach which indicated that the effective speed of sound is given by Eq. 7.12 where n_0 is indeed the condensate density at the radial center (i.e. the peak density). However, in later treatments [223, 257, 258], it was found that the radial density inhomogeneity causes the one-dimensional sound speed to be reduced by a factor $1/\sqrt{2}$ by using the radially-averaged density rather than the peak density in determining c . These treatments include an illuminating diversity of approaches in which the Gross–Pitaevskii equation is cast into the form of a hydrodynamic equation and the Bose condensed gas is treated in the manner of fluid mechanics.

In light of these findings, we re-examined our previous method and found that our prediction was based on an incorrect use of the energy functional. A correct variational method [8] which is in agreement with the results obtained by others is presented in detail below. Such a treatment should be generally useful for considering other dynamic processes in narrow Bose–Einstein condensates, such as the metastability of and tunneling across spin domains in optically trapped spinor Bose–Einstein condensates, and can be easily extended to include higher-order radial excitations and structure.

Time-dependent quantum-mechanics can be derived by considering the quantum Lagrangian

$$L = \int d^3\vec{r} \left[\frac{i\hbar}{2} \left(\psi^* \frac{\partial\psi}{\partial t} - \psi \frac{\partial\psi^*}{\partial t} \right) - E(\psi^*, \psi) \right] \quad (7.13)$$

where the variational expression

$$\frac{\delta E(\psi^*, \psi)}{\delta \psi^*} = \mathcal{H}\psi \quad (7.14)$$

yields the system Hamiltonian \mathcal{H} . The Schrödinger equation is then obtained by minimizing the action $S = \int dt L$ with respect to variations in ψ^* . This method allows for the use of trial wavefunctions to obtain approximations to dynamical behaviour.

We consider the energy functional

$$E(\psi^*, \psi) = \frac{\hbar^2}{2m} \nabla \psi^* \cdot \nabla \psi + U(x, y) + \frac{g}{2} |\psi|^4 \quad (7.15)$$

which describes an interacting Bose condensed gas held in a cylindrical confining potential

which varies in the radial plane as $U(x, y)$. We make the following ansatz:

$$\psi = \phi_2 \phi_z \quad (7.16)$$

$$\phi_2 = \left(1 - \frac{U(x, y)}{g|\phi_z|^2} \right)^{1/2} \quad (7.17)$$

$$\phi_z = ae^{i(\phi - \mu t/\hbar)} \quad (7.18)$$

Here, ϕ_2 is the Thomas–Fermi solution to the two-dimensional Gross–Pitaevskii equation

$$\mathcal{H}_2 \phi_2 = \left(\frac{p_x^2 + p_y^2}{2m} + U(x, y) + g|\phi_z|^2 |\phi_2|^2 \right) \phi_2 = \mu(z) \phi_2 \quad (7.19)$$

where the radial kinetic energy is ignored.

Let us now calculate the Lagrangian and integrate out the radial coordinates. With

$$\psi^* \frac{\partial \psi}{\partial t} = a \phi_2 \left[\left(\frac{U(x, y)}{ga^2} \frac{1}{\phi_2} + \phi_2 \right) \frac{\partial a}{\partial t} + ia \phi_2 \left(\frac{\partial \phi}{\partial t} - \frac{\mu}{\hbar} \right) \right] \quad (7.20)$$

we have

$$\frac{i\hbar}{2} \left(\psi^* \frac{\partial \psi}{\partial t} - \psi \frac{\partial \psi^*}{\partial t} \right) = a^2 \phi_2^2 \left(\mu - \hbar \frac{\partial \phi}{\partial t} \right) \quad (7.21)$$

Integrating over radial coordinates gives, for $U(x, y) = 1/2 m\omega^2 r^2$ where $r^2 = x^2 + y^2$,

$$\int dx dy \frac{i\hbar}{2} \left(\psi^* \frac{\partial \psi}{\partial t} - \psi \frac{\partial \psi^*}{\partial t} \right) = \pi \frac{g}{m\omega^2} a^4 \left(\mu - \hbar \frac{\partial \phi}{\partial t} \right) \quad (7.22)$$

In the kinetic energy term, we neglect second order radial derivatives in accordance with the Thomas–Fermi condition and obtain

$$\nabla \psi^* \cdot \nabla \psi = \left(\frac{\partial \phi_2}{\partial z} \right)^2 |\phi_z|^2 + \phi_2 \frac{\partial \phi_2}{\partial z} \left(\phi_z \frac{\partial \phi_z^*}{\partial z} + \phi_z^* \frac{\partial \phi_z}{\partial z} \right) + \phi_2^2 \frac{\partial \phi_z}{\partial z} \frac{\partial \phi_z^*}{\partial z} \quad (7.23)$$

Consider the first term in the sum. We may write

$$\frac{\partial \phi_2}{\partial z} = -r \frac{\partial \phi_2}{\partial r} \frac{1}{a} \frac{\partial a}{\partial z} \quad (7.24)$$

After squaring and integrating the radial part we obtain

$$\int_0^R 2\pi r dr r^2 \left(\frac{\partial \phi_2}{\partial r} \right)^2 = 2\pi r^3 \phi_2 \frac{\partial \phi_2}{\partial r} \Big|_0^R - \int_0^R 2\pi dr \phi_2 \left(3r^2 \frac{\partial \phi_2}{\partial r} + r^3 \frac{\partial^2 \phi_2}{\partial r^2} \right) \quad (7.25)$$

where the boundary of the condensate is at $R = \sqrt{2g/m\omega^2}a$. Directly using the Thomas–Fermi solution here gives divergences because the discontinuity in the slope of ϕ_2 gives infinite contributions to the second-order radial derivatives. However, if one correctly smoothes the Thomas–Fermi solution at R and neglects again the second-order radial derivatives, one

obtains for the above just $2\pi R^2$. For the second term in the kinetic energy we integrate

$$\int 2\pi r dr \left(-r \frac{\partial \phi_2}{\partial r} \frac{\partial a}{\partial z} \frac{1}{a} \right) \phi_2 = \frac{\pi}{a} \frac{\partial a}{\partial z} \int r^2 dr \frac{\partial \phi_2^2}{\partial r} \quad (7.26)$$

$$= \frac{\pi}{a} \frac{\partial a}{\partial z} \frac{R^2}{2} \quad (7.27)$$

while for the third term, $\int 2\pi r dr \phi_2^2 = \pi R^2/2$. Finally, then, we obtain

$$\int dx dy \frac{\hbar^2}{2m} \nabla \psi^* \cdot \nabla \psi \simeq \frac{\hbar^2}{2m} \frac{\pi g}{m \omega^2} a^2 \left[7 \left(\frac{\partial a}{\partial z} \right)^2 + a^2 \left(\frac{\partial \phi}{\partial z} \right)^2 \right] \quad (7.28)$$

After adding the contributions of the other two terms in the energy functional (potential and interaction energies), we obtain for the action

$$S = \int dz dt \frac{\pi g}{m \omega^2} \left[n^2 \left(\mu - \hbar \frac{\partial \phi}{\partial t} \right) - \frac{\hbar^2}{2m} \left(\frac{7}{4} \left(\frac{\partial n}{\partial z} \right)^2 + n^2 \left(\frac{\partial \phi}{\partial z} \right)^2 \right) - \frac{2}{3} g n^3 \right] \quad (7.29)$$

where $n(z) = a^2$ is the density at the radial center of the condensate.

Minimizing the action with respect to variations of either n or ϕ , we obtain the coupled equations which describe the effective one-dimensional dynamical behavior:

$$2n \left(\mu - \hbar \frac{\partial \phi}{\partial t} \right) + \frac{\hbar^2}{2m} \left(\frac{7}{2} \frac{\partial^2 n}{\partial z^2} - 2n \left(\frac{\partial \phi}{\partial z} \right)^2 \right) - 2gn^2 = 0 \quad (7.30)$$

$$\hbar \frac{\partial n^2}{\partial t} + \frac{\hbar^2}{2m} 2 \frac{\partial}{\partial z} \left(n^2 \frac{\partial \phi}{\partial z} \right) = 0 \quad (7.31)$$

In the long wavelength limit, let us neglect the second derivative term in Eq. 7.30. Letting $n = n_0 + \delta n$ we have to zeroth order in δn

$$\mu = gn_0 \quad (7.32)$$

and to first order

$$(\mu - gn) - \hbar \frac{\partial \phi}{\partial t} - \frac{\hbar^2}{2m} \left(\frac{\partial \phi}{\partial z} \right)^2 = 0 \quad (7.33)$$

Taking the z -derivative of the latter equation and identifying the axial velocity $v_z = (\hbar/m) \times (\partial \phi / \partial z)$ gives

$$m \frac{\partial v_z}{\partial t} = \frac{\partial}{\partial z} \left(g \delta n + \frac{1}{2} m v_z^2 \right) \quad (7.34)$$

From Eq. 7.31, which is the continuity equation for the line density, we obtain

$$2 \frac{\partial \delta n}{\partial t} + n_0 \frac{\partial v_z}{\partial z} = 0 \quad (7.35)$$

Neglecting the v_z^2 term at long wavelengths, these last two equations are combined to give the equation for axial sound propagation in a Bose–Einstein condensate confined radially by a harmonic oscillator potential:

$$\frac{\partial^2 \delta n}{\partial t^2} - \frac{gn_0}{2m} \frac{\partial^2 \delta n}{\partial z^2} = 0 \quad (7.36)$$

This gives the speed of axial sound propagation as $c = \sqrt{gn_0/2m}$, which correctly accounts for the $1/\sqrt{2}$ reduction from the maximum sound speed.

Chapter 8

Probing and manipulating a Bose–Einstein condensate with optical Bragg scattering

In this chapter I present a comprehensive description of the use of Bragg scattering to measure the dynamical structure factor of a Bose–Einstein condensate. I discuss the results of two experiments:

- *J. Stenger, S. Inouye, A.P. Chikkatur, D.M. Stamper-Kurn, D.E. Pritchard, and W. Ketterle, “Bragg spectroscopy of a Bose-Einstein condensate,” Phys. Rev. Lett. **82**, 4569 (1999).*
- *D.M. Stamper-Kurn, A.P. Chikkatur, A. Görlitz, S. Inouye, S. Gupta, D.E. Pritchard and W. Ketterle, “Excitation of phonons in a Bose–Einstein condensate by light scattering,” Phys. Rev. Lett. **83**, 2876 (1999). Included in Appendix J.*

Optical probes have been the mainstay of experimental investigations of gaseous Bose–Einstein condensates. Near-resonant light has been used to image condensates *in situ* or in free flight, and off-resonant light has been used in a variety of applications to manipulate or trap condensates. Such techniques are based in different ways on the elementary process of light scattering. Recently, our group has begun studying the process of light scattering itself, and exploring a number of ways in which light scattering from Bose–Einstein condensates can illuminate their properties. This chapter describes two experiments in which we have studied stimulated light scattering from Bose–Einstein condensates [18, 21].

Let us consider first the interaction between a single atom and an incident beam of light. The initial state of the atom–light system is $|N_k, \dots 0_l \dots; i\rangle$ where N_k photons are in the incident beam with wavevector k , no photons are in other photon modes (such as mode l), and the atom is in state $|i\rangle$ which can be either a trapped or untrapped state. After

adiabatically eliminating the excited atomic state from a consideration of the light–atom interaction, the coupling between the atom and the light is described by the operator

$$\mathcal{H}' = C \sum_{k,l,m,n} \hat{c}_k^\dagger \hat{a}_l^\dagger \hat{c}_m \hat{a}_n \delta_{k+l-m-n} \quad (8.1)$$

Here \hat{c}_k (\hat{c}_k^\dagger) is the destruction (creation) operator for optical waves, and \hat{a}_k (\hat{a}_k^\dagger) is the destruction (creation) operator for atomic waves of wavevector k . The atomic waves are here written in the momentum basis, and the δ –function enforces momentum conservation. The strength of atomic resonances and the detuning of the light determines the strength of the coupling, summarized in the coefficient C .

Due to the coupling, light is scattered from the incident beam to wavevector $l = k - q$ with a cross–section proportional to

$$\frac{d\sigma}{d\Omega} \propto |C|^2 \left(\left| \langle N_k - 1, \dots, 1_l, \dots; i | \sum_m \hat{c}_l^\dagger \hat{a}_{m+q}^\dagger \hat{c}_k \hat{a}_m | N_k, \dots, 0_l, \dots; i \rangle \right|^2 + \sum_{j \neq i} \left| \langle N_k - 1, \dots, 1_l, \dots; j | \sum_m \hat{c}_l^\dagger \hat{a}_{m+q}^\dagger \hat{c}_k \hat{a}_m | N_k, \dots, 0_l, \dots; i \rangle \right|^2 \right) \quad (8.2)$$

Two contributions to the light scattering are separated in the above expression. The first part describes “coherent” light scattering, i.e. diffraction and refraction, in which the atom is left in its original state, and the scattered light has the same frequency as the incident light. The coupling shifts the phase of the elastically scattered light by an amount proportional to $\langle N_k - 1, \dots, 1_l, \dots; i | \mathcal{H}' | N_k, \dots, 0_l, \dots; i \rangle$. This phase shift provides the signal for dispersive imaging.

The second part of the scattering cross–section describes “incoherent” light scattering in which the state of the atom is changed. Incoherent, or inelastic light scattering is responsible for the signal in absorption imaging. Diffracted light from an object which is larger than the resolution of the imaging system is collected, while light scattered inelastically is not collected and is missing from the probe light in the image.

However, there is more information to be obtained about the object which scatters light inelastically than just the sum total of scattered photons. Since the atomic state changes as a result of the scattering, the inelastically scattered photon is generally shifted in frequency from the incident photon. Furthermore, since the recoil energy of the massive atom is much smaller than the incident photon energy, the outgoing angle of the scattered photon precisely determines the momentum $\hbar q$ which is imparted to the sample. Thus, a spectroscopic analysis of inelastically scattered photons at a given angle from the incident light beam determines the energy–resolved response of the atomic sample to a given momentum transfer (in the range 0 to $2\hbar k$).

Actually performing such an experiment with a Bose–Einstein condensate would be a

difficult task. One would hope to scatter light from a small fraction of the $\approx 10^7$ atoms, giving $10^4 - 10^5$ scattered photons over a 4π solid angle. Thus, only a handful of photons would be collected in a reasonably sized detector, and one would need to determine their frequency amidst a general background of incident and scattered light.

Instead, we have adopted a different approach. Rather than detecting spontaneous scattering from a single beam, we study light scattering as a stimulated process induced by two near-resonant laser beams which illuminate the atomic sample. The momentum and energy transfer to the atomic sample from a stimulated light scattering event is *pre-determined* by the angle and frequency difference between the incident beams, respectively, rather than *post-determined* by the position of a photo-detector and by a difficult frequency measurement. Furthermore, since the momentum transfer from a light scattering event can be much greater than the momentum spread of the sub-recoil atomic sample, and since the stimulated light scattering can be made to dominate over spontaneous scattering, the response of the system can be determined by the nearly background-free detection of recoiling atoms. The two-photon transition in which an atom changes its momentum and energy (center-of-mass quantum numbers) without changing its internal state is called Bragg scattering, and can be regarded as a Raman transition between different momentum states but identical internal states.

We have studied magnetically-trapped and freely-expanding Bose-Einstein condensates by the spectroscopic measurement of the Bragg scattering resonance. In this chapter, I describe two applications of Bragg spectroscopy to study excitations of a Bose-Einstein condensate in either the free-particle [18] (large momentum transfer) or the phonon [21] (small momentum transfer) regime. The discussion includes a comprehensive description of the dynamic structure factor of a Bose-Einstein condensate which leads to the interpretation of the measured Bragg scattering line shapes as an observation of the zero-point momentum distribution of trapped condensates, as a measurement of the energies of free-particle and phonon excitations, and as evidence for correlations in the many-body condensate wavefunction introduced by interatomic interactions.

8.1 Scattering atoms and matter waves

The scattering of neutral atoms in an atomic beam by an optical standing wave was studied by several groups in the early 1980's. Quantitative studies which focused on the effect of conservative optical potentials were performed by Pritchard and collaborators [259, 260]. In two different experiments, a collimated atomic beam of sodium was incident upon a standing light wave formed by retro-reflected laser beams which were either tightly or loosely focused. In the case of a tight focus, an atomic beam incident perpendicular to the standing wave orientation was scattered to several transverse momentum peaks at even multiples of the photon momentum [259]. In the case of a loose focus, the transverse momentum of the

atomic beam was only affected at specific incidence angles (not perpendicular) of the sodium beam to the standing wave. At these angles, a single diffraction peak was observed, again at an even multiple of the photon momentum [260].

The difference between the two types of atomic scattering, known as Kapitza–Dirac and Bragg scattering, arises from energy and momentum conservation. Consider an atom with initial momentum P perpendicular to the standing wave orientation. In these steady-state atomic beam experiments, the kinetic energy of the atom, and thus the magnitude of its momentum, is unchanged. Momentum is imparted to the atom by the absorption of one photon from the standing wave and stimulated emission of another, resulting in two momentum kicks of magnitude $\hbar k$ where k is the wavevector of the standing wave photons. Thus, for an atom to be scattered to the first order diffraction peak, the optical field must include photons propagating at a tilt angle $\Delta\theta = \hbar k/P$ from the standing wave orientation. A lower bound on the angular spread of photons in the standing wave $\Delta\phi$ is given by the Heisenberg uncertainty relation as $(\hbar k\Delta\phi) \cdot \Delta w > \hbar/2$ where Δw is the beam waist at the optical focus. Atomic scattering is allowed if $\Delta\phi > \Delta\theta$. This criterion is satisfied in the case of a tight optical focus (small Δw and thus large $\Delta\phi$), and thus the atomic scattering is not limited to specific angles; indeed, simultaneous Kapitza–Dirac scattering to several angles is allowed. In the case of a broad focus, the angular divergence of the photons is too small to allow non-specific Kapitza–Dirac scattering. Rather, at specific incident angles $\theta_N = \arcsin N\hbar k/P$ of the atomic beam to the standing wave, a single final momentum state can be reached by $2N$ momentum kicks along the direction of the standing wave. This is the condition for a Bragg scattering resonance.

Kapitza–Dirac [261] and Bragg [262] scattering of Bose–Einstein condensates has also been demonstrated. These experiments were performed by the BEC group at NIST, Gaithersburg with nearly stationary, pulsed atomic sources. Rather than varying the width of the optical grating, one varies the duration T of a pulse of light from two intersecting laser beams, and rather than varying the incidence angle of the atomic beam, one varies the differential detuning ω between the two laser beams. These two different techniques (atomic beam vs. pulsed optical grating) are identical when viewed in the frame of reference of the atoms. An atom traveling at momentum P in an atomic beam which passes through a standing wave of width Δw “sees” a pulse of light of duration $T = \Delta w m/P$. If the momentum P is tilted by an angle θ from the perpendicular to the standing wave orientation, the atom “sees” not a standing wave, but rather a wave traveling at velocity $v_\perp = (P/m) \sin \theta$. This corresponds to a differential detuning of $\omega = 2kv_\perp$ between the two beams of the optical “walking” wave.

The condition for Kapitza–Dirac scattering, $\Delta\phi > \Delta\theta$ can be rewritten as

$$\frac{1}{T} > \frac{1}{\hbar} \frac{(2\hbar k)^2}{2m} = \frac{(4E_r)}{\hbar} \quad (8.3)$$

where E_r is the recoil energy $\hbar^2 k^2 / 2m$. Thus, Kaptiza–Dirac scattering can occur if the duration of the pulse is short enough so that the pulse contains frequency components necessary to excite the atom to the energy $4E_r$ of an atom after its having acquired a momentum of two photon recoils. Similarly, the condition for Bragg scattering becomes a condition on the differential detuning of the counter-propagating laser beams

$$\hbar\omega = N \times \frac{(2\hbar k)^2}{2m} = 4NE_r \quad (8.4)$$

This is simply the resonance condition for exciting an atom to an excited momentum state. A single Bragg scattering event imparts a momentum $2\hbar k$, and an energy of $4E_r$ to the atom; thus, the first-order Bragg scattering resonance for free atoms occurs at a differential detuning of $\hbar\omega = 4E_r$. Higher-order Bragg scattering imparts a momentum of $2N\hbar k$ and thus an energy of $4N^2 E_r$. This energy is transferred by the exchange of N photons, giving the resonance condition $N\hbar\omega = 4N^2 E_r$ as in Eq. 8.4.

As this discussion regarding Bragg scattering exemplifies, the Bragg resonance condition is sensitive to the motion of the atom with respect to the optical standing wave orientation. By simple energy and momentum conservation, the energy transferred to an atom with initial velocity \vec{v}_i by a momentum kick of $\hbar\vec{q}$ is

$$\hbar\omega = \frac{(\hbar\vec{q} + m\vec{v}_i)^2}{2m} - \frac{mv_i^2}{2} = \frac{\hbar^2 q^2}{2m} + \hbar\vec{q} \cdot \vec{v}_i \quad (8.5)$$

Thus, the Bragg resonance is Doppler sensitive and can be used to determine spectroscopically the velocity distribution of an atomic sample.

Optical standing (and “walking”) waves have been important tools in the field of atom optics. Atomic beam interferometers have been constructed employing both Kaptiza–Dirac [263] and Bragg scattering [264] from three consecutive standing waves, and Bragg scattering de Broglie wave frequency shifters have been demonstrated [265]. These techniques have been recently extended by the demonstration of Kapitza–Dirac [169] and Bragg scattering [266] interferometers using Bose–Einstein condensates, giving very high contrast fringes. Such atom interferometers should benefit from having atoms in both arms of the interferometer be in the same internal state, thereby minimizing the deleterious effect of stray fields.

8.2 Measuring the dynamical structure factor of a many-body system

Light scattering and neutron scattering have long been used to probe the properties of condensed-matter systems. In particular, scattering experiments on superfluid helium, the interpretation of which was begun with the theoretical work of van Hove [267], have

revealed the spectrum of microscopic excitations in that quantum fluid [37, 75, 76, 268]. The spectroscopic analysis of inelastically scattered light from a Bose–Einstein condensate has been discussed by a number of authors. Javanainen and Ruostekoski [269, 270] developed the relation between the spectrum of scattered light and properties of a trapped, ideal–gas Bose–Einstein condensate, while Graham and Walls [271] extended their analysis to the case of an interacting, homogeneous condensate. Their work directly follows the interpretation of scattering from liquid helium, except that the scattering is treated beginning from an atomic basis due to the diluteness of gaseous condensates.

Let us discuss how light scattering as a stimulated process, i.e. Bragg scattering, is used to probe the properties of a many–body system. An atomic sample is exposed to two laser beams, with wavevectors k_1 and k_2 with a frequency difference ω which is generally much smaller than the detuning Δ of the beams from an atomic resonance. The two laser beams interfere to form a “walking” wave intensity modulation $I_{\text{mod}}(\vec{r}, t) = I \cos(\vec{q} \cdot \vec{r} - \omega t)$ where $\vec{q} = \vec{k}_1 - \vec{k}_2$. Due to the AC Stark effect (see Sec. 3.6), atoms exposed to this intensity modulation experience a conservative optical potential with a spatial modulation of $V_{\text{mod}} = \hbar\Gamma^2/8\Delta \times I_{\text{mod}}/I_{\text{sat}}$ where Γ is the line width of the atomic resonance and I_{sat} the saturation intensity. Just as the scattering of x–rays or neutrons off a crystal, neutral atoms may Bragg scatter of the moving optical grating.

To determine the Bragg scattering response of a many–body system, we express the modulated potential in second quantized notation as

$$V_{\text{mod}} = V/2 \left(\hat{\rho}^\dagger(\vec{q}) e^{-i\omega t} + \hat{\rho}^\dagger(-\vec{q}) e^{+i\omega t} \right) \quad (8.6)$$

where $\hat{\rho}(\vec{q}) = \sum_m \hat{a}_{m+q}^\dagger \hat{a}_m$ is the Fourier transform of the atomic density operator at wavevector \vec{q} . Equivalently, V_{mod} is found by isolating those terms in the light–atom coupling operator \mathcal{H}' of Eq. 8.1 which involve the macroscopically occupied optical modes at wavevectors \vec{k}_1 and \vec{k}_2 , and replacing the photon creation and destruction operators with c–numbers proportional to the electric field strength of the Bragg scattering laser beams.

We may then determine the Bragg scattering rate using Fermi’s golden rule. Considering scattering out of the many–body ground state $|g\rangle$, we neglect the counter–rotating term in V_{mod} and obtain the excitation rate per particle as

$$\frac{W}{N} = \frac{2\pi}{N\hbar} \left(\frac{V}{2} \right)^2 \sum_f |\langle f | \hat{\rho}^\dagger(\vec{q}) | g \rangle|^2 \delta(\hbar\omega - (E_f - E_g)) \equiv 2\pi\omega_R^2 S(\vec{q}, \omega) \quad (8.7)$$

Here N is the number of atoms in the system, and the sum is performed over all final excited states $|f\rangle$ with energy E_f . In this equation we have defined the dynamic structure factor $S(\vec{q}, \omega)$ which is the Fourier transform of density–density fluctuations in state $|g\rangle$

with spatial and temporal frequencies of \vec{q} and ω , respectively

$$S(\vec{q}, \omega) = \int d^3\vec{r} dt \langle g | \hat{\rho}(\vec{r}, t) \hat{\rho}^\dagger(0, 0) | g \rangle e^{i\vec{q}\cdot\vec{r}-i\omega t} \quad (8.8)$$

The dynamic structure factor generally characterizes the response of the system to longitudinal perturbations of any source, not solely to optical excitation. The density fluctuation spectrum is directly determined by the Bragg scattering response, normalized by the two-photon Rabi frequency $\omega_R = V/2\hbar$. Integrating over all frequencies ω (positive and negative), one obtains the static structure factor $S(\vec{q}) = \langle g | \hat{\rho}(\vec{q}) \hat{\rho}^\dagger(\vec{q}) | g \rangle$ which is equivalent to the line strength of the Bragg resonance.

8.3 The dynamic structure factor of a Bose–Einstein condensate

As discussed in Sec. 7.1, a Bose–Einstein condensate is quite different from other fluids in that the *microscopic* (i.e. single-atom) excitations of the system become manifest as *macroscopic* density fluctuations due to interference with the macroscopic wavefunction. This effect can be equivalently discussed in terms of the dynamic structure factor. Considering density fluctuations in a homogeneous Bose–Einstein condensate, we may approximate

$$\hat{\rho}^\dagger(\vec{q}) |g\rangle = \sum_m \hat{a}_{m+q}^\dagger \hat{a}_m |g\rangle \simeq (\hat{a}_q^\dagger \hat{a}_0 + \hat{a}_0^\dagger \hat{a}_{-q}) |g\rangle \quad (8.9)$$

Here, the macroscopic occupation of the zero-momentum state picks out two terms in the sum. Following Bogoliubov, we identify $\hat{a}_0^\dagger = \hat{a}_0 = \sqrt{N_0}$ and transform to Bogoliubov operators by substituting $\hat{a}_k = u_k \hat{b}_k - v_k \hat{b}_{-k}^\dagger$. The many-body wavefunction of the condensate $|g\rangle$ is defined by the relations $\hat{b}_k |g\rangle = 0, \forall k$. Thus, we find

$$\hat{\rho}^\dagger(\vec{q}) |g\rangle \simeq \sqrt{N_0} (u_q - v_q) \hat{b}_q^\dagger |g\rangle \quad (8.10)$$

From this, it follows naturally that for a homogeneous Bose–Einstein condensate $S(\vec{q}, \omega) \simeq (u_q - v_q)^2 \delta(\omega - \omega_q^B)$, and $S(\vec{q}) = (u_q - v_q)^2 = \omega_q^0 / \omega_q^B$. Here, $\hbar\omega_q^0 = \hbar^2 q^2 / 2m$, and $\hbar\omega_q^B = \sqrt{\hbar\omega_q^0(\hbar\omega_q^0 + 2\mu)}$ is the energy of a Bogoliubov quasi-particle of wavevector \vec{q} where μ is the chemical potential.

Thus, we expect Bragg scattering from an interacting, homogeneous Bose–Einstein condensate to differ from the Bragg scattering of a non-interacting condensate in two ways. First, the Bragg resonance occurs at the Bogoliubov quasi-particle energy which is higher than the free-particle recoil energy, i.e. the Bragg resonance line at a momentum transfer of $\hbar\vec{q}$ is thus shifted upwards in frequency from the free particle resonance by

$$\Delta\omega = \omega_q^B - \omega_q^0. \quad (8.11)$$

Second, the Bragg scattering response is weakened from that of free particles by a factor $S(\vec{q}) = (u_q - v_q)^2 < 1$. In other words, light scattering from a Bose–Einstein condensate is suppressed by the presence of repulsive interatomic interactions. Indeed, these two statements are equivalent: by the f –sum rule which states that $\int \omega S(\vec{q}, \omega) d\omega = \omega_q^0$, an increase in the resonance frequency implies a decrease in the excitation strength [76].

Let us evaluate the structure factor in two limits of the Bragg scattering wavevector \vec{q} . The wavevector which corresponds to the interaction energy is the inverse healing length $\xi^{-1} = \sqrt{2}mc_s/\hbar$ where c is the speed of Bogoliubov sound. For large wavevectors ($q \gg \xi^{-1}$), Bragg scattering occurs in the free–particle regime. The Bragg resonance is shifted upwards by the chemical potential $\Delta\omega \simeq \mu/\hbar$, and the line strength tends to $S(\vec{q}) \rightarrow 1 - \mu/\hbar\omega_q^0$. Thus, Bragg scattering in the free–particle regime can be used to directly measure the chemical potential [18].

For small wavevectors ($q \ll \xi^{-1}$), the Bose–Einstein condensate responds to optical excitation collectively with the creation of phonons. The static structure factor tends to $S(\vec{q}) \rightarrow \hbar q/\sqrt{2}mc$ and vanishes in the long wavelength limit, as required of a zero–temperature system with finite compressibility [272].

8.4 Bragg scattering as a probe of correlations in the condensate

It is interesting to re-examine these modifications to light scattering from a Bose–Einstein condensate in terms of the structure of the many–body condensate wavefunction. What is it about a dilute, weakly–interacting Bose–Einstein condensate that suppresses light scattering? As discussed above, the static structure factor $S(\vec{q})$ is the magnitude of the state vector

$$\frac{1}{\sqrt{N}}\hat{\rho}^\dagger(\vec{q})|g\rangle \simeq \frac{1}{\sqrt{N}}(\hat{a}_q^\dagger\hat{a}_0|g\rangle + \hat{a}_0^\dagger\hat{a}_{-q}|g\rangle) = |e^+\rangle + |e^-\rangle \quad (8.12)$$

The states $|e^+\rangle$ and $|e^-\rangle$ represent two means by which momentum is imparted to the condensate: either by promoting a zero-momentum particle to momentum $\hbar\vec{q}$, or else by demoting a particle from momentum $-\hbar\vec{q}$ to zero momentum.

If correlations could be neglected, the total rate of excitation would simply be the sum of the independent rates for these two processes, proportional to $\langle e^+|e^+\rangle = \langle N_q^0 \rangle + 1 = u_q^2$ and $\langle e^-|e^-\rangle = \langle N_{-q}^0 \rangle = v_q^2$ where $\langle N_k^0 \rangle$ is the expected number of atoms of momentum $\hbar\vec{k}$ in the condensate. This would apply, for example, to a condensate in a pure number state, or to an ideal gas condensate with a thermal admixture of atoms with momenta $\pm\hbar\vec{q}$, and would always lead to $S(\vec{q}) > 1$.

Yet, for the many-body ground state of the interacting Bose gas, the behavior is dramatically different. Collisions of zero-momentum atoms admix into the condensate pairs of atoms at momenta $\pm\hbar\vec{q}$ (as discussed in Sec. 7.1) the population of which comprises the

quantum depletion. As a result, the two momentum transfer mechanisms described above produce indistinguishable states, and the rate of momentum transfer is given by the interference of two amplitudes, not by the sum of two rates. Pair excitations in the condensate are correlated so as to minimize the total energy (see Eq. 7.8), and thereby give destructive interference between the two momentum transfer processes, so $S(\vec{q}) = (u_q - v_q)^2 < 1$. For high momentum, $\langle N_q^0 \rangle \ll 1$ and the interference plays a minor role. In the phonon regime, while the independent rates u_q^2 and v_q^2 (and hence $\langle N_{\pm q}^0 \rangle$) diverge as $1/q$, the correlated quantum depletion extinguishes the rate of Bragg excitation.

Finally, it is interesting to note that the extinction of Bragg scattering at low momentum, i.e. the minus sign in the amplitude $u_q - v_q$ of state $|e\rangle$, arises from minimizing the energy of an interacting Bose gas with positive scattering length. If the sign of the scattering length is changed, the interactions between atoms become attractive. While Bose–Einstein condensation for such a gas is excluded in a homogeneous system, it is allowed in a trapped gas due to a kinetic energy barrier which prevents the collapse of the condensate [130, 273]. In such a condensate, light scattering at low momentum should be *enhanced* by the correlated excitations. However, since the stability of the condensate relies on the condensate being smaller than the healing length ξ , inelastic light scattering at $q < \xi^{-1}$ should be suppressed in favor of elastic scattering by the Mössbauer effect.

8.5 Mean–field theory determination of $S(\vec{q}, \omega)$

While the suppression of the Bragg excitation rate in the phonon regime is an indicator for correlations in the many–body condensate wavefunction, the same result is obtained also in a self–consistent mean–field approach. Considering again the homogeneous case, we introduce the perturbation

$$V_{\text{mod}} = \frac{V}{2} \left(e^{i\vec{q}\cdot\vec{r}-i\omega t} + e^{-i\vec{q}\cdot\vec{r}+i\omega t} \right) \quad (8.13)$$

to the time–dependent Gross–Pitaevskii equation (Eq. 5.18), and use a wavefunction of the form

$$\psi(\vec{r}, t) = e^{-i\mu t/\hbar} \left(\psi_0(\vec{r}, t) + u(t)e^{i\vec{q}\cdot\vec{r}-i\omega t} + v^*(t)e^{-i\vec{q}\cdot\vec{r}+i\omega t} \right) \quad (8.14)$$

Here, $\mu = ng$ is the chemical potential where n is the condensate density and $g = 4\pi\hbar^2 a/m$. The condensate wavefunction $\psi_0(\vec{r}, t) = \sqrt{n}$ is obtained by solving the time–independent Gross–Pitaevskii equation (Eq. 5.20) and is uniform for the case of a homogeneous condensate at rest.

The weak potential V_{mod} introduces the small perturbations $u(t)e^{i\vec{q}\cdot\vec{r}-i\omega t}$ and $v(t)e^{-i\vec{q}\cdot\vec{r}+i\omega t}$ where the amplitudes $u(t)$ and $v(t)$ are slowly varying functions of time. Their time evolution is given by the Gross–Pitaevskii equation. Considering terms proportional to $e^{i\vec{q}\cdot\vec{r}-i\omega t}$

and $e^{-i\vec{q}\cdot\vec{r}+i\omega t}$, we obtain the set of equations

$$\hbar\omega u + i\hbar \frac{du}{dt} = \left(\frac{\hbar^2 q^2}{2m} + ng \right) u + n g v + \frac{V}{2} \psi_0 \quad (8.15)$$

$$-\hbar\omega v - i\hbar \frac{dv}{dt} = \left(\frac{\hbar^2 q^2}{2m} + ng \right) v + n g u + \frac{V}{2} \psi_0 \quad (8.16)$$

Let us now apply the Bogoliubov transformation, and write

$$\begin{pmatrix} u \\ v \end{pmatrix} = \alpha \begin{pmatrix} u_q \\ -v_q \end{pmatrix} + \beta \begin{pmatrix} v_q \\ -u_q \end{pmatrix} \quad (8.17)$$

The two component vectors $\begin{pmatrix} u_q \\ -v_q \end{pmatrix}$ and $\begin{pmatrix} v_q \\ -u_q \end{pmatrix}$ are solutions of the equations [28, 188]

$$\begin{bmatrix} (\hbar\omega_q^0 + \mu) & \mu \\ -\mu & -(\hbar\omega_q^0 + \mu) \end{bmatrix} \begin{pmatrix} u \\ v \end{pmatrix} = \hbar\tilde{\omega} \begin{pmatrix} u \\ v \end{pmatrix} \quad (8.18)$$

with frequencies $\tilde{\omega} = \omega_q^B$ and $\tilde{\omega} = -\omega_q^B$, respectively. The negative frequency solution corresponds to excitations in the $-\vec{q}$ direction. With this substitution, Eqs. 8.15 and 8.16 are decoupled:

$$\hbar\omega\alpha + i\hbar \frac{d\alpha}{dt} = \hbar\omega_q^B \alpha + (u_q - v_q) \frac{V}{2} \psi_0 \quad (8.19)$$

$$\hbar\omega\beta + i\hbar \frac{d\beta}{dt} = -\hbar\omega_q^B + (u_q - v_q) \frac{V}{2} \psi_0 \quad (8.20)$$

These equations are identical to those of first-order perturbation theory for a single-particle Schrödinger equation. Thus, applying Fermi's Golden Rule, we obtain

$$\frac{d|\alpha|^2}{dt} = \frac{2\pi}{\hbar} (u_q - v_q)^2 \left(\frac{V}{2} \right)^2 N_0 \delta(\hbar\omega - \hbar\omega_q^B) \quad (8.21)$$

$$\frac{d|\beta|^2}{dt} = \frac{2\pi}{\hbar} (u_q - v_q)^2 \left(\frac{V}{2} \right)^2 N_0 \delta(\hbar\omega + \hbar\omega_q^B) \quad (8.22)$$

The response of the condensate to Bragg scattering can be evaluated by calculating the momentum imparted to the condensate

$$\langle \psi(\vec{r}, t) | \hat{p} | \psi(\vec{r}, t) \rangle = \hbar\vec{q} \times (|u|^2 - |v|^2) = \hbar\vec{q} \times (|\alpha|^2 - |\beta|^2) \quad (8.23)$$

Normalizing by the Bragg scattering momentum $\hbar q$, we obtain the Bragg excitation rate per particle as

$$\frac{\langle \psi(\vec{r}, t) | \hat{p} | \psi(\vec{r}, t) \rangle}{\hbar q N_0} = 2\pi\omega_R^2 (u_q - v_q)^2 [\delta(\hbar\omega - \hbar\omega_q^B) - \delta(\hbar\omega + \hbar\omega_q^B)] \quad (8.24)$$

$$= 2\pi\omega_R^2 S(\vec{q}, \omega) - S(-\vec{q}, -\omega) \quad (8.25)$$

where, again, ω_R is the two-photon Rabi frequency.

This treatment reveals two important points. First, the mean-field treatment reproduces the suppression of the structure factor, even though, as discussed in Sec. 8.4, this suppression is indicative of correlations in the many-body condensate wavefunction. In the mean-field theory, correlations in the condensate wavefunction are explicitly neglected by the use of a Hartree wavefunction. Nevertheless, when the excitation of the condensate is also treated in a Hartree approximation (i.e. assuming all particles are in the same, albeit time-varying, single-particle wavefunction given by Eq. 8.14), the dynamic response is correctly obtained. This emphasizes that many manifestations of the quantum depletion are already accounted for by the use of a mean-field interaction energy which represents the two-particle correlations introduced by binary interactions. Thus, the identification of effects “beyond the Gross–Pitaevskii equation” must be made with care.

Second, this treatment takes into account both the positive and negative frequency terms in V_{mod} , unlike in Sec. 8.2 where we chose to consider only the positive frequency part for simplicity. One finds that the momentum imparted by stimulated scattering from the two Bragg beams measures the difference $S(\vec{q}, \omega) - S(-\vec{q}, -\omega)$. This arises because stimulated Bragg scattering can occur by the absorption of a photon from either of the two Bragg beams and stimulated emission into the other. In contrast, spectroscopic measurements of light scattering from a *single* laser beam would measure just $S(\vec{q}, \omega)$ [269–271]. This difference is important when one considers Bragg scattering from a non-zero temperature system. The dynamic structure factor for a non-zero temperature Bose–Einstein condensate is given as [37, 76]

$$S(\vec{q}, \omega) = (u_q - v_q)^2 \left[(\langle N_q^B \rangle + 1) \delta(\hbar\omega - \hbar\omega_q^B) + \langle N_{-q}^B \rangle \delta(\hbar\omega + \hbar\omega_q^B) \right] \quad (8.26)$$

where $\langle N_q^B \rangle$ is the thermal population of *quasi-particles*. Light scattering is thus quite sensitive to the presence of excitations in the condensate, as confirmed by the recent observation of superradiant light scattering from a condensate which is due to the buildup of excited particles in a preferred mode [20]. However, the effects of thermally-excited particles is cancelled out in the Bragg scattering response, and thus one extracts the zero-temperature structure factor even in a finite-temperature sample.

A related numerical calculation using the Gross–Pitaevskii equation has been made by Choi and Niu [274] who study the behaviour of an interacting Bose–Einstein condensate in an optical lattice. They examine two situations in which an optical lattice is used either to slow down a moving Bose condensate, or else to accelerate a condensate at rest similar to experiments using laser-cooled, non-condensed atoms [275]. They note that the presence of strong atomic interactions can make the motion of the condensate insensitive to an external potential because it leads to $S(\vec{q}) < 1$.

Finally, let us note that the above mean-field treatment can be naturally extended to inhomogeneous Bose–Einstein condensates. Approximate treatments in the free-particle regime and using a local density approximation are discussed along with a description of experiments in the following sections.

8.6 Bragg scattering in the free-particle regime

I now turn to the discussion of two Bragg spectroscopy experiments performed by our group. In the first [18], which was performed primarily by my colleagues Jörn Stenger, Shin Inouye, and Ananth Chikkatur, Bose–Einstein condensates were exposed to counter-propagating laser beams along a radial direction of the cigar-shaped clouds (Fig. 8-1). The beams, detuned to the red of the $3S_{1/2}, |F = 1\rangle \rightarrow 3P_{3/2}, |F' = 0, 1, 2\rangle$ optical transitions by about $\Delta = 1.7$ GHz, were derived from a common source (zero-order light from the $F = 2$ acousto-optic modulator (AOM), see Fig. 3-3e). A small frequency difference ω between the counter-propagating beams, on the order of $2\pi \times 100$ kHz, was introduced either by using two independently-controlled AOM’s to control the frequency of two independent beams, or by using a single AOM to generate a single beam with two different frequencies which was retro-reflected. The Bragg resonance spectrum for both trapped and untrapped Bose–Einstein condensates was determined by scanning the frequency difference ω and determining the fraction of Bragg scattered atoms in a time-of-flight image.

As discussed above, the Bragg scattering resonance is sensitive both to the velocity (Doppler shift) and the density (mean-field shift) of the atomic sample. In our experiments, both these effects are present. The momentum distribution of a trapped Bose–Einstein condensate, assuming its full coherence, is given by the Fourier transform of the condensate wavefunction. Thus, neglecting the mean-field shift, the Bragg excitation rate $I_D(\omega)$ from a Bose–Einstein condensate at a frequency difference of ω between the two Bragg beams is

$$I_D(\omega)d\omega \propto \int d^3\vec{k} \delta\left(\frac{\hbar\vec{k}\cdot\vec{q}}{m} - (\omega - \omega_q^0)\right) \left| \int d^3\vec{r} e^{-i\vec{k}\cdot\vec{r}} \psi(\vec{r}) \right|^2 d\omega \quad (8.27)$$

$$\propto \int dx_1 dx_2 e^{-ik(\omega)\cdot(x_2-x_1)} \int dy dz \psi^*(x_1, y, z) \psi(x_2, y, z) d\omega \quad (8.28)$$

where $\hbar\vec{q}$ is the Bragg scattering momentum and $\psi(\vec{r})$ is the condensate wave function. In the second line, a coordinate system is chosen so that $\hbar\vec{q}$ lies in the \hat{x} -direction, and $k(\omega) = m(\omega - \omega_q^0)/\hbar q$. In the Thomas–Fermi regime, for Bragg scattering along one of the principal axes of the harmonic trap, the Doppler line shape is then

$$I_D(\omega)d\omega \propto \frac{2(4 + \kappa^2)J_1(\kappa)J_2(\kappa) + \kappa J_0(\kappa)[5\kappa J_1(\kappa) - 16J_2(\kappa) + 3\kappa J_3(\kappa)]}{\kappa^3} d\omega \quad (8.29)$$

where $\kappa = k(\omega)x_{c,0}$ and $x_{c,0}$ is the Thomas–Fermi radius of the condensate along the

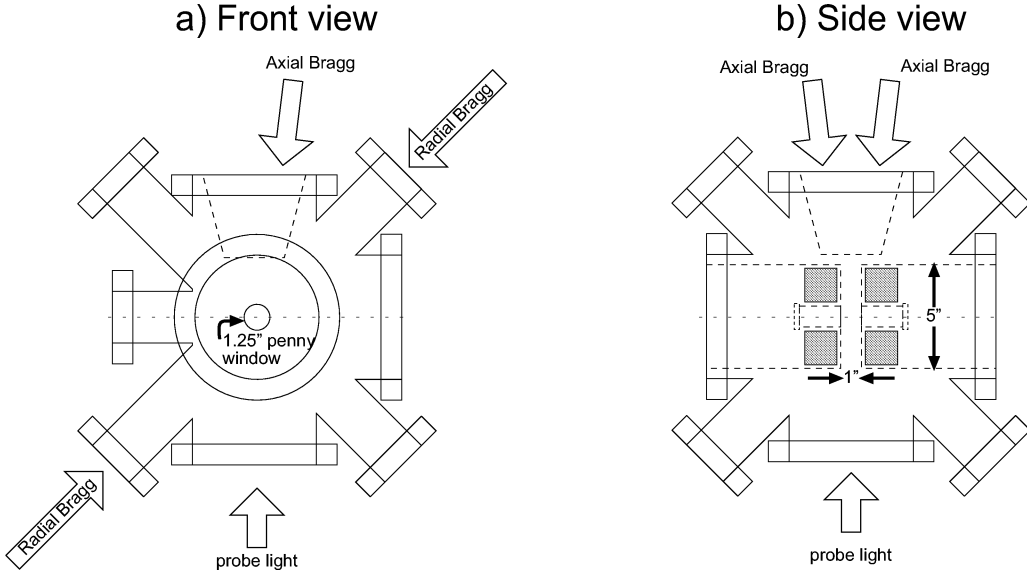


Figure 8-1: Optical setup for Bragg scattering, shown (a) front and (b) side views of the main UHV chamber (see also Fig. 3-1). Counter propagating beams from the diagonal ports (labeled “Radial Bragg”) imparted a recoil momentum kick along a radial direction of the condensate which was tilted at 45° with respect to the object plane of the imaging system. Beams intersecting at a small angle ($\sim 14^\circ$) were directed at the condensate from the top of the chamber and imparted an axial momentum kick.

direction of scattering*. The rms-width of a Gaussian which is fitted to this line shape is

$$\Delta\omega_D \simeq 1.58 \frac{\hbar q}{mx_{c,0}} \quad (8.30)$$

The Bragg resonance is also affected by the inhomogeneous density distribution of the trapped condensate. As discussed above (Sec. 8.3), the Bragg resonance in a homogeneous Bose–Einstein condensate of density n is shifted upwards in the free-particle regime by $\delta\omega = gn/\hbar$. In the limit that the Doppler width can be neglected, i.e. if the condensate radius is so large that $gn/\hbar \gg \Delta\omega_D$, the Bragg resonance line shape can be calculated using a local density approximation, giving [18, 21]

$$I_\mu(\omega)d\omega \propto \frac{15}{4} \frac{\omega - \omega_q^0}{(\mu/\hbar)^2} \sqrt{1 - \frac{\omega - \omega_q^0}{(\mu/\hbar)}} d\omega \quad (8.31)$$

The line center is shifted upwards from the free-particle resonance frequency by $4\mu/7\hbar$, and

*In our paper [18], an incorrect form of the line shape was given. However, when the two line shapes are fitted with Gaussians, the Gaussian widths are equal within 3%. This difference does not affect the conclusions of our paper.

broadened to an rms-width of

$$\Delta\omega_\mu = \sqrt{\frac{8}{147}} \frac{\mu}{\hbar} \quad (8.32)$$

For a typical maximum condensate density of $4 \times 10^{14} \text{ cm}^{-3}$ ($\mu/\hbar \simeq 2\pi \times 6 \text{ kHz}$) and a radial trap frequency of $\omega_r = 2\pi \times 200 \text{ Hz}$, the rms Doppler width and mean-field width are nearly equal ($\Delta\omega_D \simeq \Delta\omega_\mu = 2\pi \times 1.4 \text{ kHz}$). Thus, to properly interpret the Bragg spectra obtained for trapped condensates, the combined effects of both the condensate velocity and density must be considered. As we now show, this can be done in the free-particle regime with the aid of simple sum rules.

As discussed above, the Bragg excitation rate from a trapped Bose-Einstein condensate is determined using Fermi's Golden Rule as a sum over all excited states of the system. The condensate wavefunction $|g\rangle$ determined by the Gross-Pitaevskii equation is a solution of the equation $\mathcal{H}_0|g\rangle = \mu|g\rangle$ where

$$\mathcal{H}_0 = \frac{\hat{p}^2}{2m} + U(\vec{r}) + gn(\vec{r}) \quad (8.33)$$

In the regime $\hbar\omega_q^0 \gg \mu$, the excitations relevant to Bragg scattering are well described as free-particle excitations which obey

$$\hbar\omega_f|f\rangle = \left(\frac{\hat{p}^2}{2m} + U(\vec{r}) + 2gn_c(\vec{r}) \right) |f\rangle = \mathcal{H}_{\text{exc}}|f\rangle \quad (8.34)$$

This can be seen, for example, by considering Eq. 8.18 in the free-particle regime where $v_q \rightarrow 0$. Thus, the excitations are eigenfunctions of the Hamiltonian $\mathcal{H}_{\text{exc}} = \mathcal{H}_0 + gn(\vec{r})$ which is different than the Hamiltonian \mathcal{H}_0 which gives the condensate wavefunction [276]. The extra term $gn(\vec{r})$ represents the repulsion of excitations from the condensate which gives rise to the mean-field shift in the free-particle regime.

An exact description of the resonance line shape requires detailed knowledge of the excitation wavefunctions. Such an explicit calculation has been performed in the context of the two-photon optical excitation from the $1S$ to the $2S$ state in hydrogen which has been employed to probe properties of a hydrogen Bose-Einstein condensate [27, 277]. The calculation showed the validity of the limiting behaviours of Doppler- and mean-field-dominated line shapes considered above [278]. However, even without this exact description, gross features of the line are determined easily by sum rules. The first moment of the spectral line is given by

$$\hbar\bar{\omega} = \frac{\int_0^\infty d\omega \omega S(\vec{q}, \omega)}{\int_0^\infty d\omega S(\vec{q}, \omega)} \quad (8.35)$$

$$= \frac{\sum_f \langle g | e^{i\vec{q} \cdot \vec{r}} | f \rangle \langle f | e^{-i\vec{q} \cdot \vec{r}} | g \rangle (\omega_f - \omega_g)}{\sum_f \langle g | e^{i\vec{q} \cdot \vec{r}} | f \rangle \langle f | e^{-i\vec{q} \cdot \vec{r}} | g \rangle} \quad (8.36)$$

$$= \langle e^{i\vec{q} \cdot \vec{r}} \mathcal{H}_{\text{exc}} e^{-i\vec{q} \cdot \vec{r}} - \mathcal{H}_0 \rangle_c \quad (8.37)$$

$$= \frac{\hbar^2 q^2}{2m} + g\langle n_c \rangle_c \quad (8.38)$$

where $\langle X \rangle_c = \langle g|X|g \rangle$, and $\langle \vec{p} \rangle_c = 0$ in the ground state. Thus the Bragg resonance line for a harmonically trapped condensate is shifted from the free-particle resonance by $4\mu/7\hbar$.

The rms-width of the line $\Delta\omega = \sqrt{\omega^2 - \bar{\omega}^2}$ is calculated using

$$\hbar^2 \overline{\omega^2} = \langle e^{i\vec{q}\cdot\vec{r}} \mathcal{H}_{exc}^2 e^{-i\vec{q}\cdot\vec{r}} - \mathcal{H}_0^2 \rangle_c \quad (8.39)$$

by which one obtain

$$\hbar^2 (\Delta\omega)^2 = \left\langle \left(\frac{\hbar\vec{q}\cdot\vec{p}}{m} \right)^2 \right\rangle_c + g^2 (\langle n_c^2 \rangle_c - \langle n_c \rangle_c^2) \quad (8.40)$$

Thus the total rms-width of the line is the sum of two widths in quadrature: the Doppler width due to the finite size of the condensate, and the line broadening due to the inhomogeneous condensate density.

These predictions were in excellent agreement with the Bragg resonance line centers and line widths obtained experimentally [18]. The shift of the line center for trapped condensates from the free-particle resonance frequency of $\omega_q^0 = 2\pi \times 99.5$ kHz was compared with measurements of the chemical potential determined from the width of condensates in time-of-flight images. The measured shift of $(0.54 \pm 0.07)\mu/\hbar$ was in agreement with the predicted $0.57\mu/\hbar$. In similar work, mean-field line shifts measured by two-photon spectroscopy of atomic hydrogen were used as a measurement of the $a_{1S,2S}$ scattering length for collisions between atoms in the $1S$ and $2S$ states [277].

Using Eq. 8.40, the Doppler line widths were extracted from Bragg spectra of both freely-expanding and trapped Bose-Einstein condensates. The Doppler width for freely-expanding condensates during the conversion of their mean-field interaction energy into kinetic energy was in full agreement with the predictions of mean-field theory [174]. Thus, both in momentum space and in coordinate space (Sec. 7.2.9), the predicted behaviour of a freely-expanding Bose-Einstein condensates has been quantitatively verified.

8.7 A measurement of the coherence length of a Bose-Einstein condensate

The Doppler width of the Bragg scattering resonance of trapped Bose-Einstein condensates measured their momentum distribution and thus measured their coherence length. By observing momentum distributions which were equal to the Heisenberg-limited momentum distribution determined by the condensate size, our measurements showed that the coherence length of the condensate was no smaller than the radial width of the condensate.

To make this statement more quantitative, let us consider the possibility that the con-

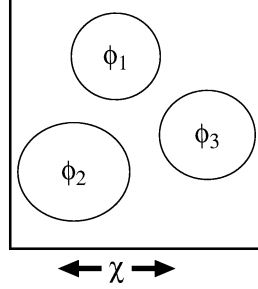


Figure 8-2: A quasi-condensate can be depicted pictorially as being composed of many smaller condensates, each with a well-defined phase which is unrelated to the phase of the other small condensates. The range of phase coherence is the coherence length χ .

densate is not fully coherent. As shown pictorially in Fig. 8-2, consider a situation in which the trapped Bose-Einstein condensate is actually composed of many smaller coherent condensates of typical size χ with no phase-relation between them. Formally, this picture is equivalent to the following

$$\langle \hat{\Psi}^\dagger(\vec{r}_1) \hat{\Psi}(\vec{r}_2) \rangle = \langle \hat{\Psi}^\dagger(\vec{r}_1) \rangle \langle \hat{\Psi}(\vec{r}_2) \rangle g^{(1)}(|\vec{r}_1 - \vec{r}_2|) \quad (8.41)$$

where $g^{(1)}(r)$ is the first-order coherence function which decays from $g^{(1)}(0) = 1$ to $g^{(1)}(r \gg \chi) = 0$. The Doppler line shape of the Bragg resonance, shown in Eq. 8.28 for the case of full coherence, now becomes

$$\begin{aligned} I_D(\omega) d\omega &\propto \int dx_1 dx_2 e^{-ik(\omega)(x_2-x_1)} \int dy dz \langle \hat{\Psi}^\dagger(x_1, y, z) \hat{\Psi}(x_2, y, z) \rangle d\omega \\ &= \int dx_1 dx_2 e^{-ik(\omega)(x_2-x_1)} g^{(1)}(|x_1 - x_2|) \int dy dz \psi^*(x_1, y, z) \psi(x_2, y, z) d\omega \end{aligned} \quad (8.42)$$

The effect of a limited coherence length is to increase the momentum distribution and thereby broaden the Doppler width of the Bragg resonance. For example, consider a condensate wavefunction which is Gaussian $\psi(\vec{r}) = \exp(-\sum x_i^2/2\sigma_i^2)$ with rms-widths of σ_i , ($i = x, y, z$), and a first-order correlation function of the form $g^{(1)}(r) = e^{-r^2/2\chi^2}$. For Bragg scattering along the \hat{x} -direction, the Doppler line width becomes $\Delta\omega_D(\chi) = \hbar q/m \times \sqrt{\sigma_x^{-2} + \chi^{-2}}$. Fig. 8-3 shows the Doppler line width $\Delta\omega_D(\chi)$ calculated using the Thomas-Fermi condensate wavefunction for different values of the coherence length χ . The calculations agree well with an approximation of the form

$$\Delta\omega_D(\chi) \simeq \sqrt{[\Delta\omega_D(\chi \rightarrow \infty)]^2 + \left[\frac{\hbar q}{m\chi} \right]^2} \quad (8.43)$$

This relation can be used to extract a coherence length measurement from the measurements in Ref. [18] of Doppler widths for trapped Bose-Einstein condensates. Taking the average

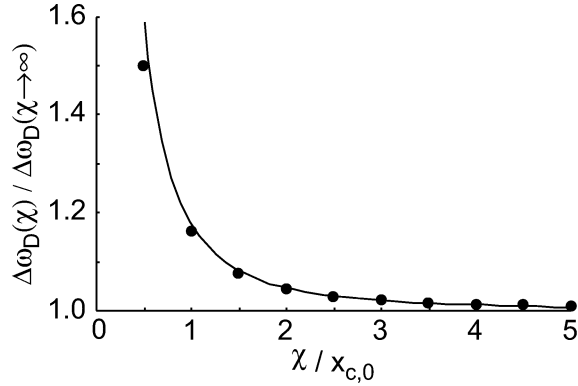


Figure 8-3: Doppler width of the Bragg resonance as a function of the coherence length χ . Shown is the ratio of the Doppler width of a partly coherent condensate to that of a fully coherent condensate, i.e. one for which $\chi \rightarrow \infty$. The coherence length is given in units of the Thomas–Fermi radius $x_{c,0}$. The results of a numerical calculation of Eq. 8.42 using a Thomas–Fermi wavefunction and $g^{(1)}(r) = \exp(-r^2/2\chi^2)$ (points) are well–described by the approximation of Eq. 8.43 (line).

for all data points shown in Fig. 3c of the paper (assuming the ratio of the coherence length to the condensate size is constant), one finds an average value for the ratio of the measured Doppler width to that predicted for a fully coherent condensate of $\Delta\omega_D(\chi)/\Delta\omega_D(\chi \rightarrow \infty) = 1.09 \pm 0.11$. Using Eq. 8.43, this corresponds to a determination of the coherence length in the range $\chi = 1.4_{-0.5}^{+\infty} \times x_{c,0}$, i.e. the measurements place a lower bound on the coherence length of $\chi \simeq x_{c,0}$ and are consistent with full coherence ($\chi \rightarrow \infty$).

8.8 Near–field and far–field measurements of the coherence length of a Bose–Einstein condensate

Let us compare these measurements with other measurements of the first–order coherence of gaseous Bose–Einstein condensates. The first evidence of the coherence of a Bose–Einstein condensate was obtained in the interference experiment of Andrews *et al.* [6]. A cigar–shaped cloud was split into two separated Bose–Einstein condensates along its long axis by the optical potential of a blue–detuned laser beam. The two condensates were then released from the trap and imaged after 40 ms time of flight, yielding a matter–wave interference pattern in regions where the two expanding clouds overlapped.

To interpret this interference experiment, let us consider first the atomic density $n(\vec{r}_1^f, t_{\text{tof}})$ observed at a point \vec{r}_1^f after the time of flight of duration t_{tof} . The expansion of both condensates was dominated by the release of the interaction energy as both condensates were well within the Thomas–Fermi regime: $\mu \gg \hbar\omega_r, \hbar\omega_z$ where ω_r and ω_z are the trap frequencies in the radial and axial directions, respectively. Thus, if we neglect the zero–point kinetic energy, the propagation can be described semi–classically. The wavefunction at \vec{r}_1^f

can be written as

$$\psi(\vec{r}_1^f, t_{\text{tof}}) \simeq \mathcal{U}(\vec{r}_{1A}^i, 0; \vec{r}_1^f, t_{\text{tof}})\psi(\vec{r}_1^f, 0) + \mathcal{U}(\vec{r}_{1B}^i, 0; \vec{r}_1^f, t_{\text{tof}})\psi(\vec{r}_B^f, 0) \quad (8.44)$$

i.e. the interference observed in time of flight arises from interference along the two classically allowed paths from one location \vec{r}_{1A}^i in one of the condensates (condensate *A*) and one location \vec{r}_{1B}^i in the other condensate (condensate *B*). The propagators $\mathcal{U}(\vec{r}_{1A}^i, 0; \vec{r}_1^f, t_{\text{tof}})$ and $\mathcal{U}(\vec{r}_{1B}^i, 0; \vec{r}_1^f, t_{\text{tof}})$ describe this classical mapping of points in the trapped condensate to points in the expanded cloud, and account for amplitude and phase evolution along the classical path.

Of course, this semi-classical picture is not entirely correct. One may estimate the effects of a fully quantum-mechanical treatment by saying that the atoms originally at \vec{r}_{1A}^i diffract from their classical trajectory to a distance $v_{\text{zp}}t_{\text{tof}} \simeq 200 \mu\text{m}$ where v_{zp} is the initial radial zero-point velocity of the condensate which is neglected in the Thomas-Fermi approach. Inasmuch as this distance is much smaller than the size of the expanding condensate (by the Thomas-Fermi condition), the interference probed in this experiment can be regarded as a near-field interference pattern in analogy with optical Fresnel or near-field diffraction [279].

To what extent does the observation of interference between two condensates by Andrews *et al.* constitute a measurement of the coherence length? The interference pattern which should result from the experimental conditions was calculated in Refs. [280, 281] using the Gross-Pitaevskii equation. Deviations between the experimentally observed interference pattern and that predicted by calculations would indicate fluctuations in the phase of the condensate, i.e. a limited coherence length of the order parameter ψ .

Phase fluctuations over a length scale χ would diffract to a length scale $d \simeq \hbar t_{\text{tof}}/m\chi$ over the duration of the time of flight. This would affect the interference pattern in different ways depending on the comparison between d and the fringe spacing $x_f \simeq 15 \mu\text{m}$. Short-range fluctuations, of length scale χ (smaller than the spacing between the two condensates) for which $d > x_f$ would diminish the contrast of the observed fringes. Long-range fluctuations for which $d < x_f$ would cause a modulation in the fringe pattern. The former of these two effects can be categorized as far-field and the latter as near-field with respect to the fringe spacing, as opposed to the distinction made above which concerns the overall size of the expanded cloud.

That straight-line interference fringes were observed across the entire $\simeq 1 \text{ mm}$ width of the expanded condensate in agreement with the predicted pattern demonstrates the presence of a long-range coherent component in the condensate. In other words, the observed interference pattern at a point \vec{r}_1^f can be considered as a measurement of the relative phase between $\psi(\vec{r}_{1A}^i, 0)$ and $\psi(\vec{r}_{1B}^i, 0)$. The close agreement between the measured and calculated density distributions across the entire interference pattern confirms that this relative phase is constant over the portion of each condensate which participates in the interference

pattern. Since about 1/2 of the atoms were involved in the interference pattern, the observations indicate a coherence length of at least $\approx 50\mu\text{m}$ which is half of the axial length of each of the two separated condensates. In later experiments using a spherical condensate which was split with a blue-detuned laser beam, the interference involved the entire population, indicating coherence across the entire condensate [165].

However, short-range fluctuations of the condensate phase about a constant, average value could not be ruled out. The contrast observed in the interference experiment, and again in later experiments with larger fringe spacing [165] was consistent with being less than 100% — a more quantitative statement is precluded by the limited resolution of the imaging system. Thus, the two-condensate interference experiment is consistent with a coherence function which decays over two length scales: an initial decay over a short length scale (less than several microns) to a non-zero average value which then persists out to the size of the condensate.

In comparison, as a measurement of atomic momenta, Bragg scattering can be regarded as a purely far-field determination of the coherence length. It is analogous to optical Fraunhofer diffraction [279] whereby, for example, the transverse coherence of laser beam can be determined by directing it at a distant wall and measuring the size of the illuminated spot. The coherence length determined by our Bragg scattering experiment is consistent with the results of the interference experiment. The narrow momentum distribution of the condensate demonstrated its long range coherence. Short-range deviations from a uniform condensate phase would give a bimodal frequency response (or a bimodal momentum distribution), where the observed narrow resonance curve would lie on top of a broad pedestal. The presence of such a pedestal could not be ruled out by our measurements.

Recently, two other groups have made measurements of the coherence length. The NIST group used two Kaptiza-Dirac pulses to perform an autocorrelation measurement of the condensate wavefunction [169]. The group of Esslinger, Bloch, and Hänsch in Munich observed the interference between two atomic beams which were output-coupled with an rf field from a Bose-Einstein condensate at different locations [160]. These measurements are performed in the near-field, i.e. the condensate wavefunction at points with a well-defined separation is probed. These measurements give evidence of a decay of the coherence length over two length scales. In particular, the Munich group ascribes the short-range decay of the first-order coherence function to the presence of thermal excitations.

8.9 Bragg scattering in the phonon regime

A second experiment explored the use of Bragg spectroscopy of a Bose-Einstein condensate in the phonon regime [21] (Appendix J). The distinction between the phonon and the free-particle regime of the Bogoliubov spectrum can be made in a number of equivalent ways. In the phonon regime, the magnitude of the Bragg scattering wavevector $q = |\vec{k}_1 - \vec{k}_2|$, which

	Phonon regime [21]	BEC	Free-particle regime [18]
Velocity	$\hbar q/m = 7 \text{ mm/s}$	$c = 10 \text{ mm/s}$	$\hbar q/m = 60 \text{ mm/s}$
Energy	$\hbar\omega_q^0 = h \times 1.5 \text{ kHz}$	$\mu = h \times 6 \text{ kHz}$	$\hbar\omega_q^0 = h \times 100 \text{ kHz}$

Table 8.1: Conditions for Bragg scattering in the phonon and the free-particle regimes. The two regimes can be distinguished by comparing the Bragg scattering velocity $\hbar q/m$ is compared to the speed of Bogoliubov sound $c = \sqrt{\mu/m}$, or, similarly, the Bragg scattering kinetic energy $\hbar\omega_q^0 = \hbar^2 q^2/2m$ to the chemical potential μ . Bragg scattering using beams inclined by 14° to one another accessed the phonon regime, while the use of counter-propagating beams accessed the free-particle regime.

is the difference between the wavevectors of the laser beams used for scattering, is smaller than the inverse healing length $\xi^{-1} = \sqrt{2m\mu/\hbar^2}$. Equivalently, the Bragg scattering velocity $\hbar q/m$ is smaller than the speed of sound c . One can also distinguish the free-particle from the phonon regime by comparing the Bragg scattering recoil energy $\hbar\omega_q^0$ to the condensate interaction energy μ : $\hbar\omega_q^0 \ll \mu$ in the phonon regime, and $\hbar\omega_q^0 \gg \mu$ in the free-particle regime.

The conditions for Bragg scattering in our two experiments are shown in Table 8.1. Bragg scattering in the free-particle regime was studied by using two counter-propagating Bragg beams, yielding a Bragg scattering velocity of $2\hbar k/m \simeq 6 \text{ cm/s}$ and a Bragg scattering kinetic energy of $h \times 100 \text{ kHz}$ which are larger than the Bogoliubov speed of sound ($\approx 1 \text{ cm/s}$) and the chemical potential ($\approx h \times 6 \text{ kHz}$), respectively. To access the phonon regime, we used Bragg beams which were inclined at a small angle of about 14° with respect to one another. This yielded $\hbar q/m \simeq 7 \text{ mm/s}$ and $\omega_q^0 \simeq 2\pi \times 1.5 \text{ kHz}$, implying that Bragg scattering in a trapped Bose-Einstein condensate would occur in the phonon regime.

In our study of Bragg scattering in the phonon regime, we used an identical optical setup to access both the phonon regime and the free-particle regime and directly compare them. This was done by performing Bragg scattering on either a trapped Bose-Einstein condensate, or on a condensate that had been allowed to freely-expand for 5 ms before the Bragg excitation. As discussed above, excitation in the trapped condensate occurred in the phonon regime. As for the expanded cloud, its density was reduced during the 5 ms time of flight by a factor of 23 and thus the speed of sound by a factor of 5 from that of a trapped Bose-Einstein condensate. Therefore, excitations in expanded cloud occurred in the free-particle regime.

As discussed in Ref. [21], the Bragg scattering spectrum was measured for trapped condensates at various densities and for expanded clouds. We found that the Bragg scattering response in the phonon regime was significantly weaker in strength and shifted upwards in frequency from that of free particles. This behaviour is predicted for homogeneous Bose-Einstein condensates, as discussed in previous sections, and can be regarded as revealing the presence of correlated pair excitations and quantum depletion in the condensate.

The theoretical description of a homogeneous Bose–Einstein condensate could be used directly to describe an inhomogeneous trapped condensate through a local density approximation. This was possible because the predicted Doppler width of the excitation, $\Delta\omega_D \sim \hbar q/mz_{c,0} \simeq 2\pi \times 4$ Hz, was much smaller than the mean–field broadening (on the order of a kHz). Using the density distribution of a condensate in the Thomas–Fermi regime and the predicted $S(\vec{q}, \omega)$ for a homogeneous condensate at the local value of the density, the Bragg resonance line shape is calculated to be

$$I(\omega) d\omega = \frac{15}{8} \frac{\omega^2 - \omega_q^{02}}{\omega_q^0(\mu/\hbar)^2} \sqrt{1 - \frac{\omega^2 - \omega_q^{02}}{2\omega_q^0\mu/\hbar}} d\omega \quad (8.45)$$

from which one can obtain the line strength $S(\vec{q})$ and center frequency by integration. In the free–particle regime ($\hbar\omega_q^0 \gg \mu$), this expression reduces to that shown in Eq. 8.31. Explicitly, the static structure factor of a harmonically–confined Bose–Einstein condensate is given by

$$S(\vec{q}) = \frac{15\eta}{64}(y + 4\eta - 2y\eta^2 + 12\eta^3 - 3y\eta^4) \quad (8.46)$$

where $\eta^2 = \hbar\omega_q^0/2\mu$ and $y = \pi - 2 \arctan((\eta^2 - 1)/2\eta)$. The line strength has the limiting values of $S(\vec{q}) \rightarrow 15\pi/32 (\hbar\omega_q^0/2\mu)^{1/2}$ in the phonon regime and $S(\vec{q}) \rightarrow 1 - 4\mu/7\hbar\omega_q^0$ in the free–particle regime. In accordance with the f –sum rule, the center frequency $\bar{\omega}$ is given as $\omega_q^0/S(\vec{q})$.

This prediction for the Bragg resonance line strength and center frequency were in excellent agreement with our measurements. The mean–field shift of the Bragg resonance in the phonon regime was clearly smaller than the $4\mu/7\hbar$ shift which was measured in the free–particle regime. This demonstrates the collective nature of phonon excitations. Dynamically, this means that the repulsion of phonons from an inhomogeneous Bose–Einstein condensate is smaller than the repulsion of free particles.

8.10 Suppression of light scattering from a Bose–Einstein condensate

The diminished line strength for stimulated light scattering observed in the phonon regime shows that inelastic spontaneous light scattering (Rayleigh scattering) from a Bose–Einstein condensate is different from the light scattering from an equal number of non–interacting atoms. Let us consider, then, Rayleigh scattering from a homogeneous Bose–Einstein condensate with a chemical potential μ . Light scattered at an angle θ from an incident beam of light with wavevector \vec{k} imparts a momentum of magnitude $\hbar q = 2\hbar k \sin(\theta/2)$. The

intensity of light scattered at this angle is diminished by a factor

$$S(q) = \sqrt{\frac{\hbar\omega_q^0}{\hbar\omega_q^0 + 2\mu}} = \frac{2k \sin(\theta/2)}{\sqrt{(2k \sin(\theta/2))^2 + 2\xi^{-2}}} \quad (8.47)$$

Integrating over all possible scattering angles θ and accounting for the dipolar emission pattern, we find that Rayleigh scattering from a homogeneous interacting Bose–Einstein condensate is suppressed in relation to scattering from free particles by a factor

$$\begin{aligned} F &= \frac{3}{8\pi} \int d\Omega (\cos^2 \theta + \sin^2 \theta \sin^2 \phi) \frac{2k \sin(\theta/2)}{\sqrt{(2k \sin(\theta/2))^2 + 2\xi^{-2}}} \\ &= \frac{\left[\sqrt{2x} (15 + 46x + 64x^2 + 64x^3) - 3\sqrt{1+2x} (5 + 12x + 16x^2) \tanh^{-1} \left(\sqrt{\frac{2x}{1+2x}} \right) \right]}{64x^3 \sqrt{1+2x}} \end{aligned} \quad (8.48)$$

where $x = \hbar\omega_k^0/\mu$.

This suppression in Rayleigh scattering should be observable in current Bose–Einstein condensation experiments (Fig. 8-4). For example, Rayleigh scattering of near-resonant light from a sodium condensate at a density of $3 \times 10^{15} \text{ cm}^{-3}$, which is the maximum density of condensates which has been obtained in optical traps [10], should be reduced by a factor of two. It would also be interesting to measure this suppression of light scattering at a Feshbach resonance [11], where the chemical potential can be made quite large by tuning the scattering length a using magnetic fields. In such experiments, light scattering may allow one to study dynamically how the pair correlations in a condensate are established in response to a sudden increase in the interaction strength.

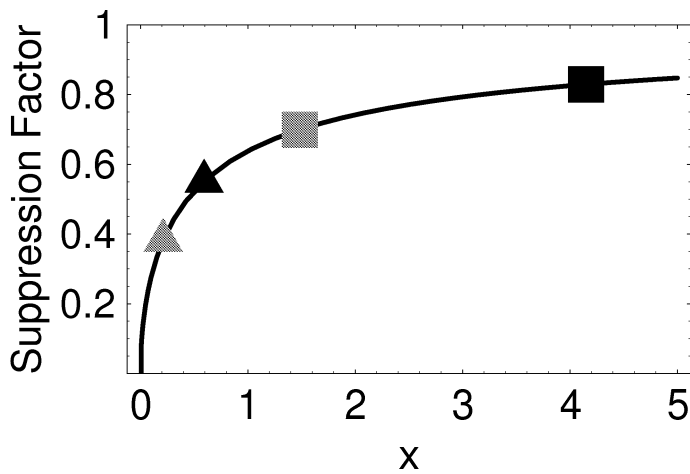


Figure 8-4: Rayleigh scattering from a homogeneous interacting Bose–Einstein condensate is suppressed with respect to scattering from free atoms. The suppression factor is plotted against $x = E_r/\mu u$ where $E_r = \hbar\omega_k^0$ is the recoil energy μ the chemical potential, and k the wavevector of the incident light. Points indicate the factor by which the scattering of near-resonant (black symbols) and infrared light at $\lambda = 985$ nm (gray symbols) is suppressed at typical condensate densities attained in our magnetic ($n = 4 \times 10^{14} \text{ cm}^{-3}$, squares) and optical ($n = 3 \times 10^{15} \text{ cm}^{-3}$, triangles) traps.

Chapter 9

An optical dipole trap for Bose–Einstein condensates

This chapter describes the optical trapping of Bose–Einstein condensates which was first presented in the following publication:

- *D.M. Stamper-Kurn, M.R. Andrews, A.P. Chikkatur, S. Inouye, H.-J. Miesner, J. Stenger and W. Ketterle, “Optical confinement of a Bose–Einstein condensate,” Phys. Rev. Lett. **80**, 2027 (1998). Included in Appendix D.*

Section 9.1 is taken for the following review paper:

- *W. Ketterle, D.S. Durfee, and D.M. Stamper-Kurn, “Making probing and understanding Bose–Einstein condensates,” in M. Inguscio, S. Stringari and C.E. Wieman eds., *Bose–Einstein Condensation in Atomic Gases, Proceedings of the “Enrico Fermi” Summer School, July 1998, Varenna, Italy (to be published)*.*

Many of the experiments in the previous chapters were performed with magnetically trapped Bose–Einstein condensates. The magnetic trap had the benefit of providing a well–characterized trapping potential which allowed for quantitative studies of condensate properties. However, magnetic traps do have limitations. For example, only weak–field seeking hyperfine states can be magnetically confined. This imposes limitations on studies of atomic properties such as collisional resonances which depend crucially on the hyperfine state, or of multi–component condensates which would be unstable in an inhomogeneous magnetic field. Magnetic traps cannot trap atoms in the magnetically neutral $|m_F = 0\rangle$ state at low field, limiting the use of condensates for precision experiments and metrological applications. Finally, the long range inhomogeneous magnetic fields interfere with the use of atom laser pulses which are output from magnetically trapped condensates (even pulses of atoms in the $|m_F = 0\rangle$ state are affected by quadratic Zeeman shifts) [5].

These limitations led us to the development of an all–optical trap for Bose–Einstein

condensates [10] (Appendix D). This trap became a central tool in our research, and enabled a variety of new experiments:

- Optical traps allow precise spatial (micrometer) and temporal (microsecond) manipulation of Bose-Einstein condensates. We used this fine spatial resolution to create the “dimple” trap in which BEC was created adiabatically and reversibly (Sect. 6.2).
- Optical traps have a new external degree of freedom: they can be operated at arbitrary external magnetic fields. We used this feature for the observation of Feshbach resonances in strong-field seeking states of sodium which cannot be confined magnetically [11, 16].
- Optical traps offer a new internal degree of freedom: the orientation of the atomic spin. This allowed for the creation of spinor condensates, condensates which populate all three hyperfine states of the $F = 1$ manifold of sodium and possess a three-component vectorial order parameter (Chapter 10).

In this chapter, I summarize this development, beginning with a section from our contribution to the proceedings of the 1998 “Enrico Fermi” Summer School in Varenna, Italy [22]. To this discussion, in Secs. 9.2 and 9.3, I append descriptions of our optical setup which was used for several experiments with optically trapped condensates, and of the typical efficiencies of transferring atoms from the magnetic to the optical trap. Further details are found in two review papers [22, 168].

9.1 Overview from the Varenna proceedings, Ref. [22]

In this section, I include the subsection entitled “Optical confinement of a Bose-Einstein condensate” from Ketterle, Durfee, and Stamper-Kurn, “Making probing and understanding Bose-Einstein condensates,” in M. Inguscio, S. Stringari and C.E. Wieman eds., *Bose-Einstein Condensation in Atomic Gases*, Proceedings of the “Enrico Fermi” Summer School, July 1998, Varenna, Italy (to be published). This text introduces the optical trap chosen for our work, and describes some properties of the optically trapped condensates such as their density, their high condensate fraction, their decay by three-body collisions, and their trap lifetime. Some minor modifications have been made to conform to the symbols and section headings used in this dissertation.

One of the long-standing goals of optical cooling and trapping techniques has been the creation, storage, and probing of Bose–Einstein condensates by purely optical means. This pursuit has provided one motivation for the development of sub-recoil cooling techniques [282, 283], various optical dipole traps [113, 139, 284–286], and Raman [117, 287, 288] and evaporative [289] cooling in such traps. However, to date, optical cooling schemes have not reached the phase-space density necessary for BEC, the closest approach being a factor of 300 short [117, 287] [*now about 50 [118, 119]*]. One major difficulty is that reaching a phase-space density of unity requires both low temperatures and high densities. Using the recoil temperature as a benchmark, a gas will Bose condense only at densities higher than one atom per cubic wavelength, coinciding with the regime where high optical densities wreak havoc with near-resonant laser cooling schemes. In contrast, evaporative cooling — which even in optical dipole traps relies on atom–atom interactions rather than atom–light interactions [289] — becomes *more efficient* at high densities.

We have taken a different approach toward controlling BEC by purely optical means: we first brought a gas to BEC by evaporative cooling in a magnetic trap, and then transferred it to an optical trap [10]. We chose the parameters of the optical trap based on two criteria: the trap had to be deep enough to confine Bose condensates, and have sufficiently low heating rates to permit studies of the condensates for long periods of time.

The confining potential of an optical trap is due to the AC Stark shift and given by

$$U(\vec{r}) = -\frac{\hbar\omega_R^2(\vec{r})}{4} \left(\frac{1}{\omega_0 - \omega_L} + \frac{1}{\omega_0 + \omega_L} \right) \simeq \frac{\hbar\omega_R^2(\vec{r})}{4\Delta} \quad (9.1)$$

where ω_0 is the resonant frequency, ω_L the laser frequency and $\Delta = \omega_L - \omega_0$ its detuning. The Rabi frequency $\omega_R(\vec{r})$ is position dependent, and conveniently defined through $2\omega_R^2(\vec{r})/\Gamma^2 = I(\vec{r})/I_{\text{SAT}}$ where the intensity is scaled by the saturation intensity $I_{\text{SAT}} = \hbar\omega_0^3\Gamma/12\pi c^2$ which is 6 mW/cm² for sodium.

Besides the conservative potential $U(\vec{r})$, the laser light can also induce heating via Rayleigh scattering and power or position jitter of the beam. The rate of Rayleigh scattering is given by

$$\gamma_R = \left(\frac{\omega_L}{\omega_0} \right)^3 \frac{\Gamma^3}{8} \left(\frac{1}{\omega_0 - \omega_L} + \frac{1}{\omega_0 + \omega_L} \right)^2 \frac{I}{I_{\text{SAT}}} \quad (9.2)$$

Neglecting counter-rotating terms ($|\Delta| \ll \omega_0$), the potential depth scales as I/Δ while the scattering rate scales as I/Δ^2 . While near-resonant light can provide large trap depths it can also cause severe heating. Thus, as indicated in Table 9.1, optical dipole traps have tended toward larger detunings which has necessitated the use of high laser powers to provide sufficient confinement for laser-cooled atoms.

In contrast, in our approach we use evaporative cooling as a precursor for optical trapping and reduce the temperature of trapped atoms by a factor of 100. Thus, even at large detunings, only milliwatts of laser power are needed as compared with several watts used to

Table 9.1: Optical dipole traps: a light sampler.

	Detuning Δ/Γ	Power (Watts)	Depth (mK)	Number of atoms	Density (cm $^{-3}$)
Chu ('86) [113]	10^4	0.2	5	500	8×10^{11}
Heinzen ('93) [284]	2×10^5	0.8	6	10^4	2×10^{12}
Chu <i>et al.</i> ('95) [289]	2×10^7	8	0.9	5×10^5	4×10^{12}
optically trapped BEC [10]	7×10^7	$\simeq 0.005$	$\simeq 0.005$	10^7	$10^{14} - 10^{15}$

directly trap laser-cooled atoms, making for traps which are easier to handle and trapped atoms which are longer lived. Furthermore, since the cloud shrinks while being cooled in the magnetic trap, the transfer efficiency into the small trapping volume of an optical dipole trap is increased. Thus, magnetic trapping and evaporative cooling are an ideal way to “funnel” atoms into an optical trap, which might be useful for a host of applications such as photoassociation spectroscopy and cavity QED.

The optical trap was formed by focusing a single near-infrared laser beam into the center of the magnetic trap along the axial direction. Similar single-beam setups have been used in the past [113, 139, 284, 285]. The light intensity distribution at the optical focus, which gives the trapping potential via eq. (9.1), is given by

$$I(r, z) = \frac{2P}{\pi w_0^2(1 + (z/z_R)^2)} \exp\left(-\frac{2r^2}{w_0^2(1 + (z/z_R)^2)}\right) \quad (9.3)$$

where P is the laser power, w_0 is the $1/e^2$ beam waist radius, z_R is the Rayleigh range, and r and z are the distance from the focus along the radial and axial directions, respectively. The length scales w_0 and z_R are related as $z_R = \pi w_0^2/\lambda$ where λ is the wavelength of the trapping laser. The bottom of the trapping potential can be approximated as a harmonic oscillator with frequencies ν_r and ν_z . At the wavelength of $\lambda = 985$ nm which we chose, the trap depth U , the radial frequency ν_r and the aspect ratio ν_r/ν_z are

$$U/k_B \simeq 1 \mu\text{K} \times \frac{P}{\text{mW}} \times \left(\frac{6 \mu\text{m}}{w_0}\right)^2 \quad (9.4)$$

$$\nu_r \simeq 1 \text{ kHz} \times \left(\frac{U}{k_B \mu\text{K}}\right)^{1/2} \times \frac{6 \mu\text{m}}{w_0} \quad (9.5)$$

$$\frac{\nu_r}{\nu_z} \simeq 28 \times \frac{6 \mu\text{m}}{w_0} \quad (9.6)$$

The benchmark $w_0 = 6 \mu\text{m}$ in the above equations is the beam radius obtained with an $f/\# = 10$ imaging lens. Finally, the small spontaneous scattering rate from the far-detuned trapping beam ($5 \times 10^{-3} \text{s}^{-1}$ per μK trap depth) has not limited our experiments, therefore there is little incentive to reduce this rate even further by using far-infrared [285] or blue-detuned traps [286, 287].

Condensates were transferred into the optical trap by holding them in a steady magnetic trap while ramping up the infrared laser power, and then suddenly switching off the magnetic trap. Nearly complete transfers of the atoms were observed, with condensate numbers in the optical trap as high as 10^7 . For various experiments, we have produced optical traps with beam radii ranging between 6 and 20 μm , and with infrared powers ranging from 5 to 50 mW.

Condensates in the optical trap are unusually pure, i.e. the condensate fraction is very high. This is because the optical trap has a small volume, forcing the number of uncondensed atoms to be very low. An estimate for this number can be obtained by assuming that the temperature T of the cloud is about 1/10th of the trap depth (the optical trap has “built-in” evaporative cooling due to the limited trap depth). The number of non-condensed atoms is approximately $(k_B T / \hbar \bar{\omega})^3$, which for typical conditions is a few times 10^4 atoms, in quantitative agreement with our measurements. With a condensate of about 5 million atoms, this estimate indicates a condensate fraction greater than 99%. “Pure” condensates in magnetic traps usually have a larger non-condensed fraction due to the smaller trapping frequencies and the technical difficulty of adjusting a small trap depth using rf-induced evaporation, since the trap depth is sensitive to stray magnetic fields. In the future, condensate “purification” by optical trapping may allow studies of various predicted zero-temperature phenomena, such as collapses and revivals of collective excitations [237], small shifts of excitation frequencies due to quantum depletion which might otherwise be masked by finite-temperature effects [244], or generally for high-coherence atom lasers.

Our optically trapped condensates were long-lived. The observed losses were dominated by three-body recombination losses, with loss rates per atom ranging from 4 s^{-1} at a peak density $n_0 = 3 \times 10^{15} \text{ cm}^{-3}$ to less than $1/10 \text{ s}^{-1}$ at $n_0 = 3 \times 10^{14} \text{ cm}^{-3}$.

From these lifetime measurements, we can estimate an upper limit for the heating caused by beam jitter and spontaneous scattering in the optical trap. An analysis of the observed number losses indicated a density independent loss rate of $0.03(2) \text{ s}^{-1}$. Assuming a trap depth of about 5 μK , this implies a heating rate of about 150 nK/s, which is larger than the 25 nK/s heating rate one would expect from spontaneous scattering alone. Another estimate of this heating rate was obtained by shining the infrared light onto a sample of gas in the magnetic trap, and monitoring the temperature of the gas in this combined potential (fig. 6-3) [14]. Accounting for the fact that atoms spent only about 10% of the time in the optical potential, we arrive again at a heating rate of about 100 nK/s.

The optical dipole force exerted by a tightly focused laser beam easily exceeds the magnetic forces of typical magnetic traps. Therefore, optically trapped condensates can be easily compressed to extremely high densities, as high as $3 \times 10^{15} \text{ cm}^{-3}$ in some of our work. At such densities, the three-body recombination rate is extremely high, but transient experiments on such dense samples are still possible. At the low-density end, we have produced condensates with several million atoms at densities of about $1 \times 10^{13} \text{ cm}^{-3}$ in a

decompressed magnetic trap with a mean frequency $\bar{\omega} = 2\pi \times 7 \text{ Hz}$. This wide range of possible condensate densities is impressive, especially considering that a few years ago there were many discussions whether the “BEC window” existed at all.

Besides opening new scientific possibilities, the optical trap may become a practical tool to manipulate and transport condensates. It may serve as an “optical tweezers” to move condensates into optical or microwave cavities or close to surfaces.

9.2 Optical setup

The infrared light for our optical dipole trap was derived from an SDL5762 diode MOPA laser operating at 985 nm, which was graciously lent to us by Erich Ippen and his colleagues at MIT. The laser was powered with a commercially available current supply and temperature controller which allowed us to switch the laser on and off within microseconds and to stabilize the laser power of the dipole trap. Light from the laser was sent into a single-mode fiber, providing a TEM_{00} Gaussian mode for use in the trap.

The divergent infrared light exiting the fiber was expanded in a three-lens telescope before being sent into the chamber through the axial “penny windows” (see Fig. 3-1). Lenses were placed on translation mounts to allow us to vary the axial focal position and the size of the infrared beam at the final focusing lens (a 50 mm diameter, 250 mm focus achromat) reproducibly. Optical access through the “penny windows” was simultaneously needed for the infrared optical trapping light and for two near-resonant beams used for the magneto-optical trap and for probing. These three beams were combined with the use of a polarizing beam-splitter and a dichroic mirror.

After passing through the chamber, the infrared light was imaged onto a CCD camera at a magnification of $M = 8$. The same imaging setup was also used to image the trapped atomic cloud with near-resonant light. This allowed us to overlap the small optical focus and the magnetically trapped cloud (both with radial dimensions of about 10 μm). Using the same imaging system for both infrared (985 nm) and near-resonant (589 nm) light resulted in substantial chromatic shifts between the apparent position of the optical focus and of the trapped cloud. These were accounted for by calibrating the imaging system with a test pattern which was illuminated by laser light of either wavelength. After such calibration, the optical trap could be aligned within about an hour, often requiring only minor adjustments throughout a night of data taking.

9.3 Transfer efficiency

The procedure for transferring the Bose-Einstein condensate from the magnetic trap to the optical trap was simple. After creating the condensate in the magnetic trap, the optical trap was ramped on over typically 125 ms, and then the magnetic trap was suddenly switched off. While it would have been preferable to transfer atoms to the optical trap by switching off the magnetic trap gradually, misalignments in our magnetic coils which displaced the center of the magnetic trap during a gradual switch-off prevented us from doing so successfully. Nevertheless, we were able to transfer nearly all the atoms into the optical trap.

The outcome of this transfer procedure is shown in Figs. 9-1 and 9-2. A Bose-Einstein condensed gas was first produced in the magnetic trap, and then the optical trap was ramped up. This produced a strong attractive potential at the center of the magnetic trap in which most of the trapped atoms accumulated (Fig. 9-2b). Then the magnetic trap

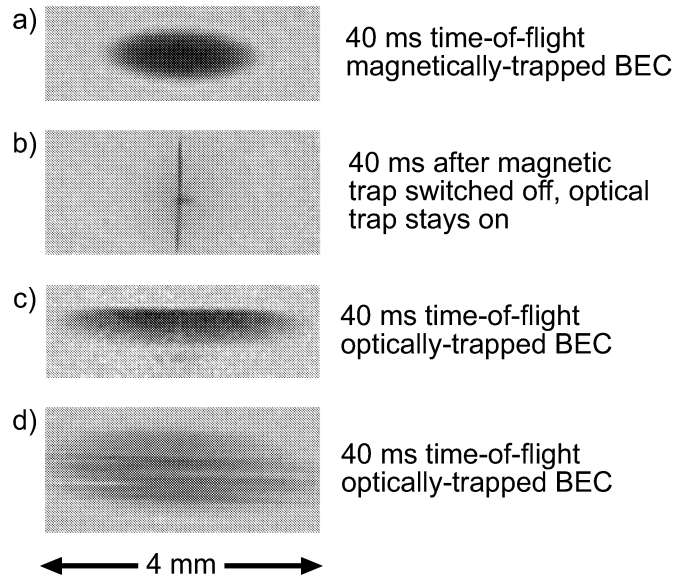


Figure 9-1: Transfer of atoms from the magnetic to the optical trap observed in time-of-flight images. (a) A Bose–Einstein condensate is produced in the magnetic trap. (b) After the infrared light is ramped on, the magnetic trap is switched off. The untrapped atoms fall away, leaving behind a dense optically-trapped cloud. (c) The anisotropic expansion of an optically-trapped cloud to a width greater than that in (a) reveals the presence of a condensate which is denser than its magnetically trapped precursor. Notice the presence of a second, smaller condensate in the lower part of the image, presumably trapped in a secondary minimum of the optical trap formed by an astigmatic trapping beam. (d) The striated appearance of an optically-trapped condensate probed soon after the transfer indicates motional excitation during the transfer, which is typically damped within about half a second.

was switched off suddenly, causing the untrapped atoms to fall away and leaving behind a purely optically-trapped gas (Figs. 9-1b, 9-2c). The optically-trapped cloud was later probed in time-of-flight. The anisotropic expansion of the optically-trapped cloud (Fig. 9-1c) indicated that the remaining gas was Bose condensed and that the density of the optically-trapped condensate was generally larger than that of its magnetically-trapped precursor.

Such images allowed us to characterize the transfer between the magnetic and optical traps and to choose optimal settings for maximizing the transfer efficiency (Fig. 9-3). For example, transfers into an optical trap with too little infrared laser power resulted in most of the atoms being untrapped and falling away from the optical trap when the magnetic trap was switched off. Transfers at too high a laser power increased the atomic density in the combined optical and magnetic trap, causing inelastic three-body collisions to deplete the trap even before the magnetic trap was switched off. Similarly, the 125 ms ramp-up time was chosen after noting that very rapid ramp-ups caused the cloud to be motionally excited and to slosh out of the optical trap, while longer ramp-up times caused the atomic

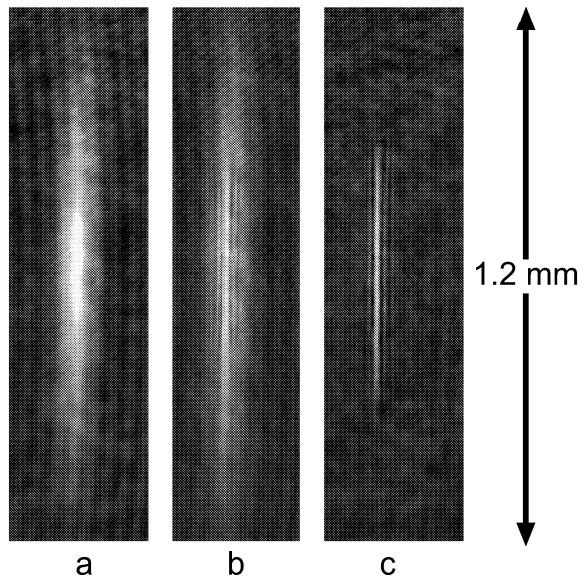


Figure 9-2: Transfer of atoms from the magnetic to the optical trap observed *in situ*. (a) A partly-condensed magnetically-trapped cloud is exposed to a focused infrared laser beam which (b) attracts some, but not all of the atoms to its focus. (c) After the magnetic trap is switched off, an extremely narrow trapped cloud remains. The width of the cloud is equal to or less than the $\simeq 5 \mu\text{m}$ resolution of our imaging system, as indicated by the sharp diffraction fringes in the phase-contrast image.

gas to be depleted by three-body losses.

The settings that were finally chosen for the optical trap were quite robust. Transfer efficiencies between 85% and 100% were repeatedly attained. While the rapid switch-off of the magnetic trap often left optically-trapped clouds with substantial motional excitations, as seen in striated time-of-flight images (e.g. 9-1d), these excitations typically damped out within a fraction of a second, at which point we could begin experiments on the optically-trapped clouds with well-characterized initial conditions.

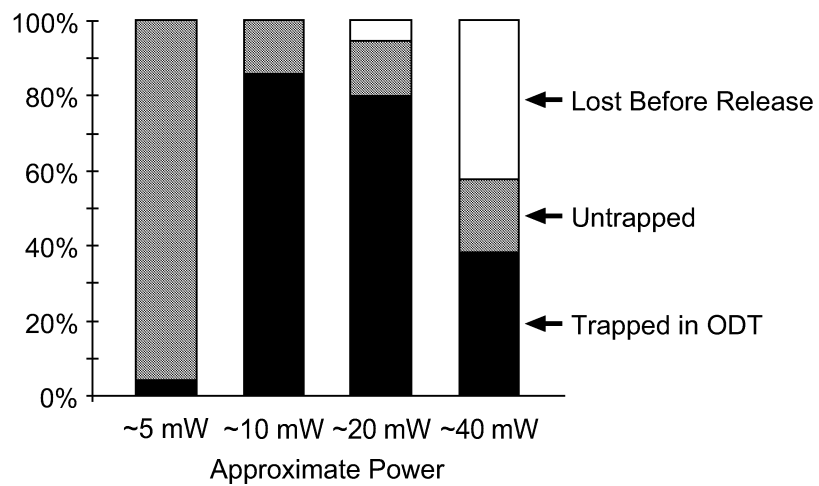


Figure 9-3: Efficiency of transfer from the magnetic to the optical trap. The transfer is characterized for different powers to which the infrared trapping light is ramped up. Atoms are divided between those transferred into the optical trap, those which are untrapped and are observed to escape the trap in time-of-flight figures (e.g. 9-1b), and those which are lost during the ramp-up time of the infrared light due to increased trap losses. An optimum infrared power (here 10 mW, but usually lower), was chosen as providing sufficient trap depth to hold the Bose condensate while maintaining a low enough density to prevent rapid losses due to three-body collisions.

Chapter 10

Spinor Bose–Einstein condensates

This chapter describes our research on spinor Bose–Einstein condensates which is reported in three publications:

- *J. Stenger, S. Inouye, D.M. Stamper-Kurn, H.-J. Miesner, A.P. Chikkatur, and W. Ketterle, “Spin domains in ground state spinor Bose-Einstein condensates,” Nature **396**, 345 (1998).*
- *H.-J. Miesner, D.M. Stamper-Kurn, J. Stenger, S. Inouye, A.P. Chikkatur and W. Ketterle, “Observation of metastable states in spinor Bose-Einstein condensates,” Phys. Rev. Lett. **82**, 2228 (1999). Included in Appendix H.*
- *D.M. Stamper-Kurn, H.-J. Miesner, A.P. Chikkatur, S. Inouye, J. Stenger and W. Ketterle, “Quantum tunneling across spin-domains in a Bose-Einstein condensate,” Phys. Rev. Lett. **83**, 661 (1999). Included in Appendix I.*

The experiments described in previous chapters explored the nature of Bose–Einstein condensates of atomic gases in which all the atoms were in the same internal state, the $|F = 1, m_F = -1\rangle$ hyperfine state of sodium. The Bose–Einstein condensation phase transition leads to a non–zero value of a *scalar* order parameter, the condensate wavefunction $\psi(\vec{r}) = \langle \hat{\Psi}(\vec{r}) \rangle$. As such, a single–component gaseous condensate can be considered as a simple, tractable model of the more complicated spinless superfluid ^4He . Many of the experiments in recent years have explored aspects of this connection between the two quantum fluids.

However, unlike ^4He , the alkali atoms which constitute the gaseous Bose–Einstein condensates have a non–zero spin and therefore numerous internal hyperfine states which are stable electronic ground states. Thus, there exists the possibility of creating a quantum fluid simultaneously composed of several, distinguishable components by Bose condensing a gas of atoms in several hyperfine states.

The study of multi–component superfluid systems has been a tantalizing goal of low–temperature physics for decades. The earliest discussion focused on $^4\text{He} – ^6\text{He}$ mixtures.

^6He is radioactive with a half-life of 1 second. An ambitious experiment by Guttman and Arnold [290] in 1953 sought evidence for the superfluid flow of ^6He mixed with ^4He to no avail. Nevertheless, this pursuit touched off a series of theoretical works on two-component superfluid hydrodynamics [291, and others since]. In 1978, Colson and Fetter [292] considered such mixtures in the context of mean-field theories which apply directly to current experiments, and discussed the criterion for interactions between the superfluids to cause miscibility or phase-separation. After progress in the stabilization of a spin-polarized atomic hydrogen gas, Siggia and Ruckenstein [93] considered the use of different hyperfine states to achieve a mixture of superfluids. Since the observation of gaseous Bose condensates, the interest in multi-component condensates has been revived with a flurry of theoretical attention [293–296, for example].

For atomic gases trapped in magnetic traps, the availability of hyperfine states is restricted by the requirement that the trapped atoms remain in weak-field seeking states (see Fig. 3-4). For example, alkali atoms with a nuclear spin of $I = 3/2$, such as ^{87}Rb and ^{23}Na , have three weak-field seeking states at zero-field: one in the lower hyperfine state ($|F = 1, m_F = -1\rangle$), and two in the upper hyperfine state ($|F = 2, m_F = +1, +2\rangle$). Generally, the simultaneous confinement of more than one of these states is unstable to exothermic hyperfine state changing collisions. For example, the rate constant for inelastic collisions between atoms in the upper ($F = 2$) and lower ($F = 1$) hyperfine manifolds of sodium is predicted to be on the order of $K_{UL} \approx 10^{-10} \text{ cm}^3/\text{s}$, giving a lifetime of about $(K_{UL} \times n)^{-1} \approx 100 \mu\text{s}$ at a typical density of $n = 10^{14} \text{ cm}^{-3}$ [256].

However, it was recently found that magnetically-trapped multi-component gases of ^{87}Rb are quite long lived due to a fortunate near-equality of the singlet and triplet scattering lengths which greatly suppresses the spin exchange collision rate [253–256]. This allowed for the creation of the first multi-component condensates at JILA [253] by the simultaneous magnetic confinement of ^{87}Rb atoms in the $|F = 1, m_F = -1\rangle$ and $|F = 2, m_F = 2\rangle$ (and, in later work, $|F = 2, m_F = 1\rangle$) states. The JILA BEC group has used magnetically trapped multi-component condensates for a remarkable series of experiments. Studies have probed the spatial separation of a two-component Bose-Einstein condensate [155, 253] and the stability of a relative phase between the two components even in the presence of dissipation [157]. More recently, the JILA group has begun to explore the nature of multi-component condensates in the presence of continuous resonant and non-resonant rf coupling between the components. Such coupling links the external center-of-mass and the internal degrees of freedom of the condensed gas and gives rise to a rich variety of dynamical effects such as Josephson-type oscillations [297] and spin-wave excitations [298, 299], as well as new techniques for manipulating the phase of the condensate wavefunction [300, 301]. Some of this work is reviewed in Refs. [302, 303].

In contrast, a far-off-resonant optical trap confines atoms regardless of their hyperfine state. Thus, the atomic spin is liberated from the requirements of magnetic trapping and

becomes a new degree of freedom. In particular, all atoms in the lower hyperfine manifold, for example the $F = 1$ hyperfine manifold of sodium, can be stably trapped simultaneously without suffering from hyperfine manifold changing collisions. Such multi-component optically trapped condensates are represented by an order parameter which is a vector in hyperfine spin space, and are thus called spinor Bose–Einstein condensates. A variety of new phenomena are predicted for this new quantum fluid such as spin textures, spin waves, and coupling between atomic spin and superfluid flow [304, 305, 307].

Spinor Bose condensates differ from other multi-component Bose condensates, such as the experimentally realized ^{87}Rb mixtures or the proposed mixtures of several atomic species, in important ways stemming from symmetries under rotations of the vectorial order parameter. Furthermore, spin relaxation collisions within the lower $F = 1$ hyperfine manifold

$$|m_F = 0\rangle + |m_F = 0\rangle \leftrightarrow |m_F = +1\rangle + |m_F = -1\rangle \quad (10.1)$$

allow for population mixing among the different hyperfine states without trap loss. In contrast, spin relaxation is the major limitation to the lifetime (about a second) of the ^{87}Rb mixtures.

Since the realization of an optical trap for Bose–Einstein condensates, our group has pioneered the experimental study of this new quantum fluid. In three different experiments we explored the ground-state spin structure of spinor condensates in external magnetic fields [15], the formation and persistence of metastable spin domain configurations [17], and the transport across spin domain boundaries by quantum tunneling [19]. In this chapter, I will summarize our current understanding of this fluid as derived from our experiments and from a growing number of theoretical works. While a portion of this work has been reviewed in Refs. [22, 168], this chapter is the first comprehensive review on spinor Bose–Einstein condensates.

10.1 The implications of rotational symmetry

An $F = 1$ spinor Bose–Einstein condensate is described by a three-component order parameter

$$\vec{\psi}(\vec{r}) = \begin{pmatrix} \psi_1(\vec{r}) \\ \psi_0(\vec{r}) \\ \psi_{-1}(\vec{r}) \end{pmatrix} \quad (10.2)$$

and can thus be regarded as a particular instance of a multi-component condensate. However, the spinor Bose–Einstein condensate is distinguished from a general, multi-component quantum fluid by the fact that the order parameter $\vec{\psi}$ transforms as a vector. The vectorial character of the order parameter has a pronounced effect on interatomic interactions, and defines important features of the spinor condensate at zero magnetic field, where the rotational symmetry of the system is preserved.

In second-quantized notation, the Hamiltonian for a multi-component gas has the general form

$$\begin{aligned}\hat{\mathcal{H}} = & \int d^3\vec{r} \left\{ \hat{\Psi}_i^\dagger(\vec{r}) \left(-\frac{\hbar^2 \nabla^2}{2m} \delta_{ij} + U_{ij}(\vec{r}) \right) \hat{\Psi}_j(\vec{r}) \right. \\ & \left. + \frac{g_{ij,kl}}{2} \int d^3\vec{r}_1 d^3\vec{r}_2 \hat{\Psi}_i^\dagger(\vec{r}_1) \hat{\Psi}_j^\dagger(\vec{r}_2) \hat{\Psi}_k(\vec{r}_2) \hat{\Psi}_l(\vec{r}_1) \delta(\vec{r}_1 - \vec{r}_2) \right\}\end{aligned}\quad (10.3)$$

where the indices i, j, k, l correspond to the N components of the gas, and repeated indices are summed. The general form of the external potential $U_{ij}(\vec{r})$ allows for a potential which is not diagonal in the hyperfine spin basis, in which case it can represent a Josephson coupling between spin components. The $U_{ij}(\vec{r})$ terms also contain the effects of magnetic fields which are discussed in later sections.

The interatomic interaction (second line of the above expression) has been approximated as a contact interaction in which the coefficients $g_{ij,kl}$ describe the strength of the various elastic and inelastic (state converting) collisions. These generally constitute a large number of free parameters. Particle exchange ($g_{ij,kl} = g_{ji,kl}$) and time-reversal ($g_{ij,kl} = g_{kl,ij}$) symmetries reduce the number of free parameters from N^4 to $[(N^2 + N + 2)(N^2 + N)]/8$ but still a large number of interaction parameters remain*. For a three-component condensate, the number of interaction parameters is 21.

This situation is greatly simplified in the case of spinor condensates due to rotational symmetry. The rotationally symmetric characterization of two-body collisions among atoms of hyperfine spin F_1 and F_2 can only depend on their total spin $F_{\text{tot}} = F_1 + F_2$. Thus, the interatomic interaction $V_{\text{int}}(\vec{r}_1 - \vec{r}_2)$ is reduced to the form [304, 305]

$$V_{\text{int}}(\vec{r}_1 - \vec{r}_2) = \frac{4\pi\hbar^2}{m} \delta(\vec{r}_1 - \vec{r}_2) \sum_{F_{\text{tot}}} a_{F_{\text{tot}}} \tilde{\mathcal{P}}_{F_{\text{tot}}}\quad (10.4)$$

where $a_{F_{\text{tot}}}$ is the scattering length for collisions between atoms with total spin F_{tot} , and $\tilde{\mathcal{P}}_{F_{\text{tot}}}$ is the projection operator for the total spin. For colliding bosons of spin F , F_{tot} can take the values $F_{\text{tot}} = 0, 2, \dots, 2F$. Furthermore, restricting ourselves to s -wave collisions, the quantity $m_{F_{\text{tot}}}$, which is the spin projection along the z -axis (somehow defined), is conserved. Therefore, the interaction parameters $g_{ij,kl}$ describing collisions among the $N = 2F + 1$ different components of a spinor condensate of spin F depend only on $F + 1 = (N + 1)/2$ scattering lengths.

In particular, for the $F = 1$ spinor system which was realized in gaseous sodium, interactions are described fully by just two parameters, the scattering lengths $a_{F_{\text{tot}}=0}$ and

*Due to particle exchange symmetry, we may denote the interaction parameter as $g_{\mathcal{A},\mathcal{B}}$ where \mathcal{A} and \mathcal{B} are elements of the set \mathbb{P} of distinct unordered pairs of indices i, j . There are $Z = N(N+1)/2$ such pairs. Due to time-reversal symmetry, the interaction parameters are enumerated as $g_{\mathcal{Z}}$ where \mathcal{Z} is an unordered pair of elements from \mathbb{P} . Thus, the number of free interaction parameters is $Z(Z+1)/2 = [(N^2 + N + 2)(N^2 + N)]/8$.

$g_{AB,AB}$	$m_F = +1$	$m_F = 0$	$m_F = -1$
$m_F = +1$	$g_0 + g_2$	$\frac{g_0 + g_2}{2}$	$\frac{g_0 - g_2}{2}$
$m_F = 0$	$\frac{g_0 + g_2}{2}$	g_0	$\frac{g_0 + g_2}{2}$
$m_F = -1$	$\frac{g_0 - g_2}{2}$	$\frac{g_0 + g_2}{2}$	$g_0 + g_2$

Table 10.1: Interaction parameters $g_{ij,kl}$ describing elastic collisions in the $F = 1$ spinor system. The interaction Hamiltonian is defined as in Eq. 10.3. The interaction parameter responsible for spin relaxation is $g_{00,-1+1} = g_2$.

$a_{F_{\text{tot}}=2}$. The interaction potential can then be written as

$$V_{\text{int}}(\vec{r}_1 - \vec{r}_2) = \left(g_0 + g_2 \vec{F}_1 \cdot \vec{F}_2 \right) \delta(\vec{r}_1 - \vec{r}_2) \quad (10.5)$$

where the parameters g_0 and g_2 are defined as

$$g_0 = \frac{4\pi\hbar^2}{m} \frac{2a_{F_{\text{tot}}=2} + a_{F_{\text{tot}}=0}}{3} \quad (10.6)$$

$$g_2 = \frac{4\pi\hbar^2}{m} \frac{a_{F_{\text{tot}}=2} - a_{F_{\text{tot}}=0}}{3} \quad (10.7)$$

and \vec{F}_1 and \vec{F}_2 are the spin operators for the two colliding particles. The spin-dependence of the interatomic interaction is thereby isolated in the term $g_2 \vec{F}_1 \cdot \vec{F}_2 \delta(\vec{r}_1 - \vec{r}_2)$. The Hamiltonian describing a weakly-interacting Bose gas of spin $F = 1$ now becomes

$$\begin{aligned} \hat{\mathcal{H}} = & \int d^3\vec{r} \left\{ \hat{\Psi}_i^\dagger(\vec{r}) \left(-\frac{\hbar^2 \nabla^2}{2m} \delta_{ij} + V_{ij}(\vec{r}) \right) \hat{\Psi}_j(\vec{r}) \right. \\ & \left. + \frac{1}{2} \left[g_0 \hat{\Psi}_i^\dagger(\vec{r}) \hat{\Psi}_j^\dagger(\vec{r}) \hat{\Psi}_i(\vec{r}) \hat{\Psi}_j(\vec{r}) + g_2 \left(\hat{\Psi}_i^\dagger(\vec{r})(F_\eta)_{ij} \hat{\Psi}_j(\vec{r}) \right) \cdot \left(\hat{\Psi}_k^\dagger(\vec{r})(F_\eta)_{kl} \hat{\Psi}_l(\vec{r}) \right) \right] \right\} \end{aligned} \quad (10.8)$$

where the index η runs over the three coordinate axes x, y, z .

Equivalently, the Hamiltonian can be written in the form of Eq. 10.3, where all non-zero $g_{ij,kl}$ are determined by g_0 and g_2 as shown in Table 10.1. Taking into account particle exchange symmetries and gathering similar terms, the interaction Hamiltonian can be written as

$$\begin{aligned} \mathcal{H}_{\text{int}} = & \frac{1}{2} \int d^3\vec{r} \left[(g_0 + g_2) \hat{\Psi}_1^\dagger \hat{\Psi}_1^\dagger \hat{\Psi}_1 \hat{\Psi}_1 + g_0 \hat{\Psi}_0^\dagger \hat{\Psi}_0^\dagger \hat{\Psi}_0 \hat{\Psi}_0 + (g_0 + g_2) \hat{\Psi}_{-1}^\dagger \hat{\Psi}_{-1}^\dagger \hat{\Psi}_{-1} \hat{\Psi}_{-1} \right. \\ & + 2(g_0 + g_2) \hat{\Psi}_1^\dagger \hat{\Psi}_0^\dagger \hat{\Psi}_1 \hat{\Psi}_0 + 2(g_0 + g_2) \hat{\Psi}_{-1}^\dagger \hat{\Psi}_0^\dagger \hat{\Psi}_{-1} \hat{\Psi}_0 + 2(g_0 - g_2) \hat{\Psi}_1^\dagger \hat{\Psi}_{-1}^\dagger \hat{\Psi}_1 \hat{\Psi}_{-1} \\ & \left. + 2g_2 (\hat{\Psi}_0^\dagger \hat{\Psi}_0^\dagger \hat{\Psi}_1 \hat{\Psi}_{-1} + \hat{\Psi}_1^\dagger \hat{\Psi}_{-1}^\dagger \hat{\Psi}_0 \hat{\Psi}_0) \right] \end{aligned} \quad (10.9)$$

The first line includes the self-scattering terms, the second the cross-scattering terms, and the third the spin relaxation terms. Note that, as written, the cross-species scattering length discussed in Sec. 10.6 is related to $g_{AB,AB}$ as $g_{AB,AB} = 2\pi\hbar^2 a_{AB}/m$.

It is important to note that this simplification of the interaction term is only strictly valid in the absence of magnetic fields, which can break the rotational symmetry. As the magnetic field is increased, the hyperfine spin F is no longer a good quantum number for describing the atomic states, and thus collisional properties deviate from the relations imposed by rotational symmetry. Dramatic deviations from rotational symmetry can be seen, for example, at a Feshbach resonance where the scattering length for one particular collisional channel is greatly varied. Nonetheless, away from Feshbach resonances and at low magnetic fields for which the Zeeman shifts are much smaller than the hyperfine splitting, one can expect the zero-field description of collisional interactions to remain valid.

The properties of spinor Bose–Einstein condensates at zero-magnetic field have been recently discussed by a number of authors. Ho [304] and Ohmi and Machida [305] considered the ground state of a spinor condensate by an extension of Bogoliubov theory, which is discussed for a single-component gas in Sec. 7.1. The N -particle condensate ground state is found by replacing the field operators $\hat{\Psi}_i$ in Eq. 10.8 with c -number order parameters ψ_i . It is convenient to express the order parameter as $\vec{\psi} = \sqrt{n}\vec{\zeta}$ where n is the atomic density and $\vec{\zeta}$ is a three-component spinor of normalization $|\vec{\zeta}| = 1$, obtaining the energy functional

$$E = \int d^3\vec{r} \left[\psi_i^*(\vec{r}) \left(-\frac{\hbar^2 \nabla^2}{2m} \right) \psi_i(\vec{r}) + (U(\vec{r}) - \mu)n(\vec{r}) + \frac{n^2}{2} (g_0 + g_2 \langle \vec{F} \rangle^2) \right] \quad (10.10)$$

Here it is assumed that the external potential is scalar, i.e. diagonal in the hyperfine spin basis and equal for each of the spin components. The chemical potential μ determines the number of atoms in the condensate.

The ground-state spinor $\vec{\zeta}$ is determined by minimizing the spin-dependent interaction energy, $n^2 g_2 \langle \vec{F} \rangle^2 / 2$, which is expressed in terms of the average condensate spin $\langle \vec{F} \rangle_\eta = \zeta_i^*(F_\eta)_{ij} \zeta_j$. There are two distinct solutions depending on the sign of the spin-dependent interaction parameter g_2 :

- $g_2 > 0$: the collisional coupling is anti-ferromagnetic as the condensate lowers its energy by minimizing its average spin, i.e. by making $|\langle \vec{F} \rangle| = 0$. The ground state spinor is then one of a degenerate set of spinors, the “polar” states, corresponding to all possible rotations of the hyperfine state $|m_F = 0\rangle$.
- $g_2 < 0$: the collisional coupling is ferromagnetic as the condensate lowers its energy by maximizing its average spin, i.e. by making $|\langle \vec{F} \rangle| = 1$. In this case the ground state spinors correspond to all rotations of the hyperfine state $|m_F = +1\rangle$.

Han, Pu, and Bigelow [307] adopted a different approach of explicitly calculating the many-body state of a homogeneous spinor Bose–Einstein condensate without assuming a Hartree form as considered by Ho, Ohmi, and Machida. They describe an elegant transformation of the spinor Hamiltonian in terms of operators which obey an angular momentum algebra, and thus immediately yield eigenstates of the many-body Hamiltonian and their

energy spectrum. Anti-ferromagnetic coupling leads to a unique ground-state which cannot be represented in the Hartree form and which has super-Poissonian fluctuations in the population of each of the three spin states. Ferromagnetic coupling yields a degenerate family of ground states with sub-Poissonian fluctuations. The relation between the Hartree solutions and these correlated many-body solutions has not yet been adequately discussed. For example, the Hartree solution with all atoms in the $|m_F = +1\rangle$ state is included in the family of ferromagnetic ground states obtained by Han, Pu and Bigelow.

The scattering lengths $a_{F_{\text{tot}}=0}$ and $a_{F_{\text{tot}}=2}$ can be calculated by incorporating data from a variety of experiments into models of the interparticle potentials. For sodium, it is predicted that $a_{F_{\text{tot}}=2} = 2.75$ nm [189] and $a_{F_{\text{tot}}=2} - a_{F_{\text{tot}}=0} = 0.29$ nm [308]. Thus, an $F = 1$ spinor condensate of sodium should be anti-ferromagnetic. As discussed below, the anti-ferromagnetic interaction of sodium spinor condensates has been established experimentally as well. For ^{87}Rb , it appears that $a_{F_{\text{tot}}=2} - a_{F_{\text{tot}}=0} < 0$ and thus an $F = 1$ spinor condensate of ^{87}Rb should be ferromagnetic [304].

10.2 Tailoring the ground-state structure with magnetic fields

These theoretical considerations differ from the conditions in our experiment in two major regards: the imposition of spin conservation, and the effects of field inhomogeneities and quadratic Zeeman shifts. These differences are exemplified by considering the outcome of an experiment we performed, in which an optically-trapped Bose condensed cloud was prepared with all atoms in the $|m_F = 0\rangle$ state. The cloud was then allowed to equilibrate to the ground state by spin relaxation and by spatial redistribution [15]. For simplicity, consider only variations in the condensate wavefunction in one dimension, the \hat{z} -direction, and define the coordinate z to give the distance from the center of the condensate. This corresponds to the experimental situation in which the spinor condensates were held in the highly anisotropic, cigar-shaped potential of an optical trap.

Let us consider the evolution of the pure $m_F = 0$ condensate as we slowly add the effects of magnetic fields and mean-field interactions and construct the relevant energy functional (Fig. 10-1).

- a) *Linear Zeeman shift from homogeneous field.* In a homogeneous magnetic field of strength B_0 , the linear Zeeman energy

$$E_{\text{LZ}} = -p \int d^3r n \langle F_z \rangle \quad (10.11)$$

is minimized by placing all atoms in the strong-field seeking $|m_F = +1\rangle$ state (a ferromagnetic state)[†]. Here, $p = g\mu_B B_0$ where g is the Landé g -factor and μ_B is the

[†]The operator F_z gives the component of the spin along the direction of the magnetic field. This direction need not be the same as the long axis of the trapped condensate.

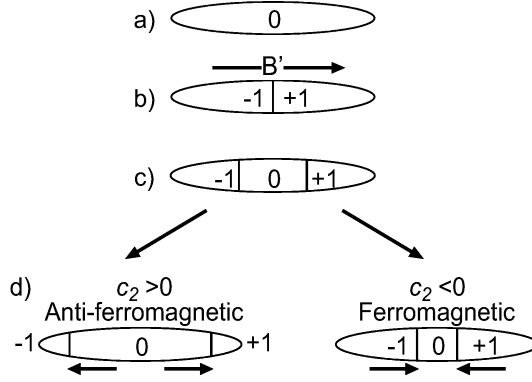


Figure 10-1: Constructing the ground-state $\langle F_z \rangle = 0$ spinor in a trap. In each step (a – d), another contribution to the Hamiltonian is considered (see text).

Bohr magneton.

However, spin non-conserving collisions (dipolar relaxation), which would be necessary to transform the $m_F = 0$ condensate to the $m_F = +1$ ground state, are negligible over the lifetime of the condensate. Thus, the total spin is a conserved quantity, and rather than considering the global ground state of the system, one must consider the lowest energy state under the restriction of spin conservation. Formally, one minimizes the restricted energy functional

$$K_{\text{tot}} = E_{\text{tot}} + \tilde{p} \int d^3\vec{r} n \langle F_z \rangle \quad (10.12)$$

in which, for the case where $\int \langle F_z \rangle n d^3\vec{r} = 0$, the linear Zeeman shift of a homogeneous magnetic field (E_{LZ}) is exactly canceled ($p_0 = \tilde{p}$).

This is an important point: spin conservation allows one to study the effects of the small spin-dependent interaction energies even at magnetic fields for which the linear Zeeman energy would otherwise be dominant. For example, in the case of sodium, the spin-dependent collisional energy is just $c_2 n \simeq h \times 50$ Hz for a typical density of $n = 3 \times 10^{14} \text{ cm}^{-3}$. Thus, without the restriction of spin conservation, the ground-state spinor would trivially consist of all atoms in the $|m_F = +1\rangle$ state at a magnetic field of just 70 μG , and any interesting structure, correlations or dynamics due to the anti-ferromagnetic coupling would be obscured. However, due to spin conservation, many of these effects can be studied even in the absence of such demanding field stability.

- b) *Linear Zeeman shift from field gradient.* A field gradient B' along the long-axis of

the condensate introduces an energy term

$$E_{\text{grad}} = - \int d^3\vec{r} p(z) n \langle F_z \rangle \quad (10.13)$$

with $p(z) = g\mu_B B' z$, which makes it energetically favorable for two $m_F = 0$ atoms to collide and produce a $m_F = +1$ atom on the high-field end of the cloud, and a $m_F = -1$ atom on the low-field end. Thus, the condensate is magnetically polarized into two pure spin domains.

- c) *Quadratic Zeeman shift from homogeneous field.* The quadratic Zeeman shift at a field B_0 introduces an energy term of the form

$$E_{\text{quad}} = q \int d^3\vec{r} n \langle F_z^2 \rangle \quad (10.14)$$

which causes the energy of a $m_F = 0$ atom to be lower than the average energy of a $m_F = +1$ and $m_F = -1$ atom by an amount $q = \hat{q}B_0^2$. For sodium, $\hat{q} = h \times 390 \text{ Hz/G}^2$. The quadratic Zeeman energy favors population in the $|m_F = 0\rangle$ state, and thus introduces a $m_F = 0$ domain at the center of the cloud with boundaries at $q = |p(z)|$.

- d) *Spin-dependent mean-field interaction.* As discussed previously, the collisional interactions give a spin-dependent energy term of the form

$$E_{\text{int}} = \frac{1}{2} \int d^3\vec{r} g_2 n^2 \langle \vec{F} \rangle^2 \quad (10.15)$$

Anti-ferromagnetic coupling ($g_2 > 0$) favors the polar state, and thus makes the central $m_F = 0$ domain larger. Ferromagnetic coupling ($g_2 < 0$) favors the ferromagnetic states $|m_f = +1\rangle$ and $|m_F = -1\rangle$ at the ends of the cloud, and thus the $m_F = 0$ domain shrinks.

Collecting spin-dependent energy terms, we now have the restricted energy functional

$$K_{\text{tot}} = \int d^3\vec{r} (K_0 + K_{\text{spin}}) \quad (10.16)$$

$$K_0 = \vec{\psi}^\dagger \left(-\frac{\hbar^2 \nabla^2}{2m} \right) \vec{\psi} + (U(\vec{r}) - \mu + g_0 n) n \quad (10.17)$$

$$K_{\text{spin}} = \left(-p(z) \langle F_z \rangle + q \langle F_z^2 \rangle + c \langle \vec{F} \rangle^2 \right) n \quad (10.18)$$

where $c = g_2 n / 2$. The ground-state spin structure of a spinor condensate is found by minimizing K_{tot} .

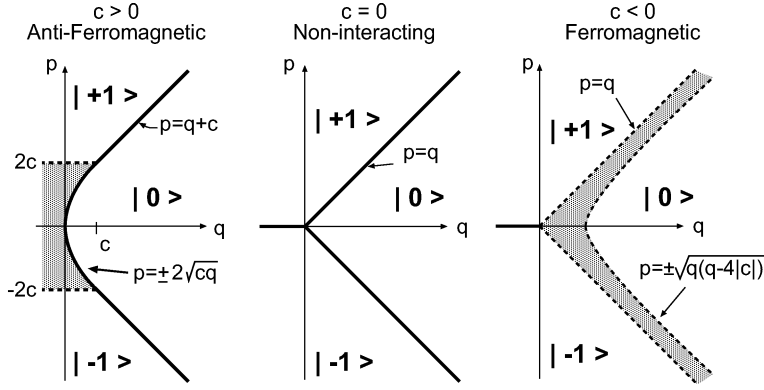


Figure 10-2: Spin–domain diagrams for $F = 1$ spinor condensates for the three cases $c > 0$ (anti–ferromagnetic collisional coupling), $c = 0$ (non–interacting gas), and $c < 0$ (ferromagnetic coupling). The ground–state spinors which minimize K_{spin} for the given values of p , q , and c are shown. Regions in which the ground state contains just one component are labeled by the magnetic hyperfine sublevel. Regions of mixed components are shaded. The ground–state spin–domain structure of a spinor condensate in the presence of a magnetic bias field and field gradient is indicated by a vertical line across the relevant domain diagram. Figure taken from [15].

10.3 Spin–domain diagrams: a local density approximation to the spin structure of spinor condensates

Focusing on the spin–dependent part, K_{spin} has a simple and elegant form. Let us step away from the specific experimental considerations and consider a homogeneous spinor condensate with some arbitrary, uniform values of the parameters p , q and c . The ground–state spinors obtained by minimizing the energy functional K_{spin} are indicated in the three diagrams of Fig. 10-2 for three conditions on the parameter c [15]. For a non–interacting gas ($c = 0$), the ground–state spinor is determined by the effects of magnetic fields alone.

In the case of anti–ferromagnetic coupling ($c > 0$), the spinor diagram changes in two significant ways. First, since the anti–ferromagnetic energy favors the $|m_F = 0\rangle$ polar state, the region in which the $|m_F = 0\rangle$ state is the ground state is enlarged. Second, at low values of q , in addition to the region of pure hyperfine states, a region is introduced in which the ground–state spinor is a superposition of the $|m_F = \pm 1\rangle$ states. While admixing the $|m_F = -1\rangle$ ($|m_F = +1\rangle$) state for $p > 0$ ($p < 0$) increases the linear Zeeman energy, it reduces the interaction energy by making the superposition state more polar in character. Explicitly, in the shaded region, $\langle F_z \rangle = p/2c$ independent of q . The effect of the linear Zeeman energy on anti–ferromagnetic condensates was considered also by Ohmi and Machida [305] whose work did not include the quadratic Zeeman energy, and thus concerned the $q = 0$ axis of the spin–domain diagram.

In the case of ferromagnetic coupling ($c < 0$), the situation is different. The higher

interaction energy for the polar state diminishes the region in which the ground state is the $|m_F = 0\rangle$ state. In between the regions of single-component ground-state spinors there is a region in which *all three* hyperfine states are generally mixed. In these regions, the $|m_F = 0\rangle$ state is mixed predominantly with a large population of only one of the $|m_F = \pm 1\rangle$ states and with a small population of the other.

Returning now to the experimental situation, the spin-domain diagram is used to describe the ground-state spin structure of a spinor condensate through a local density approximation. The values of q and c (but not its sign) are determined by the magnetic bias field and by the condensate density, which we assume for now to be constant across the condensate. The coefficient p varies across the condensate due to the presence of a magnetic field gradient; thus, the variations in the condensate spin structure across the length of the condensate are determined by scanning along a vertical line in the spin-domain diagrams. The length of this line is determined by the condensate length and the field gradient B' . The center of this vertical line is determined by the total spin in the condensate: it moves upwards (larger p) as $\langle F_z \rangle$ is increased and moves downwards (smaller p) as $\langle F_z \rangle$ is decreased. Thus, by adjusting the condensate density, the magnetic bias field, and the total spin of the cloud, all regions of the spin-domain diagrams are accessible.

10.4 Experimental methods

Having introduced this new quantum fluid, let us describe how we made it, and how we probed it. First, magnetically-trapped Bose-Einstein condensates were produced in the $|F = 1, m_F = -1\rangle$ hyperfine state and transferred to the optical trap. Then, we pulsed on rf fields of variable strength which were swept in frequency to distribute the optically-trapped atoms among the $F = 1$ hyperfine sublevels by the method of adiabatic rapid passage [5]. High amplitudes or slow sweep rates transferred all the atoms from one hyperfine state to another, while low amplitudes or fast sweep rates transferred just a fraction of the atoms. Rf frequency sweeps of variable frequency range, sweep rate, and amplitude, were generated using a pair of SRS DS345 function generators which could be triggered by the computer control of the experiment. The output from these function generators was combined with the rf signal used for evaporative cooling using two current switches in series in order to adequately suppress rf noise during the evaporative cooling cycle. To achieve an arbitrary hyperfine distribution, it was necessary to make these rf-transitions at large (15 – 30 G) bias fields, separating the $|m_F = +1\rangle \rightarrow |m_F = 0\rangle$ and $|m_F = 0\rangle \rightarrow |m_F = -1\rangle$ transition frequencies by about 1 MHz due to the quadratic Zeeman shift. Otherwise, at low fields where level spacings between the hyperfine sublevels are equal, rf fields can only be used to rotate the atomic spin vector and cannot, for example, change the atoms from the ferromagnetic $|m_F = +1\rangle$ state to the polar $|m_F = 0\rangle$ state.

After state preparation, the optically-trapped spinor condensates were allowed to evolve

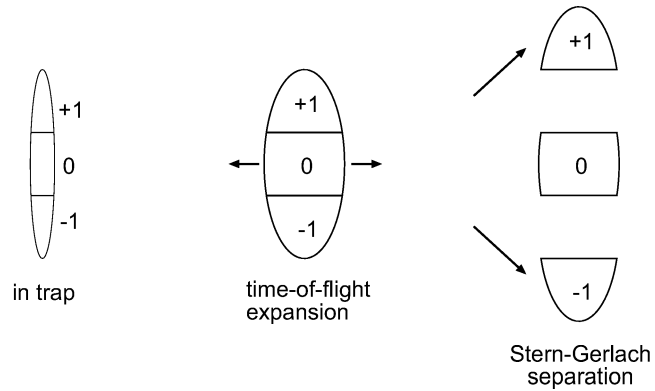


Figure 10-3: Probing spinor condensates. After release from the elongated optical trap, the trapped spinor condensate expands primarily radially while maintaining the axial hyperfine distribution. A magnetic field gradient is then used to separate out the different components while preserving their shape. A subsequent absorption probe reveals the spatial and hyperfine distributions in the trap.

in the presence of variable magnetic bias fields and field gradients. Bias fields along the long axis of the condensates were generated using a pair of electromagnets powered by current stabilized, externally controlled power supplies. The bias fields were easily calibrated by measuring the frequency of spin flip transitions. Magnetic field gradients along the long axis of the condensate were generated using a pair of magnet coils wound around the vacuum chamber at a distance of about 6" from the atoms which produced weak gradients ($\sim \text{mG/cm}$), or using the curvature and anti-bias coils of the cloverleaf magnetic trap which were also used to produce a magneto-optical trap and which produced stronger gradients ($\sim \text{G/cm}$). The field gradients were determined by applying the gradients while atoms were confined in the magnetic trap, and measuring the resulting axial displacement of the cloud.

After a variable dwell time in the optical trap, the spinor condensates were probed by time-of-flight imaging combined with a Stern-Gerlach spin separation (Fig. 10-3). The optical trap was suddenly switched off, allowing the atoms to expand primarily radially from the highly anisotropic optical trap. Then, after allowing about 5 ms for the interaction energy to be completely converted to kinetic energy, a magnetic field gradient was applied which separated the spin state populations without distorting them. Finally, after 15 – 30 ms, the atoms were optically pumped to the $|F = 2\rangle$ hyperfine manifold. This gave the same cross-section for all the atoms in the subsequent absorption probing on the $|F = 2, m_F = 2\rangle \rightarrow |F' = 3, m_{F'} = 3\rangle$ cycling transition. This probing method determined both the spatial and hyperfine distributions along the axis of the optical trap.

10.5 The formation of ground-state spin domains in spinor Bose–Einstein condensates

In our first experiment [15], which was led by Jörn Stenger and Shin Inouye, we explored the ground-state structure of spinor Bose–Einstein condensates with an average spin of $\langle F_z \rangle = 0$. Condensates were prepared either with all atoms in the $|m_F = 0\rangle$ state or in a 50–50 mixture of the $|m_F = \pm 1\rangle$ states. The atoms were then allowed to relax to their equilibrium distribution in the presence of a variable magnetic bias field and field gradient. Probing at variable times after the state preparation revealed that the condensates relaxed to the same spin structure from either of the initial conditions, and remained thereafter in the same equilibrium state.

Figure 10-4 shows three examples of the spin structures which were observed. The corresponding representations of these structures in the anti-ferromagnetic spin-domain diagram are indicated in Fig. 10-5. Fig. 10-4b shows the equilibrium structure of a spinor condensate for which the quadratic Zeeman energy is larger than the interaction energy ($q > c$). The magnetic field gradient is sufficiently strong so that $|p| > q + c$ at the ends of the cloud, and thus the condensate consists of three pure spin domains with a $m_F = +1$ domain on the high-field end of the cloud, a $m_F = 0$ domain in the center, and a $m_F = -1$ domain at the low-field end.

In Fig. 10-4a, the magnetic field is weaker, and thus the central $m_F = 0$ domain is now flanked by regions in which the $m_F = \pm 1$ components are mixed. The appearance of a population in the $m_F = 1$ ($m_F = -1$) component on the low-field (high-field) end of the cloud provides a qualitative confirmation of the anti-ferromagnetic collisional coupling in the $F = 1$ hyperfine manifold of sodium. The division between the $m_F = 0$ domain and the domains containing the $m_F = \pm 1$ components indicates the immiscibility of the $m_F = 0$ component with the others.

Finally, in Fig. 10-4c, a condensate is shown for which the total spin is greater than zero. The magnetic field gradient is about zero, and thus the condensate corresponds to a point on the spin-domain diagram in which the $m_F = \pm 1$ components are mixed. This situation nicely demonstrates the miscibility of the $m_F = \pm 1$ components with each other. The different widths of the two components may be due to the curvature of stray magnetic fields, which has opposite effects on the $|m_F = \pm 1\rangle$ states due to their different magnetic moments. Another explanation was recently given by Huang and Gou [309] who ascribe the different widths to the inhomogeneous density of the condensate. The anti-ferromagnetic interaction energy which favors a mixture of the $m_F = +1$ and $m_F = -1$ components is proportional to the condensate density. The energy gain from mixing the components at the center of the condensate, where the density is highest, is larger than at the ends of the cloud, where the density is smaller. Thus, the component with the smaller population, the $m_F = -1$ component in Fig. 10-4c, is concentrated at the center of the cloud, leaving only

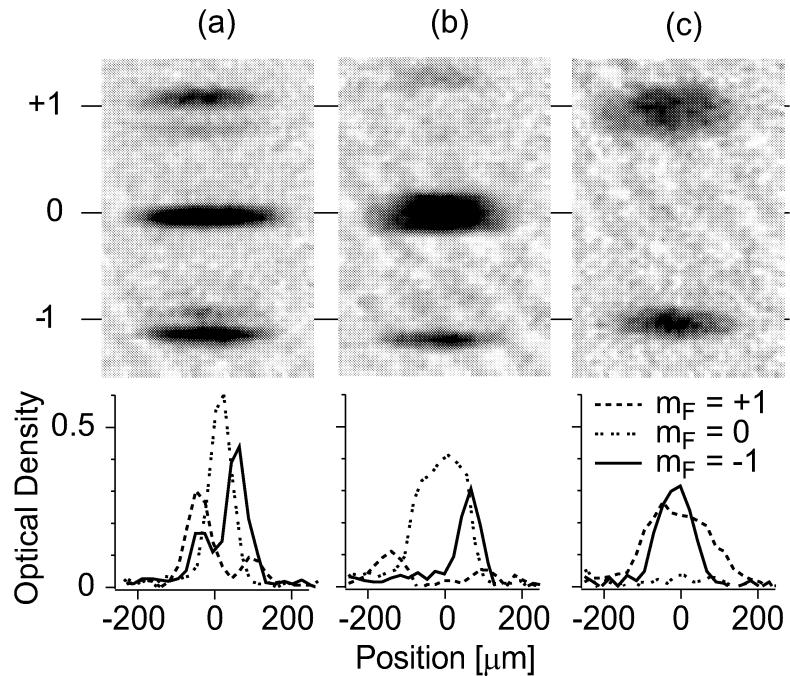


Figure 10-4: Ground state spin domains in $F = 1$ spinor Bose-Einstein condensates. Time-of-flight images after Stern-Gerlach separation are shown, along with the indicated axial density profiles in the optical trap, for which the Stern-Gerlach separation was “undone.” Images (a) and (b) show spin domains of all three components. Image (c) shows a miscible $m_F = \pm 1$ component condensate. Conditions are: (a) $B = 20$ mG, $B' = 11$ mG/cm; (b) $B = 100$ mG, $B' = 11$ mG/cm; (c) $B = 20$ mG, $B' \simeq 0$, $\langle F_z \rangle > 0$.

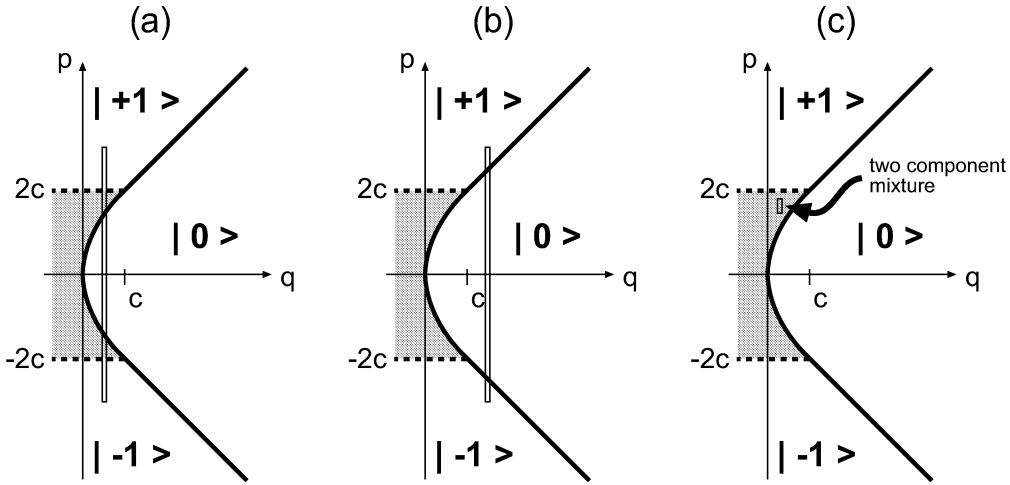


Figure 10-5: Representation of ground-state spin–domain structures of Fig. 10-4 on the spin–domain diagram. The spin structures shown in Fig. 10-4a and b correspond to long vertical lines through the spin–domain diagram, centered at $p = 0$ to correspond to an average spin $\langle F_z \rangle = 0$. (a) At low magnetic field $q < c$ and mixed-spin domains are introduced. (b) At higher fields, they are absent. (c) Lowering the gradient focuses on a small portion of the diagram in which a cloud of non-zero spin consists of overlapping $m_F = \pm 1$ components.

the $m_F = +1$ component at the ends.

There were some apparent discrepancies between our observations and the local density description (Sec. 10.3). For instance, as shown in Figs. 10-4a and b, the separation between the central $m_F = 0$ domain and the neighboring $m_F = \pm 1$ domains was not sharp, as would have been predicted by the spin–domain diagram. The Thomas–Fermi description predicts a sudden variation of the condensate spinor between the $m_F = 0$ and its surrounding $m_F = \pm 1$ domains. However, when one includes the kinetic energy term one finds the variation of the condensate spinor between the domains to be gradual. As discussed in Secs. 10.7 and 10.8, if one considers just the $m_F = 0$ and $m_F = 1$ components, the repulsion of an $m_F = 0$ atom from a $m_F = 1$ domain is due to an interaction energy barrier of size

$$\Delta E = \mu_0 \left(\sqrt{\frac{g_0 + g_2}{g_0}} - 1 \right) \simeq 0.018\mu_0 \quad (10.19)$$

where $\mu_0 = g_0 n$ is the chemical potential of the $m_F = 0$ atoms at a condensate density of n . Balancing the kinetic energy at the boundary with this energy barrier, one expects the spin structure of the condensate to vary gradually across the spin domain boundary which has a width of approximately $\xi_s = \sqrt{\hbar^2/2m\Delta E}$. This width ξ_s can be called a “spin healing length” in analogy with the healing length $\xi = \sqrt{\hbar^2/2m\mu}$ which is the minimum length for density variations. Taking $\mu_0 \simeq k_B \times 300$ nK, one expects a boundary width of approximately $\xi_s = 1.4 \mu\text{m}$. In contrast, however, the time-of-flight images indicated an

overlap between the components of tens of microns.

This discrepancy may just be an artifact of the indirect time-of-flight technique from which the spin structure of the trapped condensate is inferred. During the expansion of the condensate, the kinetic energy at the spin-domain boundaries is released axially, imparting velocities of $\sqrt{2\Delta E/m} \simeq 2$ mm/s. During the 25 ms time of flight, this would cause a sharp boundary between spin components to be smeared out by $\simeq 50\mu\text{m}$, consistent with the width of the overlap between the $m_F = 0$ and $m_F = \pm 1$ components indicated by our images. It is interesting to note that the radial expansion of the cigar-shaped condensate occurs at a velocity near the speed of Bogoliubov sound, which describes the propagation of density waves, while the axial expansion of a spin domain boundary occurs at a “spin sound velocity” which would describe the propagation of spin waves.

Thus, our time-of-flight imaging technique cannot properly characterize the boundary between neighboring spin domains. In future work, it would be interesting to examine such boundaries with a more reliable *in situ* imaging technique, perhaps to observe effects recently discussed by Isoshima, Machida and Ohmi [310] in a theoretical analysis of our experimental setup. They examined the differences between an effective one-dimensional description of the spinor ground state, as employed in our local-density approach [15], and a three-dimensional treatment of the spinor wavefunction. A one-dimensional treatment of the spin-domain structure is strictly valid only when the length scale for variations in the condensate spin is larger than the radius of the narrow optically-confined condensate. Taking a typical radial trap frequency of $\omega_r = 1$ kHz and a chemical potential $\mu \simeq k_B \times 300$ nK, the Thomas-Fermi radius of the condensate $\sqrt{2\mu/m\omega_r^2} = 2.3\mu\text{m}$ is slightly larger than the spin healing length ξ_s . Thus, one expects to see some discrepancies between a one-dimensional and a full three-dimensional prediction of the location and shape of the domain boundaries.

The authors of Ref. [310] also found that the variation of the condensate spin at the domain boundaries could occur on a length scale much larger than ξ_s when one considered the effects of all three components, rather than just the $m_F = 0$ and $m_F = 1$ components as discussed above. The three-component nature of domain boundaries has important implications for the observed metastability [17] of and quantum tunneling [19] across spin domains and is discussed further in Sec. 10.8.

10.6 Miscibility and immiscibility of spinor condensate components

As discussed above, the spin-domain diagram and the observed ground-state spin structures showed evidence for the miscibility of the $m_F = -1$ and $m_F = +1$ components and the immiscibility of $m_F = \pm 1$ and $m_F = 0$ components. The bulk miscibility or immiscibility of two-component condensate mixtures is predicted by mean-field theory [292–295, 311]. The

interaction energy density of such condensates is given by

$$E = \frac{1}{2}(n_a^2 g_a + n_b^2 g_b + 2n_a n_b g_{ab}) \quad (10.20)$$

where m is the common atomic mass, and n_a and n_b are the densities of each of the components. The interaction parameters are given generally as $g = 4\pi\hbar^2 a/m$ where a_a and a_b are the same-species scattering lengths, and a_{ab} is the scattering length for interspecies collisions. Consider a two-component mixture in a box of volume V with N atoms in each component. If the condensates overlap, their total mean-field energy is

$$E_O = \frac{N^2}{2V} (g_a + g_b + 2g_{ab}) \quad (10.21)$$

If they phase separate, their energy is

$$E_S = \frac{N^2}{2} \left(\frac{g_a}{V_a} + \frac{g_b}{V_b} \right) \quad (10.22)$$

The volumes V_a and V_b occupied by each of the separated condensates are determined by the condition of equal pressure:

$$g_a \left(\frac{N}{V_a} \right)^2 = g_b \left(\frac{N}{V_b} \right)^2 \quad (10.23)$$

Comparing the energies E_O and E_S the condensates will phase-separate if $g_{ab} > \sqrt{g_a g_b}$, and will mix if $g_{ab} < \sqrt{g_a g_b}$.

In the $F = 1$ three-component spinor system, the scattering lengths are determined by $a_{F_{\text{tot}}=0}$ and $a_{F_{\text{tot}}=2}$. Defining $\bar{a} = (2a_{F_{\text{tot}}=2} + a_{F_{\text{tot}}=0})/3$ and $\Delta a = (a_{F_{\text{tot}}=2} - a_{F_{\text{tot}}=0})/3$, the scattering lengths for the $m_F = 1, 0$ two-component system (or equivalently the $m_F = -1, 0$ system) are given by $a_0 = \bar{a}$, and $a_1 = a_{01} = \bar{a} + \Delta a$. Since Δa is positive for sodium, the condition $a_{01} > \sqrt{a_0 a_1}$ applies and the components should phase-separate, as we have observed [15, 17]. Interestingly, this phase-separation should not occur in the non-condensed cloud because the same-species mean-field interaction energies are doubled due to exchange terms.

In the $m_F = \pm 1$ two component system, the scattering lengths are $a_1 = a_{-1} = \bar{a} + \Delta a$ and $a_{1,-1} = \bar{a} - \Delta a$. Thus, $a_{1,-1} < \sqrt{a_1 a_{-1}}$, and these two components should mix. Indeed, as shown in Fig. 10-4c, an equilibrium spinor condensate with $\langle F_z \rangle \neq 0$, small field gradient, and near-zero field consists of an overlapping mixture of atoms in the $m_F = \pm 1$ states. This particular miscible two-component system has an important advantage. If the trapping potential varies across a two-component condensate, the lowest energy state may be a phase-separated state if $a_a \neq a_b$ even though the condition $a_{ab} < \sqrt{a_a a_b}$ is fulfilled [312]. In this case, the atoms with the smaller scattering length concentrate near the trap center, making it harder to observe miscibility. However, in the $m_F = \pm 1$ system,

the two scattering lengths a_1 and a_{-1} are equal by rotational symmetry, so the components mix completely even in a trapping potential.

10.7 Metastable states of spinor Bose–Einstein condensates

Having observed and explained ground state spin–domain structures, we began to explore dynamical properties of spinor Bose–Einstein condensates. Our first study [17] (Appendix H) discussed the observation of long–lived excited states of spinor Bose–Einstein condensates. We observed two complementary types of metastable states: one type in which a two–component condensate was stable in spin composition but which persisted in a non–equilibrium structure of spin domains, and another in which a spatially uniform condensate was metastable with respect to spin relaxation to an equilibrium spin composition. In each case, the energy barriers to relaxation to the ground state (the activation energy) were identified and found to be much smaller than the nanokelvin–scale thermal energies of the metastable gases; thus, such states would not be metastable in a non–condensed cloud. However, in a Bose condensed cloud with a large condensate fraction, the thermal energy is only available to the scarce thermal component and thus thermal relaxation is considerably slowed. In other words, Bose–Einstein condensation allows the study of weak effects in an energy regime which is much lower than the temperature of the gas.

10.7.1 Metastable spin–domain structures

The first type of metastability was observed in spinor Bose–Einstein condensates in a high magnetic field (15 G) which caused a two–component $m_F = 0, 1$ cloud to be stable in spin composition. This occurs because the large quadratic Zeeman shift makes $|m_F = 0\rangle + |m_F = 0\rangle \rightarrow |m_F = +1\rangle + |m_F = -1\rangle$ collisions endothermic, even if the $|m_F = \pm 1\rangle$ atoms would move to the ends of the condensate. We prepared clouds in an equal superposition of the two hyperfine states using a brief rf pulse, and then allowed the system to equilibrate.

Because of the immiscibility of the $m_F = 0$ and $m_F = 1$ components, the ground–state spin structure in this case consists of two phase–separated spin domains, one for each of the components, on opposite sides of the elongated trap with a domain boundary in the middle. What we observed was dramatically different: a spontaneously formed, metastable arrangement of alternating $m_F = 0$ and $m_F = 1$ spin domains (Fig. 10-6).

These spin striations began forming within about 50 ms of the initial preparation of two overlapping, immiscible components. The striations were initially angled due to radial excitations in the narrow spinor condensates which soon damped out, leaving strictly horizontal striations. The observed width of the spin domains grew to an equilibrium value of about 40 μm within about 100 ms (Fig. 10-7).

Thereafter, the clouds were essentially unchanged, remaining in the metastable state for 10 or more seconds as the number of trapped atoms slowly decayed due to three–body trap

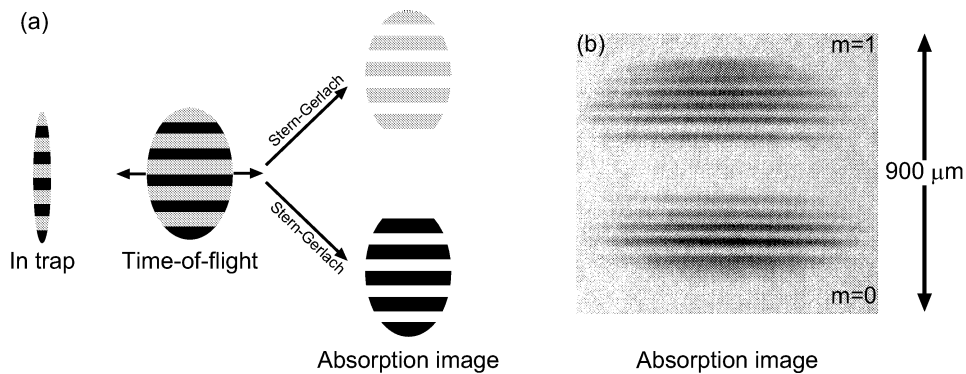


Figure 10-6: Quantum bubbles: a metastable arrangement of alternating spin domains in a two-component condensate. (a) A two-component optically-trapped condensate composed of atoms in the $|m_F = 0\rangle$ (black) and $|m_F = 1\rangle$ (grey) hyperfine states expands primarily radially once the trap is switched off. A magnetic field gradient is used to separate the two spin states before imaging, allowing a determination of the axial distribution of the two components in the trap. (b) The observed density striations indicate that the trapped condensate was composed of alternating $m_F = 0$ and $m_F = 1$ spin domains.

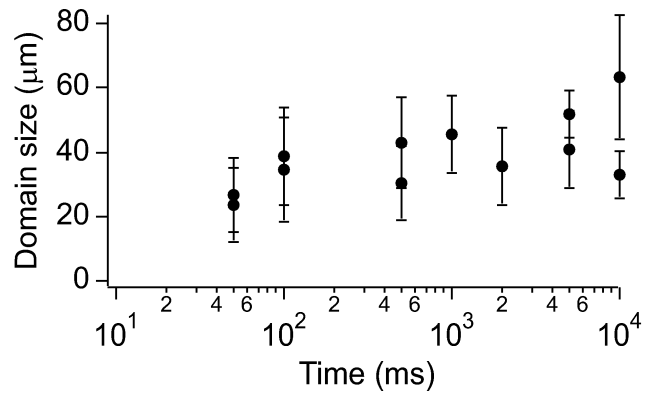


Figure 10-7: Evolution of metastable domain sizes. Shown is the average size (points) and standard deviation (one sigma error bars) of the spin domains observed at various time after the initial state preparation at a bias field of 15 G. Each point corresponds to measurements made on a different condensate.

losses. To understand the reason for the metastability, let us consider two adjacent spin domains of the $m_F = 0$ and $m_F = 1$ components, as shown in Fig. 10-8. Suppose that, in order for the condensate to decay to its ground state, the atoms of each spin domain must be transported somehow across the spin-domain boundary. For this to occur, the atoms of one component pass must either pass around or pass through the other component.

If one component passes around the other, the condensate wavefunction must be varied spatially in the radial direction. This gives a kinetic energy barrier to decay of about $\hbar^2/2mr^2 \simeq k_B \times 3$ nK where $r \simeq 2\mu\text{m}$ is the condensate radius. The passage of one component through the other is limited by an interaction barrier since the components are immiscible. As explained in Ref. [19], the interaction energy barrier for atoms in the $|m_F = 0\rangle$ state to pass through a $m_F = 1$ domain is (see Eq. 10.19) $\Delta E \simeq g_2/2g_0 \times \mu_0 = c$ where μ_0 is the chemical potential of atoms in the $m_F = 0$ spin domain, and c is the spin-dependent interaction energy introduced in Sec. 10.1. At a chemical potential $\mu_0 = k_B \times 300$ nK, the interaction energy barrier height is $c \simeq k_B \times 5$ nK. The probability of tunneling through the spin domains is exceedingly small because the axial length of the domains $z_B \simeq 40\mu\text{m}$ is much larger than the spin healing length $\xi_s \simeq 1.4\mu\text{m}$. Thus, because of these two energy barriers, the non-equilibrium arrangement of spin-domains is metastable.

The formation of these metastable spin-domains was considered recently by Chui and Ao [313] as a spinodal decomposition in a binary-solution system with analogies to non-equilibrium states in other condensed matter systems. Equilibration occurs on two time scales. First, on a short time scale determined by the spin-dependent interaction energy c as $t \simeq \hbar/c$, the homogeneous initial state begins to phase separate into small domains of length scale $\xi_s = \sqrt{\hbar^2/2mc}$. Thereafter, the domains grow by the coalescence of small spin domains on the long time scales required for quantum tunneling. This work supports the physical picture which we suggested in Ref. [17]. A similar picture emerges from the work of Pu *et al.* [314] who consider the quantum dynamics (without dissipation) of a trapped condensate composed of two overlapping components which tend to phase separate. In their calculations, they observe the evolution of fine spatial features which exemplify the instability of such a system against spin domain formation.

10.7.2 Metastable spin composition

Another type of metastability was discovered in the studies of ground-state spin domains of a $\langle F_z \rangle = 0$ condensate discussed in Sec. 10.5. Condensates were prepared either with all atoms in the $|m_F = 0\rangle$ state or in an equal mixture of the $|m_F = \pm 1\rangle$ states. While the ground state reached from either starting condition was the same, equilibration occurred on much different time scales. When starting from the $|m_F = 0\rangle$ state, the condensate remained unchanged for several seconds before evolving over the next few seconds to the ground state. When starting from the $|m_F = \pm 1\rangle$ superposition, the fraction of atoms in the $|m_F = 0\rangle$ state grew without delay, arriving at equilibrium within less than a second.

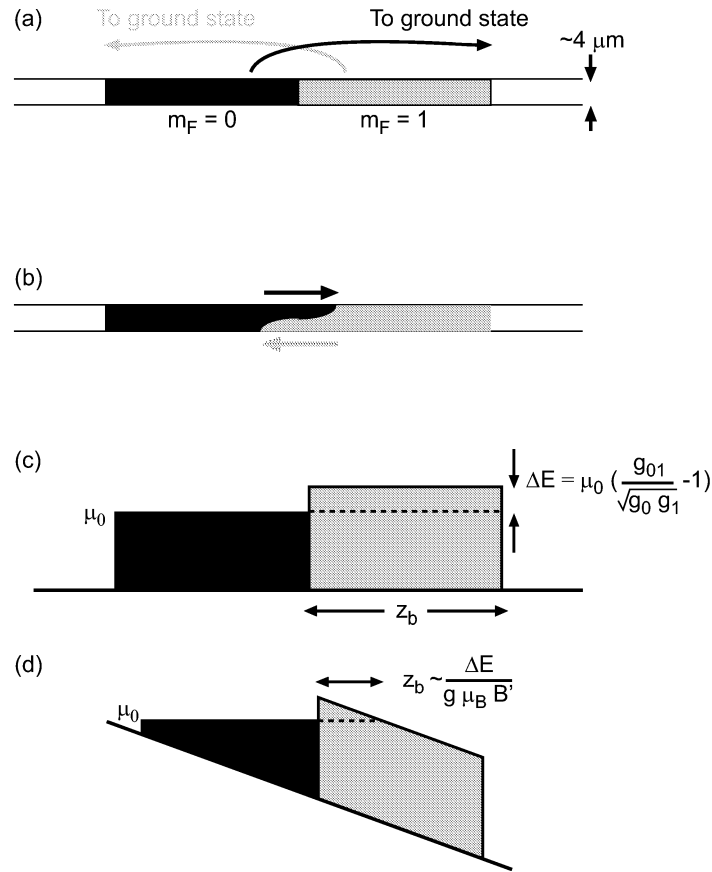


Figure 10-8: Energy barriers responsible for the metastability of spin domains in a two-component $m_F = 0, 1$ condensate. (a) Metastable domains of the $m_F = 0$ (black) and $m_F = 1$ (gray) components are held in a narrow optical trap. For the population in these domains to decay to the ground state they must either pass each other without overlapping, or pass through each other. (b) The former is prohibited due to the kinetic energy barrier of modifying the condensate wavefunction on a radial length scale. (c) The latter is prohibited due to an interaction energy barrier ΔE , shown here for the passage of an $m_F = 0$ domain of chemical potential μ_0 through the neighboring $m_F = 1$ domain. (d) If a magnetic field gradient B' is imposed, the width of the classically forbidden region for the passage of $m_F = 0$ atoms through the $m_F = 1$ domain is reduced to $z_b = \Delta E/g\mu_B B'$, and the tunneling rate which governs the decay of the metastable domains is increased.

The metastability in this case may be due to the quadratic Zeeman shift q which acts as a *local* barrier for spin relaxation between two $m_F = 0$ atoms in the condensate. Indeed, the metastability time was found to depend strongly on the quadratic Zeeman energy which was varied by changing the magnetic bias field. Importantly, the equilibration time changed significantly when q was varied by less than a nanokelvin; this dependency excludes thermal spin relaxation (in a gas at a temperature $T \sim 100$ nK $\gg q/k_B$) as the equilibration mechanism, and suggests that the metastable condensate decays to the ground state via quantum tunneling. In such tunneling, a pair of atoms in the $|m_F = \pm 1\rangle$ states would be produced in a classically forbidden collision, and would then tunnel to opposite ends of the cloud where their energy is lowered due to the magnetic field gradient. It would be interesting to study this process further in the future.

10.8 Quantum tunneling

Metastable states can generally overcome the activation energy barrier for decay to the ground state in two ways. Classically, the system can decay by acquiring thermal energy larger than the activation energy. However, even without this thermal energy, the system can decay to the ground state by quantum tunneling. Tunneling describes a wide range of phenomena such as nuclear decay, field ionization of neutral atoms, and scanning tunneling microscopy. In macroscopic quantum systems, coherent tunneling can lead to a variety of Josephson effects [315] which have been observed in superconductors and quantum fluids. As exemplified by the observation of metastable states which persist in spite of temperatures higher than the activation energy, gaseous Bose–Einstein condensates are an appealing new system to study tunneling and Josephson oscillations [215, 316–318].

In our third paper on spinor Bose–Einstein condensates, we studied the decay of metastable spin domains via quantum tunneling through the spin domain boundaries [19] (Appendix I). Tunneling barriers were formed not by an external potential, but rather by the intrinsic repulsion between two immiscible components of a quantum fluid. Tunneling across spin domain boundaries is a spin transport mechanism inherent to such a fluid (emphasized in [313]), and the tunneling rates are sensitive probes of the structure of the domain boundaries. From a practical viewpoint, the use of phase-separated spin domains rather than externally imposed potentials is an attractive option for future studies of tunneling in Bose condensates since the energy barriers for tunneling are naturally of nanokelvin-scale height and micron-scale width.

The system we chose for our study was a simple, well-characterized metastable arrangement of spin domains in a spinor condensate composed of the $m_F = 1$ and $m_F = 0$ components. Such a state was obtained by first preparing a spinor condensate in a superposition of the $|m_F = 0, 1\rangle$ states, as in earlier work [17]. A strong field gradient (several G/cm) was applied to break up the many-domain metastable state (discussed in the pre-

vious section) and separate the spin components into the two-domain ground state. Then, a weak gradient was applied in the opposite direction, which energetically favored the rearrangement of the spin domains on opposite ends of the optical trap, and thus yielded a two-domain metastable state. This simple system allowed for the characterization of the decay of metastable states by the easy identification of atoms in the metastable and ground-state spin domains of each component.

To ascribe the decay of these metastable spin domains to quantum tunneling, it was first necessary to rule out thermal relaxation as a decay mechanism. Figure 10-9 shows a series of time-of-flight images reflecting the state of the two-domain metastable state at various times after the state was initially prepared and held under a 0.1 G/cm gradient. One can identify two stages in the decay of this metastable cloud to the ground state: a slow decay over the first 12 seconds, followed by a rapid decay to the ground state within less than one second. The slow decay was found to be rather insensitive to changes in the condensate density and field gradient, and was thus consistent with thermal relaxation wherein condensate atoms from the metastable state are thermally excited, and then recondense into the ground state domains. The number of atoms which accumulated in the ground-state domains reached a nearly constant value of about 5×10^4 , perhaps due to a dynamic equilibrium between the growth of the domain via re-condensation and its depletion via inelastic losses. The data in Fig. 10-9 also show that the total population in the $|m_F = 0\rangle$ spin state decreases more rapidly than that in the $|m_F = 1\rangle$ state, indicating higher inelastic collision rates for the $|m_F = 0\rangle$ state.

The rapid decay which ensued (after 12 seconds) was due to quantum tunneling. As discussed below, the tunneling rate is acutely sensitive to the condensate density. While the condensate is stored in the optical trap, its density decreases as atoms are lost from the trap due to three-body inelastic collisions. Thus, as time progressed, the density of the metastable condensate in Fig. 10-9 decreased until the tunneling rate was fast enough to cause a rapid (within about 1 second) relaxation to the ground state.

The dependence of the relaxation time on the condensate density is also shown in Fig. 10-10. Metastable condensates were prepared with different initial numbers of atoms, and held in a constant magnetic field gradient. The metastable lifetimes for the two starting conditions were different, with the denser condensate decaying to the ground state at a later time.

A mean-field description of the tunneling rates was developed [19]. We considered the one-dimensional motion of a Bose-Einstein condensate composed of two immiscible components of atoms in states $|a\rangle$ and $|b\rangle$ and atomic mass m , as in Fig. 10-8 for the experimental realization of the $m_F = 1$ and $m_F = 0$ components. The chemical potentials of the two components $\mu_i = g_i n_i$ are related by the condition of constant pressure $\mu_a^2/g_a = \mu_b^2/g_b$ where $g_i = 4\pi\hbar^2 a_i/m$, a_i is the same-species scattering length, and $i \in a, b$ labels the component. The mean-field interaction energy for each component is $U_i = g_i n_i + g_{ab} n_j$

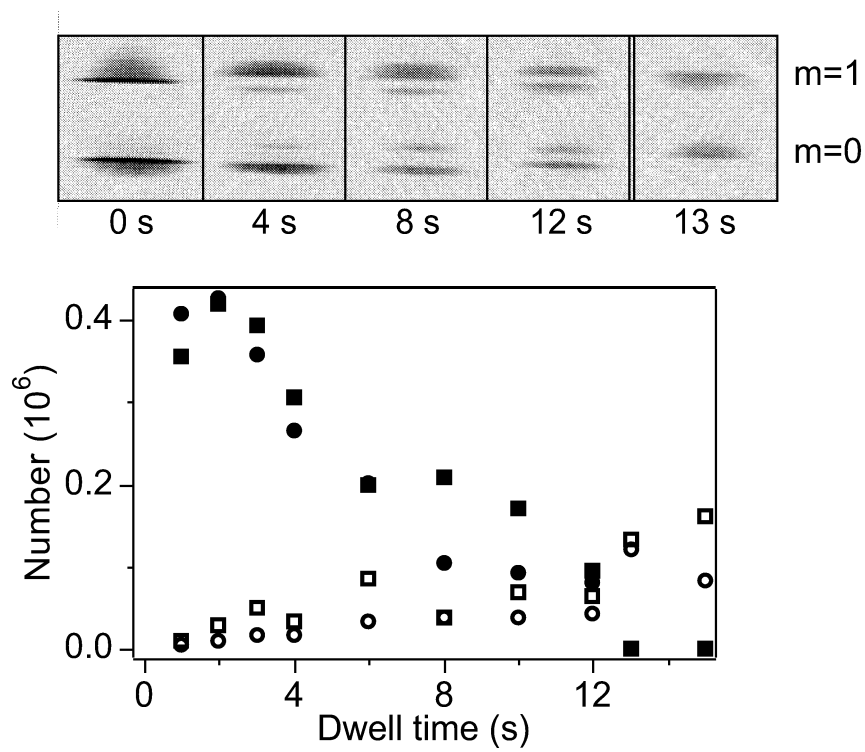


Figure 10-9: Decay of a metastable state by thermal relaxation and quantum tunneling. A two-domain metastable state was prepared at a 15 G axial bias field and a 0.1 G/cm gradient. Images show metastable (outer) and ground state (inner) spin domains of $|m_F = 1\rangle$ and $|m_F = 0\rangle$ atoms, probed at various times after state preparation. The height of each image is 1.3 mm. Also shown are the measured numbers of atoms in the metastable (closed symbols) and ground-state domains (open symbols) of the $|m_F = 1\rangle$ (squares) and $|m_F = 0\rangle$ (circles) states. The number of atoms in the ground state domains grew slowly over the first 12 s, after which the atoms tunneled quickly to the ground state. The total number of atoms (and thus the condensate density) decreased during the dwell time due to inelastic three-body collisions. Thus, the slow thermal relaxation gives way to a rapid tunneling once the density reaches a threshold value.

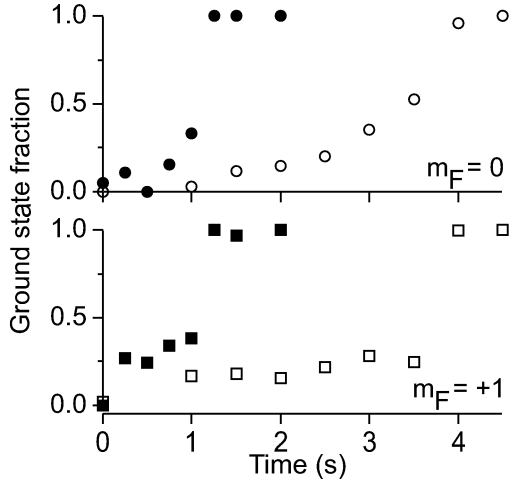


Figure 10-10: A comparison of the decay of metastable states at different densities. Shown is the fraction of $m_F = 0$ and $m_F = 1$ atoms found in the ground-state domains after a variable delay time at a constant field gradient of 0.35 G/cm and a 2 G bias field. The evolution is shown for condensates prepared with different populations in the initial state, either 1×10^6 (open symbols) or 2.5×10^5 atoms (closed symbols). The decay of the denser condensate occurred at a later time.

$(i \neq j)$ where g_{ab} is determined by the cross-species scattering length a_{ab} .

If we assume the boundary between the spin domains to be sharp, component a is excluded from the domain of component b by an energy barrier ΔE given by

$$\Delta E = g_{ab}n_b - g_a n_a = \left(\frac{g_{ab}}{\sqrt{g_a g_b}} - 1 \right) \mu_a \quad (10.24)$$

This energy barrier is responsible for the metastability of spin domains which have an axial length z_b which is much larger than the spin healing length $\xi_s = \sqrt{\hbar^2/2m\Delta E}$.

In the presence of a state-selective force F , which was experimentally applied in our experiments using a magnetic field gradient B' , the energy barrier decreases away from the domain boundary as $\Delta E(z) = \Delta E - Fz$. Thus the width of the energy barrier is reduced to $z_b = \Delta E/F$, and tunneling can occur when $z_b \sim \xi_s$. More precisely, the tunneling rate across the barrier is given by the Fowler–Nordheim (WKB) equation

$$\frac{dN_a}{dt} = \gamma \exp \left(-2\sqrt{\frac{2m}{\hbar^2}} \int_0^{z_b} \sqrt{\Delta E(z)} dz \right) \quad (10.25)$$

$$= \gamma \exp \left(-\frac{4}{3}\sqrt{\frac{2m}{\hbar^2}} \frac{\Delta E^{3/2}}{F} \right) \quad (10.26)$$

which also describes the analogous phenomenon of the field emission of electrons from cold metals [319]. Here γ is the total tunneling attempt rate (i.e. not the rate per particle), and

the exponential is the tunneling probability. This relation explains the strong dependence of the tunneling rate on the condensate density n , which causes the density threshold behaviour observed in Fig. 10-9.

This mean-field description was tested experimentally by measuring the tunneling rate across barriers of constant height and variable width. For this, metastable condensates were prepared at a constant density (giving a constant barrier height of ≈ 5 nK), exposed to a variable gradient (giving barrier widths between 4 and 20 μm), and allowed to decay for a period $\tau = 2$ s which was short enough that the condensate density did not vary appreciably due to trap losses. We then measured the number of atoms of each component in the metastable and ground-state spin domains by time-of-flight absorption imaging (Fig. 10-11). When the barrier was wide (small field gradients), the tunneling rate was small and only a small fraction of atoms were observed in the ground-state domains. When the barrier was narrow (large field gradients), the tunneling rate was large and a large fraction of atoms were observed in the ground-state domains. The data were in quantitative agreement with our mean-field approach using the scattering lengths calculated by Burke *et al.* in Ref. [308].

10.9 Field dependence of the structure of spin-domain boundaries

These measurements of the tunneling rate at high magnetic fields (15 G) were in quantitative agreement with a model of tunneling in a two-component Bose condensate. At lower magnetic fields, a dramatic increase in the tunneling rate was observed. As described in our paper (see Fig. 4 of Ref. [19], Appendix I), the threshold chemical potential for tunneling at a constant field gradient dramatically increased at magnetic fields below about 1 G. Fig. 10-12 shows similar data, in which we measured the lifetime of a metastable state prepared at a constant initial density for different values of the magnetic bias field and field gradient. As discussed above, because the density of the optically-trapped condensates decreased in time due to trap losses, a shorter lifetime indicates that the tunneling rate at a given density is higher. This strong increase in the tunneling rate at low fields reveals that the structure of the domain boundary is changed by the presence of the third spin component, the $|m_F = -1\rangle$ state.

The local density approximation discussed in Sec. 10.3 provides a basic but incomplete description of the boundary between spin domains. According to this approximation, for the case of anti-ferromagnetic collisional interactions, the average value of the spin projection on the magnetic field axis $\langle F_z \rangle$ changes suddenly at the boundary of $m_F = 0$ spin domains due to the bulk immiscibility of the $m_F = 0$ component with the $m_F = \pm 1$ components. The boundaries studied in our experiment between an $m_F = 0$ domain and a region of $\langle F_z \rangle > 0$ are described in this approximation by a short vertical line at constant q (determined by the magnetic field) which straddles the border of the $m_F = 0$ region in the $p > 0$ half-plane. The

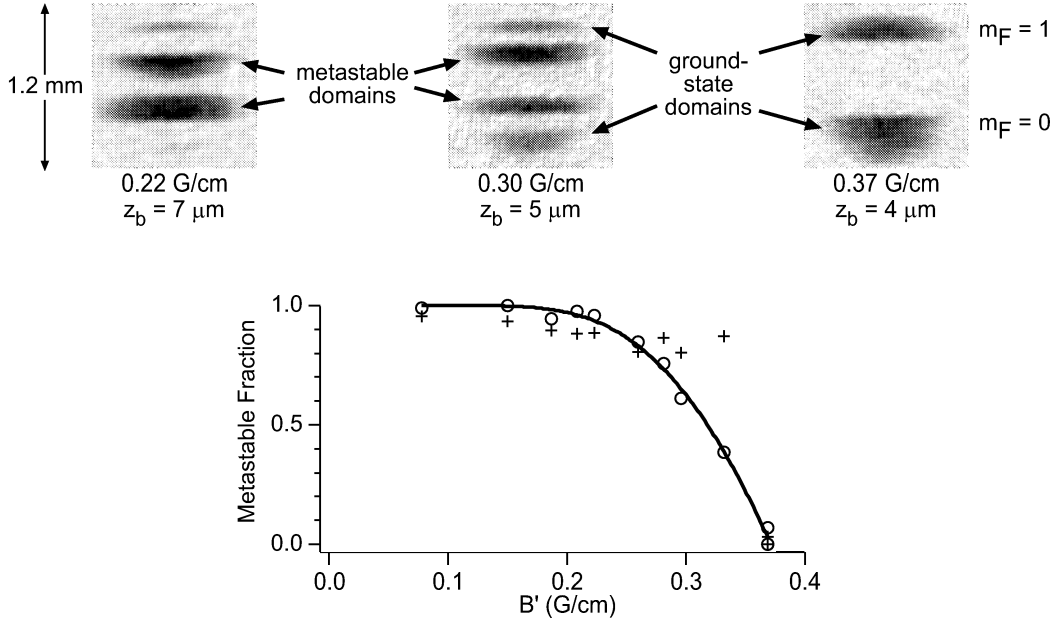


Figure 10-11: Tunneling across spin domains of constant height and variable width z_b . Condensates at constant density were probed after 2 seconds of tunneling at a variable field gradient B' . The population of atoms in the metastable and ground-state domains of each spin state were easily identified in time-of-flight images. Also shown is the fraction of atoms of each spin state in their metastable domain. Circles represent the $m_F = 0$ atoms, and pluses the $m_F = 1$ atoms. The energy barrier height was $\approx 5 \text{ nK}$ at the chemical potential of $\mu_0 \simeq 300 \text{ nK}$. The tunneling rate depended strongly on the width of the energy barrier $z_b = \Delta E/g\mu_B B'$: at $z_b = 7 \mu\text{m}$ ($B' = 0.22 \text{ G/cm}$) little tunneling was observed, while at $z_b = 4 \mu\text{m}$ ($B' = 0.37 \text{ G/cm}$) the atoms had completely tunneled to the ground state in 2 s. The barrier attempt rate and tunneling probability were determined by a fit to the $m_F = 0$ data (solid line), and found to agree with a mean-field model. The data indicate that the tunneling rate for $m_F = 0$ atoms is larger than that for $m_F = 1$ atoms.

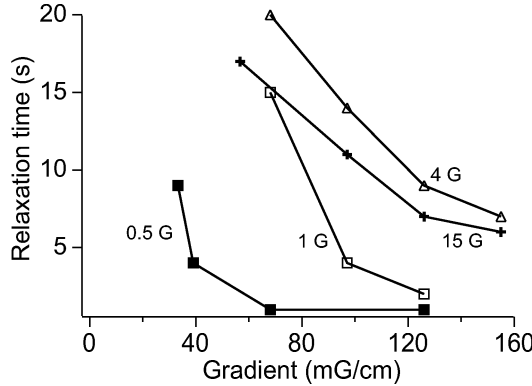


Figure 10-12: Variation of the metastable state lifetime with magnetic field and field gradient. Metastable condensates at a constant initial chemical potential of $\mu_0 \simeq 600$ nK were allowed to decay at a variable bias field and field gradient. Shown is the time at which the condensates were observed to have relaxed completely to the ground state. The dependence of the lifetime on the field gradient at 15 G and 4 G was similar. At fields of 1 G or lower, the lifetime was dramatically shortened, indicating a substantially higher tunneling rate at low magnetic fields.

diagram thus suggests that a pure two-component description of the boundary is correct for magnetic fields at which the quadratic Zeeman energy is larger than the spin-dependent interaction energy ($q > c$). Taking a typical value of the chemical potential of $\mu_0 = 300$ nK, this condition indicates that the two-component description of tunneling should be valid for magnetic fields greater than 500 mG[†].

Below this magnetic field, according to the local density approach, the $m_F = 0$ component is bordered not by a pure $m_F = 1$ domain, but rather by a region in which the $|m_F = 1\rangle$ and $|m_F = -1\rangle$ states are mixed. The introduction of the third spin component to the barrier has the effect of reducing the energy barrier for the tunneling of $m_F = 0$ atoms. This can be seen by considering a mixture of components a and b where $|a\rangle = |m_F = 0\rangle$ and $|b\rangle = \cos\theta|m_F = 1\rangle - \sin\theta|m_F = -1\rangle$ ($0 \leq \theta \leq \pi/2$). The interaction energy density of this system can be written in the form of Eq. 10.20 with the definitions

$$g_a = g_0 \quad (10.27)$$

$$g_b = g_0 + \Delta g \cos^2 2\theta \quad (10.28)$$

$$g_{ab} = g_0 + \Delta g(1 - \sin 2\theta) \quad (10.29)$$

where $\Delta g = g_2$. Using these interaction parameters, the energy barrier height which governs

[†]Unlike in Ref. [15], we do not apply here a one-dimensional approximation to reduce the effective interaction energy.

the tunneling of the $m_F = 0$ component becomes

$$\Delta E(\theta) = \left(\frac{g_0 + \Delta g(1 - \sin 2\theta)}{\sqrt{g_0(g_0 + \Delta g \cos^2 2\theta)}} - 1 \right) \mu_0 \simeq \frac{\Delta g}{g_0} (1 - \sin 2\theta - \cos^2 2\theta) \mu_0 \quad (10.30)$$

for $\Delta g \ll g_0$. For $\theta = 0$ or $\theta = \pi/2$, one recovers the energy barrier for tunneling through a pure $m_F = 1$ or $m_F = -1$ barrier. For intermediate values, the height of the energy barrier is reduced. Indeed, at $\theta = \pi/4$, the energy barrier disappears completely. In this case, $|b\rangle = \frac{1}{\sqrt{2}}(|m_F = 1\rangle - |m_F = -1\rangle)$ describes a polar state obtained by rotating the $|m_F = 0\rangle$ state. The condensate spinor can thus evolve continuously from state $|a\rangle$ to $|b\rangle$ by a gradual rotation which is associated with a gap-less (i.e. no barrier) Goldstone excitation mode. Recent calculations by Isoshima, Machida and Ohmi [310] confirm the disappearance of the energy barrier when the populations in the $|m_F = \pm 1\rangle$ states become equal.

These changes of effective interaction parameters in the presence of the $|m_F = -1\rangle$ state provide a mechanism for the variation of the tunneling rates with magnetic fields. However, the local density approach fails to explain why the tunneling rates should increase even at magnetic fields for which $q > c$, as we observed.

This failure stems from the incomplete description of the spin domain boundary. The local density treatment of Sec. 10.3 only describes bulk spin domains for which $\langle F_z \rangle$ lies in a limited range. However, at the boundary between spin domains, $\langle F_z \rangle$ must vary continuously due to the kinetic energy terms which are absent in the local density approach. In particular, in the boundary between the $m_F = 0$ and $m_F = 1$ spin domains, the spin projection $\langle F_z \rangle$ must vary continuously between 0 and 1. Let us approximate the spin composition of the boundary region by explicitly minimizing the energy of a spinor with a given value of $\langle F_z \rangle$, and then applying a local density approximation in which we assume that the spinor at each location in the boundary is determined by the local value of $\langle F_z \rangle$. We can write a spinor for which $\langle F_z \rangle > 0$ as

$$\vec{\zeta} = \begin{pmatrix} \sqrt{\langle F_z \rangle + \epsilon^2} \\ \sqrt{1 - \langle F_z \rangle - 2\epsilon^2} \\ -\epsilon \end{pmatrix} \quad (10.31)$$

where a choice of complex phases has already been made which reduces the anti-ferromagnetic interaction energy. The spin-dependent energy K_{spin} is then

$$c \left(\langle F_z \rangle^2 + 2(1 - 2\epsilon^2 - \langle F_z \rangle)(\sqrt{\epsilon^2 + \langle F_z \rangle} - \epsilon)^2 \right) + q(2\epsilon^2 + \langle F_z \rangle) \quad (10.32)$$

which is minimized to determine the fractional population ϵ^2 in the $|m_F = -1\rangle$ state.

At high magnetic fields ($q \gg c$) one finds the approximate solution

$$\epsilon^2 \simeq \frac{1}{(q/c)^2} \langle F_z \rangle (1 - \langle F_z \rangle)^2 \quad (10.33)$$

which indicates that atoms in the $|m_F = -1\rangle$ are *always* energetically favored to reside in the domain boundary[§]. Their population scales with the magnetic field B_0 as $q^{-2} \propto B_0^{-4}$. At a magnetic field of 15 G where $q/c \approx 400$, the fraction of atoms in the $|m_F = -1\rangle$ state is exceedingly small and thus the two-component approximation to the domain boundary should be quite accurate, as indicated by our data. At lower magnetic fields, the population in the $|m_F = -1\rangle$ state plays an increasingly important role.

Guided by these simple approximate treatments, one can also explicitly calculate the spinor wavefunction at the domain boundary which minimizes the total energy. Results of such a calculation, the details of which are presented in Appendix B, are presented in Figs. 10-13, 10-14, and 10-15. One finds indeed that the fractional population of atoms in the $|m_F = -1\rangle$ state is non-zero at all magnetic fields and scales as B_0^{-4} at high magnetic fields. The introduction of $m_F = -1$ atoms in the boundary layer increases the penetration depth of $m_F = 0$ atoms in the boundary region, and thus should increase the rate of tunneling across the domain boundary. The magnetic field at which this effect becomes significant, about 1 G for the conditions we considered (Appendix B), agrees with our observations.

[§]In our paper, an incorrect solution was given which indicated a high-field scaling of $\epsilon^2 \propto B_0^{-2}$ [19].

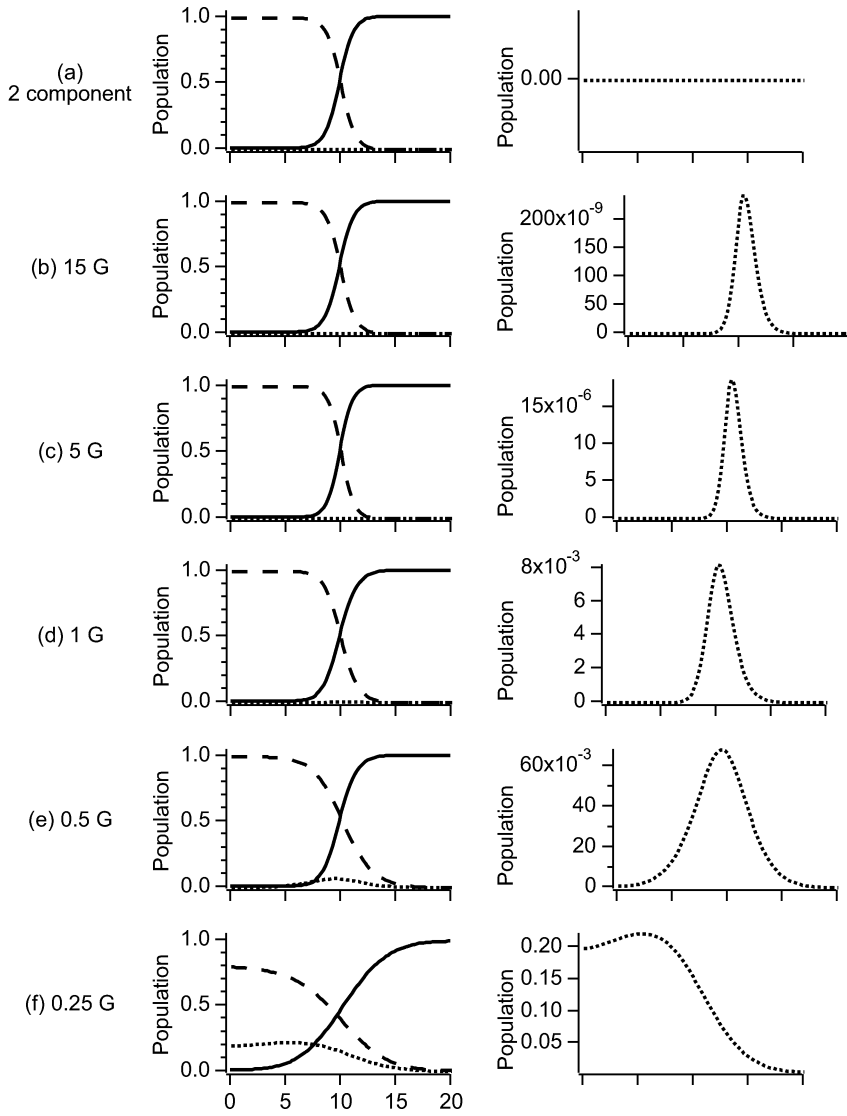


Figure 10-13: Numerical calculation of the spin structure at the domain boundaries at different magnetic fields. Shown are the fractional population in the $|m_F = 1\rangle$ (dashed line), $|m_F = 0\rangle$ (solid line), and $|m_F = -1\rangle$ (dotted line) states, with the $|m_F = -1\rangle$ population shown at right on an expanded scale. In (a), the calculation was restricted to just the $m_F = 0$ and $m_F = 1$ components, and hence the results are magnetic field independent. In the remaining graphs, all three components were considered at magnetic fields of (b) 15 G, (c) 5 G, (d) 1 G, (e) 0.5 G, and (f) 0.25 G. As the magnetic field is decreased, the population in the $|m_F = -1\rangle$ state increases, and the boundary region becomes wider. Further details are found in Appendix B.

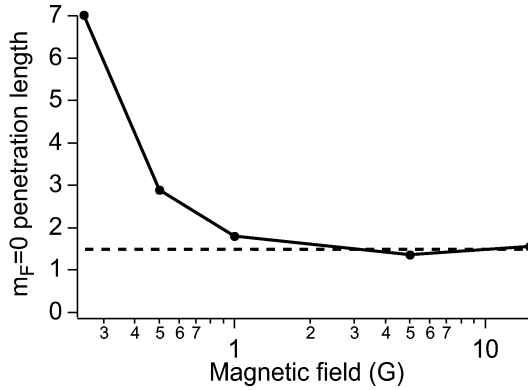


Figure 10-14: Variation of the spin–domain boundary width with magnetic field. The calculated spatial variation of the fractional population of atoms in the $|m_F = 0\rangle$ state was fitted to the function $f(z) = (1 - \text{Erf}((z - z_0)/\xi_0)) / 2$, where ξ_0 characterizes the penetration length of the $m_F = 0$ component in the boundary region. The points correspond to graphs (b – f) of Fig. 10-13, while the dashed line shows the penetration length calculated for the two–component case. The penetration length is close to the two–component limit at high magnetic fields, and then increases sharply at lower fields beginning at about 1 G, in agreement with our measurements.

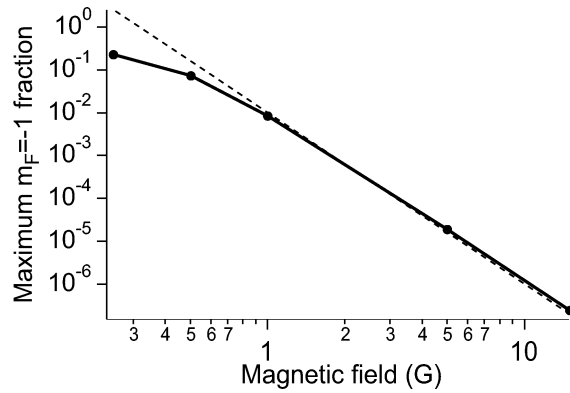


Figure 10-15: Maximum fractional population in the $|m_F = -1\rangle$ state in the spin–domain boundary at different magnetic fields. Points show the results of calculations of the domain boundary. The populations at high field scale as B_0^{-4} (indicated by dashed line) as predicted by the approximation of Eq. 10.33.

Chapter 11

Conclusion

After the achievement of gaseous Bose–Einstein condensation four years ago, culminating years of tenacious effort and innovation, researchers embarked on a scientific quest to learn about this unexplored quantum realm. As described in this work, my colleagues and I contributed to this quest through the development of new tools and their use for experiments covering a wide range of topics. To conclude the chronicle of my part of this journey, let me briefly assess what has been accomplished by this work, what questions remain unanswered, and what may lie in store for future explorers.

A great deal of the research by our group has tested, by various means, predictions of the well-developed theory of the weakly-interacting dilute Bose gas. The diluteness of the condensates used in current experiments indicates that a mean-field theory should give an accurate description of these condensates. A number of experiments probing the behaviour of Bose–Einstein condensates at the limit of zero-temperature have confirmed this prediction. Static properties such as the size of a trapped condensate, its density and momentum distributions, and its interaction energy have all compared favorably with predictions of a mean-field theory. Furthermore, the observation of changes in the interaction energy of a condensate at a Feshbach resonance [11] confirmed that the connection between the microscopic description of atomic interactions and its macroscopic effects on a bulk sample is sound. These tests are complemented by probes of dynamic properties. A wide range of excitations (small and large amplitudes, short and long wavelengths) in Bose condensates have been studied, and have all been described well by the Bogoliubov theory and its extension to inhomogeneous gases. Indeed, the comparison between our measurements of the frequency of collective excitations at the limit of zero temperature and the prediction of mean-field theories constitutes the most stringent test of these theories, and offers the possibility of studying the onset of effects which go beyond the mean-field approximation.

We have also confirmed the picture of Bose–Einstein condensates as coherent quantum objects. The first observation of matter-wave interference between two independent Bose–Einstein condensates gave stark evidence for the phase coherence of a condensate. This phase coherence has been further characterized by the use of Bragg spectroscopy to mea-

sure the innate momentum distribution of a condensate, and one finds the width of this distribution to be limited by the size of the condensate in accord with the Heisenberg uncertainty relation. Recent work by other groups has confirmed this picture [160, 169]. The coherence of a condensate is also indicated by the evidence of Bose-enhanced growth in the formation of a Bose-Einstein condensate. Evidence for higher-order coherence, such as second [320] and third [251] order, has been observed through its effect on two- and three-body collisions, respectively. These studies of the coherence properties of Bose-Einstein condensates have also led to the conceptual and experimental development of the atom laser, a device which emits a coherent matter wave.

Finally, with the realization of multi-component and spinor Bose-Einstein condensates, our research has clearly advanced beyond the confirmation of existing theoretical predictions to the exploration of entirely new macroscopic quantum systems. In particular, studies of optically-trapped spinor Bose-Einstein condensates have explored various static and dynamic effects in a weakly-interacting quantum fluid described by a vectorial order parameter. The specific realization of an $F = 1$ spinor condensate with sodium was discovered to have anti-ferromagnetic collisional interactions which dictate the formation of ground-state and metastable spin domains. In studying the equilibration of metastable spinor condensates, we discovered mechanisms by which nanokelvin-scale interactions, such the effects of externally imposed magnetic fields or the intrinsic effect of collisions, can greatly affect quantum transport in these fluids. From my perspective, this last study of quantum tunneling in spinor condensates is perhaps the best example of how the experimental field of Bose-Einstein condensation has advanced and diversified in the four years since the initial confirmation of Einstein's 1925 prediction.

This broad experimental opus has been enabled by a number of technical developments which will certainly find further use in future studies of ultra-cold atoms. With the development of the cloverleaf magnetic trap and four years' worth of experience, we have learned how to make Bose-Einstein condensates reliably. We have demonstrated the feasibility and flexibility of magnetic and optical traps for storing and manipulating ultra-cold atoms. Various imaging types and techniques have been developed, ranging from single-shot time-of-flight absorption imaging to repeated *in situ* phase-contrast imaging. Finally, along with our colleagues at NIST, we have developed Bragg scattering as a flexible tool for the study of sub-recoil atomic samples generally, and Bose-Einstein condensates in particular.

For as many questions as this research has answered, new unanswered questions have emerged. For example, measurements of collective excitations in partly condensed gases have challenged the mean-field theories which have been proposed for their description. This challenge has led to further exploration of finite-temperature theories which has focused on a realistic dynamic treatment of both the condensate and the thermal cloud and on elucidating the effects of correlations which are neglected in the simplest mean-field models. Perhaps this theoretical crisis will be solved by making use of the complex many-body theories

which were developed, for example, in the study of liquid helium. One could then “strip down” such theories to recover the simplest approximation which still adequately describes the behaviour of the dilute gases.

Another set of questions which remains largely unanswered concerns the dynamical evolution of the phase of the condensate. As discussed in Chapter 6, the question of how a uniform phase of a condensate is established during its formation has attracted theoretical scrutiny, and should be addressed experimentally in future studies. Other works have discussed how a condensate which is prepared with a definite phase, for example by an interference measurement with another condensate, will eventually lose that phase due to phase dispersion caused by interatomic interactions [321–324]. This effect can be explored experimentally by measuring the temporal correlation between two measurements of the relative phase between two trapped condensates. Such investigations would allow one to study the possible locking of the relative phase due to a weak coupling between the condensates [325]. Alternately one could study the stability of the condensate phase as the condensate number is changed, perhaps by means of adiabatically deforming the trapping potential as described in Sec. 6.2.

Another unmet challenge is the identification and study of effects which cannot be described by mean-field theories which neglect correlations between particles. As discussed above, the rapid sequence imaging method which we used for the study of collective excitations already has sufficient precision to detect the possible effects of quantum depletion, which should change the frequency of the excitations at a $\approx 1\%$ level [244]. Other experimental probes may result from examining more closely what is meant by a “collision” in a Bose–Einstein condensate. For example, a variety of effects such as the elastic scattering which leads to the formation of a condensate [9], inelastic three–body collisions [16, 251], and photoassociation (studied in recent work by the Heinzen group) are both sensitive to and can affect the correlations between particles at close range. Further scrutiny of such processes, for example by detecting the possible depletion of the short–range correlation function at during an intense photoassociation pulse or near a Feshbach resonance, may probe effects which go beyond the Gross–Pitaevskii mean–field description of Bose condensates. Other opportunities for the study of correlation effects may arise in the study of spinor condensates, as described at the end of Sec. 10.1.

Beyond these immediate questions, I foresee at least two fruitful directions for future research. First, as exemplified by our research on spinor condensates, we now have the ability to design a variety of new quantum systems. For example, one could study quantum gases in reduced dimensions (achieved by tight confinement) or in periodic potentials. A second important direction is the implementation of an atom laser for use in atom optics. The atoms laser could be used as a bright atomic source (due to its first–order coherence) to improve atom interferometry (see e.g. [326]) and atom holography [327]. Proposed uses of higher–order coherence to perform Heisenberg limited measurements ($1/N$ rather than

$1/\sqrt{N}$ resolution with N atoms) may yield further advances [328]. Given the plethora of proposed experiments and the growing number of experimentalists in the field, rapid progress in these and many other research directions appears certain.

I have come to the end of a long and thrilling journey, of four years in the exploration of quantum gases and of the many years of learning that brought me to this day. This is the end of my tale, for now, and I am weary from the telling.

Appendix A

Image processing

This appendix includes the section entitled “Image Processing” from Ketterle, Durfee, and Stamper-Kurn, “Making probing and understanding Bose-Einstein condensates,” in M. Inguscio, S. Stringari and C.E. Wieman eds., *Bose-Einstein Condensation in Atomic Gases*, Proceedings of the “Enrico Fermi” Summer School, July 1998, Varenna, Italy. To be published.

Some minor modifications have been made to conform to the symbols and section headings used in this dissertation.

The imaging techniques discussed in Sec. 3.7 are used in an imperfect environment in which background light, scattered probe light, and imperfect optics obscure the desired signal. The goal is to determine the integrated column density $\tilde{n}(x, y)$ across the image. In this section, I discuss the image processing methods by which this is done. These methods differ for absorption and phase-contrast imaging, as discussed below.

A.1 Absorption image processing

An absorption image measures a photon fluence field $F_I(x, y)$ which has three components given by

$$F_I(x, y) = F_{I0} \left[P(x, y) e^{-\tilde{D}(x, y)} + S(x, y) \right] + N(x, y) \quad (\text{A.1})$$

The first component describes light which passes through the cloud, is collected by the imaging system, and imaged onto the camera. The fluence of the probe beam is given by F_{I0} , and $P(x, y)$ describes the normalized beam profile in the object plane. This beam profile is typically far from Gaussian due to flawed optical elements and multiple reflections in the beam path before the object plane. The quantity $\tilde{D}(x, y)$ is the optical density of the cloud, from which the column density $\tilde{n}(x, y)$ can be derived. The second component, $F_{I0}S(x, y)$ describes probe light scattered after the object plane. The last component, $N(x, y)$, describes background light from all sources other than the probe beam. Useful data cannot typically be extracted from the absorption image alone (see for example fig. A-1a). Thus, we take two additional images for each absorption image: a bright-field image $F_B(x, y)$ where the probe beam is imaged with no absorbing atoms, and a dark-field image $F_D(x, y)$ with no atoms and no probe light. The intensity measured in these images are given by

$$F_B(x, y) = F_{B0} [P(x, y) + S(x, y)] + N(x, y) \quad (\text{A.2})$$

$$F_D(x, y) = N(x, y) \quad (\text{A.3})$$

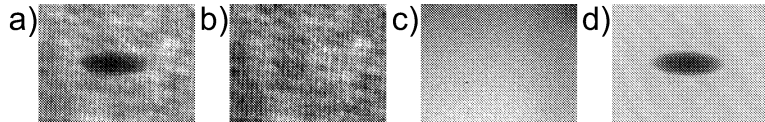


Figure A-1: Obtaining a reliable transmission image. Three images are collected: a) an image of the probe light after passing through the atoms, b) a bright-field image, and c) a dark-field image. These are processed according to Eq. (A.5) to give a transmission image (d).

We obtain a transmission image $\tilde{T}(x, y) = t^2$ by the normalization

$$\tilde{T}(x, y) = \frac{F_I(x, y) - F_D(x, y)}{F_B(x, y) - F_D(x, y)} \quad (\text{A.4})$$

$$= \frac{F_{I0}}{F_{B0}} \frac{P(x, y)e^{-\tilde{D}(x, y)} + S(x, y)}{P(x, y) + S(x, y)} \quad (\text{A.5})$$

We can compensate for shot-to-shot probe intensity fluctuations ($F_{I0} \neq F_{B0}$) by examining a portion of each image in which there are no atoms. With this, and assuming that the $S(x, y)$ “noise” term is small, we get

$$\tilde{T} \simeq e^{-\tilde{D}(x, y)} + \left[1 - e^{-\tilde{D}(x, y)}\right] \frac{S(x, y)}{P(x, y)} \quad (\text{A.6})$$

For small $S(x, y)$ and small optical densities, this normalization directly measures the absorption of the probe light by the atoms. An example of this normalization is given in Fig. A-1. Notice that even with substantial inhomogeneities in the probe beam a high-quality absorption image is obtained. This normalization scheme does have its limitations. For example, $\tilde{D}(x, y) = -\ln[\tilde{T}(x, y)]$, and thus the error in the optical density is given by $d\tilde{D} = -d\tilde{T}/\tilde{T}$. Therefore, measurements of high optical densities (larger than about two) are highly sensitive to technical noise.

A second limitation is the difficulty of canceling out high-spatial frequency noise in the presence of vibrations of the imaging system. Consider a component in $P(x, y)$ of wavevector \mathbf{k} (i.e. $P(x, y) = P_0[1 + \epsilon \cos(\mathbf{k} \cdot \mathbf{r})]$ where \mathbf{r} is the vector (x, y)) and suppose the imaging system is displaced by a small distance \mathbf{d} between the absorption and bright field image. Then, neglecting $N(x, y)$ and $S(x, y)$, after normalization we obtain

$$\tilde{T}(x, y) = \frac{[1 + \epsilon \cos(\mathbf{k} \cdot \mathbf{r})] e^{-\tilde{D}(x, y)}}{1 + \epsilon \cos(\mathbf{k} \cdot (\mathbf{r} - \mathbf{d}))} \quad (\text{A.7})$$

$$\simeq e^{-\tilde{D}(x, y)} [1 + \epsilon [\mathbf{k} \cdot \mathbf{d}] \sin(\mathbf{k} \cdot \mathbf{r})] \quad (\text{A.8})$$

This noise can be minimized by reducing the amplitude ϵ of the noise, decreasing the spatial frequency of the noise, and minimizing the vibrations of the imaging system. It is often possible to ensure that the predominant technical noise is at spatial frequencies that are orthogonal to the typical displacements or in directions that are not relevant to interpreting the images.

A.2 Phase-contrast image processing

The spatial filtering in phase-contrast imaging adds one complication: high spatial frequency components of the probe beam can miss the phase-shifting spot in the Fourier plane (Fig. 3-9b). Therefore, different normalization methods are required for absorption

and phase contrast images. In phase contrast imaging there are two sources of imaging error: (1) inhomogeneities in the probe light, and (2) probe light which is scattered onto the camera in a random pattern. To simplify the discussion, let us consider the presence of only one of these error sources at a time.

For the first case, we consider a beam incident on the atoms with an inhomogeneity described by $\epsilon(x, y)$: $E_1(x, y) = E_0[1 + \epsilon(x, y)]$. After passing through the atomic sample and acquiring a phase shift $\phi(x, y)$, the electric field becomes $E_2(x, y) = E_0[1 + (e^{-i\phi} - 1) + \epsilon(x, y)e^{-i\phi}]$. The uniform part of this light comes to a tight focus at the Fourier plane of the imaging system and is phase-shifted, resulting in a field at the camera $E_3(x, y) = E_0[-i + (e^{-i\phi} - 1) + \epsilon e^{-i\phi}]$. The light fluence collected in the image is then

$$F_I(x, y) = F_{I0} \left[3 - 2\sqrt{2} \cos(\phi + \frac{\pi}{4}) + |\epsilon|^2 + 2\operatorname{Re} [\epsilon e^{-i\phi} (e^{i\phi} - 1 + i)] \right] + N(x, y) \quad (\text{A.9})$$

To try to eliminate the errors in this signal, we collect two more images as before, a bright field image $F_B(x, y)$ and a dark-field image $F_D(x, y)$ given by

$$F_B(x, y) = F_{B0} [1 + |\epsilon|^2 + 2\operatorname{Re}[i\epsilon]] + N(x, y) \quad (\text{A.10})$$

$$F_D(x, y) = N(x, y) \quad (\text{A.11})$$

We have used two methods to recover the phase-contrast signal. The first method is the same we use for analyzing absorption images. This gives a phase-contrast signal

$$PC^{(1)}(x, y) = 1 + 2 \left[\frac{1 - \sqrt{2} \cos(\phi + \frac{\pi}{4}) + \operatorname{Re}[\epsilon(1 - e^{-i\phi})(1 - i)]}{1 + |\epsilon|^2 - 2\operatorname{Im}[\epsilon]} \right] \quad (\text{A.12})$$

In this method the noise ϵ in the probe beam is mixed into the phase-contrast signal.

The second normalization method is to subtract out the dark-field images, and separately normalize $F_I(x, y)$ and $F_B(x, y)$ by dividing each by the average fluence in a portion of the image where the atom cloud is not visible (usually a far corner of the image). We then subtract the normalized $F_B(x, y)$ from $F_I(x, y)$ obtaining

$$PC^{(2)}(x, y) = 2 \left[1 - \sqrt{2} \cos(\phi + \frac{\pi}{4}) + \operatorname{Re}[\epsilon(1 - e^{-i\phi})(1 - i)] \right] \quad (\text{A.13})$$

Now the mixing of the signal with the noise in the denominator has been eliminated.

Let us now consider the noise $\epsilon(x, y)$ to be a speckle pattern which originates from scattering off surfaces after the object plane. Thus, the noise ϵ is not affected by the atoms, i.e. the electric field at the camera is $E_3(x, y) = E_0[-i + \epsilon + (e^{-i\phi} - 1)]$. The data image collected at the camera is described by

$$F_I(x, y) = F_{I0} \left[3 - 2\sqrt{2} \cos(\phi + \frac{\pi}{4}) + |\epsilon|^2 + 2\operatorname{Re} [\epsilon(e^{i\phi} - 1 + i)] \right] + N(x, y) \quad (\text{A.14})$$

In this case, the two normalization approaches yield

$$PC^{(1)}(x, y) = 1 + 2 \left[\frac{1 - \sqrt{2} \cos(\phi + \frac{\pi}{4}) + \operatorname{Re}[\epsilon(e^{i\phi} - 1)]}{1 + |\epsilon|^2 - 2 \operatorname{Im}[\epsilon]} \right] \quad (\text{A.15})$$

$$PC^{(2)}(x, y) = 2[1 - \sqrt{2} \cos(\phi + \frac{\pi}{4}) + \operatorname{Re}[\epsilon(e^{i\phi} - 1)]] \quad (\text{A.16})$$

In this case, if the phase of ϵ varies spatially, the second method of normalization is clearly superior since the errors are random.

In the end, we turned to our data to answer the question of which normalization procedure to use. Figure A-2 compares data from images of a partly condensed cloud which was normalized using both normalization procedures. The second normalization method gives a better fit to the expected parabolic density profile of a condensate, and thus is preferable.

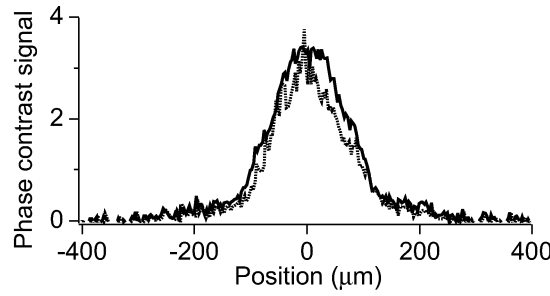


Figure A-2: Comparison of two normalization methods for phase-contrast images. Dotted line shows result of normalization $PC^{(1)}$, and the solid line shows $PC^{(2)}$, which gives a more reliable signal.

Appendix B

Method for the numerical calculation of the spin structure of domain boundaries

As discussed in Chapter 10, the ground-state structure of an $F = 1$ spinor Bose–Einstein condensate under the restriction of spin conservation is obtained by minimizing the restricted energy K_{tot} given in Eq. 10.16. To determine the structure of spin domain boundaries, we considered a one-dimensional situation, and minimized K_{tot} by the numerical method of imaginary-time propagation (see relevant description in Ref. [329]).

This numerical procedure is quite simple to understand. The temporal evolution of a wavefunction ψ is given by the Schrödinger equation

$$-i\hbar \frac{\partial \psi}{\partial t} = \mathcal{H}\psi \quad (\text{B.1})$$

which gives a solution of the form

$$\psi(t) = \sum_i c_i e^{-itE_i/\hbar} |i\rangle \quad (\text{B.2})$$

where ψ has been expanded in terms of the states $|i\rangle$ which are eigenstates of the Hamiltonian \mathcal{H} with energies E_i . If we make the transformation $t \rightarrow -i\tau$, the temporal evolution becomes

$$\psi(\tau) = \sum_i c_i e^{-\tau E_i/\hbar} |i\rangle \quad (\text{B.3})$$

Thus, if we propagate the wavefunction ψ forward in “imaginary time” τ using the equation

$$-\hbar \frac{\partial \psi}{\partial \tau} = \mathcal{H}\psi, \quad (\text{B.4})$$

the wavefunction $\psi(\tau \rightarrow \infty)$ will converge toward the state with lowest energy $|0\rangle$ as long

as $c_0 \neq 0$.

To obtain the ground-state spin domain structure, we calculated the temporal evolution of the vectorial order parameter $\vec{\psi}(z, \tau)$ according to the following set of equations:

$$\begin{aligned} -\hbar \frac{\partial \psi_1}{\partial \tau} &= \left(-\frac{\hbar^2}{2m} \frac{d^2}{dz^2} - \mu + q - p(z) \right) \psi_1 \\ &\quad + [(g_0 + g_2)|\psi_1|^2 + (g_0 + g_2)|\psi_0|^2 + (g_0 - g_2)|\psi_{-1}|^2] \psi_1 \\ &\quad + g_2 \psi_{-1}^* \psi_0^2 \end{aligned} \quad (\text{B.5})$$

$$\begin{aligned} -\hbar \frac{\partial \psi_0}{\partial \tau} &= \left(-\frac{\hbar^2}{2m} \frac{d^2}{dz^2} - \mu \right) \psi_0 \\ &\quad + [(g_0 + g_2)|\psi_1|^2 + g_0 |\psi_0|^2 + (g_0 + g_2)|\psi_{-1}|^2] \psi_0 \\ &\quad + 2g_2 \psi_0^* \psi_{-1} \psi_{-1} \end{aligned} \quad (\text{B.6})$$

$$\begin{aligned} -\hbar \frac{\partial \psi_{-1}}{\partial \tau} &= \left(-\frac{\hbar^2}{2m} \frac{d^2}{dz^2} - \mu + q + p(z) \right) \psi_{-1} \\ &\quad + [(g_0 - g_2)|\psi_1|^2 + (g_0 + g_2)|\psi_0|^2 + (g_0 + g_2)|\psi_{-1}|^2] \psi_{-1} \\ &\quad + g_2 \psi_1^* \psi_0^2 \end{aligned} \quad (\text{B.7})$$

The right-hand sides of the above equations are given by

$$\mathcal{H}\psi_i = \frac{\delta K_{\text{tot}}}{\delta \psi_i^*} \quad (\text{B.8})$$

The interaction parameters g_0 and g_2 were defined as in Eq. 10.6 with $a_{F_{\text{tot}}=2} = 2.75$ nm [189] and $(a_{F_{\text{tot}}=2} - a_{F_{\text{tot}}=0})/3 = 0.1$ nm [308].

In our calculation method, number conservation was explicitly enforced by renormalizing the spinor wavefunction $\vec{\psi}(z)$ after every time step to give an average density of $n = 4.15 \times 10^{14}$ cm⁻³. The chemical potential was set initially to $\mu = (g_2 + g_0)n = k_B \times 300$ nK, and was adjusted during the calculation so that the average density was unchanged after each time step. In this way, μ converged to the ground-state chemical potential, although its value was not relevant for this calculation.

The structure of the boundaries at different magnetic bias fields B_0 were calculated by setting the quadratic Zeeman energy to $q = \hat{q}B_0^2$ where $\hat{q} = k_B \times 20$ nK/G² for sodium. The linear Zeeman term $p(z)$ was set to $p(z) = p_0 + p'z$. We set p_0 to the value determined by the Thomas–Fermi approach of Sec. 10.3 for the location of the spin-domain boundary (see Fig. 10-2)

$$p_0 = \begin{cases} q, & q > c \\ 2\sqrt{qc}, & q < c \end{cases} \quad (\text{B.9})$$

where $c = g_2 n/2$. A field gradient term $p'z$ was added to ensure that the $m_F = 1$ domain

remained on one side of the boundary and the $m_F = 0$ domain on the other. A setting of $p' = -g\mu_B B'$ with $B' = 50$ mG/cm was chosen where $g = -1/2$ is the Landé g -factor and μ_B the Bohr magneton.

The results of these calculations are presented in Sec. 10.9

Appendix C

Bosonic stimulation in the formation of a Bose-Einstein condensate

This appendix includes the following paper [9]: H.-J. Miesner, D.M. Stamper-Kurn, M.R. Andrews, D.S. Durfee, S. Inouye, and W. Ketterle, “Bosonic stimulation in the formation of a Bose-Einstein condensate.” Reprinted with permission from Science **279**, 1005 (1998). Copyright 1998 American Association for the Advancement of Science.

Bosonic Stimulation in the Formation of a Bose-Einstein Condensate

H.-J. Miesner, D. M. Stamper-Kurn, M. R. Andrews,
D. S. Durfee, S. Inouye, W. Ketterle

The formation of a Bose-Einstein condensate of a dilute atomic gas has been studied *in situ* with a nondestructive, time-resolved imaging technique. Sodium atoms were evaporatively cooled close to the onset of Bose-Einstein condensation and then suddenly quenched to below the transition temperature. The subsequent equilibration and condensate formation showed a slow onset distinctly different from simple relaxation. This behavior provided evidence for the process of bosonic stimulation, or coherent matter-wave amplification, crucial to the concept of an atom laser.

At low temperature, many properties of systems are determined by the quantum statistics of their constituents. For one type of particles, known as bosons, transition rates into a given quantum state are enhanced by the presence of other identical bosons in that state. Explicitly, if N bosons occupy a given state, the transition rates into that state are proportional to $(N + 1)$. This effect, known as Bose stimulation, is most familiar as the gain mechanism in an optical laser, where the presence of photons in the lasing mode stimulates the emission of more photons into it. Similarly, in the case of bosonic atoms, Bose stimulation can lead to matter-wave amplification and constitutes the gain mechanism of an atom laser, a device that creates a coherent beam of atoms by means of a stimulated process. The Bose-Einstein distribution function can be derived from Bose stimulation and detailed balance. In particular, a Bose-Einstein condensate is only stable because of the enhanced elastic scattering into the condensate. Bose-Einstein condensation (BEC) was recently observed in dilute atomic gases (1) and was used to realize an atom laser. Our first demonstration of an atom laser (2, 3) focused on the direct proof that atoms coupled out from a condensate were coherent. In this work, we consider the gain process by studying the formation of the condensate.

The theoretical description of BEC in weakly interacting dilute gases has a long history and has accounted for most of the experimental results (4, 5). In contrast, a full description of the dynamics of condensate formation has not yet been developed. Predictions for the time scale of condensation varied between infinite (6) and extremely short (7). The early prediction for infinite time was based on a Boltzmann equation; in this framework, the condensate fraction cannot grow from zero (6, 8, 9). Thus, a separate

process of nucleation had to be introduced with Boltzmann equations describing the dynamics only before (10) and after (11) the nucleation. Stoof suggested that a condensate nucleates in a short coherent stage (7, 9, 12) and then grows according to a kinetic equation. Kagan and collaborators discussed the formation of a quasi-condensate that, in contrast to a condensate, has phase fluctuations; they die out on a time scale that increases with the size of the system (13–16). In the thermodynamic limit, it would take infinite time to establish off-diagonal long-range order. Recently, a fully quantum mechanical kinetic theory for a Bose gas has been formulated and was used to model the formation process of the condensate (17).

The experimental realization of BEC certainly proved that condensates form within a finite time. Likewise, the observation of high-contrast interference between two condensates demonstrated that condensates develop long-range coherence in a finite time (2). However, a determination of the intrinsic time scales was not possible because the cooling was slow enough that the system stayed close to thermal equilibrium. Thus, the buildup of the condensate followed the externally controlled temperature and did not reveal the more rapid intrinsic dynamics of condensate formation. In the work presented here, we cooled the system to a temperature slightly above the phase transition and then suddenly created a nonequilibrium configuration of lower energy in order to observe the intrinsic relaxation toward a new condensed equilibrium.

The experimental setup for cooling to the onset of BEC was similar to our previous work. Sodium atoms were optically cooled and trapped and then transferred into a cloverleaf magnetic trap (18). Further cooling by radio frequency (rf) evaporation (19) was conducted with a trapping potential determined by the axial curvature of the magnetic field of $B'' = 125 \text{ G cm}^{-2}$, the radial gradient of up to $B' = 150 \text{ G cm}^{-1}$, and the bias field

of typically $B_0 = 1.5 \text{ G}$. Most of this study was performed with a weaker trap, where the magnetically trapped cloud was adiabatically expanded after evaporative cooling by reducing B' to 80 G cm^{-1} . In the strong (weak) trap the transition was reached after 26 s of evaporation at $1.5 \mu\text{K}$ ($1 \mu\text{K}$) with 2×10^7 (9×10^7) sodium atoms in the $F = 1$, $m_F = -1$ ground state. The atom clouds were cigar-shaped, with the long axis horizontal.

The temperature of the cloud was controlled by the final frequency of the rf sweep during evaporative cooling and was brought to slightly above the phase-transition temperature. A nonequilibrium situation was then created by concluding the evaporation with a fast sweep of the rf frequency, ramping down by 200 kHz in 10 ms. This sweep caused a sudden truncation of the wings of the spatial distribution, where atoms were resonantly spin-flipped to a nontrapped state. The final frequency of the sweep depended critically on drifts in the magnetic bias field B_0 on the order of 10 mG. Rapid “quenching” of the cloud into the BEC regime was essential to clearly observe the onset of condensate formation. After the rf sweep, the intrinsic dynamics of condensate growth was observed without any further cooling in a completely isolated system.

The condensate was directly observed by nondestructive phase-contrast imaging (20, 21) with the use of a vertical probe laser beam at a detuning of 1.7 GHz. A series of 18 images was taken (Fig. 1) by a charge-coupled device (CCD) camera in kinetics mode (21), allowing for a time-resolved measurement of the formation of single condensates. The probe laser power was

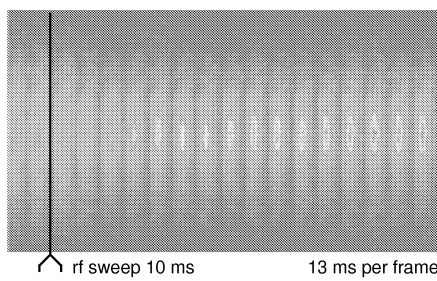


Fig. 1. Formation of a Bose-Einstein condensate. Shown is a sequence of 18 phase-contrast images of the same condensate taken *in situ*. The first two frames show a thermal cloud at a temperature above the transition temperature. The following 16 frames were taken after the cloud was quenched to below the BEC transition and show the growth of a condensate at the center of the cloud at 13-ms intervals. Note the decrease in the number of thermal atoms and their smaller width after the rf sweep. The column density of atoms is shown in false color: yellow to red marks the high density of the condensate. The length of the images is 630 μm .

Department of Physics and Research Laboratory of Electronics, Massachusetts Institute of Technology, Cambridge, MA 02139, USA.

chosen low enough that heating during the detection process was negligible. The initial and final equilibrium conditions were characterized by taking the first images before the sweep and the last three images 300 to 400 ms after. The ability to obtain real-time “movies” of the formation was used to overcome shot-to-shot fluctuations in initial conditions. The numbers of condensate and thermal atoms as well as the temperatures were extracted from one- and two-dimensional fits to the density distributions (Fig. 2). A bimodal function was fit to the density distribution with a Bose-Einstein distribution for the thermal fraction and an inverted parabola for the condensate density $n_0(r) = n_0(0) - V(r)/\tilde{U}$. The latter is the solution of the nonlinear Schrödinger equation in the Thomas-Fermi approximation (22). Here, $V(r)$ denotes the trapping potential as a function of radial distance r , and $\tilde{U} = 4\pi\hbar^2a/m$ describes the interaction between the atoms of mass m , where \hbar is the Planck constant divided by 2π , and $a = 2.75$ nm is the scattering length. The temperatures were obtained by fits to the wings of the thermal fraction, and the absolute numbers of condensate atoms were determined from the axial length of the condensate assuming the Thomas-Fermi approximation. This result provided an accurate calibration for the phase-contrast signal. Condensates smaller than 10^5 atoms could not be discerned against the background of the thermal cloud.

Figure 3A shows a single-shot growth of the condensate. Equilibrium was reached within 200 ms after the rf sweep. Better statistics were obtained by averaging over

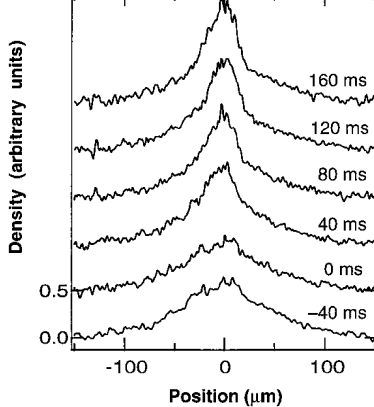


Fig. 2. Representative profiles of atom clouds during condensate formation. These are longitudinal cuts through the column densities obtained from phase-contrast images similar to those in Fig. 1. The rf sweep, which quenched the cloud, was applied between $t = -10$ ms and $t = 0$. Labels show the time elapsed after the rf sweep. The formation of the condensate is reflected by the growth of the central peak.

several traces (Fig. 3B) with the same equilibrium condensate number. Temporal fluctuations of about 20 ms were eliminated by shifting the curves before averaging. The fluctuations in condensate number are probably due to shot-to-shot variations in loading conditions ($\sim 20\%$) and to variations in the truncation caused by drifts of the magnetic field B_0 . Also, because of these fluctuations, there was sometimes a small condensate already produced before the rapid rf sweep. The final condensate fraction varied between 5 and 20%. When no condensate was present right after the rf sweep, the growth started slowly and sped up after 50 to 100 ms. In contrast, if there was already a substantial condensate fraction at the beginning of the rf sweep, rapid growth of the condensate commenced immediately (Fig. 3B). These different behaviors are in agreement with the model based on bosonic stimulation described below.

Because the formation of the condensate is expected to be a Bose-stimulated process, the number of condensate atoms N_0 should grow initially as $N_0 = \gamma N_0$, where γ is the initial growth rate. Eventually, when the cloud reaches equilibrium ($N_{0,eq}$ condensate atoms), the growth rate becomes zero, which can be parameterized by assuming

$$\dot{N}_0 = \gamma N_0 \left[1 - \left(\frac{N_0}{N_{0,eq}} \right)^\delta \right] \quad (1)$$

The exponent δ was set to 2/5, consistent

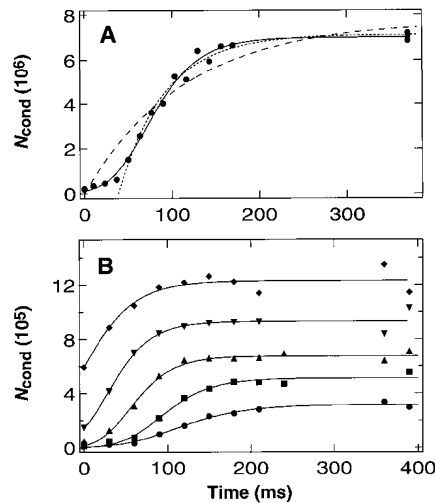


Fig. 3. Growth of the condensate fraction toward equilibrium. Shown is the number of condensate atoms versus the time after the end of the rf sweep. The number of condensate atoms in equilibrium was measured about 400 ms after the rf sweep. (A) Growth of a single condensate in the weak trap (circles); (B) average of about 10 traces with similar equilibrium values for the number of condensate atoms in the strong trap (symbols). The solid lines correspond to the solution of Eq. 1; the dashed and dotted lines in (A) are solutions of Eq. 3.

with an approximate microscopic theory (17) for which the rate of growth is linear in the difference of the chemical potentials of the condensate (which is proportional to $N_0^{2/5}$) and the surrounding thermal cloud. All condensate growth curves in Figs. 3 and 4 were fit with the solution of Eq. 1

$$N_0(t) = N_{0,i} e^{\gamma t} \left[1 + \left(\frac{N_{0,i}}{N_{0,eq}} \right)^\delta (e^{\delta \gamma t} - 1) \right]^{-1/\delta} \quad (2)$$

The only free parameters were γ and the initial number of condensate atoms $N_{0,i}$ at time $t = 0$, that is, right after the rf sweep. Treating δ as a free parameter did not improve the quality of the fits. Equation 2 describes the observed growth curves very well (Figs. 3 and 4).

It should be pointed out that Eq. 1 is quite different from the differential equation for a pure relaxation process, which is described by

$$N_0 = \tilde{\gamma}(N_{0,eq} - N_0) \quad (3)$$

The solution of Eq. 3 is an exponential approach to equilibrium

$$N(t) = N_{0,eq}(1 - e^{-\tilde{\gamma}t})$$

that starts right after the rf sweep (dashed line in Fig. 3A); it describes the data very poorly.

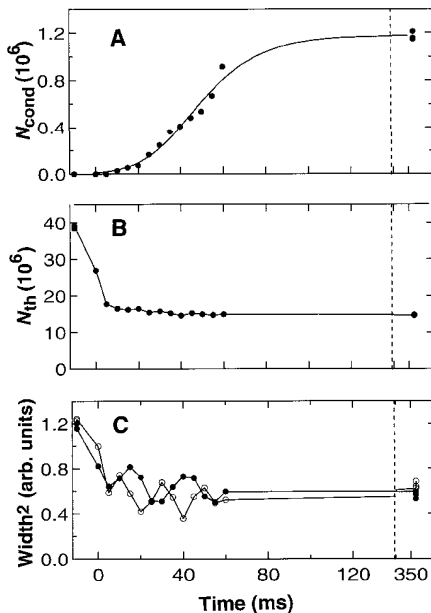


Fig. 4. Initial stage of the formation process, recorded for a single formation event. (A) The number of atoms in the condensate, (B) the number of thermal atoms, and (C) the effective temperature of the cloud, represented by the square of the widths of the thermal cloud in the radial (open circles) and axial (full circles) directions. Note the break in the time axis indicated by the dashed line. The solid line in (A) corresponds to the solution of Eq. 1; those in (B) and (C) connect the data points.

We also added an induction time as an additional free parameter (dotted line in Fig. 3A). With a value of 40 ms, it describes the data fairly well after a small condensate has formed and shows that the main effect of bosonic stimulation is an induction time before the onset of rapid growth. In Eq. 2, this induction time corresponds to the time of pure exponential growth, that is, bosonic stimulation, which is short and prominent only for small N_0 because of the small value of $\delta = 2/5$.

The early stage of condensate formation was studied by taking pictures every 5 ms (Fig. 4). The thermal density showed no major deviation from a Bose-Einstein distribution; the effective temperature quickly relaxed toward half the initial value (Fig. 4C), accompanied by weak, strongly damped quadrupole-type oscillations at a frequency of about two times the axial trap frequency. The total number of thermal atoms reached a quasi-stationary value about 5 ms after the end of the rf sweep and was fairly constant during the formation of the (small) condensate. This quick “equilibration” is in accord with time scales set by the magnetic trap—that is, a quarter cycle in the harmonic potential, which was 3 ms radially and 14 ms axially—and by the elastic scattering rate $\gamma_{\text{el}} = n\sigma v \approx 500 \text{ s}^{-1}$; here n is the atom density, $\sigma = 8\pi a^2$ denotes the elastic collision cross section, $v = 4(k_B T/\pi m)^{1/2}$ is the thermal velocity, k_B is the Boltzmann constant, and T is the temperature. Therefore, the condensate growth, which happens on a time scale of 100 ms, should only be weakly perturbed by transients from the initial truncation process. Furthermore, Fig. 3B is evidence that the transients did not suppress the initial condensate growth: the condensate started growing without a notable induction time in those cases where a considerable condensate fraction was already present. These results suggest that condensation occurred in two steps: a fast relaxation that produced an

oversaturated “thermal” cloud, followed by a slower growth of the condensate within the thermal cloud.

A detailed discussion of the second phase of formation has recently been formulated by Gardiner and collaborators (17) for the inhomogeneous Bose gas. They assume that the condensate is in contact with a thermal cloud at a constant temperature below the transition point. Using a master equation based on quantum kinetic theory (17), they derived a growth equation for the condensate (valid for large N_0 , as in our experiment)

$$\dot{N}_0 = 2W^+(N_0) \left\{ \left[1 - \exp\left(\frac{\mu_N - \mu}{k_B T}\right) \right] N_0 + 1 \right\} \quad (4)$$

The first term in the curly brackets is the stimulated scattering term, which is non-vanishing as long as the chemical potential of the thermal bath μ is different from the chemical potential μ_N of the condensate. The last term (the number one) stands for spontaneous scattering into the condensate mode. The function $W^+(N_0)$ is only weakly dependent on N_0 during the formation and, for $\mu \ll k_B T$, is approximately equal to $W^+ = \sqrt{8}\zeta(3/2)\gamma_{\text{el}}$, where $\zeta(3/2) \approx 2.612$ is the Riemann zeta function. If we assume μ and $\mu_N \ll k_B T$ in Eq. 4, use a Thomas-Fermi expression for

$$\mu_N = (15\hbar^2 a \sqrt{m \bar{\omega}^3} N_0 / \sqrt{8})^{2/5} \quad (5)$$

(and similarly for μ , with N_0 replaced by $N_{0,\text{eq}}$), and neglect the spontaneous scattering term, we obtain our Eq. 1 with

$$\gamma = 2W^+ \frac{\mu}{k_B T} \propto N_{0,\text{eq}}^{2/5} T \quad (6)$$

where $\bar{\omega}$ denotes the geometric mean of the trapping frequencies.

Our results for the rate parameter γ are larger than this theoretical prediction by a factor that ranges between 3 and 15. Furthermore, Eq. 6 predicts an increase of the rate γ with both temperature T and the number of condensate atoms in equilibrium $N_{0,\text{eq}}$. The observed trend is in the opposite direction (Fig. 5), that is, γ decreases when $N_{0,\text{eq}}$ and T simultaneously increase. This trend is independent of the value assumed for δ between 0.2 and 5 (23). A tentative explanation is saturation of the stimulated growth rate of the condensate. This rate should ultimately be limited by the rate of elastic collisions within the volume of the condensate; strong stimulation would create some local depletion of the thermal cloud, which is not included in the theory.

In order to obtain a full quantitative understanding of the condensate formation,

more detailed studies are necessary experimentally and, especially, theoretically. On the experimental side, an improved signal-to-noise ratio could reveal more clearly the details of the initial phase of condensate formation, dominated by a pure exponential growth, which would provide a direct proof of Bose stimulation. Ultimately, the nucleation process and fluctuations in the onset of condensate formation (9, 14, 16) might be observed. Also, a further characterization of the nonequilibrium situation would be helpful. Theory could include a realistic model of the spatial truncation process, but it seems that a more refined approach is necessary to resolve the discrepancies with our observations.

REFERENCES AND NOTES

1. M. H. Anderson, J. R. Ensher, M. R. Matthews, C. E. Wieman, E. A. Cornell, *Science* **269**, 198 (1995); K. B. Davis *et al.*, *Phys. Rev. Lett.* **75**, 3969 (1995); C. C. Bradley, C. A. Sackett, R. G. Hulet, *ibid.* **78**, 985 (1997); see also C. C. Bradley *et al.*, *ibid.* **75**, 1687 (1995).
2. M. R. Andrews *et al.*, *Science* **275**, 637 (1997).
3. M.-O. Mewes *et al.*, *Phys. Rev. Lett.* **78**, 582 (1997).
4. A. Griffin, D. W. Snoke, S. Stringari, Eds., *Bose-Einstein Condensation* (Cambridge Univ. Press, Cambridge, 1995).
5. Abstracts from a workshop on Bose-Einstein condensation, Castelvecchio, Italy, 12 to 17 July 1997.
6. E. Levich and V. Yakhot, *Phys. Rev. B* **15**, 243 (1977).
7. H. T. C. Stoof, *Phys. Rev. Lett.* **66**, 3148 (1991).
8. S. G. Tikhodeev, *Sov. Phys. JETP* **70**, 380 (1990) [*Zh. Eksp. Teor. Fiz.* **97**, 681 (1990)].
9. H. T. C. Stoof, in (4), pp. 226–245.
10. D. W. Snoke and J. P. Wolfe, *Phys. Rev. B* **39**, 4030 (1989); H. Wu, E. Arimondo, C. J. Foot, *Phys. Rev. A* **56**, 560 (1997).
11. U. Eckern, *J. Low Temp. Phys.* **54**, 333 (1984); B. V. Svistunov, *J. Moscow Phys. Soc.* **1**, 373 (1991); D. V. Semikoz and I. I. Tkachev, *Phys. Rev. Lett.* **74**, 3093 (1995).
12. H. T. C. Stoof, *Phys. Rev. Lett.* **78**, 768 (1997).
13. Yu. Kagan, B. V. Svistunov, G. V. Shlyapnikov, *Sov. Phys. JETP* **75**, 387 (1992).
14. Yu. Kagan and B. V. Svistunov, *ibid.* **78**, 187 (1994) [*Zh. Eksp. Teor. Fiz.* **105**, 353 (1994)].
15. _____, *Phys. Rev. Lett.* **79**, 3331 (1997).
16. Yu. Kagan, in (4), pp. 202–225.
17. C. W. Gardiner, P. Zoller, R. J. Ballagh, M. J. Davis, *Phys. Rev. Lett.* **79**, 1793 (1997).
18. M.-O. Mewes *et al.*, *ibid.* **77**, 416 (1996).
19. W. Ketterle and N. J. van Druten, in *Advances in Atomic, Molecular, and Optical Physics*, B. Bederson and H. Walther, Eds. (Academic Press, San Diego, 1996), vol. 27, pp. 181–236; and references therein.
20. E. Hecht, *Optics* (Addison-Wesley, Reading, MA, ed. 2, 1989); M. R. Andrews *et al.*, *Science* **273**, 84 (1996).
21. M. R. Andrews *et al.*, *Phys. Rev. Lett.* **79**, 553 (1997).
22. G. Baym and C. J. Pethick, *ibid.* **76**, 6 (1996).
23. The main effect of changing δ is a change in γ by the inverse factor.
24. We thank C. Gardiner and D. Pritchard for stimulating discussions. This work was supported by the Office of Naval Research, the National Science Foundation, the Joint Services Electronics Program (Army Research Office), and the Packard Foundation. D.M.S.-K. acknowledges support from an NSF Graduate Research Fellowship, and H.-J.M. from Deutscher Akademischer Austauschdienst (NATO Science Fellowship).

18 December 1997; accepted 7 January 1997

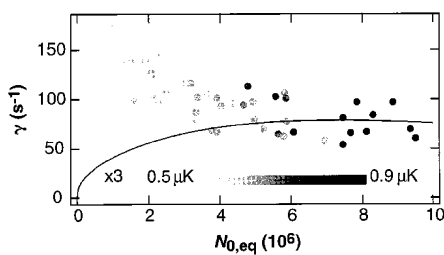


Fig. 5. Condensate growth rate γ versus number of condensate atoms in equilibrium $N_{0,\text{eq}}$. The points are fits to single growth curves. The shade of the points indicates the final temperature T of the cloud. $N_{0,\text{eq}}$ and T were coupled by the depth of the truncation in the rf sweep. The solid line indicates the theoretical prediction for γ according to Eq. 6, multiplied by a factor of 3.

Appendix D

Optical confinement of a Bose–Einstein condensate

This appendix includes the following paper [10]: D.M. Stamper–Kurn, M.R. Andrews, A.P. Chikkatur, S. Inouye, H.-J. Miesner, J. Stenger and W. Ketterle, “Optical confinement of a Bose–Einstein condensate,” *Phys. Rev. Lett.* **80**, 2027 (1998).

Optical Confinement of a Bose-Einstein Condensate

D. M. Stamper-Kurn, M. R. Andrews, A. P. Chikkatur, S. Inouye, H.-J. Miesner, J. Stenger, and W. Ketterle

*Department of Physics and Research Laboratory of Electronics, Massachusetts Institute of Technology,
Cambridge, Massachusetts 02139*

(Received 7 November 1997)

Bose-Einstein condensates of sodium atoms have been confined in an optical dipole trap using a single focused infrared laser beam. This eliminates the restrictions of magnetic traps for further studies of atom lasers and Bose-Einstein condensates. More than 5×10^6 condensed atoms were transferred into the optical trap. Densities of up to $3 \times 10^{15} \text{ cm}^{-3}$ of Bose condensed atoms were obtained, allowing for a measurement of the three-body loss rate constant for sodium condensates as $K_3 = 1.1(3) \times 10^{-30} \text{ cm}^6 \text{s}^{-1}$. At lower densities, the observed $1/e$ lifetime was longer than 10 s. Simultaneous confinement of Bose-Einstein condensates in several hyperfine states was demonstrated. [S0031-9007(98)05537-9]

PACS numbers: 03.75.Fi, 05.30.Jp, 32.80.Pj, 64.60.-i

The recent realization of Bose-Einstein condensation [1–3] and of an atom laser [4,5] have sparked many theoretical and experimental studies of coherent atomic matter [6]. Yet, these studies are limited by the magnetic traps used by all experiments so far. For example, in the first demonstration of an atom laser, coherent atomic pulses were coupled out into an inhomogeneous magnetic field, which served to confine the remaining condensate. Thus, during propagation, the pulses were exposed to Zeeman shifts. While these shifts were mitigated by producing $m_F = 0$ atoms, quadratic Zeeman shifts may preclude precision experiments on such pulses. Magnetic trapping also imposes limitations on the study of Bose-Einstein condensates, because only the weak-field seeking atomic states are confined. Since the atomic ground state is always strong-field seeking, weak-field seeking states can inelastically scatter into the ground state (dipolar relaxation), resulting in heating and trap loss. Furthermore, trap loss may dramatically increase through spin relaxation collisions when different hyperfine states are simultaneously trapped, restricting the study of multicomponent condensates. Although in ^{87}Rb this increase is less dramatic due to a fortuitous cancellation of transition amplitudes [7], spin relaxation is still the dominant decay mechanism for double condensates in this system.

All these problems are avoided if Bose-Einstein condensation is achieved in an optical trap based on the optical dipole force which confines atoms in all hyperfine states. This has been one motivation for the development of subrecoil cooling techniques [8,9], the development of various optical dipole traps [10–14], and for pursuing Raman cooling [15,16] and evaporative cooling [17] in such traps. The highest phase space density achieved by purely optical means was a factor of 400 below that required for Bose-Einstein condensation [15].

In this paper, we report the successful optical trapping of a Bose-Einstein condensate using a different approach: first evaporatively cooling the atoms in a magnetic trap, and

then transferring them into an optical trap. This approach circumvents many difficulties usually encountered with optical dipole traps. Since the temperature of atoms is reduced through rf evaporation by a factor of 100, only milliwatts of laser power are needed as compared with several watts used to directly trap laser-cooled atoms. This ameliorates trap loss from heating processes in an optical dipole trap which are proportional to laser power, such as off-resonant Rayleigh scattering, and heating due to fluctuations in the intensity and position of the laser beam [18]. Furthermore, since the cloud shrinks while being cooled in the magnetic trap, the transfer efficiency into the small trapping volume of an optical dipole trap is increased.

The experimental setup for creating Bose-Einstein condensates was similar to our previous work [19]. Sodium atoms were optically cooled and trapped, and transferred into a magnetic trap where they were further cooled by rf-induced evaporation. The transition point was reached at densities of $\sim 1 \times 10^{14} \text{ cm}^{-3}$ and temperatures of 1–2 μK . Further evaporation produced condensates containing $5 - 10 \times 10^6$ atoms in the $F = 1, m_F = -1$ electronic ground state. The atom clouds were cigar-shaped with the long axis horizontal, and had a typical aspect ratio of 15 due to the anisotropic trapping potential of the cloverleaf magnetic trap.

The optical trap was formed by focusing a near-infrared laser beam into the center of the magnetic trap along the axial direction. For this, the output of a diode laser operating at 985 nm was sent through a single-mode optical fiber and focused to a spot with a beam-waist parameter w_0 ($1/e^2$ radius for the intensity) of about 6 μm . This realized the simple single-beam arrangement for an optical dipole trap [10–13]. The infrared laser focus and the atom cloud were overlapped in three dimensions by imaging both with a CCD camera. It was necessary to compensate for focal and lateral chromatic shifts of the imaging system which were measured using an optical test pattern illuminated either at 589 or 985 nm.

The parameters of the optical trapping potential are characterized by the total laser power P and the beam-waist parameter w_0 . The trap depth is proportional to P/w_0^2 . For a circular Gaussian beam with $w_0 = 6 \mu\text{m}$, the trap depth is $1 \mu\text{K}/\text{mW}$ [20], and the aspect ratio of the atom cloud is 27. At $P = 4 \text{ mW}$, the geometric mean trapping frequency $\bar{\nu}$ is 670 Hz. The measured frequencies [see Eq. (1)] were about half the expected values, presumably due to imperfect beam quality and the coarse measurements of P and w_0 (an underestimation of w_0 by 40% would account for this discrepancy). Finally, due to the large detuning, the spontaneous scattering rate is small ($5 \times 10^{-3} \text{ s}^{-1}$ per μK trap depth), leading to an estimated trapping time of 400 s.

Condensates were transferred into the optical trap by holding them in a steady magnetic trap while ramping up the infrared laser power, and then suddenly switching off the magnetic trap. A ramp-up time of 125 ms was chosen as slow enough to allow for adiabatic transfer, yet fast enough to minimize trap loss during the ramp-up due to high densities in the combined optical and magnetic traps. The highest transfer efficiency (85%) was observed for a laser power of about 4 mW, with a measured mean trapping frequency $\bar{\nu} = 370 \text{ Hz}$ [see Eq. (1)]. The transfer efficiency dropped for higher laser power due to trap loss during the ramp-up, and decreased rapidly for smaller laser power due to the smaller trap depth. The sudden switch-off of the magnetic fields was necessitated by imperfections in the trapping coils which displaced the center of the magnetic trap during a slow switch-off. This caused transient oscillations of the atom cloud and can be overcome in the future with auxiliary steering coils.

After 500 ms of purely optical trapping, the transferred atoms were probed by suddenly switching off the optical trap, and observing the freely expanding cloud using absorption imaging (Fig. 1). The strong anisotropic expansion after 40 ms time of flight is characteristic of Bose-Einstein condensates in strongly anisotropic trapping potentials.

We also loaded the optical trap with magnetically trapped atoms at higher temperatures and lower densities than those used in Fig. 1. In this case, depending on the temperature of the atoms loaded into the optical trap, we observed the sudden onset of a dense, low energy core of atoms amidst a broad background of noncondensed atoms (Fig. 2). Two aspects are worth noting. First, the number of thermal atoms ($\sim 10^4$) is small compared both to the number of atoms before transfer ($\sim 10^8$) and to the number of condensed atoms transferred under the optimum conditions described above ($\sim 10^6$). This is due to the small trapping volume and shallow trap depth of the optical trap which leads to a very small transfer efficiency for thermal atoms. In comparison, in magnetic traps, the number of noncondensed atoms at the transition temperature is much larger than the largest number of condensate atoms eventually produced [19,21]. The maxi-

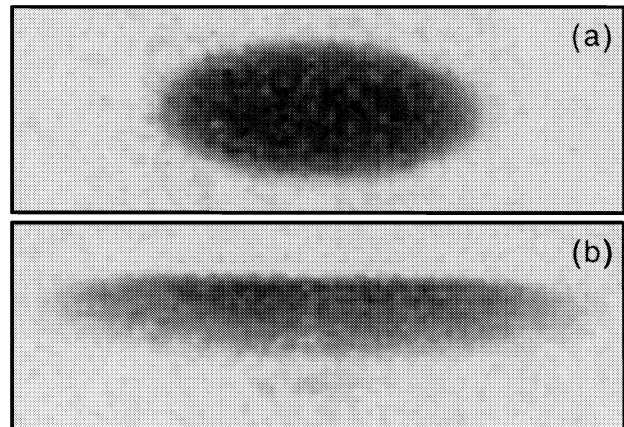


FIG. 1. Absorption images of expanding Bose-Einstein condensates, released (a) from the magnetic trap, and (b) from the optical trap ($\bar{\nu} = 370 \text{ Hz}$, $P \sim 4 \text{ mW}$). The faster expansion in (b) is indicative of the higher densities of the optical trap. The time of flight was 40 ms. The field of view for each image is 2.2 by 0.8 mm.

mum number of thermal atoms in Fig. 2 was measured to be 24 000, in agreement with a prediction based on the observed trap depth and trapping frequencies, and the assumption that the thermal atoms arrive at a temperature 1/10 of the trap depth by evaporation. Second, condensates were observed in the optical trap even when there was no condensate in the magnetic trap from which it was loaded. This was due to the partial condensation of the gas during the adiabatic deformation of the trapping potential when the infrared light was ramped up. During this deformation, the entropy remained constant through collisional equilibration while the phase space density increased [22]. A detailed study of this effect will be reported elsewhere.

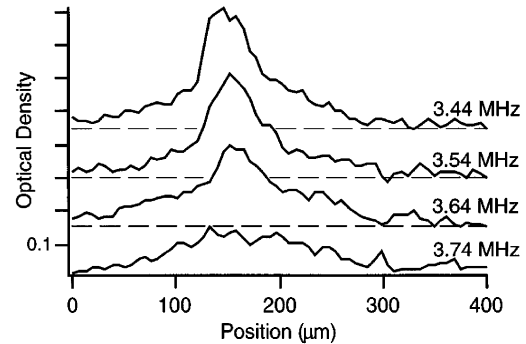


FIG. 2. Optical density profiles of optically trapped atoms at the onset of Bose-Einstein condensation. Because of the short time of flight (1 ms), the profiles show the spatial distribution along the long axis of the optical trap. Data were obtained after 125 ms of purely optical trapping. Labels give the final rf frequency used in the evaporative cooling cycle. The bimodality observed below 3.74 MHz indicates the presence of a small ($\sim 10^4$ atoms) Bose-Einstein condensate.

After the trap is switched off, the internal repulsive (mean-field) energy of the condensate is transformed into kinetic energy of the expanding cloud. This allows for the determination of peak densities n_0 and mean trapping frequencies $\bar{\nu}$ from time-of-flight data [19]. For a harmonic trapping potential in the Thomas-Fermi approximation, the average mean-field energy per atom is $2/7 n_0 \tilde{U}$, where $\tilde{U} = 4\pi\hbar^2 a/m$ is proportional to the scattering length $a = 2.75$ nm [23]. Assuming a predominantly radial expansion, the peak density was determined from the maximum velocity observed in time-of-flight images v_{\max} by $n_0 \tilde{U} = mv_{\max}^2/2$. The number of condensed atoms N was measured by integrating the optical density in time-of-flight images. The mean trapping frequencies $\bar{\nu}$ are related to N and n_0 by [19]

$$\bar{\nu} = 0.945 \frac{\hbar\sqrt{a}}{m} n_0^{5/6} N^{-1/3}. \quad (1)$$

The density of condensates in the optical trap was varied by either doubling or halving the infrared power in the all-optical trap, after having transferred the atoms at settings which maximized the initial transfer efficiency (see above). Thereafter, the infrared power was kept constant for lifetime studies. The peak densities achieved in this manner ranged from 3×10^{14} cm $^{-3}$ in the weakest optical trap to 3×10^{15} cm $^{-3}$ in the tightest. For the lowest infrared power used ($P \sim 2$ mW), atoms were observed spilling out of the optical trap, indicating that the depth of the trap was comparable to the 200 nK mean-field energy of the condensate which remained.

The lifetime of condensates was studied by measuring the number of condensed atoms in time-of-flight images after a variable storage time in the optical trap. Results are shown in Fig. 3 and compared to those for the magnetic trap. The lifetime in the magnetic trap was

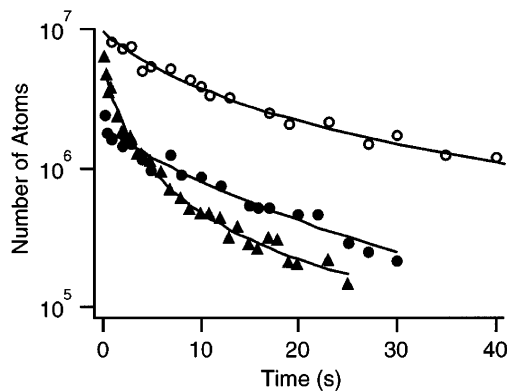


FIG. 3. Lifetime of Bose-Einstein condensates in the optical and magnetic traps. Shown is the number of condensed atoms vs trapping time. Closed triangles and circles represent data for the optical traps with the best transfer efficiency ($\bar{\nu} = 370$ Hz, $P \sim 4$ mW) and the slowest decay (weakest trap, $P \sim 2$ mW), respectively. Open circles represent data for the rf-shielded magnetic trap. Error in the number measurements is estimated as 10%. Lines are fits based on Eq. (2).

very short unless the trap depth was lowered by “rf shielding” [19,24], allowing collisionally heated atoms to escape. Similarly, the long lifetimes observed in the optical trap were made possible by its limited trap depth. The observed loss rates per atom in the optical trap ranged from 4 s $^{-1}$ at a peak density $n_0 = 3 \times 10^{15}$ cm $^{-3}$ to less than $1/10$ s $^{-1}$ at $n_0 = 3 \times 10^{14}$ cm $^{-3}$.

The decay curves in Fig. 3 are described by

$$\frac{dN}{dt} = -K_1 N - K_3 N \langle n^2 \rangle, \quad (2)$$

where K_1 accounts for density independent loss processes such as residual gas scattering, Rayleigh scattering, and other external heating processes, and K_3 is the loss rate constant for three-body decay. For a harmonic trap, the mean squared density $\langle n^2 \rangle$ is related to the measured peak density by $\langle n^2 \rangle = 8/21 n_0^2$ [25].

Three-body decay was found to be the dominant loss mechanism in both the optical and the magnetic trap. By fitting the solution of Eq. (2) to the decay curves for the various optical traps we obtained $K_1 = 0.03(2)$ s $^{-1}$ and $K_3 = 1.1(3) \times 10^{-30}$ cm 6 s $^{-1}$. This three-body loss rate constant for ^{23}Na is a factor of 5 smaller than for ^{87}Rb [24], and can be ascribed completely to collisions among condensed atoms due to the small number of noncondensed atoms in the optical trap. Our result lies between two theoretical predictions for the loss rate constant of $K_3 = 3 \times 10^{-29}$ cm 6 s $^{-1}$ [26] and $K_3 = 3.9\hbar a^4/2m = 3 \times 10^{-31}$ cm 6 s $^{-1}$ [27,28]. The loss rate due to dipolar relaxation (two-body decay) was predicted to be negligible at the densities considered [29]. While the decay curves show three-body decay to be the dominant loss mechanism, they do not exclude two-body decay rates comparable to K_1 .

One major advantage of the optical trap over magnetic traps is its ability to confine atoms in arbitrary hyperfine states. To demonstrate this, the atoms were put into a superposition of $F = 1$ hyperfine states by applying an rf field which was swept from 0 to 2 MHz in 2 ms. Parameters were chosen in such a way that the sweep was neither adiabatic nor diabatic, similar to our work on the rf output coupler [5]. The distribution over hyperfine states was analyzed through Stern-Gerlach separation by pulsing on a magnetic field gradient of a few G/cm during the 40 ms time of flight. Figure 4 demonstrates that all three states were optically trapped. By extending the time between the rf sweep and the probing, we confirmed that all $F = 1$ hyperfine states were stored stably for several seconds. The optical potential for the three sublevels is nearly identical, the relative difference being less than the ratio of the fine structure splitting to the large detuning (2.5×10^{-3}).

In conclusion, we have realized an optical trap for Bose-Einstein condensates. Because of the low energy of the condensates, just milliwatts of far-detuned laser radiation were sufficient to provide tight confinement.

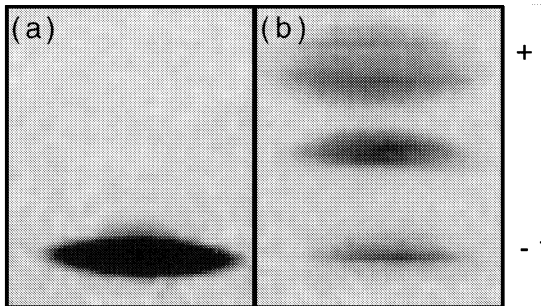


FIG. 4. Optical trapping of condensates in all $F = 1$ hyperfine states. Shown are absorption images after (a) 250 ms, and (b) 340 ms of optical confinement. Hyperfine states were separated by a magnetic field gradient pulse during the 40 ms time of flight. Atoms remain spin polarized in the optical trap (a). In (b) the atoms were exposed to an rf sweep which populated all hyperfine states, 90 ms before release from the trap. The absorption of the σ^- probe light is weaker for the $m_F = 0, +1$ states than for the $m_F = -1$ state. The field of view for each image is 1.6 by 1.8 mm.

More than five million condensed atoms were trapped, and lifetimes comparable to those in our dc magnetic trap were observed. Densities of $3 \times 10^{15} \text{ cm}^{-3}$ were achieved, unprecedented for both Bose condensates and for optically trapped atomic clouds. High densities and high condensate fractions allowed for a determination of the three-body loss rate constant in sodium as $K_3 = 1.1(3) \times 10^{-30} \text{ cm}^6 \text{ s}^{-1}$. This trap offers many new opportunities to study Bose-Einstein condensates and atom lasers. Since the optical trap works at arbitrary external magnetic fields, Feshbach resonances in the scattering length [30] might now be observed for strong-field seeking states. One can study condensates in superpositions of degenerate hyperfine sublevels, and, since the spin degree of freedom is no longer constrained by magnetic trapping, it may be possible to study spin waves [31] in a Bose-condensed gas. The shallow and well controlled trap depth allows for new output-coupling schemes [32]. Finally, the optical trap may also serve as an “optical tweezers” to move condensates, and, for example, place them in optical and microwave cavities and close to surfaces.

We are grateful to Günter Steinmeyer, Erik Thoen, and Erich Ippen for their help with the infrared laser. This work was supported by the Office of Naval Research, NSF, Joint Services Electronics Program (ARO), and the David and Lucile Packard Foundation. A.P.C. and D.M.S.-K. would like to acknowledge support from the NSF, and J.S. from the Humboldt Foundation.

- [1] M.H. Anderson *et al.*, Science **269**, 198 (1995).
- [2] K.B. Davis *et al.*, Phys. Rev. Lett. **75**, 3969 (1995).
- [3] C.C. Bradley, C.A. Sackett, and R.G. Hulet, Phys. Rev. Lett. **78**, 985 (1997); see also C.C. Bradley *et al.*, Phys. Rev. Lett. **75**, 1687 (1995).

- [4] M.R. Andrews *et al.*, Science **275**, 637 (1997).
- [5] M.-O. Mewes *et al.*, Phys. Rev. Lett. **78**, 582 (1997).
- [6] Proceedings of the Workshop on Bose-Einstein Condensation, Castelvecchio, Italy, 1997, Book of Abstracts (unpublished).
- [7] C.J. Myatt *et al.*, Phys. Rev. Lett. **78**, 586 (1997).
- [8] A. Aspect *et al.*, Phys. Rev. Lett. **61**, 826 (1988).
- [9] M. Kasevich and S. Chu, Phys. Rev. Lett. **69**, 1741 (1992).
- [10] S. Chu, J.E. Bjorkholm, A. Ashkin, and A. Cable, Phys. Rev. Lett. **57**, 314 (1986).
- [11] W.D. Phillips, in *Laser Manipulation of Atoms and Ions*, Proceedings of the International School of Physics “Enrico Fermi,” Course CXVIII, edited by E. Arimondo, W.D. Phillips, and F. Strumia (North-Holland, Amsterdam, 1992), p. 289.
- [12] J.D. Miller, R.A. Cline, and D.J. Heinzen, Phys. Rev. A **47**, R4567 (1993).
- [13] T. Takekoshi and R.J. Knize, Opt. Lett. **21**, 77 (1996).
- [14] T. Kuga *et al.*, Phys. Rev. Lett. **78**, 4713 (1997).
- [15] H.J. Lee *et al.*, Phys. Rev. Lett. **76**, 2658 (1996).
- [16] A. Kuhn, H. Perrin, W. Hänsel, and C. Salomon, in *Ultracold Atoms and Bose-Einstein Condensation*, edited by K. Burnett, OSA Trends in Optics and Photonics Series Vol. 7 (Optical Society of America, Washington, DC, 1996), p. 58.
- [17] C.S. Adams *et al.*, Phys. Rev. Lett. **74**, 3577 (1995).
- [18] T.A. Savard, K.M. O’Hara, and J.E. Thomas, Phys. Rev. A **56**, R1095 (1997).
- [19] M.-O. Mewes *et al.*, Phys. Rev. Lett. **77**, 416 (1996).
- [20] 25% of the trap depth comes from the “counter-rotating” term usually neglected in the rotation-wave approximation.
- [21] D.S. Jin *et al.*, Phys. Rev. Lett. **78**, 764 (1997).
- [22] P.W.H. Pineske *et al.*, Phys. Rev. Lett. **78**, 990 (1997).
- [23] E. Tiesinga *et al.*, J. Res. Natl. Inst. Stand. Technol. **101**, 505 (1996).
- [24] E.A. Burt *et al.*, Phys. Rev. Lett. **79**, 337 (1997).
- [25] The assumption of a harmonic trap holds when the mean-field energy is much smaller than the trap depth. In determining K_3 , we considered only data for which this was true. We estimate the effects of anharmonicity on our measured K_3 to be less than 10%.
- [26] A.J. Moerdijk, H.M.J.M. Boesten, and B.J. Verhaar, Phys. Rev. A **53**, 916 (1996).
- [27] P.O. Fedichev, M.W. Reynolds, and G.V. Shlyapnikov, Phys. Rev. Lett. **77**, 2921 (1996).
- [28] References [26] and [27] give the three-body event rate constant for thermal atoms which is $2K_3$, since the event rate is 6 times larger for thermal atoms than for condensate atoms [24], while three atoms are lost per collision event.
- [29] H.M.J.M. Boesten, A.J. Moerdijk, and B.J. Verhaar, Phys. Rev. A **54**, R29 (1996).
- [30] E. Tiesinga, B.J. Verhaar, and H.T.C. Stoof, Phys. Rev. A **47**, 4114 (1993).
- [31] B.R. Johnson *et al.*, Phys. Rev. Lett. **52**, 1508 (1984); P.J. Nacher *et al.*, J. Phys. (Paris), Lett. **45**, L441 (1984); W.J. Gully and W.J. Mullin, Phys. Rev. Lett. **52**, 1810 (1984).
- [32] G.M. Moy, J.J. Hope, and C.M. Savage, Phys. Rev. A **55**, 3631 (1997).

Appendix E

Collisionless and hydrodynamic excitations of a Bose–Einstein condensate

This appendix includes the following paper [12]: D.M. Stamper–Kurn, H.-J. Miesner, S. Inouye, M.R. Andrews and W. Ketterle, “Collisionless and hydrodynamic excitations of a Bose–Einstein condensate,” *Phys. Rev. Lett.* **81**, 500 (1998).

Collisionless and Hydrodynamic Excitations of a Bose-Einstein Condensate

D. M. Stamper-Kurn, H.-J. Miesner, S. Inouye, M. R. Andrews,* and W. Ketterle

*Department of Physics and Research Laboratory of Electronics, Massachusetts Institute of Technology,
Cambridge, Massachusetts 02139*

(Received 26 January 1998)

Collective excitations of a dilute Bose gas were probed above and below the Bose-Einstein condensation temperature. The temperature dependencies of the frequency and damping rates of condensate oscillations indicate significant interactions between the condensate and the thermal cloud. Hydrodynamic oscillations of the thermal cloud analogous to first sound were observed. An out-of-phase dipolar oscillation of the thermal cloud and the condensate was also studied, analogous to second sound. The excitations were observed *in situ* using nondestructive imaging techniques. [S0031-9007(98)06661-7]

PACS numbers: 03.75.Fi, 05.30.Jp, 51.40.+p, 67.90.+z

Bose-Einstein condensation in dilute atomic gases [1–3] has provided a testing ground for well-developed many-body theories of quantum fluids. Many studies have focused on the collective excitations of such gases. Experiments have studied low-lying collective excitations over a range of temperatures [4–6] and higher-lying modes [7]. Zero-temperature findings have agreed well with predictions based on a mean-field description of the weak interatomic interactions [8–10]. However, the behavior at nonzero temperature, which involves interactions between the condensate and the thermal cloud, is not fully understood, pointing to the need for new theoretical developments.

The physical nature of collective excitations depends on the hierarchy of three length scales: the wavelength of the excitation λ , the healing length ξ which is given by the condensate density n_0 and the scattering length a as $\xi = (8\pi a n_0)^{-1/2}$, and the mean-free path l_{mfp} for collisions between the collective excitation and other excitations which compose the thermal cloud. The collisionless regime, defined by $\lambda \ll l_{\text{mfp}}$ (or by $\omega\tau \gg 1$ where ω is the frequency of the excitation and τ its collision time), occurs at zero temperature and for low densities of the thermal cloud. There, free-particle excitations are obtained at short wavelengths ($\lambda \ll \xi$), while phononlike excitations known as Bogoliubov sound (also referred to as zero sound in recent literature) are obtained at long wavelengths ($\lambda \gg \xi$) [11]. For excitations where λ is comparable to the size of the sample, this latter condition defines the Thomas-Fermi regime. Experiments have been performed either in the limit of Bogoliubov sound excitations [5,7] or intermediate to the two limits [4,6].

At higher densities of the normal component, when $\lambda \gg l_{\text{mfp}}$ ($\omega\tau \ll 1$), collective excitations become hydrodynamic in nature, and one expects two phononlike excitations, which are the in-phase or out-of-phase oscillations of two fluids (the normal fraction and the superfluid). The presence of two hydrodynamic modes is similar to the case of superfluid ^4He , where they are known as first and sec-

ond sound. However, in superfluid ^4He both fluids participate equally in first and second sound, while in a dilute Bose gas the oscillations of each fluid are nearly uncoupled: the in-phase oscillation involves mainly the thermal cloud, whereas the out-of-phase mode is confined mainly to the condensate [11,12].

In this Letter, we study collective excitations at nonzero temperature, and extend earlier work [6] in several ways. First, we study condensate oscillations entirely in the Thomas-Fermi regime. In contrast, results of Ref. [6] were complicated by the transition of the condensate from the Thomas-Fermi to the free-particle regime with increasing temperature. Second, near the critical temperature we approach the hydrodynamic limit and observe the onset of hydrodynamic excitations of the thermal cloud, analogous to first sound. Finally, we observe a new out-of-phase dipolar oscillation of the condensate and the thermal cloud, analogous to the out-of-phase second sound mode in liquid helium [12].

The excitations were probed generally in three steps. First, as described in a previous paper [13], we produced a magnetically confined, ultracold gas of atomic sodium in an equilibrium state which was controlled by changing the final frequency used in rf-evaporative cooling. The clouds were cigar shaped with weak confinement along one direction (axial) and tight confinement in the other two (radial). Second, the cloud was manipulated with either time-dependent magnetic fields or off-resonant light to excite low-lying collective modes. Finally, the cloud was allowed to oscillate freely and probed *in situ* with repeated, nondestructive phase-contrast imaging [7].

To accurately characterize the magnetic trapping potential, we excited center-of-mass oscillations of the cloud in the axial direction by sinusoidally moving the trap center. The subsequent free oscillation of the cloud gave the axial trapping frequency as $\nu_z = 16.93(2)$ Hz. The radial frequency was estimated to be 230(20) Hz.

The $m = 0$ quadrupolar modes of the condensate and the thermal cloud [5] were excited by a 5-cycle pulsed

modulation of the axial magnetic field curvature. Data were evaluated for oscillations with a relative amplitude of about 10% [14]. The oscillations of each cloud were probed with 22 nondestructive images: one before the excitation to characterize the initial conditions and three groups of 7 images during the free oscillation. The three groups were separated by a delay time which was varied between 1 and 200 ms according to the damping time of the oscillation. This method of probing gave highly accurate single-shot measurements of oscillation frequencies and damping rates, and overcame the additional fluctuations introduced when combining data from observations on several clouds.

Phase-contrast images were analyzed by fitting the observed column densities $\tilde{n}(r, z)$ [15] with the function

$$\begin{aligned} \tilde{n}(r, z) = h_c \max\left(0, 1 - \frac{r^2}{(r_c/2)^2} - \frac{z^2}{(z_c/2)^2}\right)^{3/2} \\ + h_t g_2\left[\exp\left(-\frac{r^2}{2(r_t/2)^2} - \frac{z^2}{2(z_t/2)^2}\right)\right]. \quad (1) \end{aligned}$$

Here, r and z are the radial and axial coordinates, respectively, while r_c and z_c are the lengths of the condensate and r_t and z_t the rms diameters of the thermal cloud. The function g_2 is defined by $g_2(x) = \sum_{i=1}^{\infty} x^i / i^2$. Equation (1) is motivated by a simple model of the mixed cloud: a mean-field dominated condensate amid a saturated noncondensed ideal gas obeying Bose-Einstein statistics [16]. Since all quantities were allowed to vary independently (including the amplitudes h_c and h_t), Eq. (1) is an almost model-independent parametrization of a bimodal distribution: z_c is determined from the cusps of the bimodal distribution, and z_t from the thermal tails.

The initial conditions for the oscillation were characterized by the total number of atoms N , the temperature T , and the chemical potential μ . N was obtained by integrating the column density, while T and μ were determined from the fits by $k_B T = \pi^2 m \nu_z^2 z_t^2$ and $\mu = \pi^2 m \nu_z^2 z_c^2 / 2$, where k_B is Boltzmann's constant. We determined T by fitting the thermal wings alone. In addition, an approximate condensate number N_0 was determined by summing the column density which is ascribed to the condensate according to the fits [first line of Eq. (1)]. These conditions are shown in Fig. 1 as a function of $\Delta\nu_{\text{rf}} = \nu_{\text{rf}} - \nu_{\text{bot}}$ where ν_{rf} is the final frequency used in the rf evaporation, and ν_{bot} is the resonant rf frequency for atoms at the bottom of the magnetic trap. The frequency ν_{bot} remained constant within 20 kHz. The Bose-Einstein condensation transition was observed at $T = 1.7 \mu\text{K}$ with about 80×10^6 atoms. The temperature varied linearly with $\Delta\nu_{\text{rf}}$, with a slope of $3.5 \mu\text{K}/\text{MHz}$, and was measurable down to $0.5 \mu\text{K}$. Reliable determinations of z_c (and μ) were obtained only below $\Delta\nu_{\text{rf}} = 350 \text{ kHz}$. For low $\Delta\nu_{\text{rf}}$, $\mu/k_B = 380 \text{ nK}$, corresponding to $N_0 = 15 \times 10^6$.

The lengths z_c and z_t were fit independently to decaying sinusoidal functions of time. We thus determined the frequency and damping rate (the inverse of the $1/e$ decay

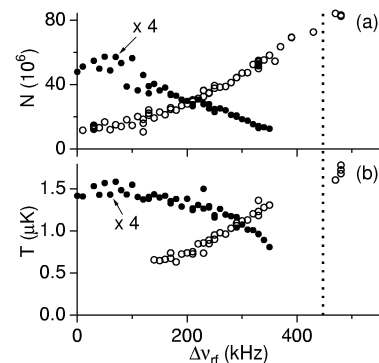


FIG. 1. Equilibrium conditions before excitation. The total number N [(a), open circles] was determined by summing over the observed column densities. The approximate condensate number N_0 [(a), closed circles, $\times 4$], temperature T [(b), open circles], and chemical potential μ/k_B [(b), closed circles, $\times 4$] were determined from fits to the data. These are plotted against $\Delta\nu_{\text{rf}}$. The dashed line indicates the observed transition temperature. We estimate systematic errors in N and N_0 of as much as 20% due to the calibration of our phase-contrast signal.

time of the oscillation amplitude) of two distinct oscillations. We observed no evidence for coupling between the oscillations in z_c and in z_t , allowing one to consider the excitations as nearly isolated oscillations of the thermal cloud and of the condensate, respectively.

The thermal cloud oscillated at a frequency of about $1.75\nu_z$ with a damping rate of about 20 s^{-1} (Fig. 2). The observed frequency ν is between the predicted collisionless limit of $\nu = 2\nu_z$ and the hydrodynamic limit of $\nu = 1.55\nu_z$ [17]. The damping rate is predicted to vanish in both the collisionless and hydrodynamic limits, and to reach a broad maximum of $\sim 1.4\nu$ when ν is between its two limiting values [18], as we observe. One can estimate the collisional mean-free path as $l_{\text{mfp}} \simeq (n_T \sigma)^{-1} = 96 \mu\text{m} \times (T/\mu\text{K})^{-3/2}$ using the peak density of the thermal cloud $n_T = 2.612(mk_B T/2\pi\hbar^2)^{3/2}$, and a collisional cross section $\sigma = 8\pi a^2$ with the scattering length $a = 2.75 \text{ nm}$ [19]. Around the transition temperature, we find $z_t \simeq 8l_{\text{mfp}}$. This comparison of length scales, the observed frequency shift away from $2\nu_z$, and the high damping rate all demonstrate that the collective behavior of the thermal cloud is strongly affected by collisions. Thus, the oscillations which we observe indicate the onset of hydrodynamic excitations. The hydrodynamic limit, characterized by low damping, would only be reached for even larger clouds.

We studied the $m = 0$ quadrupolar condensate oscillations in greater detail. Typical oscillation data (Fig. 3) demonstrate that the oscillation has a slightly lower frequency and is damped more rapidly at high temperature than at low temperature. At low temperatures, the condensate oscillation frequency approached a limiting value of $1.569(4)\nu_z$, close to the zero-temperature, high-density

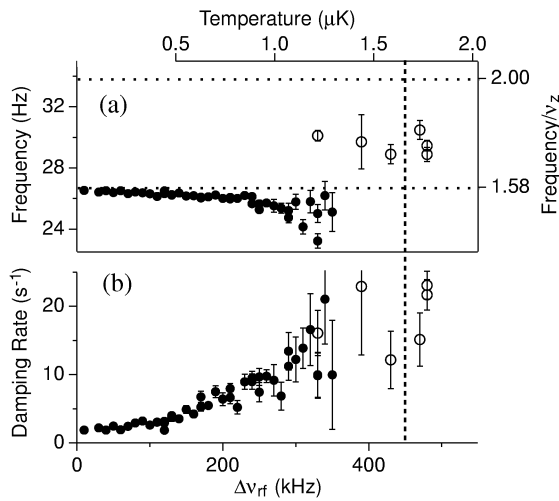


FIG. 2. Temperature dependent frequency and damping rates of $m = 0$ quadrupolar collective modes. Points show measurements for oscillations of the thermal cloud (open circles) and condensate (closed circles). The free-particle limit of $2\nu_z$ and the zero-temperature condensate oscillation limit of $1.580\nu_z$ are indicated. The vertical dashed line marks the observed transition temperature. The temperature axis is based on a linear fit to the data in (b), and is determined only for $T > 0.5 \mu\text{K}$, where temperature could be measured.

prediction of $1.580\nu_z$ [9]. The slight difference between these values may be due to nonzero-temperature effects even for small $\Delta\nu_{\text{rf}}$. At higher temperatures, the frequency drops below the low-temperature limit. This trend might be explained by the weakening of the effective trapping potential for the condensate by the mean-field potential of the thermal cloud. Considering a thermal density $n_T \propto e^{-U(r,z)/k_B T}$, one can estimate a downward frequency shift of as much as 5% due to this effect, consistent with our observations.

Damping rates for the condensate oscillations varied strongly with temperature, rising from a low-temperature limit of about 2 s^{-1} to as much as 20 s^{-1} . Recent treatments based on Landau damping [20–22] provide qualitative agreement with our findings. A quantitative prediction for these damping rates [22] could not be checked because our data were collected for $k_B T \leq 6\mu$, where the high-temperature prediction might not be applicable, while the inability to measure T for low $\Delta\nu_{\text{rf}}$ prevents a comparison at low temperatures.

For the condensate oscillations at high temperatures, a comparison of length scales ($z_c \approx 4l_{\text{mfp}}$) indicates that hydrodynamic effects may already be present. This suggests that these oscillations may constitute second sound in a Bose gas [11]. However, there are no theoretical predictions regarding the transition from collisionless to hydrodynamic condensate oscillations with which to compare our data. In future experiments with larger condensates, the signature of this crossover may appear in the damping rate of the oscillations, which should decrease

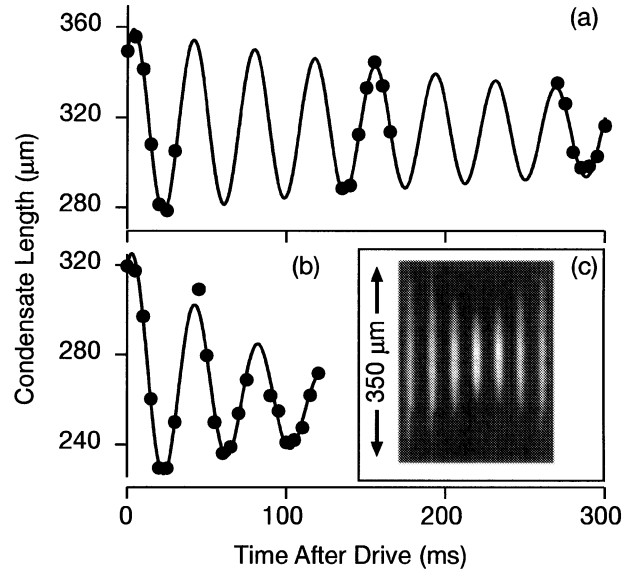


FIG. 3. Quadrupolar condensate oscillations. Axial condensate lengths determined from fits to phase-contrast images are shown for (a) low and (b) high temperature. (a) $\Delta\nu_{\text{rf}} = 30 \text{ kHz}$ and $T < 0.5 \mu\text{K}$; (b) $\Delta\nu_{\text{rf}} = 250 \text{ kHz}$ and $T = 0.95 \mu\text{K}$. Lines are fits to a damped sinusoidal oscillation with a downward slope to account for heating. (c) *In situ* images, taken at 5 ms intervals, show large-amplitude oscillations of a low-temperature Bose-Einstein condensate. Final data were evaluated for oscillation amplitudes of about 10%.

again at high temperatures as one reaches the hydrodynamic limit.

To further probe the interaction between the thermal cloud and the condensate, we studied an excitation of a different symmetry: the rigid-body, out-of-phase motion of the condensate and the thermal cloud in the harmonic trapping potential [12]. This mode is analogous to second sound in liquid helium, where the superfluid and the normal fluid undergo out-of-phase density oscillations of equal magnitude.

We excited this mode with focused off-resonant, blue-detuned laser light, which produced a $3-\mu\text{K}$ -high repulsive potential similar to that used in Ref. [7]. After a partly condensed cloud was formed, the light was turned on and directed at the edge of the cloud, where it overlapped only with the thermal cloud. By tilting a motorized mirror, the laser beam was steered toward and then away from the center of the cloud, pushing the thermal cloud in the axial direction while not directly affecting the condensate. The light was then turned off, and the cloud allowed to freely oscillate.

The position of the center of mass of the condensate [Fig. 4(a)] was monitored with repeated phase-contrast images. The condensate motion was initially slow, and then grew to an asymptotic sinusoidal oscillation, corresponding to the in-phase motion of the entire cloud (condensate plus thermal cloud) at the trapping frequency ν_z . By subtracting the undamped center-of-mass motion of the entire

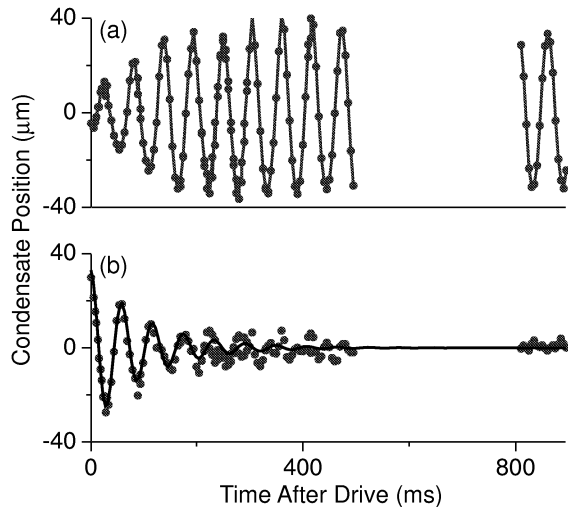


FIG. 4. Out-of-phase dipole mode of a partly condensed cloud. The center-of-mass of the condensate in the trap (a) was monitored after displacing the thermal cloud with a far-detuned laser beam. The condensate oscillated relative to the center-of-mass of the entire sample (b) at a frequency smaller than ν_z , with a damping rate of $9(1) \text{ s}^{-1}$. The line in (a) is a guide to the eye, and that in (b) is a fit to the data. Data were collected in several repetitions of the experiment, for which $T = 1 \mu\text{K}$, $\mu/k_B = 200 \text{ nK}$, and $N = 40 \times 10^6$.

cloud, we isolated the out-of-phase oscillation of the condensate and the thermal cloud [Fig. 4(b)].

The frequency of the out-of-phase dipole mode of $17.26(9) \text{ Hz}$ was significantly lower than the trapping frequency which was $\nu_z = 18.04(1) \text{ Hz}$ at that time. This $\sim 5\%$ frequency shift is again evidence of the interaction between the thermal cloud and the condensate. The motion we observed, in which the condensate is driven by the moving thermal cloud, cannot be described by recent theories which assume a stationary thermal cloud [23], and requires more sophisticated treatments [12,21].

In conclusion, we have studied the collective excitations of a dilute Bose gas at nonzero temperatures in the Thomas-Fermi limit, and near the hydrodynamic regime. The hydrodynamic oscillation of the thermal cloud, corresponding to first sound, was indicated by measurements both above and below the Bose-Einstein condensation transition. The accurately determined frequency shift of the $m = 0$ quadrupole oscillations away from their zero-temperature limit and of the out-of-phase oscillation away from the trap frequency are measures of the forces exerted by the condensate and the thermal cloud on one another.

We are grateful to Allan Griffin, Jason Ho, Dan Rokhsar, and Sandro Stringari for insightful discussions, and to Dallin Durfee for experimental assistance. This work was supported by the Office of Naval Research,

NSF, Joint Services Electronics Program (ARO), and the David and Lucile Packard Foundation. D. M. S.-K. acknowledges support from the NSF.

*Present address: Bell Labs, Lucent Technologies, Murray Hill, NJ 07974.

- [1] M. H. Anderson *et al.*, Science **269**, 198 (1995).
- [2] K. B. Davis *et al.*, Phys. Rev. Lett. **75**, 3969 (1995).
- [3] C. C. Bradley, C. A. Sackett, and R. G. Hulet, Phys. Rev. Lett. **78**, 985 (1997); see also C. C. Bradley *et al.*, Phys. Rev. Lett. **75**, 1687 (1995).
- [4] D. S. Jin *et al.*, Phys. Rev. Lett. **77**, 420 (1996).
- [5] M.-O. Mewes *et al.*, Phys. Rev. Lett. **77**, 988 (1996).
- [6] D. S. Jin *et al.*, Phys. Rev. Lett. **78**, 764 (1997).
- [7] M. R. Andrews *et al.*, Phys. Rev. Lett. **79**, 553 (1997).
- [8] M. Edwards *et al.*, Phys. Rev. Lett. **77**, 1671 (1996).
- [9] S. Stringari, Phys. Rev. Lett. **77**, 2360 (1996).
- [10] E. Zaremba, Phys. Rev. A **57**, 518 (1998); G. M. Kavoulakis and C. J. Pethick, e-print cond-mat/9710130.
- [11] T. D. Lee and C. N. Yang, Phys. Rev. **113**, 1406 (1959); A. Griffin, *Excitations in a Bose-Condensed Liquid* (Cambridge University Press, Cambridge, 1993), and references therein; A. Griffin and E. Zaremba, Phys. Rev. A **56**, 4839 (1997); V. B. Shenoy and T.-L. Ho, Phys. Rev. Lett. **80**, 3895 (1998).
- [12] E. Zaremba, A. Griffin, and E. Nikuni, e-print cond-mat/9705134.
- [13] M.-O. Mewes *et al.*, Phys. Rev. Lett. **77**, 416 (1996).
- [14] The condensate oscillation frequency rose by as much as 1 Hz from its low-amplitude limit as the relative amplitude of oscillation increased from 10% to 50%. This shift agrees with predictions of F. Dalfovo, C. Minniti, and L. P. Pitaevskii, Phys. Rev. A **56**, 4855 (1997).
- [15] A phase-contrast image gives the optical phase ϕ accrued by off-resonant light passing through a dense medium. For our setup, the column density $\tilde{n} = \phi \times 6.2 \times 10^{11} \text{ cm}^{-2}$.
- [16] V. Bagnato, D. E. Pritchard, and D. Kleppner, Phys. Rev. A **35**, 4354 (1987).
- [17] A. Griffin, W.-C. Wu, and S. Stringari, Phys. Rev. Lett. **78**, 1838 (1997); Yu. Kagan, E. L. Surkov, and G. V. Shlyapnikov, Phys. Rev. A **55**, R18 (1997).
- [18] G. M. Kavoulakis, C. J. Pethick, and H. Smith, Phys. Rev. A **57**, 2938 (1998).
- [19] E. Tiesinga *et al.*, J. Res. Natl. Inst. Stand. Technol. **101**, 505 (1996).
- [20] W. V. Liu, Phys. Rev. Lett. **79**, 4056 (1997); L. P. Pitaevskii and S. Stringari, Phys. Lett. A **235**, 398 (1997).
- [21] S. Giorgini, Phys. Rev. A **57**, 2949 (1998).
- [22] P. O. Fedichev, G. V. Shlyapnikov, and J. T. M. Walraven, Phys. Rev. Lett. **80**, 2269 (1998).
- [23] D. A. W. Hutchinson, E. Zaremba, and A. Griffin, Phys. Rev. Lett. **78**, 1842 (1997); R. J. Dodd, M. Edwards, C. W. Clark, and K. Burnett, Phys. Rev. A **57**, R32 (1998).

Appendix F

Analytical description of a trapped semi-ideal Bose gas at finite temperature

This appendix includes the following paper [13]: M. Naraschewski and D.M. Stamper-Kurn, “Analytical description of a trapped semi-ideal Bose gas at finite temperature,” *Phys. Rev. A* **58**, 2423 (1998).

Analytical description of a trapped semi-ideal Bose gas at finite temperature

M. Naraschewski

*Jefferson Laboratory, Department of Physics, Harvard University, Cambridge, Massachusetts 02138
and Institute for Theoretical Atomic and Molecular Physics, Harvard-Smithsonian Center for Astrophysics, 60 Garden Street,
Cambridge, Massachusetts 02138*

D. M. Stamper-Kurn

*Department of Physics and Research Laboratory of Electronics, Massachusetts Institute of Technology, Cambridge, Massachusetts 02139
(Received 18 March 1998)*

Present experiments with Bose condensed gases can be largely described by a semi-ideal two-gas model. In this model, the condensate is influenced only by the mean-field repulsion among condensed atoms, while the thermal cloud is considered an ideal gas confined by an effective potential that consists of the external trap and the mean-field repulsion by the condensate. This simple, intuitive model provides explicit analytical expressions for the density distributions of the condensate and the thermal component. It describes the reduction of the condensate fraction relative to that of an ideal gas as a consequence of the positive chemical potential due to interactions in the condensate. [S1050-2947(98)09209-9]

PACS number(s): 03.75.Fi, 05.30.Jp

Recent experiments with Bose-Einstein condensed alkali gases (cf., e.g., Refs. [1,2]) have been successfully described by different approximation schemes. The diluteness of these gases, expressed as $na^3 \ll 1$, where a is the two-body scattering length, allows a description in terms of an effective mean-field theory. At zero temperature the condensate can be described by the Gross-Pitaevskii equation [3,4], a nonlinear Schrödinger equation. In present experiments interactions are strong enough so that the chemical potential μ is much larger than the level spacings $\hbar\omega_x$, $\hbar\omega_y$, and $\hbar\omega_z$ of the external harmonic potential. Therefore the use of the Thomas-Fermi approximation [5,6], which neglects the kinetic energy of the condensate, has led to a tremendous simplification in the understanding of these experiments.

Recently, much theoretical and experimental attention has been focused on finite-temperature properties of Bose-condensed gases. A semiclassical Hartree-Fock-Popov description produced excellent agreement with experimentally measured equilibrium quantities [7]. Further, unlike in a spatially homogeneous gas, it was found that collective elementary excitations contribute very little to thermodynamic properties [7], due to the relatively small spatial overlap between condensate and thermal components in a harmonic trap. Thus, even a semiclassical Hartree-Fock approximation is a fairly accurate description of these gases, except for a small temperature range close to the critical temperature. For example, excellent agreement has been achieved by a comparison of Hartree-Fock density profiles with the results of a comprehensive path-integral Monte Carlo calculation [8].

In this paper we introduce a further simplification of the self-consistent Hartree-Fock model by neglecting atomic interactions in the thermal component of the gas. Like the introduction of the Thomas-Fermi approximation [5] the reduction to Eqs. (4)–(6) and (12) has the important advantage of providing an explicit analytical description of a trapped Bose gas at finite temperature.

We consider atoms that are trapped in a generally anisotropic harmonic potential. Under the appropriate rescaling of

energy and lengths, the harmonic potential has the form $V(\mathbf{r}) = r^2/2$. Here the dimensionless Cartesian coordinates of \mathbf{r} are given in units of $\sqrt{\hbar\omega/m}\omega_{x,y,z}^{1/2}$, with $\omega = (\omega_x\omega_y\omega_z)^{1/3}$. Other lengths, like the thermal wavelength λ_T and the scattering length a , are scaled in units of the natural length $\sqrt{\hbar/m\omega}$ of a harmonic oscillator with angular frequency ω . The energy $V(\mathbf{r})$ as well as other energies are implicitly given in units of $\hbar\omega$.

Then, in the self-consistent Hartree-Fock model, the densities of the condensate and the thermal component are given as solutions of the two coupled equations [5,7]

$$n_0(\mathbf{r}) = \frac{\mu - r^2/2 - 2Un_T(\mathbf{r})}{U} \theta(\mu - r^2/2 - 2Un_T(r)), \quad (1)$$

$$n_T(\mathbf{r}) = \frac{1}{\lambda_T^3} g_{3/2}(e^{-(r^2/2 + 2U[n_0(\mathbf{r}) + n_T(\mathbf{r})] - \mu)/k_B T}). \quad (2)$$

Here the Thomas-Fermi approximation has been applied, which neglects the kinetic energy of the condensate and implicitly finite-size effects. The strength of the atomic interactions is given by $U = 4\pi a$. We use the thermal wavelength $\lambda_T = \sqrt{2\pi/k_B T}$ and the Bose function $g_{3/2}$ is defined by $g_\alpha(z) = \sum_{j=1}^{\infty} z^j/j^\alpha$. The chemical potential μ is determined by the constraint of a given total atom number

$$N = \int d\mathbf{r}[n_0(\mathbf{r}) + n_T(\mathbf{r})]. \quad (3)$$

For further reference, Eqs. (1)–(3) will be denoted as the interacting model. Even though the model already represents a relatively concise description, these equations still have to be solved self-consistently. This is done numerically by an iterative procedure [7].

If one further neglects the mean-field repulsion from non-condensed atoms, Eqs. (1) and (2) are solved by the explicit relations

$$n_0(\mathbf{r}) = \frac{\mu - r^2/2}{U} \theta(\mu - r^2/2), \quad (4)$$

$$n_T(\mathbf{r}) = \frac{1}{\lambda_T^3} g_{3/2}(e^{-|r^2/2 - \mu|/k_B T}), \quad (5)$$

with the chemical potential μ given by

$$\mu = \frac{1}{2} (15Na)^{2/5} \left(\frac{N_0}{N} \right)^{2/5}. \quad (6)$$

These relations summarize a simple model of the partly condensed gas, which we denote as the semi-ideal model. The condensate density n_0 is that of a zero-temperature condensate with N_0 atoms, while the density n_T of the noncondensed cloud is that of an ideal gas of bosons confined in the combination of the external potential and the repulsive mean-field potential due to the condensate atoms. Its wide range of validity has been confirmed by a numerical analysis in Ref. [9]. However, in order to make it an intuitively appealing, usable description of a trapped Bose gas, the condensate fraction has to be determined analytically as a function of temperature.

For later convenience let us introduce the reduced chemical potential $\bar{\mu}$,

$$\bar{\mu} = \frac{\mu}{k_B T} = \eta \left(\frac{N_0}{N} \right)^{2/5} \left(\frac{T}{T_c} \right)^{-1}. \quad (7)$$

Here, the critical temperature T_c is that of a trapped ideal gas [10,11] $k_B T_c = [N/\zeta(3)]^{1/3}$, where $g_\alpha(1) = \zeta(\alpha)$ was expressed in terms of the Riemann zeta function. The reduced chemical potential depends on the scaling parameter η [7]

$$\eta = \frac{\mu_{T=0}}{k_B T_c} = \frac{1}{2} \zeta(3)^{1/3} (15N^{1/6}a)^{2/5}, \quad (8)$$

which describes the strength of the atomic interactions within the condensate. The scaling parameter is independent of the system size when the thermodynamic limit is taken in the usual way ($N \rightarrow \infty, \omega \rightarrow 0, N\omega^3 = \text{const}$). Due to its relatively weak N dependence, η assumes a value close to 0.3 in most recent experiments [7].

The condensate fraction is determined by integration over the thermal density distribution. For $T < T_c$, the result can be written in terms of incomplete gamma functions [12]

$$\begin{aligned} \frac{N_0}{N} &= 1 - \frac{2}{\sqrt{\pi}} \frac{1}{\zeta(3)} \left(\frac{T}{T_c} \right)^3 \sum_{j=1}^{\infty} \frac{1}{(jk_B T)^{3/2}} \left(\int_0^{\mu} d\epsilon \sqrt{\epsilon} e^{j(\epsilon - \mu)/k_B T} \right. \\ &\quad \left. + \int_{\mu}^{\infty} d\epsilon \sqrt{\epsilon} e^{-j(\epsilon - \mu)/k_B T} \right) \\ &= 1 - \frac{2}{\sqrt{\pi}} \frac{1}{\zeta(3)} \left(\frac{T}{T_c} \right)^3 \sum_{j=1}^{\infty} \frac{1}{j^3} [e^{-j\bar{\mu}} \gamma(\frac{3}{2}, -j\bar{\mu}) \\ &\quad + e^{j\bar{\mu}} \Gamma(\frac{3}{2}, j\bar{\mu})]. \end{aligned} \quad (9)$$

Equation (9) is still an implicit expression, since it depends again on the reduced chemical potential. Therefore, $\bar{\mu}$ and

N_0/N are given as simultaneous solutions of Eqs. (7) and (9). For temperatures $T > T_c$ a condensate does not exist, and the reduced chemical potential $\bar{\mu} < 0$ is trivially defined by the single equation $g_3(e^{\bar{\mu}}) = \zeta(3)(T/T_c)^{-3}$.

Let us consider the results of the semi-ideal model in the limits of small and large $\bar{\mu}$, corresponding to $T \approx T_c$ and $T \approx 0$. Equation (9) is therefore rewritten

$$\frac{N_0}{N} = 1 - \frac{2}{\sqrt{\pi}} \frac{1}{\zeta(3)} \left(\frac{T}{T_c} \right)^3 \sum_{j=1}^{\infty} \frac{1}{j^3} f(j\bar{\mu}) \quad (10)$$

in terms of the function

$$f(x) = \int_0^x d\bar{\epsilon} \sqrt{\bar{\epsilon}} e^{-\bar{\epsilon}-x} + \int_x^{\infty} d\bar{\epsilon} \sqrt{\bar{\epsilon}} e^{-(\bar{\epsilon}-x)}, \quad (11)$$

where the reduced energy $\bar{\epsilon} = \epsilon/k_B T$ has been introduced. The function $f(j\bar{\mu})$ can be expressed as a power series in $\sqrt{j\bar{\mu}}$, where $\bar{\mu}$ runs from 0 ($T=T_c$) to ∞ ($T=0$). Truncating the series after the lowest nontrivial order yields

$$\begin{aligned} \frac{N_0}{N} &= 1 - \left(\frac{T}{T_c} \right)^3 \left[1 + \frac{\zeta(2)}{\zeta(3)} \bar{\mu} \right] \\ &= 1 - \left(\frac{T}{T_c} \right)^3 - \eta \frac{\zeta(2)}{\zeta(3)} \left(\frac{T}{T_c} \right)^2 \left(\frac{N_0}{N} \right)^{2/5}. \end{aligned} \quad (12)$$

The first two terms of Eq. (12) correspond to the condensate fraction of an ideal gas, whereas the third describes the influence of the condensate repulsion to lowest order in $\bar{\mu}$. This expansion adequately describes the solution of Eq. (9) over the entire range of temperatures, provided that $\eta \ll 1$. A further simplification is derived by solving Eq. (12) to lowest order in η , arriving at

$$\frac{N_0}{N} = 1 - \left(\frac{T}{T_c} \right)^3 - \eta \frac{\zeta(2)}{\zeta(3)} \left(\frac{T}{T_c} \right)^2 \left[1 - \left(\frac{T}{T_c} \right)^{3/2} \right]^{2/5}. \quad (13)$$

Within Eqs. (12) and (13), the only effect of the condensate interactions is to shift the chemical potential to positive values, raising the bottom of the effective potential which the thermal atoms experience. The effect of changing the shape of the potential enters only at higher orders of the expansion. Equation (12) is thus a good approximation of Eq. (9) if most of the thermal atoms are spatially separated from the condensate, a condition satisfied for temperatures close to T_c and for small η .

Equation (12) is not expected to be a good description for extremely low temperatures. The understanding of this limit is facilitated by $f(x)$ obeying the differential equation

$$\frac{d^2}{dx^2} f = f - 2\sqrt{x}. \quad (14)$$

The function $f(x)$ has to grow slower than $x^{3/2}$ for large values of x . Otherwise, the power series in Eq. (10) would not converge. As a consequence, the second derivative in Eq.

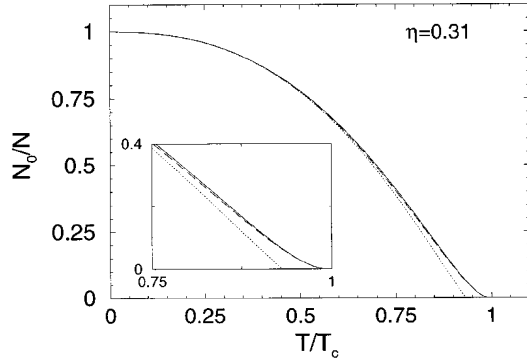


FIG. 1. Condensate fraction as a function of temperature, given by the semi-ideal model. The dashed line shows the exact solution [Eq. (9)] of the semi-ideal model. The solid line represents its high-temperature limit [Eq. (12)]. The explicit expression of Eq. (13) is given by the dotted line. This plot demonstrates the validity of Eq. (12) over the whole range of temperatures $T < T_c$. The explicit approximation of Eq. (13) fails only in the vicinity of the critical temperature (shown in the inset).

(14) vanishes for large x . Thus, the asymptotic limit of the condensate fraction for low temperatures is given by $f(x) = 2\sqrt{x}$ or

$$\frac{N_0}{N} = 1 - \sqrt{\eta} \frac{4}{\sqrt{\pi}} \frac{\zeta(5/2)}{\zeta(3)} \left(\frac{T}{T_c} \right)^{5/2}. \quad (15)$$

However, it has been shown [7] that the leading term of the uncondensed fraction around zero temperature scales like

$$\frac{N_0}{N} = 1 - \eta \frac{\pi^2}{2\sqrt{2}\zeta(3)} \left(\frac{T}{T_c} \right)^2 \quad (16)$$

due to quasiparticle contributions which are included in neither the semi-ideal nor the interacting Hartree-Fock treatment.

According to Fig. 1, where $\eta = 0.31$ has been assumed, the high-temperature expansions Eqs. (12) and to some extent Eq. (13) are very good approximations of the exact condensate fraction [Eq. (9)] of the semi-ideal model over the whole range of temperatures $T < T_c$. In contrast, we have found that the validity of the low temperature limits of Eqs. (15) and (16) are restricted to a very small range around zero temperature, which makes them nearly irrelevant for practical purposes.

The condensate fraction given by the approximate solution of the semi-ideal model in Eq. (12) is compared in Fig. 2 with the result of an iterative solution of the interacting model [Eqs. (1)–(3)]. The difference between the curves is small except near the critical temperature, where the interactions among thermal atoms shift the critical temperature [13]. This shift is not exhibited by the semi-ideal model. The wide range of validity of the semi-ideal model has also been confirmed by a numerical comparison with a Hartree-Fock-Popov calculation [9]. The latter includes collective excitations, which are ignored in the models shown in Fig. 2. These lead to an additional but negligible decrease of the condensate fraction [7].

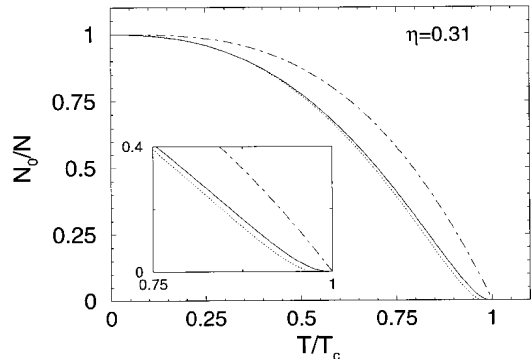


FIG. 2. Condensate fraction plotted as a function of temperature, comparing the discussed models. The ideal gas condensate fraction is given by the dash-dotted line. The dotted line is a numerical solution of the Hartree-Fock equations (1)–(3). The solid line is obtained from the analytical approximation [Eq. (12)], corresponding to the solid line of Fig. 1. Except near the critical temperature (shown in the inset), the semi-ideal model well approximates the solution of the interacting model. The critical temperature T_c refers to the case of an ideal gas.

A direct comparison between the density distributions of the different models is given in Fig. 3 for $T/T_c = 0.5$. Here the Thomas-Fermi solution of the condensate density of Eq. (1) has been replaced by a solution of the full Gross-Pitaevskii equation. The main implication of the included kinetic energy of the condensate is a smoothed out condensate surface. Within the Thomas-Fermi approximation almost no difference is seen between the two curves. Even though the unaccounted existence of collective excitations changes the densities of condensate and thermal component close to the center of the trap by a significant amount, their

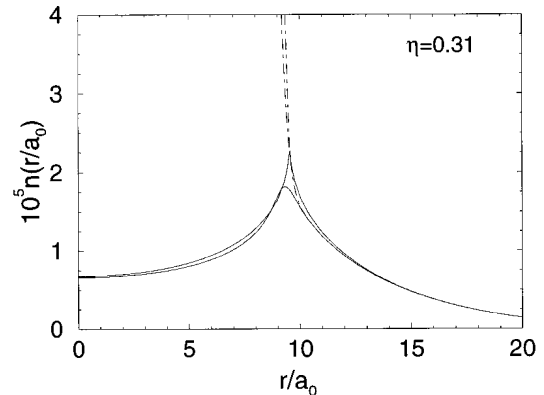


FIG. 3. A comparison of the density distributions at $T/T_c = 0.5$ predicted by the two discussed models. The upper solid line shows the density of the thermal component as given by Eq. (5). In comparison, the lower solid line has been calculated numerically using Eq. (2). However, a numerical solution of the full Gross-Pitaevskii equation has been used instead of the Thomas-Fermi approximation of Eq. (1). A small difference exists at the edge of the condensate due to the neglect of the kinetic energy in the semi-ideal model. However, the total density is only weakly affected by this effect, as is seen by the two dash-dotted lines. Again, the upper dash-dotted line refers to the total density given by the semi-ideal model, while the lower curve corresponds to the self-consistent Hartree-Fock approximation. Here a total atom number of $N = 5 \times 10^6$ was assumed.

influence on the total density is negligibly small for most temperatures [8].

In recent experiments, trapped Bose gases have been probed *in situ* using either nondestructive dispersive imaging techniques [14] or off-resonant absorption imaging [15]. These methods are important new tools in the understanding of trapped Bose gases, with distinct advantages over the previously used time-of-flight measurements of expanding atom clouds [1,2]. We therefore expect that the results of this paper will become useful for future *in situ* experiments with trapped Bose gases. These new optical detection techniques measure column or line density profiles; we therefore determine these profiles from Eqs. (4) and (5) by integration over one or two dimensions.

In cylindrical coordinates, where the probe beam is directed along the z axis, the according column densities are given by

$$n_0(\rho) = \frac{4\sqrt{2}}{3} \frac{(\mu - \rho^2/2)^{3/2}}{U} \theta(\mu - \rho^2/2), \quad (17)$$

$$n_T(\rho) = \frac{2\pi}{\lambda_T^4} \begin{cases} g_2(e^{\bar{\mu}(\rho)}), & \bar{\mu}(\rho) < 0 \\ \int_0^\infty d\bar{\epsilon} \frac{1}{\sqrt{\pi\bar{\epsilon}}} g_{3/2}(e^{-|\bar{\epsilon} - \bar{\mu}(\rho)|}), & \bar{\mu}(\rho) > 0, \end{cases} \quad (18)$$

where $\bar{\mu}(\rho) = (\mu - \rho^2/2)/k_B T$. Equivalently, we obtain the line densities

$$n_0(z) = \pi \frac{(\mu - z^2/2)^2}{U} \theta(\mu - z^2/2), \quad (19)$$

$$n_T(z) = \frac{(2\pi)^2}{\lambda_T^5} \begin{cases} g_{5/2}(e^{\bar{\mu}(z)}), & \bar{\mu}(z) < 0 \\ 2\zeta(5/2) - g_{5/2}(e^{-\bar{\mu}(z)}), & \bar{\mu}(z) > 0, \end{cases} \quad (20)$$

$$\text{with } \bar{\mu}(z) = (\mu - z^2/2)/k_B T.$$

We therefore conclude that the proposed semi-ideal model of Eqs. (4)–(6) and (12) represents a rather good description of a trapped Bose gas at finite temperature, provided that η is not larger than the values $\eta \approx 0.3$ –0.4 achieved in recent experiments. Its mathematical simplicity gives a much clearer conceptual picture than the self-consistent approaches that have been used before. The observed agreement of the semi-ideal model with a self-consistent Hartree-Fock calculation has confirmed that the density of the thermal component is too low to necessitate an interacting gas description. Instead, the observed depletion of the condensate fraction arises from condensate interactions, leading to a positive value of the chemical potential, or equivalently to a raised bottom of the effective potential in which the thermal component resides. It is well described by Eq. (12), which is a low-order expansion in $\bar{\mu}$. In contrast, the changed shape of the effective potential does not influence the thermal population in a noticeable way.

This work was supported by the Deutsche Forschungsgemeinschaft (DFG) and also the Office of Naval Research, the Joint Services Electronics Program (ARO), and the JSEP Graduate Fellowship Program. It is a pleasure to thank M. Olshanii, H.-J. Miesner, and W. Ketterle for many valuable discussions. After the completion of this work, E. Mueller brought to our attention a numerical calculation of the condensate fraction within the semi-ideal model [16].

-
- [1] M. H. Anderson *et al.*, Science **269**, 198 (1995).
 - [2] K. B. Davis *et al.*, Phys. Rev. Lett. **75**, 3969 (1995).
 - [3] E. P. Gross, Nuovo Cimento **20**, 454 (1961).
 - [4] L. P. Pitaevskii, Zh. Eksp. Teor. Fiz. **40**, 646 (1961) [Sov. Phys. JETP **13**, 451 (1961)].
 - [5] V. V. Goldman, I. F. Silvera, and A. J. Leggett, Phys. Rev. B **24**, 2870 (1981).
 - [6] G. Baym and C. J. Pethick, Phys. Rev. Lett. **76**, 6 (1996).
 - [7] S. Giorgini, L. P. Pitaevskii, and S. Stringari, J. Low Temp. Phys. **109**, 309 (1997).
 - [8] M. Holzmann, W. Krauth, and M. Naraschewski (unpublished).
 - [9] R. J. Dodd, K. Burnett, M. Edwards, and C. W. Clark, Acta Phys. Pol. A **93**, 45 (1998).
 - [10] V. Bagnato, D. E. Pritchard, and D. Kleppner, Phys. Rev. A **35**, 4354 (1987).
 - [11] W. Ketterle and N. J. van Druten, Phys. Rev. A **54**, 656 (1996).
 - [12] I. S. Gradshteyn and I. M. Ryzhik, *Table of Integrals, Series, and Products*, 4th ed. (Academic, London, 1980).
 - [13] S. Giorgini, L. P. Pitaevskii, and S. Stringari, Phys. Rev. A **54**, R4633 (1996).
 - [14] M. R. Andrews *et al.*, Science **273**, 84 (1996).
 - [15] L. V. Hau *et al.*, Phys. Rev. A **58**, R54 (1998).
 - [16] A. Minguzzi, S. Conti, and M. P. Tosi, J. Phys. Condens. Matter (Paris) **9**, L33 (1997).

Appendix G

Reversible formation of a Bose–Einstein condensate

This appendix includes the following paper [14]: D.M. Stamper–Kurn, H.-J. Miesner, A.P. Chikkatur, S. Inouye, J. Stenger, and W. Ketterle, “Reversible formation of a Bose–Einstein condensate,” *Phys. Rev. Lett.* **81**, 2194 (1998).

Reversible Formation of a Bose-Einstein Condensate

D. M. Stamper-Kurn, H.-J. Miesner, A. P. Chikkatur,
S. Inouye, J. Stenger, and W. Ketterle

*Department of Physics and Research Laboratory of Electronics, Massachusetts Institute of Technology,
Cambridge, Massachusetts 02139*
(Received 1 May 1998)

We present a method of adiabatically changing the local phase-space density of an ultracold gas using a combination of magnetic and optical forces. Applying this method, we observe phase-space density increases in a gas of sodium atoms by as much as 50-fold. The transition to Bose-Einstein condensation was crossed reversibly, attaining condensate fractions of up to 30%. Measurements of the condensate fraction reveal its reduction due to interactions. [S0031-9007(98)07066-5]

PACS numbers: 03.75.Fi, 05.30.-d, 32.80.Pj

The physical properties of atomic gases change dramatically when quantum degeneracy is reached, i.e., when the ground state population approaches unity [1]. Recent successes in reaching quantum degeneracy with Bose gases [2–4] have relied on nonadiabatic, irreversible methods such as laser and evaporative cooling. The possibility of changing the ground state population by an adiabatic (i.e., isentropic) change in the trapping potential had been overlooked for quite some time [5]. Indeed, in the case of an ideal gas, adiabatic changes in the *strength* of the trapping potential do not change the ground state population [6,7]. However, Pinkse and collaborators [8] recently showed, both theoretically and experimentally, that by changing the *form* of the trapping potential, the population in the ground state can be changed without changing the entropy. For a nondegenerate gas the ground state population is identical to the phase-space density $\Gamma = n\lambda_T^3$, where n is the density of the gas and λ_T is the thermal de Broglie wavelength. Within the type of trap deformations considered in Ref. [8] the maximum increase of phase-space density is limited to a factor of 20.

In this Letter, we show that a more general deformation of the trapping potential can increase the phase-space density by an arbitrary factor, and we implement this scheme using a combination of magnetic and optical forces. Furthermore, we demonstrate the ability to cross the Bose-Einstein condensation (BEC) phase transition reversibly.

Adiabatic increase in phase-space density.—The type of trap deformations which we study can be understood with the following “two-box” model. Consider a classical gas of N atoms confined in a box of volume $V_0 = V_1 + V_2$ with an initial phase-space density Γ_0 . Suppose that the potential within a subvolume V_2 of the box is lowered to a final well depth U . In this final potential, the gas equilibrates at a temperature T_f , and the density in V_2 will be higher than that in V_1 by the Boltzmann factor $e^{U/k_B T_f}$. Using the condition of constant entropy and constant particle number, one obtains the relative increase of phase-space density in V_2 compared to that in V_0 before

compression:

$$\ln(\Gamma_2/\Gamma_0) = \frac{U/k_B T_f}{1 + (V_2/V_1)e^{U/k_B T_f}}. \quad (1)$$

For deep potential wells, where $U/k_B T_f \gg \ln(V_1/V_2)$, there is no increase in phase-space density since all of the gas becomes confined in V_2 , and the adiabatic deformation corresponds simply to a uniform compression of the gas. For shallow potential wells [$U/k_B T_f \ll \ln(V_1/V_2)$], the phase-space density in V_2 increases as $e^{U/k_B T_f}$. As U is varied between these limits, the phase-space density increase reaches a maximum which is greater than $(V_1/V_2)^{1/2}$. Thus, by choosing an extreme ratio of volumes V_1/V_2 , an arbitrarily large increase in phase-space density Γ_2/Γ_0 is possible.

To demonstrate this phase-space density increase in a gas of trapped atoms, a narrow potential well (analogous to V_2) was added to a broad harmonic potential (corresponding to V_1) by focusing a single infrared laser beam at the center of a magnetic trap. First, a gas of atomic sodium was evaporatively cooled to a temperature higher than the BEC phase transition temperature in the cloverleaf magnetic trap [9]. The number of atoms and their temperature were adjusted by varying the final radio frequency (rf) used in the rf-evaporative-cooling stage [10]. Afterwards, the magnetically trapped cloud was decompressed by slowly reducing the currents in the magnetic trapping coils. Time-of-flight absorption imaging was used to characterize the cloud. The total number of atoms N was determined by integrating the column density across the cloud, and the initial temperature T_0 was determined by one-dimensional Gaussian fits to the wings of the density distribution. From these, we determined the fugacity z of the gas by the relation $g_3(z) = N(\hbar\bar{\omega}/k_B T_0)^3$, and then its phase-space density by $\Gamma_0 = g_{3/2}(z)$, where $g_n(z) = \sum_{i=1}^{\infty} z^i/i^n$ [11]. Here, $\bar{\omega}$ is the geometric-mean trapping frequency of the magnetic trap, as determined by *in situ* measurements [12]. These phase-space density measurements were calibrated with images from magnetically trapped clouds at the phase transition.

The optical setup was similar to that used in Ref. [13]. The infrared laser power was gradually ramped-up from zero to a power P_c at which the onset of BEC was seen in time-of-flight images of clouds released from the deformed trap; this implied $\Gamma_f = g_{3/2}(1) = 2.612$ for the final phase-space density. These time-of-flight images allowed us to determine the final temperature T_f . The depth of the optical potential well was given by $U_c/k_B = (37 \mu\text{K})P_c/w_0^2 (\mu\text{m}^2/\text{mW})$, where w_0 is the $1/e^2$ beam-waist radius at the focus. The ramp-up time was made long enough to ensure that the trap deformation was adiabatic, but also short enough to minimize heating and trap loss. Ramp-up times of up to 10 s were used.

Figure 1a shows the increases in phase-space density which were measured at three different settings of the trap parameters. A maximum increase by a factor of 50 was obtained. Condensates were observed in clouds with temperatures as high as $5 \mu\text{K}$. Further increases were hindered by limitations in laser power and by limits to the ramp-up time set by the various heating and loss processes in the deformed trap. The scatter in the data is primarily due to statistical errors at the level of 30% in our measurements of $U_c/k_B T_f$, and in the determination of the transition point.

The well depth U_c required to reach BEC can be understood by a simple model depicted in Fig. 1. We begin with a harmonically trapped gas with a chemical potential $\mu < 0$ (Fig. 1b). Then, by lowering a potential well to a depth U_c at which BEC occurs, one essentially measures μ as $\mu = -U_c$ (Fig. 1c). However, this simple picture neglects the change in the chemical potential and the temperature of the gas during the adiabatic compression. Thus, let us consider instead the condition of constant entropy. The entropy per noncondensed particle in a harmonically confined Bose gas is determined uniquely by its fugacity z [8]:

$$\frac{S}{N}(z) = 4 \frac{g_4(z)}{g_3(z)} - \ln z. \quad (2)$$

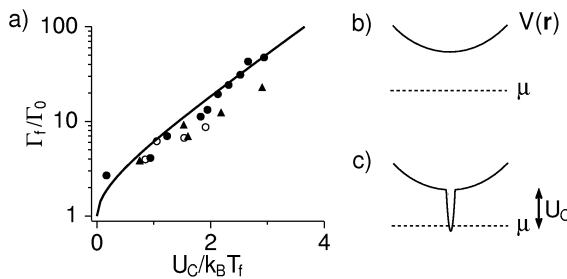


FIG. 1. Phase-space density increase to reach BEC vs normalized well depth (a). Various trap settings were used: $\bar{\omega} = 2\pi \times 100 \text{ Hz}$, $w_0 = 9 \mu\text{m}$ (triangles); $\bar{\omega} = 2\pi \times 100 \text{ Hz}$, $w_0 = 18 \mu\text{m}$ (open circles); and $\bar{\omega} = 2\pi \times 33 \text{ Hz}$, $w_0 = 18 \mu\text{m}$ (closed circles). The solid line gives the prediction of Eq. (3). (b) Prior to deformation, the harmonic trapping potential $V(r)$ holds a cloud above the BEC transition temperature ($\mu < 0$). (c) When a potential well with depth $U_c = -\mu$ is added, a small condensate forms.

This equation describes the entropy of the gas before compression, with the fugacity given by z_0 . After compression, because of the small volume of the potential well, the entropy per particle is approximately that of a harmonically trapped gas [Eq. (2)] with fugacity $z_f = e^{-U_c/k_B T_f}$ [14]. Here T_f is the final temperature of the gas. Constant entropy then implies $z_0 = z_f$. The initial phase-space density of the gas is $\Gamma_0 = g_{3/2}(z_0)$ and its final phase-space density is $\Gamma_f = g_{3/2}(1)$. Thus we obtain

$$\frac{\Gamma_f}{\Gamma_0} = \frac{g_{3/2}(1)}{g_{3/2}[\exp(-U_c/k_B T_f)]}. \quad (3)$$

This prediction, shown in Fig. 1a, describes our data well, and accounts for the universal behavior of our measurements over a wide range of temperatures and well depths.

One may also consider the process of adiabatically increasing the phase-space density as a change in the density of states $D(\epsilon)$ of the system. By increasing the well depth in a small region of the trap, we lowered only the energy of the ground state and a few excited states. Thus Γ , a local quantity, increases as the ground state energy is brought closer to the chemical potential, while the entropy, a global property of the gas, is unchanged by the minimal modification of $D(\epsilon)$.

The fact that global properties of the gas are not affected by the trap deformation can also be seen in the momentum distributions probed by time-of-flight imaging [9,15]. The onset of BEC in the combined optical and magnetic trap is signaled only by the formation of a condensate peak. The remaining thermal cloud is well fit by a Maxwell-Boltzmann distribution, which describes a magnetically trapped cloud far from condensation (Fig. 2a). In contrast, at the BEC transition in the harmonic magnetic trap, the momentum distribution of the thermal cloud is clearly Bose enhanced at low momenta (Fig. 2b).

Adiabatic condensation.—We now turn to the studies of adiabatic, i.e., reversible, condensate formation. A cloud

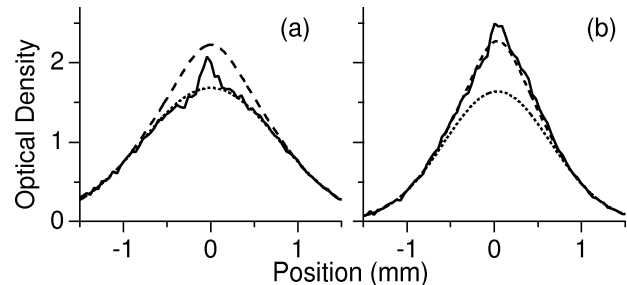


FIG. 2. Momentum distributions of the thermal cloud at the BEC phase transition show no Bose enhancement for the deformed trap (a), but a clear Bose enhancement for the purely magnetic trap (b). Both distributions show a small condensate peak. Lines show a Maxwell-Boltzmann distribution (dotted line) and a Bose-Einstein distribution (for $z = 1$) (dashed line) for clouds in a harmonic trap, which were fit to the thermal wings. The momentum distribution is shown as a profile across absorption images taken after 40 ms of ballistic expansion.

of about 50×10^6 atoms was cooled to the transition temperature in the magnetic trap, at trap frequencies of $\omega_r = 2\pi \times 20$ Hz and $\omega_z = 2\pi \times 13$ Hz in the radial and the axial direction, respectively. The power of the infrared laser beam (of radius $w_0 = 20 \mu\text{m}$) was ramped up over 1 s and held at a constant power for a dwell time of 1.5 s. Condensate fractions as small as 1% could be distinguished from the normal fraction by their anisotropic expansion in time-of-flight images [2,3]. The condensate number N_0 was determined by subtracting out the thermal cloud background using Gaussian fits to the thermal cloud in regions where the condensate was clearly absent.

As shown in Fig. 3, the adiabatic trap deformation yielded condensate fractions of up to 15%; we observed condensate fractions of 30% with different trap settings. By varying the dwell time, we confirmed that clouds for which $U/k_B T_f < 1.5$ suffered no significant losses of condensate number due to three-body decay or heating, whereas those points with higher values of $U/k_B T_f$ were affected by such losses.

For an ideal Bose gas, the result of this adiabatic change can be understood as follows. Before compression, the cloud of N particles at the BEC transition has an entropy S_i given by Eq. (2) as $S_i = N \times 4g_4(1)/g_3(1)$. After compression, the situation is similar to that indicated in Fig. 1c, i.e., because of the small volume of the attractive well, the cloud is well described as a harmonically trapped gas with $\mu = -U$. Thus, accounting for the fact that condensate particles carry no entropy and again using Eq. (2), which gives the entropy per *noncondensed* particle, we equate the entropy before and after compression and obtain

$$\frac{N_0}{N} = 1 - \frac{4g_4(1)/g_3(1)}{4g_4(e^{-U/k_B T_f})/g_3(e^{-U/k_B T_f}) + U/k_B T_f}. \quad (4)$$

However, this simple prediction does not describe our findings well. The theory described above has two shortcomings. First, the approximation of using Eq. (2) for the deformed trap is not strictly valid. However, calculations which accounted for the true shape of the deformed potential changed the prediction of Eq. (4) only

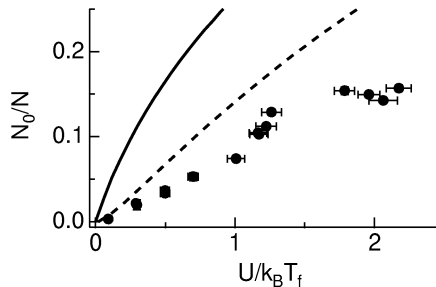


FIG. 3. Condensate formation by adiabatic trap deformation. The condensate fraction is plotted against the (normalized) well depth. Lines show predictions for an ideal gas (solid line) and for an interacting gas (dashed line).

for $U/k_B T_f > 1$, and only slightly improved the fit to our data.

A second shortcoming is the neglect of interactions. It has been shown that the condensate fraction of harmonically trapped Bose gases with repulsive interactions is reduced in comparison to that of an ideal gas [16,17]. To estimate this effect in our system, we use the “semi-ideal” model of Ref. [17]. The thermal cloud is described as an ideal gas for which the chemical potential is raised by $gn_0 = 4\pi\hbar^2 an_0/m$, where n_0 is the maximum condensate density, m the mass of sodium, and $a = 2.75 \text{ nm}$ its scattering length [18]. This simply corresponds to using Eq. (4) with the substitution $U \rightarrow U - gn_0$. We determined n_0 using the Gross-Pitaevskii equation in the Thomas-Fermi limit [19] and a harmonic approximation for the deformed trap potential at its center. Both approximations are valid for all data in Fig. 3.

This approach predicts a significant reduction of the condensate fraction (Fig. 3, dashed line), and the improved agreement with our data is strong evidence for this effect. In contrast to related studies in purely harmonic traps [9,15], which did not show evidence for interaction effects, this depletion is strongly enhanced by the shape of the deformed potential. The mean-field energy of the condensate gn_0 is large because the condensate forms in the tight optical potential, while the transition temperature T_c is small since it is determined by the weak magnetic potential. The remaining discrepancy between the semi-ideal prediction and our data may be due to our approximation of the entropy of the interacting gas, which fails for large values of $gn_0/k_B T_f$ [20].

The reversibility of crossing the BEC phase transition was demonstrated by preparing a magnetically trapped cloud just above T_c . We then sinusoidally modulated the power of the infrared light at 1 Hz, between 0 and 7 mW. This modulation frequency was significantly smaller than the magnetic trap frequencies ($\omega_r = 2\pi \times 48$ Hz and $\omega_z = 2\pi \times 16$ Hz). These low frequencies and a large optical focus ($w_0 = 18 \mu\text{m}$) were used to minimize trap loss due to inelastic collisions.

During the first seven condensation cycles the condensate fraction oscillated between zero and 6% (Fig. 4); later probing showed repeated condensation for at least 15 cycles. The peak of these oscillations decreased slowly in time. The temperature oscillated with an amplitude of about 100 nK, while gradually rising by about 10 nK/s. This heating and the decrease of the peak condensate fraction are consistent with similar behavior in clouds held at a constant infrared power [13]. Thus, within the stability limitations of our optical setup, the repeated crossing of the BEC phase transition appears fully adiabatic.

This method of creating condensates provides insight into their formation, which was recently studied experimentally [21] and theoretically [22]. For example, in the experiment described above, the condensate fraction was found to lag about 70 ms behind the modulation of the laser power, which is a measure for the formation time.

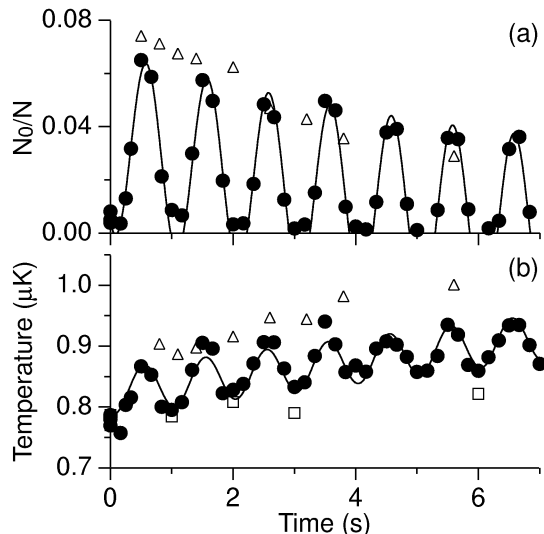


FIG. 4. Adiabatic cycling through the phase transition. Shown is the condensate fraction (a) and the temperature (b) vs time for the case of a modulated infrared beam (closed circles), an infrared beam ramped up to a constant power (open triangles), and no infrared light (open squares). The solid lines are guides to the eye.

That this lag time is much shorter than the time scale for deforming the potential (≈ 1 s) confirms that the repeated condensation is performed adiabatically.

In other experiments, by switching on the infrared light instantly, we observed condensation on time scales much faster than the oscillation periods in the magnetic trap and along the weakly confining axis of the optical trap. The resulting condensates showed striations in time-of-flight images, indicating that the condensates formed into excited states of the deformed potential. Such studies of shock condensation might give new insight into the formation of quasicondensates and condensation into excited states [23,24].

In conclusion, we have demonstrated the adiabatic Bose-Einstein condensation of an ultracold gas of atomic sodium. Changes in the trapping potential resulted in large phase-space density increases and allowed for repeated crossings of the BEC phase transition. This method allows for detailed studies of condensate formation and the phase transition. The combined trapping potential widens the range of trap parameters over which BEC can be studied. This was used to strikingly enhance the role of interactions and led to higher transition temperatures (up to $5 \mu\text{K}$) than achieved in purely magnetic traps.

We thank Michael R. Andrews for discussions. This work was supported by the Office of Naval Research, NSF, Joint Services Electronics Program (ARO), NASA, and the David and Lucile Packard Foundation. A.P.C. acknowledges additional support from the NSF,

D. M. S.-K. from JSEP, and J. S. from the Alexander von Humboldt Foundation.

- [1] A. Griffin, D. W. Snoke, and S. Stringari, *Bose-Einstein Condensation* (Cambridge University Press, Cambridge, England, 1995); Georgia Southern University BEC home page, <http://amo.phy.gasou.edu/bec.html>
- [2] M. H. Anderson *et al.*, *Science* **269**, 198 (1995).
- [3] K. B. Davis *et al.*, *Phys. Rev. Lett.* **75**, 3969 (1995).
- [4] C. C. Bradley, C. A. Sackett, and R. G. Hulet, *Phys. Rev. Lett.* **78**, 985 (1997); see also C. C. Bradley *et al.*, *Phys. Rev. Lett.* **75**, 1687 (1995).
- [5] W. Ketterle and D. E. Pritchard, *Phys. Rev. A* **46**, 4051 (1992).
- [6] F. Reif, *Fundamentals of Statistical and Thermal Physics* (McGraw-Hill Book Company, New York, 1965).
- [7] For weakly interacting Bose gases this argument has to be modified; see M. Houbiers, H. T. C Stoof, and E. A. Cornell, *Phys. Rev. A* **56**, 2041 (1997).
- [8] P. W. H. Pinkse *et al.*, *Phys. Rev. Lett.* **78**, 990 (1997).
- [9] M.-O. Mewes *et al.*, *Phys. Rev. Lett.* **77**, 416 (1996).
- [10] W. Ketterle and N. J. van Druten, in *Advances in Atomic, Molecular, and Optical Physics*, edited by B. Bederson and H. Walther (Academic Press, San Diego, 1996), Vol. 37, p. 181.
- [11] This assumes an ideal Bose gas and harmonic confinement; see V. Bagnato, D. E. Pritchard, and D. Kleppner, *Phys. Rev. A* **35**, 4354 (1987).
- [12] D. M. Stamper-Kurn *et al.*, *Phys. Rev. Lett.* **81**, 500 (1998).
- [13] D. M. Stamper-Kurn *et al.*, *Phys. Rev. Lett.* **80**, 2027 (1998).
- [14] This approximation is valid for shallow potential wells [$U/k_B T \ll \ln(V_1/V_2)$], as discussed in the two-box model. Numerical calculations confirmed its validity for all data in Fig. 1a. Note that the effective volume of the magnetic trap (V_1) increases with temperature.
- [15] J. R. Ensher *et al.*, *Phys. Rev. Lett.* **77**, 4984 (1996).
- [16] V. V. Goldman, I. F. Silvera, and A. J. Leggett, *Phys. Rev. B* **24**, 2870 (1981); R. J. Dodd, K. Burnett, M. Edwards, and C. W. Clark, *Acta Phys. Pol. A* **93**, 45 (1998); S. Giorgini, L. P. Pitaevskii, and S. Stringari, *Phys. Rev. A* **54**, R4633 (1996).
- [17] M. Naraschewski and D. M. Stamper-Kurn, *Phys. Rev. A* (to be published).
- [18] E. Tiesinga *et al.*, *J. Res. Natl. Inst. Stand. Technol.* **101**, 505 (1996).
- [19] G. Baym and C. J. Pethick, *Phys. Rev. Lett.* **76**, 6 (1996).
- [20] S. Giorgini (private communication).
- [21] H.-J. Miesner *et al.*, *Science* **279**, 1005 (1998).
- [22] C. W. Gardiner, P. Zoller, R. J. Ballagh, and M. J. Davis, *Phys. Rev. Lett.* **79**, 1793 (1997).
- [23] Yu. Kagan, B. V. Svistunov, and G. V. Shlyapnikov, *Sov. Phys. JETP* **75**, 387 (1992).
- [24] C. W. Gardiner *et al.*, e-print cond-mat/9801027.

Appendix H

Observation of metastable states in spinor Bose–Einstein condensates

This appendix includes the following paper [17]: H.-J. Miesner, D.M. Stamper–Kurn, J. Stenger, S. Inouye, A.P. Chikkatur and W. Ketterle, “Observation of metastable states in spinor Bose–Einstein condensates,” *Phys. Rev. Lett.* **82**, 2228 (1999).

Observation of Metastable States in Spinor Bose-Einstein Condensates

H.-J. Miesner, D. M. Stamper-Kurn, J. Stenger, S. Inouye, A. P. Chikkatur, and W. Ketterle

*Department of Physics and Research Laboratory of Electronics, Massachusetts Institute of Technology,
Cambridge, Massachusetts 02139*

(Received 10 November 1998)

Bose-Einstein condensates have been prepared in long-lived metastable excited states. Two complementary types of metastable states were observed. The first is due to the immiscibility of multiple components in the condensate, and the second to local suppression of spin-relaxation collisions. Relaxation via recondensation of noncondensed atoms, spin relaxation, and quantum tunneling was observed. These experiments were done with $F = 1$ spinor Bose-Einstein condensates of sodium confined in an optical dipole trap. [S0031-9007(99)08657-3]

PACS numbers: 03.75.Fi, 05.30.Jp, 64.60.My, 67.40.Fd

Metastable states of matter, excited states which relax only slowly to the ground state, are commonly encountered. This slow relaxation often arises from the presence of free-energy barriers that prevent a system from directly evolving toward its ground state; if the thermal energy to overcome this barrier is not available, the metastable state may be long lived.

Many properties of Bose-Einstein condensates in dilute atomic gases [1–4] arise from metastability; indeed, such condensates are themselves metastable, since the true equilibrium state is a solid at these low temperatures. Bose-Einstein condensates in gases with attractive interactions [3] are metastable against collapse due to a kinetic energy barrier [5]. The persistence of rotations in condensates with repulsive interactions hinges on whether vortices are metastable in singly [6] or multiply connected [7,8] geometries. Similarly, dark solitons in restricted geometries are predicted to be long lived [9] akin to the recently observed metastable states in superfluid $^3\text{He-B}$ [10]. Finally, Pu and Bigelow discussed spatial distributions of two-species condensates which are metastable due to repulsion between the two species [11].

In this Letter, we report on the observation of two complementary types of metastability in $F = 1$ spinor Bose-Einstein condensates of sodium. In one, a two-component condensate in the $|F = 1, m_F = 1, 0\rangle$ hyperfine states was stable in spin composition, but spontaneously formed a metastable spatial arrangement of spin domains. In the other, a single component $|m_F = 0\rangle$ condensate was metastable in spin composition with respect to the development of $|m_F = \pm 1\rangle$ ground-state spin domains. In both cases, the energy barriers which caused the metastability (as low as 0.1 nK) were much smaller than the temperature of the gas (about 100 nK) which would suggest a rapid thermal relaxation. However, since the thermal energy is only available to noncondensed atoms, this thermal relaxation was slowed considerably due to the high condensate fraction and the extreme diluteness of the noncondensed cloud.

Spinor Bose-Einstein condensates were prepared as in previous work [12]. Condensates in the $|F = 1, m_F =$

$-1\rangle$ state were created in a magnetic trap [13] and then transferred to an optical dipole trap formed by a single infrared laser beam [14]. The beam was weakly focused, producing cigar-shaped traps with depths of $1\text{--}2 \mu\text{K}$, radial trap frequencies of about 500 Hz, and aspect ratios of about 70. After transfer, Landau-Zener rf-sweeps placed the optically trapped atoms into the desired initial spin states. Condensates were then held for as long as 20 s during which time the condensate numbers decayed from about 10^6 to 10^5 . Condensate densities ranged from $(5\text{ to }1) \times 10^{14} \text{ cm}^{-3}$.

The spin-state distribution along the long axis of the optical trap was probed by a Stern-Gerlach spin separation combined with time-of-flight imaging [12]. After a sudden switch off of the optical trap, the condensate expanded primarily radially. After 5 ms, a magnetic field gradient of several G/cm separated the different spin-state populations without distorting them. Axial striations observed in time-of-flight images therefore reflected the spatial structure of the trapped condensate. After a total time-of-flight of 15–30 ms, the atoms were optically pumped to the $|F = 2, m_F = 2\rangle$ hyperfine state, and imaged with resonant light.

For our first set of experiments, a condensate in a superposition of the $|F = 1, m_F = 1, 0\rangle$ hyperfine states was prepared by first transferring all of the atoms to the $|m_F = 1\rangle$ state with an adiabatic rf-sweep at low field (1 G), and then transferring half of the population to the $|m_F = 0\rangle$ state with a nonadiabatic sweep at high field (15 G). The sample then evolved freely in a 15 G bias field which prevented the formation of $|m_F = -1\rangle$ spin domains due to the large quadratic Zeeman energy barrier [12].

Following their preparation, the two spin components began to separate radially (Fig. 1, sideways in images). Within 50 ms, axial density striations were observed, indicating the formation of $|m_F = 1\rangle$ and $|m_F = 0\rangle$ spin domains. The striations were initially angled due to radial excitations which tilted the domain walls at various angles to the long axis of the cloud. After about 100 ms, the striations became horizontal, indicating the dissipation of radial motion and the orientation of the domain walls

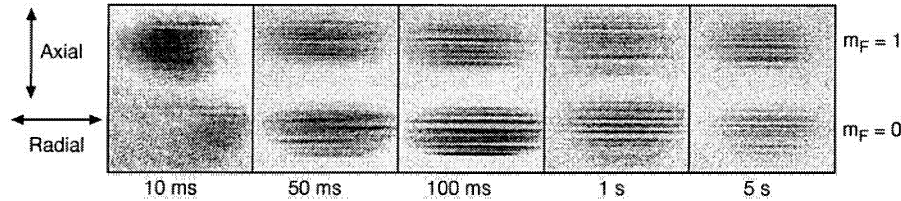


FIG. 1. Spontaneous formation of metastable states in a 15 G bias field. Condensates were probed at various times after an overlapping $|m_F = 1, 0\rangle$ mixed condensate was prepared. The $|m_F = 1\rangle$ (top) and $|m_F = 0\rangle$ (bottom) states were separated during their free expansion. Striations reflect the presence of alternating $\approx 40 \mu\text{m}$ axial spin domains which form 50 ms after state preparation. Only a $200 \mu\text{m}$ slice of the cloud was imaged, by using a narrow optical pumping beam, to improve resolution. Arrows indicate the axial and radial directions in the optical trap. The height of each image is 1.3 mm.

perpendicular to the axis of the cloud. The spin domains reached typical sizes of $40 \pm 15 \mu\text{m}$, slightly larger than their size after 50 ms. Thereafter, the clouds were essentially unchanged—only the total number of atoms diminished due to three-body losses. Matching the images of the $|m_F = 1\rangle$ and $|m_F = 0\rangle$ spin distributions showed that these long-lived states consist of persistent, alternating $|m_F = 1\rangle$ and $|m_F = 0\rangle$ spin domains.

Phase separation in two-component condensate mixtures is predicted by mean-field theory [15–18]. The mean-field interaction energy of such condensates is given by $2\pi\hbar^2/m \times (n_a^2 a_a + n_b^2 a_b + 2n_a n_b a_{ab})$, where m is the common atomic mass, n_a and n_b are the densities of each of the components, a_a and a_b are the same-species scattering lengths, and a_{ab} is the scattering length for interspecies collisions. The mean-field energy is minimized by phase separation when the scattering lengths obey the relation $a_{ab} > \sqrt{a_a a_b}$. At low magnetic fields, the scattering lengths in the $F = 1$ spinor system are determined by $a_{F_{\text{tot}}=0}$ and $a_{F_{\text{tot}}=2}$ which describe collisions between atoms with total angular momentum $F_{\text{tot}} = 0, 2$ [19]. Defining $\bar{a} = (2a_{F_{\text{tot}}=2} + a_{F_{\text{tot}}=0})/3$ and $\Delta a = (a_{F_{\text{tot}}=2} - a_{F_{\text{tot}}=0})/3$, the scattering lengths for the $|m_F = 1, 0\rangle$ two-component system are given by $a_0 = \bar{a}$, and $a_1 = a_{01} = \bar{a} + \Delta a$. Since $\Delta a > 0$ [12], $a_{01} > \sqrt{a_0 a_1}$ and the components phase separate. Interestingly, this phase separation should not occur in the noncondensed cloud because the same-species mean-field interaction energies are doubled due to exchange terms.

The tendency of a two-component mixture to phase separate implies the presence of imaginary frequencies for out-of-phase collective excitations of the overlapping components (spin waves) [18,20]. This means that such condensates are unstable, and slight perturbations grow exponentially. In our experiment, density and magnetic field inhomogeneities may yield slight perturbations in the initial state, corresponding to an initial distribution of spin wave excitations. The spontaneous formation of spin domains thus constitutes an observation of spin waves with imaginary frequencies at wavelengths of $10\text{--}50 \mu\text{m}$, corresponding to the size of the spin domains which are initially formed.

The many-domain spin distribution is a macroscopically occupied excited state; the ground state of the two-component system would contain only one domain

each of $|m_F = 0\rangle$ and $|m_F = 1\rangle$ atoms, minimizing the surface energy of the domain walls [21]. For the many-domain state to decay directly to the ground state, the two condensate components would have to either overlap or else pass by each other without overlapping. Such motion is energetically forbidden: the former due to the mean-field energy (typically 50 Hz or 2.5 nK [12]), and the latter due to the large kinetic energy required to vary the condensate wave function radially (the condensate is about $5 \mu\text{m}$ wide, yielding a kinetic energy barrier of 50–100 Hz) [22]. For this reason, the excited states we observe are metastable. In comparison, experiments on two-component mixtures of ^{87}Rb showed no metastability, due in part to the nearly spherical traps (aspect ratio of $1/\sqrt{8}$) which were used [23].

The typical size of the metastable spin domains can be understood by considering the width of the domain walls ($\approx 3 \mu\text{m}$ [24]). Spin domains smaller than this width do not prevent the tunneling of unlike-spin atoms through the domain, and thus small spin domains are free to migrate through the cloud and coalesce with other like-spin domains. Spin domains which are several times larger than the boundary width prevent the tunneling of atoms across the domain, and are thus stable. Metastable domains shorter than $\approx 25 \mu\text{m}$ were not observed, although the above description suggests that domains as short as $\approx 10 \mu\text{m}$ could be stable. This may be due to either an axial smearing of small domains during their free expansion prior to imaging, or perhaps the destabilization of small domains by the initial radial excitations in the trapped cloud.

The spontaneously formed metastable states persisted for at least 20 s in the absence of an externally applied magnetic field gradient. The lifetime of the metastable state was shortened by applying a magnetic field gradient along the axis of the trap. At field gradients of 0.1 G/cm or greater, the metastable states decayed to the ground state within experimentally accessible times of 10 s or less.

To study this decay with a well-defined initial state, we first created a metastable two-domain system. A strong magnetic field gradient was applied, causing the many spin domains to collapse into the ground state of two domains with the $|m_F = 1\rangle$ domain at the high-field end of the cloud. A weaker field gradient (0.1 G/cm) was then applied in the opposite direction, which energetically

favored the rearrangement of the spin domains at opposite ends of the cloud. In spite of this gradient, the two-domain system was metastable (Fig. 2). It decayed slowly to equilibrium via two processes: a slow process which dominated for the first 12 s, and a fast process (between 12 and 13 s) which suddenly depleted the metastable domains.

The slow process caused a gradual increase in the number of atoms in the two ground-state spin domains, which saturated at about 5×10^4 atoms in each. The rate of accumulation did not depend strongly on condensate density, which was varied by decreasing the total number of atoms before creating the metastable state. Thus, the slow process is probably due to recondensation of the dilute thermal cloud into ground-state spin domains, driven by a difference $\Delta\mu$ between the chemical potential of the thermal cloud and the energy of the ground state.

Studies of the formation of one-component Bose condensates in harmonic traps [25,26] considered the case $T \gg \mu$, where T is the temperature of the cloud, and μ is the chemical potential of the condensate ($\mu > 0$ due to interactions). For optically trapped Bose condensates, the temperature is about 1/10 of the optical trap depth due to evaporation, i.e., $T \approx 100$ nK [14]. For typical densities of 3×10^{14} cm $^{-3}$, $\mu = 220$ nK $> T$. Thus, previous studies of condensate formation may not apply to these metastable states.

The sudden decay to the ground state after the slow relaxation indicated the onset of a faster relaxation mechanism, which occurred once the decaying condensate had reached a critical density. The dependence of this critical density on the applied field gradient suggests the onset of quantum tunneling across the metastable spin domains. Such behavior will be reported in greater detail elsewhere.

The metastable states discussed so far involved multi-component mixtures stable in composition, but metastable in their spatial distribution. Conversely, we identified another form of metastability in which a single component condensate was stable in its spatial distribution, but metastable in its hyperfine composition. This was observed in spinor condensates with an overall spin projection $\langle F_z \rangle = 0$ along the magnetic field axis. Condensates were prepared using Landau-Zener rf-sweeps at high fields (30 G) in one of two ways: Either the entire trapped

condensate was placed in the $|m_F = 0\rangle$ state by a single rf-sweep, or the condensate was placed in a 50-50 mixture of the $|m_F = +1\rangle$ and $|m_F = -1\rangle$ states using two rf-sweeps. The condensates were then allowed to reach the ground state at a magnetic bias field B_0 and axial field gradient B' . The ground-state spin structure was studied previously as a function of B_0 and B' in Ref. [12].

The evolution to equilibrium from the two starting conditions was quite different (Fig. 3). When starting from the $|m_F = 0\rangle$ state, the condensate remained in that state for about three seconds before evolving over the next few seconds to the ground state. On the other hand, starting from an equal mixture of $|m_F = +1\rangle$ and $|m_F = -1\rangle$ atoms, the fraction of atoms in the $|m_F = 0\rangle$ state grew without delay, arriving at equilibrium within just 200 ms.

This difference can be understood by considering a spin-relaxation collision, in which two $|m_F = 0\rangle$ atoms collide to produce a $|m_F = 1\rangle$ and a $|m_F = -1\rangle$ atom. In the presence of a magnetic field B_0 , quadratic Zeeman shifts cause the energy of the two $|m_F = 0\rangle$ atoms to be lower than that of the $|m_F = 1\rangle$ and $|m_F = -1\rangle$ atoms by 2×390 Hz $\times (B_0/G)^2$. Because of this activation energy, condensate atoms in the $|m_F = 0\rangle$ state cannot undergo spin-relaxation collisions. Thus, even though the creation of $|m_F = 1\rangle$ and $|m_F = -1\rangle$ spin domains at the ends of the condensate is energetically favored *globally* in the presence of a magnetic field gradient, the $|m_F = 0\rangle$ condensate cannot overcome the *local* energy barrier for spin relaxation. On the other hand, condensate atoms in the $|m_F = 1\rangle$ and $|m_F = -1\rangle$ states can directly lower their energy through such collisions, and equilibrate quickly.

The decay of the metastable $|m_F = 0\rangle$ state was studied by varying the bias field B_0 , the field gradient B' , and the trap depth U . Evolution curves under various conditions (Fig. 4) were characterized by a delay time T_d before the fraction of condensate atoms in the $|m_F = 0\rangle$ state decayed exponentially to equilibrium with a relaxation time constant τ . Increasing the bias field B_0 did not affect τ significantly, but increased the delay time from $T_d \approx 1.9$ s at small bias fields (55 mG) to $T_d \approx 3.6$ s for larger fields (250 mG). Lowering the trap depth from 2 to 1.2 μ K increased both T_d from about 0.6 to 4 s, and τ from about 3.8 to 6.6 s. Increasing the magnetic field gradient from 11 to 44 mG/cm induced only a weak lowering of τ , and T_d was not affected significantly.

The delay time T_d should reflect the time scale for the gradual accumulation of $|m_F = \pm 1\rangle$ atoms in the thermal cloud before they reach a critical density and condense into the ground-state spin domains. Increasing the bias field increases the quadratic Zeeman energy barrier for spin relaxation, lengthening T_d . However, the clear variation of T_d as the energy barrier is changed from 0.1 nK at 55 mG to 2.5 nK at 250 mG, energies much smaller than the temperature of $T \approx 100$ nK, cannot be explained on the basis of thermal spin-relaxation collisions. Further study of these relaxation time scales is warranted [27].

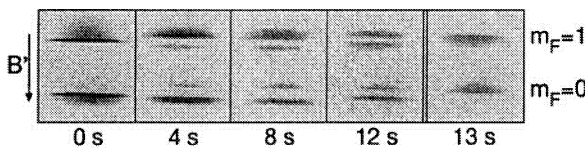


FIG. 2. Relaxation of metastable states in a 15 G axial bias field and a 0.1 G/cm gradient. Images show metastable (outer) and ground-state (inner) spin domains of $|m_F = 1\rangle$ and $|m_F = 0\rangle$ atoms, probed at various times after state preparation. The metastable domains decayed slowly for 12 s before tunneling quickly to the ground state. The direction of the field gradient (B') is indicated. The height of each image is 1.3 mm.

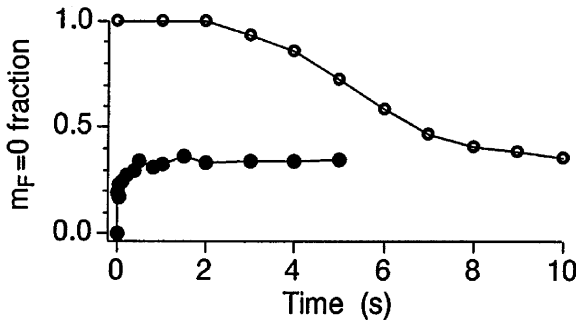


FIG. 3. Metastability of the pure $|m_F = 0\rangle$ state in the presence of a magnetic bias field (250 mG), and gradient (44 mG/cm). The evolution toward equilibrium of an initially pure $|m_F = 0\rangle$ condensate (open symbols), and a mixture of $|m_F = 1\rangle$ and $|m_F = -1\rangle$ (closed symbols) is shown by plotting the fraction of atoms in the $|m_F = 0\rangle$ state vs dwell time in the optical trap.

In conclusion, we have identified a novel form of metastability in Bose-Einstein condensates which occurs at temperatures much higher than the energy barrier for evolution to the ground state. This metastability arises due to the high condensate fraction which dramatically slows down thermal relaxation. This offers the opportunity to study the kinetics of condensation and of the dissolution of metastable condensates in “slow motion,” on time scales much longer than collision times, and periods of collective excitations. Furthermore, we have observed spontaneous phase separation in a two-component mixture in accordance with the predictions of mean-field theory.

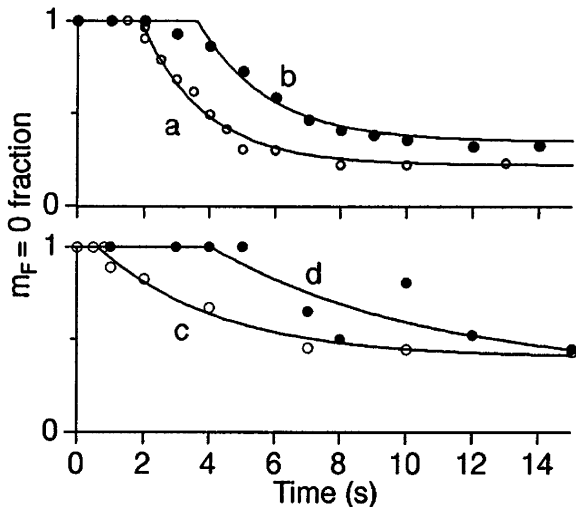


FIG. 4. Decay of $|m_F = 0\rangle$ metastable states. The lines are exponential decay fits to the $|m_F = 0\rangle$ fraction after a delay time T_d . Increasing the bias field (top) increased T_d . Lowering the temperature of the gas (bottom) increased both T_d and the exponential decay time τ . The magnetic bias field B_0 , the gradient B' , and the trap depth U for each curve are the following: (a) 55 mG, 44 mG/cm, 2 μK ; (b) 250 mG, 44 mG/cm, 2 μK ; (c) 20 mG, 11 mG/cm, 2 μK ; and (d) 20 mG, 11 mG/cm, 1.2 μK .

This work was supported by the Office of Naval Research, NSF, Joint Services Electronics Program (ARO), NASA, and the David and Lucile Packard Foundation. A. P. C. acknowledges additional support from the NSF, D. M. S.-K. from JSEP, and J. S. from the Alexander von Humboldt-Foundation.

- [1] M. H. Anderson *et al.*, Science **269**, 198 (1995).
- [2] K. B. Davis *et al.*, Phys. Rev. Lett. **75**, 3969 (1995).
- [3] C. C. Bradley, C. A. Sackett, and R. G. Hulet, Phys. Rev. Lett. **78**, 985 (1997); see also C. C. Bradley *et al.*, Phys. Rev. Lett. **75**, 1687 (1995).
- [4] D. S. Fried *et al.*, Phys. Rev. Lett. **81**, 3811 (1998).
- [5] Yu. Kagan, G. V. Shlyapnikov, and J. T. M. Walraven, Phys. Rev. Lett. **76**, 2670 (1996).
- [6] D. S. Rokhsar, Phys. Rev. Lett. **79**, 2164 (1997).
- [7] D. S. Rokhsar, cond-mat/9709212.
- [8] E. J. Mueller, P. M. Goldbart, and Y. Lyanda-Geller, Phys. Rev. A **57**, R1505 (1998).
- [9] S. A. Morgan, R. J. Ballagh, and K. Burnett, Phys. Rev. A **55**, 4338 (1997); W. P. Reinhardt and C. W. Clark, J. Phys. B **30**, L785 (1997); T. F. Scott, R. J. Ballagh, and K. Burnett, J. Phys. B **31**, L329 (1998); A. D. Jackson, G. M. Kavoulakis, and C. J. Pethick, Phys. Rev. A **58**, 2417 (1998).
- [10] S. Backhaus *et al.*, Nature (London) **392**, 687 (1998).
- [11] H. Pu and N. P. Bigelow, Phys. Rev. Lett. **80**, 1134 (1998).
- [12] J. Stenger *et al.*, Nature (London) **396**, 345 (1998).
- [13] M.-O. Mewes *et al.*, Phys. Rev. Lett. **77**, 416 (1996).
- [14] D. M. Stamper-Kurn *et al.*, Phys. Rev. Lett. **80**, 2027 (1998).
- [15] W. B. Colson and A. L. Fetter, J. Low. Temp. Phys. **33**, 231 (1978).
- [16] T.-L. Ho and V. B. Shenoy, Phys. Rev. Lett. **77**, 3276 (1996); E. Timmermans, Phys. Rev. Lett. **81**, 5718 (1998).
- [17] B. D. Esry, C. H. Greene, J. P. Burke, Jr., and J. L. Bohn, Phys. Rev. Lett. **78**, 3594 (1997).
- [18] E. V. Goldstein and P. Meystre, Phys. Rev. A **55**, 2935 (1997).
- [19] T.-L. Ho, Phys. Rev. Lett. **81**, 742 (1998).
- [20] R. Graham and D. Walls, Phys. Rev. A **57**, 484 (1998).
- [21] P. Ao and S. T. Chui, Phys. Rev. A **58**, 4836 (1998).
- [22] In contrast, *radially* separated components in the anisotropic trap would quickly relax by *axial* variation of the condensate wave function, i.e., by forming axially separated domains.
- [23] D. S. Hall *et al.*, Phys. Rev. Lett. **81**, 1539 (1998).
- [24] Approximating the two condensate wave functions in the boundary region ($0 \leq z \leq L$) to be $\psi_1 = \sqrt{n_1} \cos \pi z / 2L$, $\psi_0 = \sqrt{n_0} \sin \pi z / 2L$, and assuming equal pressure ($n_1^2 a_1 = n_0^2 a_0$) across the boundary of length L , the kinetic and mean-field (see text) energies are minimized at $L^2 = \pi \xi_1^2 [(a_1 + \sqrt{a_1 a_0})/(a_{01} - \sqrt{a_1 a_0})]$. Here, $\xi_1 = (8\pi n_1 a_1)^{-1/2}$. For $n_1 = 3 \times 10^{14} \text{ cm}^{-3}$, $a_1 = 52 \text{ bohr}$, and $L = 3 \mu\text{m}$.
- [25] H.-J. Miesner *et al.*, Science **279**, 1005 (1998).
- [26] C. W. Gardiner, P. Zoller, R. J. Ballagh, and M. J. Davis, Phys. Rev. Lett. **79**, 1793 (1997).
- [27] See related discussion in C. K. Law, H. Pu, and N. P. Bigelow, Phys. Rev. Lett. **81**, 5257 (1998).

Appendix I

Quantum tunneling across spin-domains in a Bose-Einstein condensate

This appendix includes the following paper [19]: D.M. Stamper-Kurn, H.-J. Miesner, A.P. Chikkatur, S. Inouye, J. Stenger and W. Ketterle, “Quantum tunneling across spin-domains in a Bose-Einstein condensate,” *Phys. Rev. Lett.* **83**, 661 (1999).

PHYSICAL REVIEW LETTERS

VOLUME 83

26 JULY 1999

NUMBER 4

Quantum Tunneling across Spin Domains in a Bose-Einstein Condensate

D. M. Stamper-Kurn, H.-J. Miesner, A. P. Chikkatur, S. Inouye, J. Stenger, and W. Ketterle

*Department of Physics and Research Laboratory of Electronics, Massachusetts Institute of Technology,
Cambridge, Massachusetts 02139*

(Received 12 February 1999)

Quantum tunneling was observed in the decay of metastable spin domains in gaseous Bose-Einstein condensates. A mean-field description of the tunneling was developed and compared with measurement. The tunneling rates are a sensitive probe of the boundary between spin domains, and indicate a spin structure which is prohibited in the bulk fluid. These experiments were performed with optically trapped $F = 1$ spinor Bose-Einstein condensates of sodium.

PACS numbers: 03.75.Fi, 05.30.Jp, 74.50.+r

A metastable system trapped in a local minimum of the free energy can decay to lower energy states in two ways. Classically, the system may decay by acquiring thermal energy greater than the depth of the local energy well (the activation energy). However, even in the absence of thermal fluctuations, the system may still decay by tunneling through the classically forbidden energy barrier. The theory of quantum tunneling describes a variety of physical and chemical phenomena [1,2] and finds common applications in, for example, scanning tunneling microscopy. In those systems, tunneling dominates over thermal activation because the energy barriers are much larger than the thermal energy.

Bose-Einstein condensates of dilute atomic gases [3] offer a new system to study quantum phenomena. Recently, metastable multicomponent Bose-Einstein condensates were observed in which the spatial structure of phase-separated domains persisted in spite of an external force which favored their rearrangement [4]. The metastability was due to the restriction of motion to one dimension by the narrow trapping potential and to the repulsive interaction between the domains. Even at temperatures (~ 100 nK) much larger than the energy barriers responsible for metastability (~ 5 nK), thermal relaxation was found to be extremely slow due to the scarcity of noncondensed atoms, to which the thermal energy is available.

In this Letter, we examine the decay of metastable spin domains in an $F = 1$ spinor condensate by quantum tun-

neling. The tunneling rates provide a sensitive probe of the boundary between spin domains and of the penetration of the condensate wave function into the classically forbidden region. Tunneling barriers are formed not by an external potential, but rather by the intrinsic repulsion between two immiscible components of a quantum fluid. These energy barriers are naturally of nanokelvin-scale height and of micron-scale width, and are thus a promising tool for future studies of quantum tunneling and Josephson oscillations [5–7].

We begin by considering the one-dimensional motion of a Bose-Einstein condensate comprised of atoms of mass m in two different internal states, $|A\rangle$ and $|B\rangle$. The condensate is held in a harmonic trapping potential which has the same strength for each component. In a mean-field description, the condensate wave function $\psi_i(z)$ is determined by two coupled Gross-Pitaevskii equations [8,9]

$$\left(-\frac{\hbar^2}{2m} \frac{d^2}{dz^2} + V_i(z) + g_i n_i(z) + g_{A,B} n_j(z) - \mu_i \right) \psi_i(z) = 0,$$

where $V_i(z)$ is the trapping potential, $n_i(z)$ the density, and μ_i the chemical potential of each component ($i, j = \{A, B\}, i \neq j$). The constants g_A , g_B , and $g_{A,B}$ (all assumed positive) are given by $g = 4\pi\hbar^2 a/m$ where a is the s -wave scattering length which describes collisions

between atoms in the same (a_A and a_B) or different ($a_{A,B}$) internal states. Bulk properties of the condensate are well described by neglecting the kinetic energy (Thomas-Fermi approximation). Under the condition $g_{A,B} > \sqrt{g_A g_B}$, the two components tend to phase separate (as observed in [4,10]). The ground state configuration consists of one domain of each component on opposite sides of the trap (Fig. 1a). The chemical potentials are determined by the densities at the boundary n_i^b as $\mu_i = g_i n_i^b$, and are related to one another by the condition of equal pressure, $\mu_A^2/2g_A = \mu_B^2/2g_B$.

Within the Thomas-Fermi approximation, the domain boundary is sharp and the two components do not overlap. Yet, the kinetic energy allows each component to penetrate within the domain of the other. The energy barrier for component A (similar for B) is $\Delta E_A(z) = V_A(z) + g_{A,B}n_B(z) - \mu_A$. Neglecting slow variations in V_A and n_B gives the barrier height

$$\Delta E_A = \mu_A \left(\frac{g_{A,B}}{\sqrt{g_A g_B}} - 1 \right). \quad (1)$$

In this work we consider a condensate of atomic sodium in the two hyperfine states $|A\rangle = |F = 1, m_F = 0\rangle$ and $|B\rangle = |F = 1, m_F = 1\rangle$, with scattering lengths of $a_1 = a_{0,1} = 2.75$ nm [11] and $(a_1 - a_0) = 0.10$ nm [12]. The barrier height for atoms in the $|m_F = 0\rangle$ state is then $0.018\mu_0$, a small fraction of the chemical potential.

A state-selective force $-F\hat{z}$ is then applied (in this case by a magnetic field gradient) and displaces the trapping potential $V_B(z)$ from $V_A(z)$ (Fig. 1b). Classically, the atoms cannot move to the other end of the trap due to the energy barrier discussed above, and thus the condensate is left in a high-energy configuration. This configuration can decay by tunneling. At a domain boundary at the center at the condensate, $dV_A/dz = g_B d n_B/dz = -F/2$,

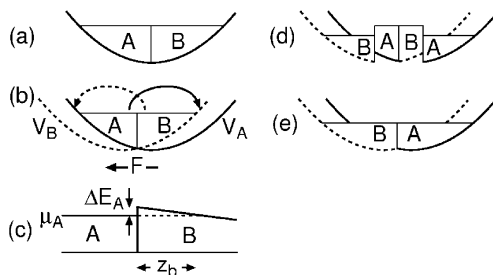


FIG. 1 Metastable spin domains and the energy barrier for decay. (a) The ground state of a two-component condensate consists of two phase-separated domains. (b) A state-selective force F displaces the trap potential V_B from V_A , creating metastable spin domains. Atoms tunnel from the metastable spin domains (direction of arrows) through an energy barrier (c) of maximum height ΔE_A and width $z_b \approx \Delta E_A/F$ (shown for component A). (d) Tunneling proceeds from the metastable domains (inner) to the ground state domains (outer) until (e) the condensate has completely relaxed to the ground state.

and so $\Delta E_A(z) = \Delta E_A - Fz$ [13] (Fig. 1c). The width of the barrier becomes $z_b = \Delta E_A/F$. Tunneling from the metastable spin domains is analogous to the field emission of electrons from cold metals [2], where the energy barrier height corresponds to the work function of the metal and the force arises from an applied electric field. The tunneling rate dN_A/dt of atoms in state $|A\rangle$ from the metastable spin domain is then given by the Fowler-Nordheim (WKB) relation [2]

$$\frac{dN_A}{dt} = \gamma \exp \left(-\frac{4}{3} \sqrt{\frac{2m}{\hbar^2}} \frac{\Delta E_A^{3/2}}{F} \right), \quad (2)$$

where γ is the total attempt rate for tunneling, and the exponential is the tunneling probability.

The rate of quantum tunneling was studied experimentally in three steps. First, condensates of sodium in the $|F = 1, m_F = -1\rangle$ hyperfine state were created in a magnetic trap [14] and transferred to a single-beam infrared optical trap [15] with a $1/e^2$ beam radius of $12 \mu\text{m}$, an aspect ratio (axial/radial length) of about 60, and a depth of $1-2 \mu\text{K}$. Chirped radio-frequency pulses were used to create two-component condensates with nearly equal populations in the $|m_F = 0\rangle$ and $|m_F = 1\rangle$ states [4,10]. Shortly afterwards, the two components were separated into two domains by the application of a strong (several G/cm) magnetic field gradient along the axis of the trap in a 15 G bias field. The spin domains were typically $100-200 \mu\text{m}$ long.

Second, the condensates were placed in a metastable state by applying a magnetic field gradient B' in the opposite direction of that used to initially separate the components [4]. This metastable state corresponds to that shown in Fig. 1b, where we identify the states $|A\rangle = |m_F = 0\rangle$ and $|B\rangle = |m_F = 1\rangle$. The field gradient exerted a state-selective force $F = g \mu_B m_F B'$ where $g = 1/2$ is the Landé g factor and μ_B the Bohr magneton. The condensate was then allowed to evolve freely at the gradient B' and a bias field B_0 for a variable time τ of up to 12 s.

Finally, the condensate was probed by time-of-flight absorption imaging combined with a Stern-Gerlach spin separation [4,10]. The radial expansion of the condensate in time of flight allowed for independent measurement of the chemical potentials μ_0 and μ_1 [14], while the axial distribution allowed for measurement of the number of atoms in the metastable and ground state domains of each spin state.

The mean-field description of tunneling from the metastable spin domains was tested by measuring the tunneling rate across energy barriers of constant height and variable width. Condensates in a 15 G bias field at a constant density (corresponding to $\mu_0/k_B = 300 \text{ nK}$) were probed after 2 s of tunneling at a variable field gradient B' (Fig. 2). Thus, the energy barrier for tunneling had a constant height of 5 nK and a width between

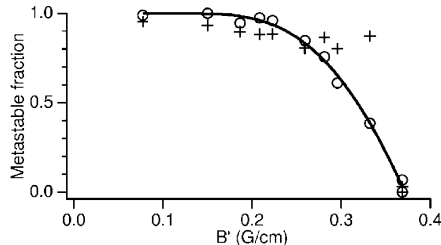


FIG. 2. Tunneling across a barrier of variable width which was adjusted by varying the field gradient B' . Condensates at constant density were probed after 2 s of tunneling. The fraction of atoms of each spin state in their metastable domain is shown. Circles represent the $m_F = 0$ atoms, and plusses the $m_F = 1$ atoms. A fit to the $m_F = 0$ data (solid line) determines the barrier attempt rate and tunneling probability. The data indicate that the tunneling rate for $m_F = 0$ atoms is larger than that for $m_F = 1$ atoms.

4 and 20 μm . As the barrier width was shortened, the tunneling rate increased, and the fraction of atoms in the $m_F = 0$ metastable spin domains decreased. As expressed in Eq. (2), the number of atoms which tunnel from the metastable to the ground state domains in a time τ should vary as $\gamma \tau e^{-\alpha/B'}$ where γ and α were determined by fits to the data as $\gamma = 1.5(5) \times 10^7 \text{ s}^{-1}$ and $\alpha = 1.5(2) \text{ G/cm}$. This value of α gives a tunneling probability of about e^{-4} for $B' = 370 \text{ mG/cm}$, at which the metastable domains were fully depleted in 2 s.

The tunneling attempt rate γ can be estimated as the product of two factors. First, a bulk flux can be estimated by considering the pressure $g_0 n_0^2/2$ to arise from an incoming atomic flux $n_0 v/2$ which collides elastically at the boundary, imparting an impulse $2mv$ per particle. This gives $\gamma_{\text{bulk}} = \langle n_0 v_s \rangle_{\text{rad}} / 2^{3/2}$ where $v_s = (g_0 n_0 / m)^{1/2}$ is the Bogoliubov speed of sound and $\langle \dots \rangle_{\text{rad}}$ denotes an integral over the radial dimension of the condensate. This bulk flux is reduced by an extinction factor f which accounts for the interpolation of the condensate wave function between the bulk spin domain and the classically forbidden region. Applying the treatment of Dalfonso *et al.* [7], we find $f \approx 1/10$. Using $\mu_0/k_B = 300 \text{ nK}$ and a radial trap frequency of 500 Hz gives an estimate of $\gamma_{\text{bulk}} \approx 5 \times 10^7 \text{ s}^{-1}$ and $\gamma \approx 5 \times 10^6 \text{ s}^{-1}$, in moderate agreement with the value extracted from our measurements.

The measured value of α can be compared with the prediction of the Fowler-Nordheim equation [Eq. (2)]. Using the scattering lengths above gives $\alpha = 1.5(2) \text{ G/cm}$, in agreement with our measurement (the error reflects a 10% systematic uncertainty in μ_0).

In addition, $g_1 > g_0$ implies $\mu_1 > \mu_0$ and thus the tunneling rate of $m_F = 1$ atoms across the $m_F = 0$ domain should be *slower* than that of the $m_F = 0$ atoms across the $m_F = 1$ domain. The data in Fig. 2 show evidence of this behavior.

The dependence of the tunneling rate on the energy barrier height was probed by varying the condensate density. For this, the number of trapped atoms was varied between about 10^5 and 10^6 by allowing for a variable duration of trap loss [15] before creating the metastable state. Figure 3 shows data collected at two different settings of the optical trap depth U and tunneling time τ (see caption). For each data series, at a given field gradient B' , there was a threshold value of the chemical potential μ_0 below which the condensates had relaxed completely to the ground state, and above which they had not. Since the total condensate number and the attempt rate γ should both scale as $\mu_0^{5/2}$ [14], one expects the chemical potential threshold to vary as $\mu_0 \propto B'^{2/3}$. The data shown in Fig. 3 suggest a slightly steeper dependence.

The chemical potential thresholds were approximately the same for both settings of the optical trap depth. Varying the optical trap depth U also changed the temperature [$T \approx (1/10)U$ [15]], and trap frequencies ($\omega \propto U^{1/2}$). That the threshold is independent of temperature confirms that the decay proceeds by quantum tunneling rather than thermal activation. That the threshold is independent of the trap frequencies confirms that the decay occurs by quantum tunneling of one spin component through the other, rather than by radial motion of one component around the other.

Thus, we have shown the decay of the metastable spin domains at high magnetic fields (15 G) to be due to quantum tunneling in a two-component condensate. At lower magnetic fields, a dramatic change in the tunneling behavior was observed. Metastable spin domains of initial chemical potential $\mu_0/k_B = 600 \text{ nK}$ were prepared at a constant field gradient of $B' = 130 \text{ mG/cm}$ and a bias field B_0 between 0.4 and 2 G. During a variable tunneling time τ of up to 12 s, the condensate density dropped due

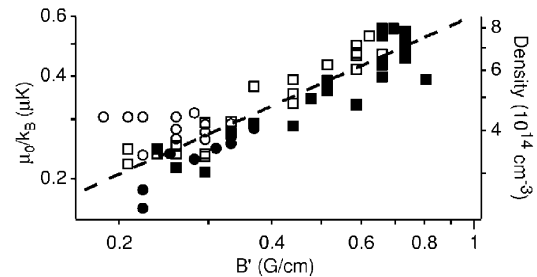


FIG. 3. Threshold behavior for tunneling. The chemical potential μ_0 and gradient B' are shown on a logarithmic scale. Closed symbols represent condensates which had fully decayed to the ground state, and open symbols those which had not. At higher condensate densities, the barrier is higher, and larger gradients B' are required to ensure tunneling. Data were taken at two different settings of the optical trap depth U and tunneling time τ : $U = 1.0 \mu\text{K}$ and $\tau = 2 \text{ s}$ (circles), and $U = 2.0 \mu\text{K}$ and $\tau = 1 \text{ s}$ (squares). The dashed line shows a $\mu_0 \propto B'^{2/3}$ dependence for the $U = 2.0 \mu\text{K}$ threshold.

to the loss of atoms from the trap. At fields below about 1 G, the tunneling rates dramatically increased, leading to relaxation of the ground state at earlier times (Fig. 4a), and thus at higher chemical potentials (Fig. 4b).

The increase in the tunneling rates at low magnetic fields is inconsistent with the dynamics of a two-component condensate. Our measurements thus serve as a probe of the spin domain boundary and reveal the presence of the third $F = 1$ spin component ($m_F = -1$).

Atoms in the $|m_F = -1\rangle$ state can be produced by spin relaxation, wherein two $m_F = 0$ atoms collide to produce an atom in the $|m_F = 1\rangle$ and the $|m_F = -1\rangle$ state. Their production is influenced by two competing effects: a quadratic Zeeman energy shift suppresses spin relaxation by lowering the energy of two $m_F = 0$ atoms below that of their spin-relaxation product, while a spin-dependent interaction energy favors a mixture of atoms in the $|m_F = \pm 1\rangle$ states [10].

Atoms in the $|m_F = -1\rangle$ state are energetically excluded from the bulk spin domains at fields $B_0 \gtrsim 250$ mG for typical densities of $n \sim 3 \times 10^{14}$ cm $^{-3}$. However, in the boundary between spin domains, where atoms in the $|m_F = 0\rangle$ and $|m_F = 1\rangle$ states overlap, the production of $m_F = -1$ atoms is always energetically favored [16]. The population of atoms in the domain boundary in the $|m_F = -1\rangle$ state scales roughly as $1/B_0^2$; thus, as the magnetic field is lowered, their population in the boundary increases. At a field of 1 G, the fraction of atoms in the domain boundary in the $|m_F = -1\rangle$ state is at most $\sim 2\%$ (about 300 atoms).

The presence of the $m_F = -1$ atoms in the barrier weakens the effective repulsion between the spin domains. Consider a two-component system as before where $|A\rangle = |m_F = 0\rangle$ and $|B\rangle = \cos\theta|m_F = 1\rangle - \sin\theta|m_F = -1\rangle$ where $0 \leq \theta \leq \pi/2$. Evaluating the spin-dependent interaction energy [10,17] one finds $g_B = g_0 + \Delta g \cos^2 2\theta$ and $g_{A,B} = g_0 + \Delta g(1 - \sin 2\theta)$, where $\Delta g = g_1 - g_0$.

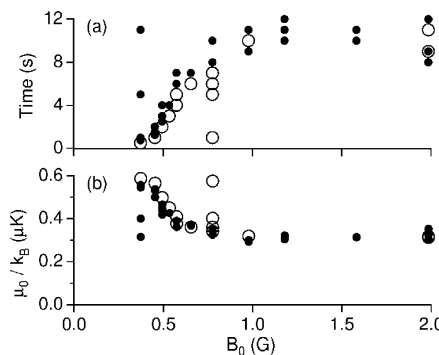


FIG. 4. Variation of tunneling threshold with magnetic bias field B_0 . Condensates probed after a variable tunneling time are represented by a closed symbol if total relaxation to the ground state was observed, and with an open symbol if not. As the field was lowered, condensates (a) relaxed in shorter times and (b) at higher chemical potentials μ_0 .

Thus, as the fraction of atoms in the $|m_F = -1\rangle$ state rises, the repulsion of the $m_F = 0$ atoms at the domain walls is weakened, and the tunneling rate is increased.

Future studies using metastable spin domains as tunneling barriers may focus on the roles of coherence and damping in quantum tunneling. In the current setup, rapid Josephson oscillations might be expected at frequencies (~ 1 kHz) given by the energy difference between the metastable and ground state spin domains. Over long time scales such oscillations are presumably damped. While no evidence for oscillatory behavior was found in the present work, the use of smaller spin domains and better time resolution is warranted.

In conclusion, we have identified and studied quantum tunneling across phase-separated spin domains in a Bose-Einstein condensate. The energy barriers due to the interatomic repulsion are a small fraction of the chemical potential, and their width is varied simply by the application of a weak force. The tunneling rates at high field ($B_0 > 1$ G) were described by a two-component mean-field model, while the tunneling at lower fields revealed changes in the spin-state composition of the domain boundaries.

This work was supported by the Office of Naval Research, NSF, Joint Services Electronics Program (ARO), NASA, and the David and Lucile Packard Foundation. A. P. C. acknowledges additional support from the NSF, D. M. S.-K. from JSEP, and J. S. from the Alexander von Humboldt-Foundation.

- [1] Examples include tunnel splittings in molecular spectra [F. Hund, Z. Phys. **43**, 805 (1927)], field ionization of neutral atoms [J. R. Oppenheimer, Phys. Rev. **31**, 66 (1928)], and nuclear decay [G. Gamow, Z. Phys. **51**, 204 (1928); R. W. Gurney and E. U. Condon, Nature (London) **122**, 439 (1928)].
- [2] R. H. Fowler and L. Nordheim, Proc. R. Soc. London A **119**, 173 (1928).
- [3] M. H. Anderson *et al.*, Science **269**, 198 (1995); K. B. Davis *et al.*, Phys. Rev. Lett. **75**, 3969 (1995); C. C. Bradley, C. A. Sackett, and R. G. Hulet, Phys. Rev. Lett. **78**, 985 (1997); D. G. Fried *et al.*, Phys. Rev. Lett. **81**, 3811 (1998).
- [4] H.-J. Miesner *et al.*, Phys. Rev. Lett. **82**, 2228 (1999).
- [5] B. D. Josephson, Phys. Lett. **1**, 251 (1962).
- [6] J. Javanainen, Phys. Rev. Lett. **57**, 3164 (1986); A. Smerzi, S. Fantoni, S. Giovanazzi, and S. R. Shenoy, Phys. Rev. Lett. **79**, 4950 (1997); I. Zapata, F. Sols, and A. J. Leggett, Phys. Rev. A **57**, R28 (1998); B. P. Anderson and M. A. Kasevich, Science **282**, 1686 (1998).
- [7] F. Dalfovo, L. Pitaevskii, and S. Stringari, Phys. Rev. A **54**, 4213 (1996).
- [8] T.-L. Ho and V. B. Shenoy, Phys. Rev. Lett. **77**, 3276 (1996).
- [9] B. D. Esry, C. H. Greene, J. P. Burke, Jr., and J. L. Bohn, Phys. Rev. Lett. **78**, 3594 (1997).

Appendix J

Excitation of phonons in a Bose–Einstein condensate by light scattering

This appendix includes the following paper [21]: D.M. Stamper–Kurn, A.P. Chikkatur, A. Görlitz, S. Inouye, S. Gupta, D.E. Pritchard and W. Ketterle, “Excitation of phonons in a Bose–Einstein condensate by light scattering,” *Phys. Rev. Lett.* **83**, 2876 (1999).

Excitation of Phonons in a Bose-Einstein Condensate by Light Scattering

D. M. Stamper-Kurn, A. P. Chikkatur, A. Görlitz, S. Inouye, S. Gupta, D. E. Pritchard, and W. Ketterle

*Department of Physics and Research Laboratory of Electronics, Massachusetts Institute of Technology,
Cambridge, Massachusetts 02139*

(Received 3 June 1999)

Stimulated small-angle light scattering was used to measure the structure factor of a Bose-Einstein condensate in the phonon regime. The excitation strength for phonons was found to be significantly reduced from that of free particles, revealing the presence of correlated pair excitations and quantum depletion in the condensate. The Bragg resonance line strength and line shift agreed with predictions for the homogeneous Bose gas using a local density approximation.

PACS numbers: 03.75.Fi, 05.30.-d, 32.80.Pj, 65.50.+m

Spectroscopic studies have been used to assemble a complete understanding of the structure of atoms and simple molecules. Similarly, neutron and light scattering have long been used to probe the microscopic excitations of liquid helium [1–4], and can be regarded as the spectroscopy of a many-body quantum system. With the realization of gaseous Bose-Einstein condensates, the spectroscopy of this new quantum fluid has begun.

The character of excitations in a weakly interacting Bose-Einstein condensed gas depends on the relation between the wave vector of the excitation q and the inverse healing length $\xi^{-1} = \sqrt{2}mc_s/\hbar$, which is the wave vector related to the speed of Bogoliubov sound $c_s = \sqrt{\mu/m}$, where $\mu = 4\pi\hbar^2an_0/m$ is the chemical potential, a is the scattering length, n_0 is the condensate density, and m is the atomic mass. For large wave vectors ($q \gg \xi^{-1}$), the excitations are particlelike with a quadratic dispersion relation. Excitations in the free-particle regime have been accessed by near-resonant light scattering [5]. For small wave vectors ($q \ll \xi^{-1}$), the gas responds collectively and density perturbations propagate as phonons at the speed of Bogoliubov sound. Such quasiparticle excitations have been observed at wavelengths comparable to the size of the trapped condensate [6] and thus were strongly influenced by boundary conditions.

In this Letter, we use Bragg spectroscopy to probe excitations in the phonon regime. Two laser beams intersecting at a small angle were used to create excitations in a Bose-Einstein condensate with wave vector $q < \xi^{-1}$,

$$\frac{2\pi}{N\hbar} \left(\frac{V}{2}\right)^2 \sum_f |\langle f | \hat{\rho}^\dagger(\mathbf{q}) | g \rangle|^2 \delta(\hbar\omega - (E_f - E_g)) = 2\pi\omega_R^2 S(\mathbf{q}, \omega),$$

where excited states $|f\rangle$ have energy E_f , and $\omega_R = V/2\hbar$ is the two-photon Rabi frequency. Thus, light scattering directly measures the dynamical structure factor, $S(\mathbf{q}, \omega)$, which is the Fourier transform of density correlations in state $|g\rangle$ [3,8]. Integrating over ω gives the static structure factor $S(\mathbf{q}) = \langle g | \hat{\rho}(\mathbf{q}) \hat{\rho}^\dagger(\mathbf{q}) | g \rangle / N$.

In this work, measurements were performed on both magnetically trapped and freely expanding Bose-Einstein condensates of sodium. Condensates of $\approx 10^7$ atoms were

thereby “optically imprinting” phonons into the gas. The momentum imparted to the condensate was measured by a time-of-flight analysis. This study is the first to explore phonons with wavelengths much smaller than the size of the trapped sample, allowing a direct connection to the theory of the homogeneous Bose gas. We show the excitation of phonons to be significantly weaker than that of free particles, providing dramatic evidence for correlated momentum excitations in the many-body condensate wave function.

In optical Bragg spectroscopy, an atomic sample is illuminated by two laser beams with wave vectors \mathbf{k}_1 and \mathbf{k}_2 and a frequency difference ω which is much smaller than their detuning Δ from an atomic resonance. The intersecting beams create a periodic, traveling intensity modulation $I_{\text{mod}}(\mathbf{r}, t) = I \cos(\mathbf{q} \cdot \mathbf{r} - \omega t)$, where $\mathbf{q} = \mathbf{k}_1 - \mathbf{k}_2$. The atoms experience a potential due to the ac Stark effect of strength $V_{\text{mod}} = \hbar\Gamma^2/8\Delta \times I_{\text{mod}}/I_{\text{sat}}$ [7], from which they may scatter. Here, Γ is the linewidth of the atomic resonance, and I_{sat} is the saturation intensity.

The response of an N -particle system to this perturbation can be evaluated using Fermi’s golden rule. We express V_{mod} in second-quantized notation $\hat{V}_{\text{mod}} = V/2[\hat{\rho}^\dagger(\mathbf{q})e^{-i\omega t} + \hat{\rho}^\dagger(-\mathbf{q})e^{+i\omega t}]$, where $\hat{\rho}^\dagger(\mathbf{q}) = \sum_k \hat{a}_{k+q}^\dagger \hat{a}_k$ is the Fourier transform of the atomic density operator at wave vector \mathbf{q} , and \hat{a}_k (\hat{a}_k^\dagger) is the destruction (creation) operator for an atom with momentum $\hbar\mathbf{k}$. For the ground state $|g\rangle$ with energy E_g , the excitation rate per particle is then

$$\text{created by laser and evaporative cooling and stored in a cigar-shaped magnetic trap with trapping frequencies of } \omega_r = 2\pi \times 150 \text{ Hz and } \omega_z = 2\pi \times 18 \text{ Hz in the radial and axial directions, respectively [9].}$$

The condensate was then exposed to two laser beams which intersected at an angle of $\approx 14^\circ$ and were aligned symmetrically about the radial direction, so that the difference wave vector \mathbf{q} was directed axially (Fig. 1a).

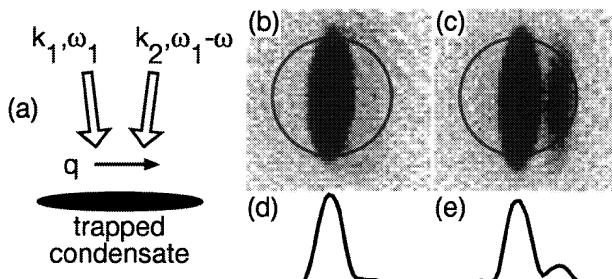


FIG. 1. Observation of momentum transfer by Bragg scattering. (a) Atoms were exposed to laser beams with wave vectors \mathbf{k}_1 and \mathbf{k}_2 and frequency difference ω , imparting momentum $\hbar\mathbf{q}$ along the axis of the trapped condensate. The Bragg scattering response of trapped condensates [(b) and (d)] was much weaker than that of condensates after a 5 ms free expansion [(c) and (e)]. Absorption images [(b) and (c)] after 70 ms time of flight show scattered atoms distinguished from the denser unscattered cloud by their axial displacement. Curves (d) and (e) show radially averaged (vertically in image) profiles of the optical density after subtraction of the thermal distribution. The Bragg scattering velocity is smaller than the speed of sound in the condensate (position indicated by circle). Images are 3.3×3.3 mm.

Both beams were derived from a common source, and then passed through two acousto-optical modulators operated with the desired frequency difference ω , giving the beams a detuning of 1.6 GHz below the $|F = 1\rangle \rightarrow |F' = 0, 1, 2\rangle$ optical transitions. Thus, at the optical wavelength of 589 nm, the Bragg recoil velocity was $\hbar q/m = 7$ mm/s, giving a predicted Bragg resonance frequency of $\omega_q^0 = \hbar q^2/2m = 2\pi \times 1.5$ kHz for free particles. The beams were pulsed on at an intensity of about 1 mW/cm² for a duration of 400 μ s. To suppress super-radiant Rayleigh scattering [10], both beams were linearly polarized in the plane defined by the condensate axis and the wave vector of the light.

The Bragg scattering of a trapped condensate was analyzed by switching off the magnetic trap 100 μ s after the end of the light pulse, and allowing the cloud to freely evolve for 70 ms. During the free expansion, the density of the atomic cloud dropped and *quasiparticles* in the condensate transformed into *free particles* and were then imaged by resonant absorption imaging (Fig. 1). Bragg scattered atoms were distinguished from the unscattered atoms by their axial displacement. The speed of Bogoliubov sound at the center of the trapped condensate is related to the velocity of radial expansion v_r as $c_s = v_r/\sqrt{2}$ [11] ($c_s = 11$ mm/s at $\mu/h = 6.7$ kHz as shown in Fig. 1). Thus, by comparing the axial displacement of the scattered atoms to the radial extent of the expanded condensate, one sees that the Bragg scattering recoil velocity is smaller than the speed of sound in the trapped condensate, i.e., the excitation in the trapped condensate occurs in the phonon regime.

For comparison, Bragg scattering of free particles was studied by applying a light pulse of equal intensity [12] after allowing the gas to freely expand for 5 ms, during

which the atomic density was reduced by a factor of 23 and the speed of sound by a factor of 5 from that of the trapped condensate. Thus, Bragg scattering in the expanded sample occurred in the free-particle regime.

The momentum transferred to the atomic sample was determined by the average axial position in time-of-flight images. To extract small momentum transfers, the images were first fitted (in regions where the Bragg scattered atoms were absent) to a bimodal distribution which correctly describes the free expansion of a condensate in the Thomas-Fermi regime, and of a thermal component [13]. The chemical potential μ of the trapped condensate was determined from the radial width of the condensate distribution [11]. The noncondensate distribution (typically less than 20% of the total population) was subtracted from the images before evaluating the momentum transfer.

By varying the frequency difference ω , the Bragg scattering spectrum was obtained for trapped and for freely expanding condensates (Fig. 2). The momentum transfer per atom, shown in units of the recoil momentum $\hbar q$, is anti-symmetric about $\omega = 0$ as condensate atoms are Bragg scattered in either the forward or the backward direction, depending on the sign of ω [14].

From these spectra, we determined the total line strength and the center frequency (Fig. 3) by fitting the momentum transfer to the difference of two Gaussian line shapes, representing excitation in the forward and the backward direction. Since $S(\mathbf{q}) = 1$ for free particles, we obtain the static structure factor as the ratio of the line strengths for the trapped and the expanded atomic samples. Spectra were taken for trapped condensates at three different densities by compressing or decompressing the condensates in the magnetic trap prior to the optical excitation.

The Bragg resonance for the expanded cloud was centered at 1.54(15) kHz with an rms width of 900 Hz consistent with Doppler broadening [15]. This frequency includes an expected 160 Hz residual mean-field shift,

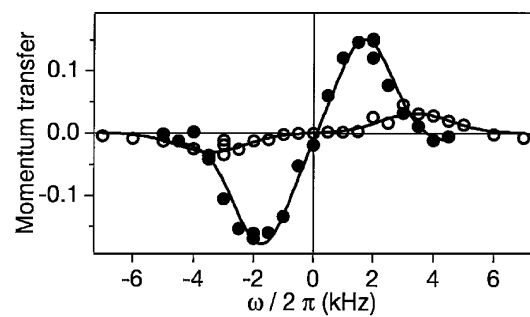


FIG. 2. Bragg scattering of phonons and of free particles. Momentum transfer per particle, in units of $\hbar q$, is shown vs the frequency difference $\omega/2\pi$ between the two Bragg beams. Open symbols represent the phonon excitation spectrum for a trapped condensate at a chemical potential $\mu/h = 9.2$ kHz. Closed symbols show the free-particle response of an expanded cloud. Lines are fits to the difference of two Gaussian line shapes representing excitation in the forward and backward directions.

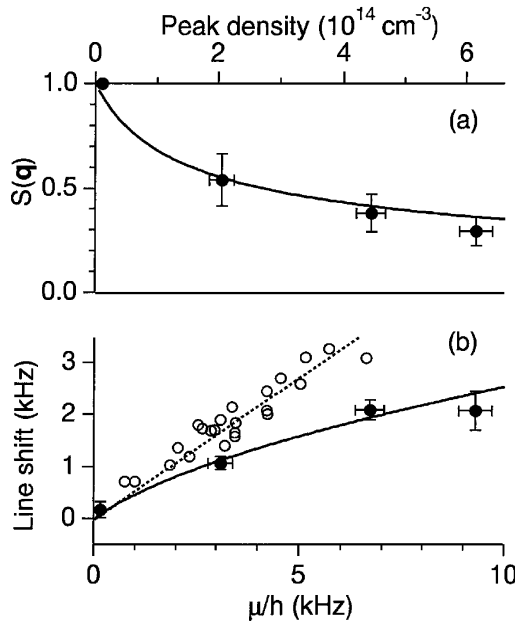


FIG. 3. (a) Static structure factor $S(\mathbf{q})$ and (b) shift of the line center from the free-particle resonance. $S(\mathbf{q})$ is the ratio of the line strength at a given chemical potential μ to that observed for free particles. As μ increases, the structure factor decreases, and the Bragg resonance frequency increases. Solid lines are predictions of a local density approximation [Eq. (5)] using $\omega_q^0 = 2\pi \times 1.38$ kHz. Dotted line indicates the mean-field shift of $4\mu/7h$ in the free-particle regime, with data from [5] shown in open symbols.

giving a measured free-particle resonance frequency of 1.38 kHz. The response of trapped condensates was strikingly different. As the density of the trapped condensates was increased, the Bragg scattering resonance was significantly weakened in strength and shifted upwards in frequency. This reflects the changing character of the excitations created by Bragg scattering as the speed of sound was increased: at a fixed Bragg scattering momentum, the excitations passed from the free-particle to the phonon regime.

To account for this behavior, we use the zero-temperature Bogoliubov description of a weakly interacting homogeneous Bose-Einstein condensate [16]. The Hamiltonian,

$$\mathcal{H} = \sum_k \hbar \omega_k^0 \hat{a}_k^\dagger \hat{a}_k + \sum_{k,l,m} \frac{2\pi \hbar^2 a}{mV} \hat{a}_k^\dagger \hat{a}_l^\dagger \hat{a}_m \hat{a}_{k+l-m}, \quad (1)$$

for a gas in volume V , where $\hbar \omega_k^0 = \hbar^2 k^2 / 2m$, is approximated by replacing the zero-momentum operators with c -numbers $\hat{a}_0^\dagger = \hat{a}_0 = \sqrt{N_0}$, where N_0 is the number of atoms with zero momentum. Neglecting terms of order $N^{-1/2}$, the Hamiltonian is diagonalized by a canonical transformation to operators defined by $\hat{a}_k = u_k \hat{b}_k - v_k \hat{b}_{-k}^\dagger$, where $u_k = \cosh \phi_k$, $v_k = \sinh \phi_k$, and $\tanh 2\phi_k = \mu / (\hbar \omega_k^0 + \mu)$. The energy of the Bogoliubov excitation created by \hat{b}_k^\dagger is $\hbar \omega_k^B = \sqrt{\hbar \omega_k^0 (\hbar \omega_k^0 + 2\mu)}$.

Neglecting small contributions representing multiparticle excitations [3,4], the single quasiparticle contribution to the static structure factor is

$$S(\mathbf{q}) = \frac{N_0}{N} \langle g | (\hat{a}_q \hat{a}_q^\dagger + \hat{a}_{-q}^\dagger \hat{a}_{-q} + \hat{a}_{-q}^\dagger \hat{a}_q^\dagger + \hat{a}_q \hat{a}_{-q}) | g \rangle. \quad (2)$$

Substituting the Bogoliubov operators, one obtains [17]

$$S(\mathbf{q}) \simeq (u_q^2 + v_q^2 - 2u_q v_q) = \omega_q^0 / \omega_q^B. \quad (3)$$

In the limit $\hbar \omega_q^0 \gg \mu$, the Bogoliubov excitations become identical to free-particle excitations ($u_q \rightarrow 1$, $v_q \rightarrow 0$), and $S(\mathbf{q}) \rightarrow 1$. For phonons ($\hbar \omega_q^0 \ll \mu$), $S(\mathbf{q}) \rightarrow \hbar q / 2mc_s$, and the line strength diminishes linearly with q .

To the same order of approximation, the quasiparticle resonance is undamped, and the dynamical structure factor is $S(\mathbf{q}, \omega) = S(\mathbf{q}) \delta(\omega - \omega_q^B)$ (satisfying the f sum rule: $\int \omega S(\mathbf{q}, \omega) d\omega = \omega_q^0$ [3]). Thus, accompanying the diminished line strength, the Bragg resonance is shifted upward from the free particle resonance by $\omega_q^B - \omega_q^0$.

Equivalently, the suppression of the Bragg resonance in the phonon regime can be understood in terms of the many-body condensate wave function. The static structure factor is the magnitude of the state vector $|e\rangle = \sum_k \hat{a}_{k+q}^\dagger \hat{a}_k |g\rangle / \sqrt{N}$. The macroscopic population of the zero-momentum state picks out two relevant terms in the summation:

$$|e\rangle \simeq (\hat{a}_q^\dagger \hat{a}_0 |g\rangle + \hat{a}_0^\dagger \hat{a}_{-q} |g\rangle) / \sqrt{N} = |e^+\rangle + |e^-\rangle. \quad (4)$$

These represent two means by which momentum is imparted to the condensate: either by promoting a zero-momentum particle to momentum $\hbar\mathbf{q}$, or else by demoting a particle from momentum $-\hbar\mathbf{q}$ to zero momentum.

If correlations could be neglected, the total rate of excitation would simply be the sum of the independent rates for these two processes, proportional to $\langle e^+ | e^+ \rangle = \langle N_q^0 \rangle + 1 = u_q^2$ and $\langle e^- | e^- \rangle = \langle N_{-q}^0 \rangle = v_q^2$, where $\langle N_k^0 \rangle$ is the expected number of atoms of momentum $\hbar\mathbf{k}$ in the condensate. This would apply, for example, to a condensate in a pure number state, or to an ideal gas condensate with a thermal admixture of atoms with momenta $\pm \hbar\mathbf{q}$, and would always lead to $S(\mathbf{q}) > 1$.

Yet, for the many-body ground state of the interacting Bose gas, the behavior is dramatically different. Collisions of zero-momentum atoms admix into the condensate pairs of atoms at momenta $\pm \hbar\mathbf{q}$, the population of which comprises the quantum depletion [18]. As a result, the two momentum transfer mechanisms described above produce indistinguishable states, and the rate of momentum transfer is given by the interference of two amplitudes, not by the sum of two rates. Pair excitations in the condensate are correlated so as to minimize the total energy, and thereby give destructive interference between the two momentum transfer processes, i.e., $S(\mathbf{q}) = (u_q - v_q)^2 < 1$. For high momentum, $\langle N_q^0 \rangle \ll 1$ and the interference plays a minor role. In the phonon regime, while the independent rates u_q^2 and v_q^2 (and, hence, $\langle N_{\pm q}^0 \rangle$) diverge

as $1/q$, the correlated quantum depletion extinguishes the rate of Bragg excitation.

These results for the homogeneous Bose gas can be applied to trapped, inhomogeneous condensates by a local density approximation since the reduced phonon wavelength q^{-1} ($0.4 \mu\text{m}$) is much smaller than the condensate size ($r > 20 \mu\text{m}$) and since the zero-point Doppler width is smaller than the mean-field shift ($\hbar q/mr \ll \mu/\hbar$) [19,20]. In the Thomas-Fermi regime, the condensate has a normalized density distribution $f(n) = 15n/4n_0\sqrt{1 - n/n_0}$, where n_0 is the maximum condensate density. The Bragg excitation line shape is then

$$I(\omega)d\omega = \frac{15}{8} \frac{\omega^2 - \omega_q^{02}}{\omega_q^0(\mu/\hbar)^2} \sqrt{1 - \frac{\omega^2 - \omega_q^{02}}{2\omega_q^0\mu/\hbar}} d\omega, \quad (5)$$

from which one can obtain the line strength $S(\mathbf{q})$ and center frequency. The line strength has the limiting values of $S(\mathbf{q}) \rightarrow 15\pi/32(\hbar\omega_q^0/2\mu)^{1/2}$ in the phonon regime and $S(\mathbf{q}) \rightarrow 1 - 4\mu/7\hbar\omega_q^0$ in the free-particle regime [21]. In accordance with the f -sum rule, the center frequency $\bar{\omega}$ is given as $\omega_q^0/S(\mathbf{q})$.

These predictions are shown in Fig. 3 using $\omega_0^q = 2\pi \times 1.38 \text{ kHz}$. Both the line strength and the shift of the Bragg resonance are well described by our treatment. For comparison, previous measurements [5] of the mean-field shift of the Bragg resonance ($4\mu/7\hbar$) in the free-particle regime are also shown, clearly indicating the many-body character of low energy excitations.

Finally, let us discuss finite temperature effects. The structure factor at nonzero temperature is increased as $S(\mathbf{q}) = (u_q - v_q)^2 \times (1 + N_q^B + N_{-q}^B)$ due to the populations $N_{\pm q}^B$ of thermally excited Bogoliubov quasiparticles at wave vectors $\pm\mathbf{q}$. However, in our measurements using stimulated scattering from two laser beams, the contribution of the thermal excitations cancels out [14], and thus we extract the zero-temperature structure factor. In contrast, by measuring light scattering from a single beam one could determine the temperature-dependent structure factor. Such a measurement could detect low-momentum thermal excitations, and thus could serve as a thermometer for a low-temperature gas.

In conclusion, stimulated light scattering was used to excite phonons in trapped Bose-Einstein condensates with wavelengths much smaller than the size of the trapped sample. The static structure factor was shown to be substantially reduced in the phonon regime. This modification of light-atom interactions arises from the presence of a correlated admixture of momentum excitations in the condensate. The observed reduction of $S(\mathbf{q})$ also implies a reduction of inelastic Rayleigh scattering of light with wave vector k by a condensate when $\hbar\omega_k^0 < \mu$ [22]. This effect may reduce heating in optical dipole traps and reduce the optical density probed in absorption imaging. For example, the absorption of near-resonant light by a homogeneous sodium condensate at a density of $3 \times 10^{15} \text{ cm}^{-3}$ [23] should be reduced by a factor of 2.

We thank Yvan Castin for insightful comments. This work was supported by the Office of Naval Research, NSF, JSEP, ARO, NASA, and the David and Lucile Packard Foundation. A.P.C. acknowledges additional support from the NSF, A.G. from DAAD, and D.M.S.-K. from JSEP.

- [1] T.J. Greytak, in *Quantum Liquids*, edited by J. Ruvalds and T. Regge (North-Holland, New York, 1978).
- [2] P.E. Sokol, in *Bose-Einstein Condensation*, edited by A. Griffin, D.W. Snoke, and S. Stringari (Cambridge University Press, Cambridge, England, 1995), p. 51.
- [3] P. Nozières and D. Pines, *The Theory of Quantum Liquids* (Addison-Wesley, Redwood City, CA, 1990).
- [4] A. Griffin, *Excitations in a Bose-Condensed Liquid* (Cambridge University Press, Cambridge, England, 1993).
- [5] J. Stenger *et al.*, Phys. Rev. Lett. **82**, 4569 (1999).
- [6] D.S. Jin *et al.*, Phys. Rev. Lett. **77**, 420 (1996); M.-O. Mewes *et al.*, Phys. Rev. Lett. **77**, 988 (1996); D.S. Jin *et al.*, Phys. Rev. Lett. **78**, 764 (1997); M.R. Andrews *et al.*, Phys. Rev. Lett. **79**, 553 (1997); D.M. Stamper-Kurn *et al.*, Phys. Rev. Lett. **81**, 500 (1998).
- [7] C. Cohen-Tannoudji, J. Dupont-Roc, and G. Grynberg, *Atom-Photon Interactions* (Wiley, New York, 1992).
- [8] J. Javanainen and J. Ruostekoski, Phys. Rev. A **52**, 3033 (1995).
- [9] M.-O. Mewes *et al.*, Phys. Rev. Lett. **77**, 416 (1996).
- [10] S. Inouye *et al.*, Science **285**, 571 (1999).
- [11] Y. Castin and R. Dum, Phys. Rev. Lett. **77**, 5315 (1996).
- [12] The laser beams had diameters of about 2 mm and were directed vertically, so the $120 \mu\text{m}$ drop of the atomic sample during the 5 ms time of flight was negligible.
- [13] W. Ketterle, D.S. Durfee, and D.M. Stamper-Kurn, in *Bose-Einstein Condensation in Atomic Gases*, Proceedings of the International School of Physics “Enrico Fermi,” edited by M. Inguscio, S. Stringari, and C.E. Wieman (to be published).
- [14] Since photons can be absorbed from either beam and then emitted into the other, we observe a momentum transfer proportional to $S(\mathbf{q}, \omega) - S(-\mathbf{q}, -\omega)$.
- [15] A tilt angle of $\approx 5^\circ$ of \mathbf{q} with respect to the axial direction introduced Doppler broadening from the radial expansion.
- [16] N.N. Bogoliubov, J. Phys. (Moscow) **11**, 23 (1947).
- [17] Shown explicitly for light scattering from a Bose-Einstein condensate in R. Graham and D. Walls, Phys. Rev. Lett. **76**, 1774 (1996).
- [18] K. Huang, *Statistical Mechanics* (Wiley, New York, 1987).
- [19] E. Timmermans and P. Tommasini (private communication).
- [20] The discrete spectrum was considered by A. Csordás, R. Graham, and P. Szépfalusy, Phys. Rev. A **54**, R2543 (1996); **57**, 4669 (1998).
- [21] $S(\mathbf{q}) = 15\eta/64(y + 4\eta - 2y\eta^2 + 12\eta^3 - 3y\eta^4)$, where $\eta^2 = \hbar\omega_q^0/2\mu$ and $y = \pi - 2\arctan[(\eta^2 - 1)/2\eta]$.
- [22] For a homogeneous Bose-Einstein condensate, inelastic scattering is reduced by a factor $(\sqrt{x(1+x)} - \sinh^{-1}\sqrt{x})/x$, where $x = 2\hbar\omega_k^0/\mu$.
- [23] D.M. Stamper-Kurn *et al.*, Phys. Rev. Lett. **80**, 2702 (1998).

Bibliography

- [1] K.B. Davis, M.-O. Mewes, M.R. Andrews, N.J. van Druten, D.S. Durfee, D.M. Kurn, and W. Ketterle, “Bose-Einstein condensation in a gas of sodium atoms,” Physical Review Letters **75**, 3969 (1995).
- [2] M.-O. Mewes, M.R. Andrews, N.J. van Druten, D.M. Kurn, D.S. Durfee, and W. Ketterle, “Bose-Einstein condensation in a tightly confining dc magnetic trap,” Physical Review Letters **77**, 416 (1996).
- [3] M.R. Andrews, M.-O. Mewes, N.J. van Druten, D.S. Durfee, D.M. Kurn, and W. Ketterle, “Direct, Non-Destructive Observation of a Bose Condensate,” Science **273**, 84 (1996).
- [4] M.-O. Mewes, M.R. Andrews, N.J. van Druten, D.M. Kurn, D.S. Durfee, C.G. Townsend, and W. Ketterle, “Collective Excitations of a Bose-Einstein condensate in a Magnetic Trap,” Physical Review Letters **77**, 988 (1996).
- [5] M.-O. Mewes, M.R. Andrews, D.M. Kurn, D.S. Durfee, C.G. Townsend, and W. Ketterle, “Output coupler for Bose-Einstein condensed atoms,” Physical Review Letters **78**, 582 (1997).
- [6] Michael R. Andrews, Christopher G. Townsend, H.-J. Miesner, Dallin S. Durfee, Dan M. Kurn, and Wolfgang Ketterle, “Observation of interference between two Bose condensates,” Science **275**, 637 (1997).
- [7] M.R. Andrews, D.M. Kurn, H.-J. Miesner, D.S. Durfee, C.G. Townsend, S. Inouye, and W. Ketterle, “Propagation of sound in a Bose-Einstein condensate,” Physical Review Letters **79**, 553 (1997).
- [8] M.R. Andrews, D.M. Stamper-Kurn, H.-J. Miesner, D.S. Durfee, C.G. Townsend, S. Inouye, and W. Ketterle, “Erratum: Propagation of Sound in a Bose-Einstein Condensate [Phys. Rev. Lett. 79, 553 (1997)],” Physical Review Letters **80**, 2967 (1998).
- [9] H.-J. Miesner, D.M. Stamper-Kurn, M.R. Andrews, D.S. Durfee, S. Inouye, and W. Ketterle, “Bosonic stimulation in the formation of a Bose-Einstein condensate,” Science **279**, 1005 (1998).
- [10] D. M. Stamper-Kurn, M.R. Andrews, A.P. Chikkatur, S. Inouye, H.-J. Miesner, J. Stenger, and W. Ketterle, “Optical Confinement of a Bose-Einstein Condensate,” Physical Review Letters **80**, 2072 (1998).

- [11] S. Inouye, M.R. Andrews, J. Stenger, H.-J. Miesner, D.M. Stamper-Kurn, and W. Ketterle, “Observation of Feshbach Resonances in a Bose-Einstein Condensate,” *Nature* **392**, 151 (1998).
- [12] D.M. Stamper-Kurn, H.-J. Miesner, S. Inouye, M.R. Andrews, and W. Ketterle, “Collisionless and Hydrodynamic Excitations of a Bose-Einstein Condensate..,” *Physical Review Letters* **81**, 500 (1998).
- [13] M. Naraschewski and D.M. Stamper-Kurn, “Analytical description of a trapped semi-ideal Bose gas at finite temperature,” *Physical Review A* **58**, 2423 (1998).
- [14] D.M. Stamper-Kurn, H.-J. Miesner, A.P. Chikkatur, S. Inouye, J. Stenger, and W. Ketterle, “Reversible Formation of a Bose-Einstein Condensate,” *Physical Review Letters* **81**, 2194 (1998).
- [15] J. Stenger, S. Inouye, D.M. Stamper-Kurn, H.-J. Miesner, A.P. Chikkatur, and W. Ketterle, “Spin domains in ground state spinor Bose-Einstein condensates,” *Nature* **396**, 345 (1998).
- [16] J. Stenger, S. Inouye, M.R. Andrews, H.-J. Miesner, D.M. Stamper-Kurn, and W. Ketterle, “Strongly enhanced inelastic collisions in a Bose-Einstein condensate near Feshbach resonances,” *Physical Review Letters* **82**, 2422 (1999).
- [17] H.-J. Miesner, D.M. Stamper-Kurn, J. Stenger, S. Inouye, A.P. Chikkatur, and W. Ketterle, “Observation of metastable states in spinor Bose-Einstein condensates,” *Physical Review Letters* **82**, 2228 (1999).
- [18] J. Stenger, S. Inouye, A.P. Chikkatur, D.M. Stamper-Kurn, D.E. Pritchard, and W. Ketterle, “Bragg Spectroscopy of a Bose-Einstein condensate,” *Physical Review Letters* **82**, 4569 (1999).
- [19] D.M. Stamper-Kurn, H.-J. Miesner, A.P. Chikkatur, S. Inouye, J. Stenger, and W. Ketterle, “Quantum tunneling across spin domains in a Bose-Einstein condensate,” *Physical Review Letters* **83**, 661 (1999).
- [20] S. Inouye, A.P. Chikkatur, D.M. Stamper-Kurn, J. Stenger, and W. Ketterle, “Superradiant Rayleigh scattering from a Bose-Einstein condensate,” *Science* **285**, 571 (1999).
- [21] D.M. Stamper-Kurn, A.P. Chikkatur, A. Görlitz, S. Inouye, S. Gupta, D.E. Pritchard, and W. Ketterle, “Excitation of phonons in a Bose-Einstein condensate by light scattering,” *Physical Review Letters* **83**, 2876 (1999).
- [22] W. Ketterle, D.S. Durfee, and D.M. Stamper-Kurn, in *Bose-Einstein condensation in atomic gases, Proceedings of the International School of Physics “Enrico Fermi,” Course CXL*, edited by M. Inguscio, S. Stringari, and C.E. Wieman (IOS Press, Amsterdam, 1999), pp. 67–176.
- [23] S. Grossman and M. Holthaus, “Lambda-Transition to the Bose-Einstein Condensate,” *Zeitschrift für Naturforschung* **50a**, 921 (1995).
- [24] S. Grossmann and M. Holthaus, “On Bose-Einstein condensation in harmonic traps,” *Physics Letters A* **208**, 188 (1995).

- [25] Wolfgang Ketterle and N. J. van Druten, “Bose-Einstein Condensation of a finite number of particles trapped in one or three dimensions,” Physical Review A **54**, 656 (1996).
- [26] K. Kirsten and D.J. Toms, “Bose-Einstein condensation of atomic gases in a general harmonic-oscillator confining potential trap,” Physical Review A **54**, 4188 (1996).
- [27] D.G. Fried, T.C. Killian, L. Willmann, D. Landhuis, S.C. Moss, D. Kleppner, and T.J. Greytak, “Bose-Einstein Condensation of Atomic Hydrogen,” Physical Review Letters **81**, 3811 (1998).
- [28] N.N. Bogoliubov, “On the theory of superfluidity,” J. Phys. (USSR) **11**, 23 (1947).
- [29] O. Penrose and L. Onsager, “Bose-Einstein condensation and liquid helium,” Physical Review **104**, 576 (1956).
- [30] A. Pais, *Subtle is the Lord, The Science and the Life of Albert Einstein* (Clarendon Press, Oxford, 1982).
- [31] A. Pais, *Inward Bound: of Matter and Forces in the Physical World* (Clarendon, New York, 1986).
- [32] O. Darrigol, “Statistics and combinatorics in early quantum theory,” Historical Studies in the Physical and Biological Sciences **19**, 17 (1988).
- [33] O. Darrigol, “Statistics and combinatorics in early quantum theory II: Early symptomata of indistinguishability and holism,” Historical Studies in the Physical and Biological Sciences **21**, 237 (1991).
- [34] A. Kastler, in *Old and New Problems in Physics, Cosmology, Philosophy, and Theoretical Biology*, edited by A. van der Merwe (Plenum, New York, 1983), p. 607.
- [35] K. Gavroglu, *Fritz London: A Scientific Biography* (Cambridge University Press, Cambridge, 1995).
- [36] K. Gavroglu and Y. Goudaroulis, “Understanding Macroscopic Quantum Phenomena: The History of Superfluidity 1941-1955,” Annals of Science **45**, 367 (1988).
- [37] A. Griffin, *Excitations in a Bose-condensed liquid* (Cambridge University Press, Cambridge, 1993).
- [38] T.J. Greytak and D. Kleppner, in *New Trends in Atomic Physics*, edited by G. Grynberg and R. Stora (North-Holland, Amsterdam, 1984), p. 1125.
- [39] I.F. Silvera and J.T.M. Walraven, in *Progress in Low Temperature Physics*, edited by D.F. Brewer (Elsevier, Amsterdam, 1986), Vol. X, p. 139.
- [40] I.F. Silvera and M. Reynolds, “Spin-Polarized Hydrogen: A Weakly Interacting Boson Gas,” Journal of Low Temperature Physics **87**, 343 (1992).
- [41] J.T.M. Walraven and T.W. Huijman, “Atomic hydrogen in magnetostatic traps,” Physica B **197**, 417 (1994).

- [42] T.J. Greytak, in *Bose-Einstein Condensation*, edited by A. Griffin, D.W. Snoke, and S. Stringari (Cambridge University Press, Cambridge, 1995), pp. 131–159.
- [43] D. Kleppner, T.J. Greytak, T.C. Killian, D.G. Fried, L. Willmann, D. Landhuis, and S.C. Moss, in *Bose-Einstein Condensation in Atomic Gases, Proceedings of the International School of Physics “Enrico Fermi,” Course CXL*, edited by M. Inguscio, S. Stringari, and C.E. Wieman (IOS Press, Amsterdam, 1999).
- [44] S. Chu, “The manipulation of neutral particles,” *Reviews of Modern Physics* **70**, 685 (1998).
- [45] C.N. Cohen-Tannoudji, “Manipulating atoms with photons,” *Reviews of Modern Physics* **70**, 707 (1998).
- [46] W.D. Phillips, “Laser cooling and trapping of neutral atoms,” *Reviews of Modern Physics* **70**, 721 (1998).
- [47] S.N. Bose, “Plancks Gesetz und Lichtquantenhypothese,” *Zeitschrift für Physik* **26**, 178 (1924).
- [48] A. Einstein, “Quantentheorie des einatomigen idealen Gases,” *Sitzungsberichte der preussischen Akademie der Wissenschaften* 261 (1924).
- [49] A. Einstein, “Quantentheorie des einatomigen idealen Gases. II,” *Sitzungsberichte der preussischen Akademie der Wissenschaften Bericht* **1**, 3 (1925).
- [50] M. Planck, *Verh. Deutsch. Phys. Ges.* **2**, 237 (1900).
- [51] O. Lummer and E. Pringsheim, *Verh. Deutsch. Phys. Ges.* **2**, 163 (1900).
- [52] H. Rubens and F. Kurlbaum, *Prussische Akademie der Wissenschaften* 929 (1900).
- [53] M. Planck, *Wissenschaftliche Abhandlungen und Vortäge* (Braunschweig, Braunschweig, 1958), Vol. 1.
- [54] P. Ehrenfest, “Zur Planckschen Strahlungstheorie,” *Physikalische Zeitschrift* **7**, 528 (1906).
- [55] P. Debye, “Der Wahrscheinlichkeitbegriff in der theorie der Strahlung,” *Annalen der Physik* **33**, 1427 (1910).
- [56] L. Natanson, “Über die Statistische Theorie der Strahlung,” *Physikalische Zeitschrift* **12**, 659 (1911).
- [57] M. Wolfke, “Zur Quantentheorie,” *Physikalische Gessellschaft Verhandlungen* **15**, 1123 (1913).
- [58] W.A. Blanpied, “Satyendranath Bose: Co-Founder of Quantum Statistics,” *American Journal of Physics* **40**, 1212 (1972).
- [59] M. Delbrück, “Was Bose-Einstein Statistics Arrived at by Serendipity?,” *Journal of Chemical Education* **57**, 467 (1980).
- [60] Letter from Einstein to Schrödinger, Feb. 28, 1925, quoted in ref. [33].

- [61] J.W. Gibbs, *Elementary principles in statistical mechanics* (Yale, New Haven, 1902).
- [62] F. London, “The λ -phenomenon of liquid helium and the Bose-Einstein degeneracy,” *Nature* **141**, 644 (1938).
- [63] K. Mendelssohn, *The Quest for Absolute Zero* (Halsted, New York, 1977).
- [64] H.G. Casimir, in *The Physicist’s Conception of Nature*, edited by M. Jagdish (D. Reidel, Boston, 1973).
- [65] P. Kapitza, “Viscosity of liquid helium below the λ -point,” *Nature* **141**, 74 (1938).
- [66] J.F. Allen and A.D. Misener, “Flow of liquid helium II,” *Nature* **141**, 75 (1938).
- [67] J.F. Allen and H. Jones, “New Phenomena Connected with Heat Flow in Helium II,” *Nature* **141**, 243 (1938).
- [68] F. London, “On the Bose-Einstein condensation,” *Physical Review* **54**, 947 (1938).
- [69] L. Tisza, “Transport Phenomena in Helium II,” *Nature* **141**, 913 (1938).
- [70] L.D. Landau, “On the theory of superfluidity,” *Physical Review series 2, 75*, 1949 (1949).
- [71] V. Peshkov, “Skorost’ vtorogo zvuka ot 1.3 do 1. pe^oK,” *JETP* **18**, 951 (1948).
- [72] J.P. Pellam and R.B. Scott, “Second sound velocity of paramagnetically cooled liquid helium II,” *Physical Review Letters* **2**, 869 (1949).
- [73] F. London, “The rare isotope of helium, ³He; a key to the strange properties of ordinary liquid helium, ⁴He,” *Nature* **163**, 646 (1949).
- [74] A.J. Leggett, “Superfluidity,” *Reviews of Modern Physics* **71**, S318 (1999).
- [75] P.E. Sokol, in *Bose-Einstein Condensation*, edited by A. Griffin, D.W. Snoke, and S. Stringari (Cambridge University Press, Cambridge, 1995), pp. 51–85.
- [76] P. Nozières and D. Pines, *The Theory of Quantum Liquids*, vol. 2 ed. (Addison-Wesley, Redwood City, CA, 1990).
- [77] B.C. Crooker, B. Hebral, E.N. Smith, Y. Takano, and J.D. Reppy, “Superfluidity in a Dilute Bose Gas,” *Physical Review Letters* **51**, 666 (1983).
- [78] J.D. Reppy, “⁴He as a dilute Bose Gas,” *Physica B* **126**, 335 (1984).
- [79] M. Rasolt, M.H. Stephen, M.E. Fisher, and P.B. Weichman, “Critical behavior of a dilute interacting Bose fluid,” *Physical Review Letters* **53**, 798 (1984).
- [80] J.P. Wolfe, J.L. Lin, and D.W. Snoke, in *Bose-Einstein Condensation*, edited by A. Griffin, D.W. Snoke, and S. Stringari (Cambridge University Press, Cambridge, 1995), pp. 281–329.
- [81] E. Fortin, E. Benson, and A. Mysyrowicz, in *Bose-Einstein Condensation*, edited by A. Griffin, D.W. Snoke, and S. Stringari (Cambridge University Press, Cambridge, 1995), pp. 519 – 523.

- [82] C.E. Hecht, *Physica* **25**, 1159 (1959).
- [83] W.C. Stwalley and L.H. Nosanow, “Possible “new” quantum systems,” *Physical Review Letters* **36**, 910 (1976).
- [84] Isaac F. Silvera and J. T. M. Walraven, “Stabilization of atomic hydrogen at low temperature,” *Physical Review Letters* **44**, 164 (1980).
- [85] R.W. Cline, D.A. Smith, T.J. Greytak, and D. Kleppner, “Magnetic confinement of spin-polarized atomic hydrogen,” *Physical Review Letters* **45**, 2117 (1980).
- [86] H. Hess, G.P. Kochanski, J.M. Doyle, N. Masuhara, D. Kleppner, and T.J. Greytak, “Magnetic Trapping of Spin-Polarized Atomic Hydrogen,” *Physical Review Letters* **59**, 672 (1987).
- [87] R. van Roijen, J.J. Berkhout, S. Jaakkola, and J.T.M. Walraven, “Experiments with Atomic Hydrogen in a Magnetic Trapping Field,” *Physical Review Letters* **61**, 931 (1988).
- [88] H.F. Hess, “Evaporative cooling of magnetically trapped and compressed spin-polarized hydrogen,” *Physical Review B* **34**, 3476 (1986).
- [89] N. Masuhara, J.M. Doyle, J.C. Sandberg, D. Kleppner, T.J. Greytak, H.F. Hess, and G.P. Kochanski, “Evaporative Cooling of Spin-Polarized Atomic Hydrogen,” *Physical Review Letters* **61**, 935 (1988).
- [90] V.V. Goldman, I.F. Silvera, and A.J. Leggett, “Atomic hydrogen in an inhomogeneous magnetic field: Density profile and Bose-Einstein condensation,” *Physical Review B* **24**, 2870 (1981).
- [91] D. A. Huse and E. Siggia, “The density distribution of a weakly interacting Bose gas in an external potential,” *Journal of Low Temperature Physics* **46**, 137 (1982).
- [92] J. Oliva, “Density profile of the weakly interacting Bose gas confined in a potential well: Nonzero temperature,” *Physical Review B* **39**, 4197 (1989).
- [93] E.D. Siggia and E.A. Ruckenstein, “Bose-Condensation in spin-polarized atomic hydrogen,” *Physical Review Letters* **44**, 1423 (1980).
- [94] H.T.C. Stoof, J.M.V.A. Koelman, and B.J. Verhaar, “Spin-exchange and dipole relaxation rates in atomic hydrogen: Rigorous and simplified calculations,” *Physical Review B* **38**, 4688 (1988).
- [95] I.F. Silvera, in *Bose-Einstein Condensation*, edited by A. Griffin, D.W. Snoke, and S. Stringari (Cambridge University Press, Cambridge, 1995), pp. 160–172.
- [96] A.P. Mosk, M.W. Reynolds, T.W. Hijmans, and J.T.M. Walraven, “Optical Observation of Atomic Hydrogen in the Surface of Liquid Helium,” *Journal of Low Temperature Physics* **113**, 217 (1998).
- [97] A. Matsubara, T. Arai, S. Hotta, J.S. Korhonen, T. Mizusaki, and A. Hiraj, in *Bose-Einstein Condensation*, edited by A. Griffin, D.W. Snoke, and S. Stringari (Cambridge University Press, Cambridge, 1995), pp. 478 – 486.

- [98] A.I. Safonov, S.A. Vasilyev, I.S. Yasnukov, I.I. Lukashevich, and S. Jaakola, “Observation of quasicondensate in two-dimensional atomic hydrogen,” Physical Review Letters **81**, 4545 (1998).
- [99] A. Einstein, “Zur Quantentheorie der Strahlung,” Physik. Zeitschr. **18**, 121 (1917).
- [100] T.W. Hänsch and A.L. Schawlow, “Cooling of gases by laser radiation,” Optics Communications **13**, 68 (1975).
- [101] D.J. Wineland and H. Dehmelt, “Proposed $10^{14}\Delta\nu < \nu$ laser fluorescence spectroscopy on TI^+ mono-ion oscillator III,” Bulletin of the American Physical Society **20**, 637 (1975).
- [102] V. Letokhov, V. Minogin, and B. Pavlik, “Cooling and trapping atoms and molecules by a resonant laser field,” Optics Communications **19**, 72 (1976).
- [103] D. Wineland, R. Drullinger, and F. Walls, “Radiation-pressure cooling of bound-resonant absorbers,” Physical Review Letters **40**, 1639 (1978).
- [104] W. Neuhauser, M. Hohenstatt, P. Toschek, and H. Dehmelt, “Optical-sideband cooling of visible atom cloud confined in parabolic well,” Physical Review Letters **41**, 223 (1978).
- [105] S. Andreev, V. Balykin, V. Letokhov, and V. Minogin, “Radiative slowing and reduction of the energy spread of a beam of sodium atoms to 1.5 K in an oppositely directed laser beam,” JETP Letters **34**, 442 (1981).
- [106] W.D. Phillips and H. Metcalf, “Laser deceleration of an atomic beam,” Physical Review Letters **48**, 596 (1982).
- [107] J.V. Prodan, W.D. Phillips, and H. Metcalf, “Laser Production of a Very Slow Monoenergetic Atomic Beam,” Physical Review Letters **49**, 1149 (1982).
- [108] W. Ertmer, R. Blatt, J.L. Hall, and M. Zhu, “Laser manipulation of atomic beam velocities: Demonstration of stopped atoms and velocity reversal,” Physical Review Letters **54**, 996 (1985).
- [109] K.-J. Kügler, W. Paul, and U. Trinks, “A magnetic storage ring for neutrons,” Physics Letters **72B**, 422 (1978).
- [110] A.L. Migdall, J.V. Prodan, W.D. Phillips, T.H. Bergeman, and H.J. Metcalf, “First Observation of Magnetically Trapped Neutral Atoms,” Physical Review Letters **54**, 2596 (1985).
- [111] S. Chu, L. Hollberg, J.E. Bjorkholm, A. Cable, and A. Ashkin, “Three-Dimensional Viscous Confinement and Cooling of Atoms by Resonance Radiation Pressure,” Physical Review Letters **55**, 48 (1985).
- [112] P.D. Lett, R.N. Watts, C.I. Westbrook, W.D. Phillips, P.L. Gould, and H.J. Metcalf, “Observatioin of Atoms Laser Cooled below the Doppler Limit,” Physical Review Letters **61**, 169 (1988).
- [113] S. Chu, J.E. Bjorkholm, A. Ashkin, and A. Cable, “Experimental Observation of Optically Trapped Atoms,” Physical Review Letters **57**, 314 (1986).

- [114] E.L. Raab, M. Prentiss, A. Cable, S. Chu, and D.E. Pritchard, “Trapping of Neutral Sodium with Radiation Pressure,” *Physical Review Letters* **59**, 2631 (1987).
- [115] J. Dalibard and C. Cohen-Tannoudji, “Laser cooling below the Doppler limit by polarization gradients: simple theoretical models,” *Journal of the Optical Society of America B* **6**, 2023 (1989).
- [116] P.J. Ungar, D.S. Weiss, E. Riis, and S. Chu, “Optical molasses and multilevel atoms: Theory,” *Journal of the Optical Society of America B* **6**, 2058 (1989).
- [117] H.J. Lee and S. Chu, “Atomic spin polarization by Raman cooling,” *Physical Review A* **57**, 2905 (1998).
- [118] M.T. DePue, C. McCormick, S.L. Winoto, S. Oliver, and D.S. Weiss, “Unity occupation of sites in a 3D optical lattice,” *Physical Review Letters* **82**, 2262 (1999).
- [119] H. Katori, T. Ido, Y. Isoya, and M. Kuwata-Gonokami, “Magneto-optical trapping and cooling of strontium atoms down to the photon recoil temperature,” *Physical Review Letters* **82**, 1116 (1999).
- [120] D.E. Pritchard, K. Helmerson, and A.G. Martin, in *Atomic Physics 11*, edited by S. Haroche, J.C. Gay, and G. Grynberg (World Scientific, Singapore, 1989), p. 179.
- [121] C. Monroe, W. Swann, H. Robinson, and C. Wieman, “Very Cold Trapped Atoms in a Vapor Cell,” *Physical Review Letters* **65**, 1571 (1990).
- [122] C. Monroe, E. Cornell, and C. Wieman, in *Laser Manipulation of Atoms and Ions*, edited by E. Arimondo, W.D. Phillips, and F. Strumia (North-Holland, Amsterdam, 1992), pp. 361–377.
- [123] W. Ketterle, K.B. Davis, M.A. Joffe, A. Martin, and D.E. Pritchard, “High densities of cold atoms in a dark spontaneous-force optical trap,” *Physical Review Letters* **70**, 2253 (1993).
- [124] K.B. Davis, M.O. Mewes, M.A. Joffe, and W. Ketterle, in *Fourteenth International Conference on Atomic Physics* (University of Colorado, Boulder, Colorado, 1994).
- [125] W. Petrich, M.H. Anderson, J.R. Ensher, and E.A. Cornell, in *Fourteenth International Conference on Atomic Physics* (University of Colorado, Boulder, Colorado, 1994).
- [126] K.B. Davis, M.-O. Mewes, M.A. Joffe, M.R. Andrews, and W. Ketterle, “Evaporative Cooling of Sodium Atoms,” *Physical Review Letters* **74**, 5202 (1995).
- [127] W. Petrich, M.H. Anderson, J.R. Ensher, and E.A. Cornell, “A Stable, Tightly Confining Magnetic Trap for Evaporative Cooling of Neutral Atoms,” *Physical Review Letters* **74**, 3352 (1995).
- [128] M.H. Anderson, J.R. Ensher, M.R. Matthews, C.E. Wieman, and E.A. Cornell, “Observation of Bose-Einstein Condensation in a Dilute Atomic Vapor,” *Science* **269**, 198 (1995).

- [129] C.C. Bradley, C.A. Sackett, J.J. Tollet, and R.G. Hulet, “Evidence of Bose-Einstein Condensation in an Atomic Gas with Attractive Interactions,” Physical Review Letters **75**, 1687 (1995).
- [130] C.C. Bradley, C.A. Sackett, and R.G. Hulet, “Bose-Einstein Condensation of Lithium: Observation of Limited Condensate Number,” Physical Review Letters **78**, 985 (1997).
- [131] W. Ketterle, A. Martin, M.A. Joffe, and D.E. Pritchard, “Slowing and cooling atoms in isotropic laser light,” Physical Review Letters **69**, 2843 (1992).
- [132] M.A. Joffe, W. Ketterle, A. Martin, and D.E. Pritchard, “Transverse cooling and deflection of an atomic beam inside a Zeeman slower,” Journal of the Optical Society of America B **10**, 2257 (1993).
- [133] M.A. Joffe, Ph.d., Massachusetts Institute of Technology, 1993.
- [134] E. Arimondo, W.D. Phillips, and F. Strumia, in *International School of Physics “Enrico Fermi”, Course CXVIII* (North-Holland, Amsterdam, 1992).
- [135] H. Metcalf and P. van der Straten, “Cooling and trapping of neutral atoms,” Physics Reports **244**, 203 (1994).
- [136] C.S. Adams and E. Riis, “Laser cooling and trapping of neutral atoms,” Progress in Quantum Electronics **21**, 1 (1997).
- [137] E. Arimondo, M. Inguscio, and P. Violino, “Experimental determinations of the hyperfine structure in the alkali atoms,” Reviews of Modern Physics **49**, 31 (1977).
- [138] W.D. Phillips, J.V. Prodan, and H.J. Metcalf, “Laser cooling and electromagnetic trapping of neutral atoms,” Journal of the Optical Society of America B **2**, 1751 (1985).
- [139] W.D. Phillips, in *Laser Manipulation of Atoms and Ions*, edited by E. Arimondo, W.D. Phillips, and F. Strumia (North-Holland, Amsterdam, 1992), pp. 289–343.
- [140] W. Ketterle and D.E. Pritchard, in *Fundamentals of Quantum Optics III*, edited by F. Ehlotzky (Springer, Berlin, 1993), pp. 77–89.
- [141] M.H. Anderson, W. Petrich, J.R. Ensher, and E.A. Cornell, “Reduction of light-assisted collisional loss rate from a low-pressure vapor-cell trap,” Physical Review A **50**, R3597 (1994).
- [142] P.D. Lett, W.D. Phillips, S.L. Rolston, C.E. Tanner, R.N. Watts, and C.I. Westbrook, “Optical molasses,” Journal of the Optical Society of America B **6**, 2084 (1989).
- [143] W.H. Wing, “On neutral particle trapping in quasistatic electromagnetic fields,” Prog. Quant. Electr. **8**, 181 (1984).
- [144] A. Aspect, 1998.
- [145] W. Ketterle and N.J. van Druten, in *Advances in Atomic, Molecular, and Optical Physics*, edited by B. Bederson and H. Walther (Academic Press, San Diego, 1996), Vol. 37, pp. 181–236.

- [146] E. Majorana, Nuovo Cimento **9**, 43 (1932).
- [147] Y.V. Gott, M.S. Ioffe, and V.G. Tel'kovskii, Nuclear Fusion Supplement **3**, 1045 (1962).
- [148] D.E. Pritchard, “Cooling Neutral Atoms in a Magnetic Trap for Precision Spectroscopy,” Physical Review Letters **51**, 1336 (1983).
- [149] V.S. Bagnato, G.P. Lafyatis, A.G. Martin, E.L. Raab, R.N. Ahmad-Bitar, and D.E. Pritchard, “Continuous Stopping and Trapping of Neutral Atoms,” Physical Review Letters **58**, 2194 (1987).
- [150] J.D. Weinstein and K.G. Libbrecht, “Microscopic magnetic traps for neutral atoms,” Physical Review A **52**, 4004 (1995).
- [151] M.-O. Mewes, Ph.d., Massachusetts Institute of Technology, 1997.
- [152] L.V. Hau, B.D. Busch, C. Liu, Z. Dutton, M.M. Burns, and J.A. Golovchenko, “Near Resonant Spatial Images of Confined Bose-Einstein Condensates in the ‘4D’ Magnetic Bottle,” Physical Review A **58**, R54 (1998).
- [153] J. Weiner, in *Advances in Atomic, Molecular, and Optical Physics*, edited by B. Bederson and H. Walther (Academic Press, San Diego, 1995), Vol. 35, pp. 45 – 78.
- [154] P.W.H. Pinkse, A. Mosk, W. Weidmuller, M.W. Reynolds, and T.W. Huijmans, “One-dimensional evaporative cooling of magnetically trapped atomic hydrogen,” Physical Review A **57**, 4747 (1998).
- [155] D.S. Hall, M.R. Matthews, J.R. Ensher, C.E. Wieman, and E.A. Cornell, “The Dynamics of Component Separation in a Binary Mixture of Bose-Einstein Condensates,” Physical Review Letters **81**, 4531 (1998).
- [156] M.R. Matthews, D.S. Hall, D.S. Jin, J.R. Ensher, C.E. Wieman, E.A. Cornell, F. Dalfovo, C. Minniti, and S. Stringari, “Dynamic Response of a Bose-Einstein Condensate to a Discontinuous Change in Internal State,” Physical Review Letters **81**, 243 (1998).
- [157] D.S. Hall, M.R. Matthews, C.E. Wieman, and E.A. Cornell, “Measurements of Relative Phase in Two-Component Bose-Einstein Condensates,” Physical Review Letters **81**, 1543 (1998).
- [158] T. Esslinger, I. Bloch, and T.W. Hänsch, “Bose-Einstein condensation in a quadrupole-Ioffe-configuration trap,” Physical Review A **58**, R2664 (1998).
- [159] I. Bloch, T.W. Hänsch, and T. Esslinger, An atom laser with a cw output coupler, 1998.
- [160] I. Bloch, T.W. Hänsch, and T. Esslinger, Measurement of the spatial coherence of a trapped Bose gas at the phase transition, 1999, preprint.
- [161] C.J. Myatt, Ph.d., University of Colorado, 1997.
- [162] E. Cornell, J.R. Ensher, and C.E. Wieman, Experiments in Dilute Atomic Bose-Einstein Condensation, 1998.

- [163] C. Cohen-Tannoudji, J. Dupont-Roc, and G. Grynberg, *Atom-Photon Interactions* (Wiley, New York, 1992).
- [164] M.R. Andrews, D.S. Durfee, S. Inouye, D.M. Stamper-Kurn, H.-J. Miesner, and W. Ketterle, “Studies of Bose-Einstein Condensates,” *Journal of Low Temperature Physics* **110**, 153 (1998).
- [165] M.R. Andrews, Ph.d., Massachusetts Institute of Technology, 1998.
- [166] D.S. Jin, J.R. Ensher, M.R. Matthews, C.E. Wieman, and E.A. Cornell, “Collective Excitations of a Bose-Einstein Condensate in a Dilute Gas,” *Physical Review Letters* **77**, 420 (1996).
- [167] D.S. Jin, M.R. Matthews, J.R. Ensher, C.E. Wieman, and E.A. Cornell, “Temperature-Dependent Damping and Frequency Shifts in Collective Excitations of a Dilute Bose-Einstein Condensate,” *Physical Review Letters* **78**, 764 (1997).
- [168] J. Stenger, D.M. Stamper-Kurn, M.R. Andrews, A.P. Chikkatur, S. Inouye, H.-J. Miesner, and W. Ketterle, “Optically confined Bose-Einstein Condensates,” *Journal of Low Temperature Physics* **113**, 167 (1998).
- [169] E.W. Hagley, L. Deng, M. Kozuma, M. Edwards, M. Doery, P.S. Julienne, K. Helmerson, S.L. Rolston, and W.D. Phillips, “Measurement of the coherence length of a Bose-Einstein condensate,” *Physical Review Letters* **83**, 2113 (1999).
- [170] V. Bagnato, D.E. Pritchard, and D. Kleppner, “Bose-Einstein condensation in an external potential,” *Physical Review A* **35**, 4354 (1987).
- [171] G. Baym and C.J. Pethick, “Ground-State Properties of Magnetically Trapped Bose-Condensed Rubidium Gas,” *Physical Review Letters* **76**, 6 (1996).
- [172] M. Edwards and K. Burnett, “Numerical solution of the nonlinear Schrödinger equation for small samples of trapped neutral atoms,” *Physical Review A* **51**, 1382 (1995).
- [173] F. Dalfovo, S. Giorgini, L.P. Pitaevskii, and S. Stringari, “Theory of Bose-Einstein condensation in trapped gases,” *Reviews of Modern Physics* **71**, 463 (1999).
- [174] Y. Castin and R. Dum, “Bose-Einstein condensation in time dependent traps,” *Physical Review Letters* **77**, 5315 (1996).
- [175] Yu. Kagan, E.L. Surkov, and G. V. Shlyapnikov, “Evolution of a Bose gas under variations of the confining potential,” *Physical Review A* **54**, R1753 (1996).
- [176] F. Dalfovo, C. Minniti, S. Stringari, and L. Pitaevskii, “Nonlinear dynamics of a Bose condensed gas,” *Physics Letters A* **227**, 259 (1997).
- [177] M. Holland, D.S. Jin, M.L. Chiofalo, and J. Cooper, “Emergence of interaction effects in Bose-Einstein condensation,” *Physical Review Letters* **78**, 3801 (1997).
- [178] S. Giorgini, L.P. Pitaevskii, and S. Stringari, “Scaling and thermodynamics of a trapped Bose-condensed gas,” *Physical Review Letters* **78**, 3987 (1997).
- [179] S. Giorgini, L.P. Pitaevskii, and S. Stringari, “Thermodynamics of a trapped Bose-condensed gas,” *Journal of Low Temperature Physics* **109**, 309 (1997).

- [180] R. J. Dodd, K. Burnett, M. Edwards, and C. W. Clark, “Two-gas description of dilute Bose-Einstein condensates at finite temperature,” *Acta Physica Polonica* **93**, 45 (1998).
- [181] R.J. Dodd, C. W. Clark, M. Edwards, and K. Burnett, “Characterizing the coherence of Bose-Einstein condensates and Atom lasers,” *Optics Express* **1**, 282 (1997).
- [182] H. Wu and E. Arimondo, “Expansion cooling and heating for a thermal magnetic trapped gas,” *Physical Review A* **58**, 3822 (1998).
- [183] H. Wu and E. Arimondo, “Expansion of the non-condensed trapped Bose gas in Bose-Einstein condensation.,” *Europhysics Letters* **43**, 141 (1998).
- [184] A.S. Parkins and D.F. Walls, “The physics of trapped dilute-gas Bose-Einstein condensates,” *Physics Reports* **303**, 1 (1998).
- [185] S.R. de Groot, G.J. Hooyman, and C.A. ten Seldam, “On the Bose-Einstein condensation,” *Proc. Roy. Soc. London Ser. A* **203**, 266 (1950).
- [186] J.R. Ensher, D.S. Jin, M.R. Matthews, C.E. Wieman, and E.A. Cornell, “Bose-Einstein Condensation in a Dilute Gas: Measurement of Energy and Ground-State Occupation,” *Physical Review Letters* **77**, 4984 (1996).
- [187] E.P. Gross, *Nuovo Cimento* **20**, 454 (1961).
- [188] L.P. Pitaevskii, *Soviet Physics JETP* **13**, 451 (1961).
- [189] E. Tiesinga, C.J. Williams, P.S. Julienne, K.M. Jones, P.D. Lett, and W.D. Phillips, “A spectroscopic determination of scattering lengths for sodium atom collisions,” *Journal of Research of the National Institute of Standards and Technology* **101**, 505 (1996).
- [190] M. Holland and J. Cooper, “Expansion of a Bose-Einstein condensate in a harmonic potential,” *Physical Review A* **53**, R1954 (1996).
- [191] S. Giorgini, L.P. Pitaevskii, and S. Stringari, “Condensate fraction and critical temperature of a trapped interacting Bose gas,” *Physical Review A* **54**, R4633 (1996).
- [192] K. Huang, *Statistical Mechanics*, second edition ed. (Wiley, New York, 1987).
- [193] M. Bijlsma and H.T.C. Stoof, “Renormalization group theory of the three-dimensional dilute Bose gas,” *Physical Review A* **54**, 5085 (1996).
- [194] P. Grüter, D. Ceperley, and F. Laloë, “Critical Temperature of Bose-Einstein Condensation of Hard-Sphere Gases,” *Physical Review Letters* **79**, 3549 (1998).
- [195] A. Griffin, “Conserving and gapless approximations for an inhomogeneous Bose gas at finite temperatures,” *Physical Review B* **53**, 9341 (1996).
- [196] N.P. Proukakis, S.A. Morgan, S. Choi, and K. Burnett, “Comparison of gapless mean-field theories for trapped Bose-Einstein condensates,” *Physical Review A* **58**, 2435 (1998).

- [197] V.N. Popov, *Functional Integrals and Collective Modes* (Cambridge University Press, New York, 1987).
- [198] D.A.W. Hutchinson, E. Zaremba, and A. Griffin, “Finite temperature excitations of a trapped Bose gas,” *Physical Review Letters* **78**, 1842 (1997).
- [199] R.J. Dodd, Mark Edwards, C.W. Clark, and K. Burnett, “Collective excitations of Bose-Einstein condensed gases at finite temperatures,” *Physical Review A* **57**, R32 (1998).
- [200] A. Minguzzi, S. Conti, and M.P. Tosi, “The internal energy and condensate fraction of a trapped interacting Bose gas,” *Journal of Physics: Condensed Matter* **9**, L33 (1997).
- [201] Yu. Kagan, in *Bose-Einstein Condensation*, edited by A. Griffin, D.W. Snoke, and S. Stringari (Cambridge University Press, Cambridge, 1995), p. 202.
- [202] H.T.C. Stoof, in *Bose-Einstein Condensation*, edited by A. Griffin, D.W. Snoke, and S. Stringari (Cambridge University Press, Cambridge, 1995), pp. 226–245.
- [203] R. Walser, J. Williams, J. Cooper, and M. Holland, “Quantum kinetic theory for a condensed bosonic gas,” *Physical Review A* **59**, 3878 (1999).
- [204] C.W. Gardiner, P. Zoller, R.J. Ballagh, and M.J. Davis, “Kinetics of Bose-Einstein Condensation in a Trap,” *Physical Review Letters* **79**, 1793 (1997).
- [205] C.W. Gardiner and P. Zoller, “Quantum kinetic theory: a quantum kinetic master equation for condensation of a weakly interacting Bose gas without a trapping potential,” *Physical Review A* **55**, 2902 (1997).
- [206] D. Jaksch, C.W. Gardiner, and P. Zoller, “Quantum kinetic theory. II. Simulation of the quantum Boltzmann master equation,” *Physical Review A* **56**, 575 (1997).
- [207] C.W. Gardiner and P. Zoller, “Quantum kinetic theory. III. Quantum kinetic master equation for strongly condensed trapped systems,” *Physical Review A* **58**, 536 (1998).
- [208] D. Jaksch, C.W. Gardiner, K.M. Gheri, and P. Zoller, “Quantum kinetic theory. IV. Intensity and amplitude fluctuations of a Bose-Einstein condensate at finite temperature including trap loss,” *Physical Review A* **58**, 1450 (1998).
- [209] C.W. Gardiner, M.D. Lee, R.J. Ballagh, M.J. Davis, and P. Zoller, “Quantum kinetic theory of condensate growth: comparison of experiment and theory,” *Physical Review Letters* **81**, 5266 (1998).
- [210] E. Arimondo, E. Cerboneschi, and H. Wu, Monte-Carlo Simulations for Evaporative Cooling in Bose-Einstein Condensation, 1998, preprint.
- [211] W. Ketterle, *McGraw-Hill 1999 Yearbook of Science and Technology* (McGraw-Hill, New York, 1999).
- [212] E.W. Hagley, L. Deng L, M. Kozuma, J. Wen, K. Helmerson, S.L. Rolston, and W.D. Phillips, “A well-collimated quasi-continuous atom laser,” *Science* **283**, 1706 (1999).

- [213] P.W.H. Pinkse, A. Mosk, M. Weidemüller, M.W. Reynolds, T.W. Huijmans, and J.T.M. Walraven, “Adiabatically changing the phase-space density of a trapped Bose gas,” *Physical Review Letters* **78**, 990 (1997).
- [214] R. Côté and V. Kharchenko, “Quasicondensate Droplet Formation in a Gas of Trapped Atomic Hydrogen,” *Physical Review Letters* **83**, 2100 (1999).
- [215] B.P. Anderson and M.A. Kasevich, “Macroscopic Quantum Interference from Atomic Tunnel Arrays,” *Science* **282**, 1686 (1998).
- [216] C. Raman, M. Köhl, R. Onofrio, D.S. Durfee, C.E. Kuklewicz, Z. Hadzibabic, and W. Ketterle, “Evidence for a critical velocity in a Bose–Einstein condensate,” *Physical Review Letters* **83**, 2502 (1999).
- [217] R. Onofrio, D.S. Durfee, C. Raman, M. Köhl, C.E. Kuklewicz, and W. Ketterle, Surface Excitations in a Bose-Einstein Condensate, 1999, preprint, cond-mat/9908340.
- [218] T.D. Lee and C.N. Yang, “Low-Temperature Behavior of a Dilute Bose System of Hard Spheres. II. Nonequilibrium Properties,” *Physical Review* **113**, 1406 (1959).
- [219] S. Stringari, “Dynamics of Bose-Einstein condensed gases in highly deformed traps,” *Physical Review A* **58**, 2365 (1998).
- [220] Mark Edwards, P.A. Ruprecht, K. Burnett, R.J. Dodd, and C.W. Clark, “Collective excitations of atomic Bose-Einstein condensates,” *Physical Review Letters* **77**, 1671 (1996).
- [221] S. Stringari, “Collective excitations of a trapped Bose-condensed gas,” *Physical Review Letters* **77**, 2360 (1996).
- [222] E. Zaremba, A. Griffin, and T. Nikuni, “Two-fluid hydrodynamic for a trapped weakly-interacting Bose gas,” *Physical Review A* **57**, 4695 (1998).
- [223] G.M. Kavoulakis and C.J. Pethick, “Quasi-one-dimensional character of sound propagation in elongated Bose-Einstein condensed clouds.,” *Physical Review A* **58**, 1563 (1998).
- [224] S.A. Morgan, R.J. Ballagh, and K. Burnett, “Solitary-wave solutions to nonlinear Schrödinger equations,” *Physical Review A* **55**, 4338 (1997).
- [225] W.P. Reinhardt and C.W. Clark, “Soliton dynamics in the collisions of Bose-Enstein condensates: an analogue of the Josephson effect,” *Journal of Physics B: Atomic, Molecular, and Optical Physics* **30**, L785 (1997).
- [226] A.D. Jackson, G.M. Kavoulakis, and C.J. Pethick, “Solitary waves in clouds of Bose-Einstein condensed atoms,” *Physical Review A* **58**, 2417 (1998).
- [227] C. Gay and A. Griffin, “First and Second Sound in a Weakly Interacting Dilute Bose Gas,” *Journal of Low Temperature Physics* **58**, 479 (1985).
- [228] D.A.W. Hutchinson, R.J. Dodd, and K. Burnett, “Gapless finite-T theory of collective modes of a trapped gas.,” *Physical Review Letters* **81**, 2198 (1998).

- [229] M. Olshanii, Finite-Temperature Collective Excitation of a Bose-Einstein Condensate, 1998, cond-mat/9807412.
- [230] M.J. Bijlsma and H.T.C. Stoof, Collisionless modes of a trapped Bose gas, 1998, cond-mat/9807051.
- [231] W.V. Liu, “Theoretical study of the damping of collective excitations in a Bose-Einstein condensate,” Physical Review Letters **79**, 4056 (1997).
- [232] L.P. Pitaevskii and S. Stringari, “Landau damping in dilute Bose gases,” Physical Letters A **235**, 398 (1997).
- [233] S. Giorgini, “Damping in dilute Bose gases: A mean-field approach,” Physical Review A **57**, 2949 (1998).
- [234] P.O. Fedichev, G.V. Shlyapnikov, and J.T.M. Walraven, “Damping of low-energy excitations of a trapped Bose-Einstein condensate at finite temperatures.,” Physical Review Letters **80**, 2269 (1998).
- [235] L.P. Pitaevskii, “Phenomenological theory of mode collapse-revival in a confined Bose gas,” Physics Letters A **229**, 406 (1997).
- [236] A.B. Kuklov, N. Chencinski N, A.M. Levine, W.M. Schreiber, and J.L. Birman, “Quantum dephasing of normal modes of a Bose-Einstein condensate in a magnetic trap,” Physical Review A **55**, R3307 (1997).
- [237] R. Graham, D.F. Walls, M.J. Collett, and E.M. Wright, “Collapses and Revivals of Collective Excitations in trapped Bose condensates,” Physical Review A **57**, 484 (1998).
- [238] A. Sinatra, P.O. Fedichev, Y. Castin, J. Dalibard, and G.V. Shlyapnikov, Dynamics of two interacting Bose-Einstein condensates, 1998, cond-mat/9809061.
- [239] A. Griffin and E. Zaremba, “First and second sound in a uniform Bose gas,” Physical Review A **56**, 4839 (1997).
- [240] V.B. Shenoy and T.-L. Ho, “First and second sound modes of a Bose-Einstein condensate in a harmonic trap.,” Physical Review Letters **80**, 3985 (1998).
- [241] A. Griffin, Wen-Chin Wu, and S. Stringari, “Hydrodynamic modes in a trapped Bose gas above the Bose-Einstein transition,” Physical Review Letters **78**, 1836 (1996).
- [242] G.M. Kavoulakis, C.J. Pethick, and H. Smith, “Damping of hydrodynamic modes in a trapped Bose gas above the Bose-Einstein transition temperature.,” Physical Review A **57**, 2938 (1998).
- [243] G.M. Kavoulakis, C.J. Pethick, and H. Smith, “Relaxation processes in clouds of trapped Bosons above the Bose-Einstein condensation temperature,” Physical Review Letters **81**, 4036 (1998).
- [244] L.P. Pitaevskii and S.Stringari, “Elementary Excitations in Trapped Bose-Einstein Condensed Gases Beyond the Mean-Field Approximation,” Physical Review Letters **81**, 4541 (1998).

- [245] M. Fliesser and R. Graham, Classical quasiparticle dynamics and chaos in trapped Bose condensates, 1998, cond-mat/9806115.
- [246] M. Naraschewski, H. Wallis, A. Schenzle, J.I. Cirac, and P. Zoller, “Interference of Bose condensates,” Physical Review A **54**, 2185 (1996).
- [247] D.S. Rokhsar, “Vortex stability and persistent currents in trapped Bose gases,” Physical Review Letters **79**, 2164 (1997).
- [248] E. J. Mueller, P.M. Goldbart, and Y. Lyanda-Geller, “Multiply connected Bose-Einstein condensed alkali-metal gases: Current carrying states and their decay,” Physical Review A **57**, R1505 (1998).
- [249] J. Javaneinen, S.M. Paik, and S.M. Yoo, “Persistent currents in a toroidal trap,” Physical Review A **58**, 580 (1998).
- [250] R.G. Hulet, 1998, invited talk at ICAP 16.
- [251] E.A. Burt, R.W. Ghrist, C.J. Myatt, M.J. Holland, E.A. Cornell, and C.E. Wieman, “Coherence, Correlations, and Collisions: What One Learns About Bose-Einstein Condensates from Their Decay,” Physical Review Letters **79**, 337 (1997).
- [252] J. Söding, D. Guéry-Odelin, P. Desbiolles, F. Chevy, H. Inamori, and J. Dalibard, Three-body decay of a rubidium Bose-Einstein condensate, 1998.
- [253] C.J. Myatt, E.A. Burt, R.W. Ghrist, E.A. Cornell, and C.E. Wieman, “Production of Two Overlapping Bose-Einstein Condensates by Sympathetic Cooling,” Physical Review Letters **78**, 586 (1997).
- [254] J.P. Burke, Jr., J.L. Bohn, B.D. Esry, and C.H. Greene, “Impact of the ^{87}Rb singlet scattering length on suppressing inelastic collisions,” Physical Review A **55**, R2511 (1997).
- [255] S.J.J.M.F. Kokkelmans, H.M.J.M. Boesten, and B.J. Verhaar, “Role of collisions in creation of overlapping Bose condensates,” Physical Review A **55**, R1589 (1997).
- [256] P.S. Julienne, F.H. Mies, E. Tiesinga, and C.J. Williams, “Collisional stability of double Bose condensates,” Physical Review Letters **78**, 1880 (1997).
- [257] E. Zaremba, “Sound propagation in a cylindrical Bose-condensed gas,” Physical Review A **57**, 518 (1998).
- [258] S. Stringari, “Dynamics of Bose-Einstein condensed gases in highly deformed traps,” Physical Review A **58**, 2385 (1998).
- [259] P.L. Gould, G.A. Ruff, and D.E. Pritchard, “Diffraction of atoms by light: the near-resonant Kapitza-Dirac effect,” Physical Review Letters **56**, 827 (1986).
- [260] P.J. Martin, B.G. Oldaker, A.H. Miklich, and D.E. Pritchard, “Bragg scattering of atoms from a standing light wave,” Physical Review Letters **60**, 515 (1988).
- [261] Yu. B. Ovchinnikov, J.H. Müller, M.R. Doery, E.J.D. Vredenbregt, K. Helmerson, S.L. Rolston, and W.D. Phillips, “Diffraction of a released Bose-Einstein condensate by a pulsed standing light wave,” Physical Review Letters **83**, 284 (1999).

- [262] M. Kozuma, L. Deng, E.W. Hagley, J. Wen, R. Lutwak, K. Helmerson, S.L. Rolston, and W.D. Phillips, “Coherent splitting of Bose–Einstein condensed atoms with optically induced Bragg diffraction,” *Physical Review Letters* **82**, 871 (1999).
- [263] E.M. Rasel, M.K. Oberthaler, H. Batelaan, J. Schmiedmayer, and A. Zeilinger, “Atom wave interferometry with diffraction gratings of light,” *Physical Review Letters* **75**, 2633 (1995).
- [264] D.M. Giltner, R.W. McGowan, and S.A. Lee, “Atom interferometer based on Bragg scattering from standing light waves,” *Physical Review Letters* **75**, 2638 (1995).
- [265] S. Bernet, M.K. Oberthaler, R. Abfalterer, J. Schmiedmayer, and A. Zeilinger, “Coherent frequency shift of atomic matter waves,” *Physical Review Letters* **77**, 5160 (1996).
- [266] Y. Torii, Y. Suzuki, M. Kozuma, T. Kuga, L. Deng, and E.W. Hagley, Mach–Zehnder Bragg interferometer for a Bose–Einstein condensate, 1999, preprint.
- [267] L. van Hove, *Physical Review* **96**, 249 (1954).
- [268] T.J. Greytak, in *Quantum Liquids*, edited by J. Ruvalds and T. Regge (North-Holland, New York, 1978).
- [269] Juha Javanainen, “Spectrum of Light Scattered from a Degenerate Bose Gas,” *Physical Review Letters* **75**, 1927 (1995).
- [270] J. Javanainen and J. Ruostekoski, “Off-resonance light scattering from low-temperature Bose and Fermi gases,” *Physical Review A* **52**, 3033 (1995).
- [271] R. Graham and D. Walls, “Spectrum of light scattered from a weakly interacting Bose–Einstein condensed gas,” *Physical Review Letters* **76**, 1774 (1996).
- [272] P.J. Price, “Density fluctuations at low temperature,” *Physical Review* **94**, 257 (1954).
- [273] Yu. Kagan, G. V. Shlyapnikov, and J. T. M. Walraven, “Bose-Einstein condensation in trapped atomic gases,” *Physical Review Letters* **76**, 2670 (1996).
- [274] D.-I. Choi and Q. Niu, “Bose-Einstein condensates in an optical lattice,” *Physical Review Letters* **82**, 2022 (1999).
- [275] M. Raizen, C. Salomon, and Q. Niu, “New light on quantum transport,” *Physics Today* **50**, 30 (1997).
- [276] F. Dalfovo, S. Giorgini, M. Guilleumas, L.P. Pitaevskii, and S. Stringari, “Collective and single-particle excitations of a trapped Bose gas,” *Physical Review A* **56**, 3840 (1997).
- [277] T.C. Killian, D.G. Fried, L. Willmann, D. Landhuis, S.C. Moss, T.J. Greytak, and D. Kleppner, “Cold Collision Frequency Shift of the 1S-2S Transition in Hydrogen,” *Physical Review Letters* **81**, 3807 (1998).
- [278] T.C. Killian, 1S–2S spectrum of a hydrogen Bose–Einstein condensate, 1999, preprint, physics/9908002.

- [279] E. Hecht, *Optics*, 2nd edition ed. (Addison-Wesley, Reading, 1989).
- [280] A. Röhrl, M. Naraschewski, A. Schenzle, and H. Wallis, “Transition from Phase Locking to the Interference of Independent Bose Condensates: Theory versus Experiment,” Physical Review Letters **78**, 4143 (1997).
- [281] H. Wallis and H. Steck, “Inseparable time evolution of anisotropic Bose-Einstein condensates,” Europhysics Letters **41**, 477 (1998).
- [282] A. Aspect, E. Arimondo, R. Kaiser, N. Vansteenkiste, and C. Cohen-Tannoudji, “Laser Cooling below the One-Photon-Recoil Energy by Velocity-Selective Coherent Population Trapping,” Physical Review Letters **61**, 826 (1988).
- [283] M. Kasevich and S. Chu, “Laser Cooling below a Photon Recoil with Three-Level Atoms,” Physical Review Letters **69**, 1741 (1992).
- [284] J.D. Miller, R.A. Cline, and D.J. Heinzen, “Far-off-resonance optical trapping of atoms,” Physical Review A **47**, R4567 (1993).
- [285] T. Takekoshi and R.J. Knize, “CO₂ laser trap for cesium atoms,” Optics Letters **21**, 77 (1995).
- [286] T. Kuga, Y. Torii, N. Shiokawa, T. Hirano, Y. Shimizu, and H. Sasada, “Novel Optical Trap of Atoms with a Doughnut Beam,” Physical Review Letters **78**, 4713 (1997).
- [287] Heun Jin Lee, Charles S. Adams, Mark Kasevich, and Steven Chu, “Raman cooling of atoms in an optical dipole trap,” Physical Review Letters **76**, 2658 (1996).
- [288] A. Kuhn, H. Perrin, W. Hänsel, and C. Salomon, in *Ultracold Atoms and Bose-Einstein-Condensation, 1996*, edited by Keith Burnett (Optical Society of America, Washington D.C., 1996), pp. 58–65.
- [289] C.S. Adams, H.J. Lee, N. Davidson, M. Kasevich, and S. Chu, “Evaporative Cooling in a Crossed Dipole Trap,” Physical Review Letters **74**, 3577 (1995).
- [290] L. Guttman and J.R. Arnold, “The nonparticipation of He⁶ in the superfluidity of He⁴,” Physical Review **92**, 547 (1953).
- [291] I.M. Khalatnikov, “Hydrodynamics of solutions of two superfluid liquids,” Soviet Physics JEPT **5**, 542 (1957).
- [292] W.B. Colson and A.L. Fetter, “Mixtures of Bose liquids at finite temperature,” Journal of Low Temperature Physics **33**, 231 (1978).
- [293] T.-L. Ho and V.B. Shenoy, “Binary mixtures of Bose condensates of alkali atoms,” Physical Review Letters **77**, 3276 (1996).
- [294] B.D. Esry, C.H. Greene, J.P. Burke, Jr., and J.L. Bohn, “Hartree-Fock theory for double condensates,” Physical Review Letters **78**, 3594 (1997).
- [295] E.V. Goldstein and P. Meystre, “Quasiparticle instabilities in multicomponent atomic condensates,” Physical Review A **55**, 2935 (1997).

- [296] C.K. Law, H. Pu, N.P. Bigelow, and J.H. Eberly, ““Stability Signature” in Two-Species Dilute Bose-Einstein Condensates,” Physical Review Letters **79**, 3105 (1997).
- [297] J. Williams, R. Walser, J. Cooper, E. Cornell, and M. Holland, “Nonlinear Josephson-type oscillations of a driven, two-component Bose-Einstein condensate,” Physical Review A **59**, R31 (1999).
- [298] M.R. Matthews, B.P. Anderson, P.C. Haljan, D.S. Hall, M.J. Holland, J.E. Williams, C.E. Wieman, and E.A. Cornell, “Watching a superfluid untwist itself: Recurrence of Rabi oscillations in a Bose-Einstein condensate,” Physical Review Letters **83**, 3358 (1999).
- [299] J. Williams, R. Walser, J. Cooper, E.A. Cornell, and M. Holland, Excitation of a Dipole Topological Mode in a Strongly Coupled Two-Component Bose-Einstein Condensate, 1999, preprint, cond-mat/9904399.
- [300] M.R. Matthews, B.P. Anderson, P.C. Haljan, D.S. Hall, C.E. Wieman, and E.A. Cornell, “Vortices in a Bose-Einstein Condensate,” Physical Review Letters **83**, 2498 (1999).
- [301] J.E. Williams and M.J. Holland, “Preparing topological states of a Bose-Einstein condensate,” Nature **401**, 568 (1999).
- [302] E.A. Cornell, D.S. Hall, M.R. Matthews, and C.E. Wieman, “Having it both ways: Distinguishable Yet Phase-Coherent Mixtures of Bose-Einstein Condensates,” Journal of Low Temperature Physics **113**, 151 (1998).
- [303] E.A. Cornell, J.R. Ensher, and C.E. Wieman, in *Bose-Einstein condensation in atomic gases, Proceedings of the International School of Physics “Enrico Fermi,” Course CXL*, edited by M. Inguscio, S. Stringari, and C.E. Wieman (IOS Press, Amsterdam, 1999).
- [304] T.-L. Ho, “Spinor Bose Condensates in Optical Traps,” Physical Review Letters **81**, 742 (1998).
- [305] T. Ohmi and K. Machida, “Bose-Einstein condensation with internal degrees of freedom in alkali atom gases,” Journal of the Physical Society of Japan **67**, 1822 (1998).
- [306] C.K. Law, H. Pu, and N.P. Bigelow, Quantum spins mixing in spinor Bose-Einstein condensates, 1998, cond-mat/9807258.
- [307] C.K. Law, H. Pu, and N.P. Bigelow, “Quantum spins mixing in spinor Bose-Einstein condensates,” Physical Review Letters **81**, 5257 (1998).
- [308] J.P. Burke, Jr., C.H. Greene, and J.L. Bohn, “Multichannel Cold Collisions: Simple Dependences on Energy and Magnetic Field,” Physical Review Letters **81**, 3355 (1998).
- [309] W.-J. Huang and S.-C. Gou, Field induced phase segregation and collective excitations of a trapped spinor Bose-Einstein condensate, 1999, preprint, cond-mat/9905435.
- [310] T. Isoshima, K. Machida, and T. Ohmi, Spin domain formation in spinor Bose-Einstein condensates, 1999, preprint, cond-mat/9905182.

- [311] P. Ao and S.T. Chui, "Binary Bose-Einstein condensate mixtures in weakly and strongly segregated phases," *Physical Review A* **58**, 4836 (1998).
- [312] H. Pu and N.P. Bigelow, "Properties of Two-Species Bose Condensates," *Physical Review Letters* **80**, 1130 (1998).
- [313] S.T. Chui and P. Ao, Quantum spinodal decomposition in multicomponent Bose-Einstein condensates, 1999, preprint, cond-mat/9902275.
- [314] H. Pu, C.K. Law, S. Raghavan, J.H. Eberly, and N.P. Bigelow, "Spin-mixing dynamics of a spinor Bose-Einstein condensate," *Physical Review A* **60**, 1463 (1999).
- [315] B.D. Josephson, *Physics Letters* **1**, 251 (1962).
- [316] J. Javanainen, "Oscillatory Exchange of Atoms between Traps Containing Bose condensates," *Physical Review Letters* **57**, 3164 (1986).
- [317] A. Smerzi, S. Fantoni, S. Giovanazzi, and S.R. Shenoy, "Quantum coherent atomic tunneling between two trapped Bose-Einstein condensates," *Physical Review Letters* **79**, 4950 (1997).
- [318] I. Zapata, F. Sols, and A.J. Leggett, "Josephson effect between trapped Bose-Einstein condensates," *Physical Review A* **57**, R28 (1998).
- [319] R.H. Fowler and L. Nordheim, "Electron emission in intense electric fields," *Proceedings of the Royal Society of London, Series A* **119**, 173 (1928).
- [320] W. Ketterle and H.-J. Miesner, "Coherence properties of Bose-Einstein condensates and atom lasers," *Physical Review A* **56**, 3291 (1997).
- [321] E.M. Wright, D.F. Walls, and J.C. Garrison, "Collapses and Revivals of Bose-Einstein Condensates Formed in Small Atomic Samples," *Physical Review Letters* **77**, 2158 (1996).
- [322] M. Lewenstein and L. You, "Quantum Phase Diffusion of a Bose-Einstein Condensate," *Physical Review Letters* **77**, 3489 (1996).
- [323] T. Wong, M.J. Collett, and D.F. Walls, "Interference of two Bose-Einstein condensates with collisions," *Physical Review A* **54**, R3718 (1996).
- [324] Juha Javanainen and Martin Wilkens, "Phase and phase diffusion of a split Bose-Einstein condensate," *Physical Review Letters* **78**, 4675 (1997).
- [325] Klaus Mølmer, "Phase collapse and excitations in Bose-Einstein condensates," *Physical Review A* **58**, 566 (1998).
- [326] P.R. Berman, *Atom Interferometry* (Academic Press, New York, 1996).
- [327] M. Morinaga, M. Yasuda, T. Kishimoto, and F. Shimizu, "Holographic Manipulation of a Cold Atomic Beam," *Physical Review Letters* **77**, 802 (1996).
- [328] P. Bouyer and M.A. Kasevich, "Heisenberg-limited spectroscopy with degenerate Bose-Einstein gases," *Physical Review A* **56**, R1083 (1997).
- [329] F. Dalfovo and S. Stringari, "Bosons in anisotropic traps: Ground state and vortices," *Physical Review A* **53**, 2477 (1996).